POLITECNICO
MILANO 1863

Department of Energy
Doctoral Program in Energy and Nuclear Science and Technology

TURBOMACHINERY OPERATING IN THE NON-IDEAL COMPRESSIBLE FLUID-DYNAMIC REGIME: A STEP TOWARDS NEXT-GENERATION POWER SYSTEMS

Doctoral dissertation of:
Alessandro Romei

Supervisor:
Prof. Giacomo Persico

Tutor:
Prof. Vincenzo Dossena

The Chair of the Doctoral Program:
Prof. Vincenzo Dossena

May 2021– Cycle XXXIII

ACKNOWLEDGEMENTS

Il dottorato di ricerca è come un lungo e faticoso giro in bicicletta. Ci sono periodi che ricordano impervie salite da affrontare, altri periodi in cui finalmente ti puoi godere la discesa. Talvolta, è necessario tirare il fiato sfruttando la scia. La maggior parte del tempo, però, lo passi pedalando a testa bassa. Ed è solo alla fine del giro che, guardando i chilometri percorsi e gli ostacoli superati, sei soddisfatto di quanto realizzato.

Il dottorato, però, non si limita ai soli contenuti di ricerca che sono discussi nella tesi. Il dottorato è un percorso che dura anni, spesso, come nel mio caso, in un momento della vita soggetto ad importanti cambiamenti. Guardandomi indietro, numerosi episodi significativi sono accaduti, molti belli, alcuni sfortunatamente meno. Proprio da quest'ultimi, si è dovuto ritrovare la forza per ripartire. Per questa ragione, ritengo doveroso ringraziare tutti coloro che hanno contribuito al successo di questo percorso.

La prima menzione è per mia madre, Maria Loreta. Grazie per esserci sempre e per tutto quello che hai fatto e fai per me. Mi rendo conto che non lo dico abbastanza spesso, ma sono infinitamente grato di essere tuo figlio.

In egual misure, uno speciale ringraziamento è riservato ad Elisa, per il suo incessante supporto in qualsiasi cosa faccia. Questo periodo di convivenza è uno dei più felice della mia vita ed il merito è interamente tuo.

Un immenso ringraziamento va ai miei nonni, nonna Elena e nonno Giovanni, per essere sempre stati i miei tifosi numero uno. Vi voglio infinitamente bene. Allo stesso modo, ringrazio mia zia Patrizia, mio zio Nando ed i miei cugini Noemi e Domenico, per essere una parte fondamentale della mia famiglia.

Infine, un sincero ringraziamento va al mio supervisore prof. Giacomo Persico, le cui qualità scientifiche sono seconde solo a quelle umane. La tua fiducia nei miei confronti mi ha reso orgoglioso e spronato a dare il massimo, la tua guida scientifica ha rappresentato un faro che ha illuminato la mia ricerca.

Milano, Maggio 2021

Alessandro Romei

A mio nonno

SUMMARY

Energy efficiency is a broad topic that can fit different fields, from transportation to buildings and power systems. In this thesis, subdivided into three main chapters, the attention is posed to novel energy-conversion systems that convert thermal energy to electrical energy, such as organic Rankine cycles (ORCs) and supercritical carbon dioxide (sCO2) power systems. For both technologies, the system efficiency is strongly connected to the achievable efficiency of the turbomachinery components, whose design practices cannot rely on several decades of experimental activities. A straightforward reworking of established design criteria may lead to shortcomings, owing to the unconventional gas dynamics underlying ORC and sCO_2 turbomachinery, which considerably differs from the one based on the ideal-gas thermodynamics. With the goal of developing dedicated design rules that can enable high-efficient ORC and sCO_2 turbomachinery, the original contribution of this research is twofold: first, to advance the present knowledge on turbomachinery operating in the so-called non-ideal compressible fluid-dynamics (NICFD) regime, and second, to develop a number of computational tools that can be instrumental for the design and the analysis of such complex energy devices.

The first chapter discusses the development of an automated shape-optimization technique based on high-fidelity computational fluid-dynamic (CFD) simulations. To tackle the prohibitive computational cost that would require a straight CFD-based optimization, a surrogate approach based on the Kriging interpolation is used. The optimization tool is then applied to a variety of test cases, involving stator and rotor cascades, transonic and supersonic flow regimes, ideal-like and significantly non-ideal flows, and accounting for single and multiple operating conditions. The substantial increase in efficiency for all reported cases indicates that shape-optimization techniques can be effectively used for the design of turbomachinery for which well-established design rules are presently not available.

The second chapter analyses the peculiar gas dynamics that onsets when $\mathit{\Gamma} < 1$, where $\mathit{\Gamma}$ is the fundamental derivative of gas dynamics. It is numerically demonstrated that non-ideal phenomena can occur in supersonic turbine flows, observing simultaneously a non-monotonic variation of the Mach number against the pressure along the expansion and non-ideal oblique shocks/rarefaction fans featuring an increase/decrease of the Mach number. Moreover, as the gas-dynamic evolution is found to be highly sensitive to the upstream stagnation state, the deviations in turbine performance given realistic field variabilities in the power cycles are quantified through an uncertainty-quantification framework based on a polynomial-chaos representation of the flow solver.

The third chapter deals with non-ideal effects arising in characteristic flows of carbon dioxide in turbomachinery for sCO_2 power systems. Based on a mean-line analysis, it is shown that competitive turbomachinery efficiencies can be obtained when accounting for the actual volumetric flow evolutions. As local flow accelerations within the compressor can promote phase transition, two CFD models capable of dealing with compressible non-ideal two-phase flows are developed and validated. Both models assume thermodynamic equilibrium but one model also introduces an additional simplification in the thermodynamic treatment. Finally, the simulation of a realistic centrifugal impeller operating in near-critical conditions is undertaken, with a particular emphasis on the effect of variable intake thermodynamic conditions on the compressor performance. As a result, an extended similitude theory that explicitly accounts for both non-ideal and two-phase effects is proposed.

CONTENTS

CHAPTER 1

INTRODUCTION

1.1 Research motivation: a more sustainable way of producing energy

While I am writing this thesis, I am taking full advantage of an easy access to electric energy: my laptop is charging, a small lamp is lighting up my desk and the espresso machine is working hard to provide me the correct amount of caffeine. Although this thesis sets a significant milestone in my career, the importance of converting and using energy is not only related to this specific achievement. Our entire society is built on the possibility of constantly making use of energy, from the manufacturing industries to the healthcare sector and transportation.

Until the beginning of the new millennium, Consumerism was the driving force of modern societies. The imperative order was to produce and consume at the expense of the environment, which was not even a tiny part of such dynamics. In a society in which the self-affirmation was mainly based on how many material things the individual can afford there were clearly no incentives in chasing sustainable development.

The turnaround occurred in 1997 with the Kyoto Protocol. On this occasion, more than one hundred and fifty countries agreed that anthropic activities were responsible for global warming and committed themselves to reduce greenhouse gas emissions. Nevertheless, the spark of sustainability did not propagate immediately in civil society but it took some years. Only in the last five years we are witnessing a heartfelt call for sustainable development by the majority of citizens, pushing industries and states to intensify their efforts into environmentally clean initiatives.

To comply with this virtuous worldview, the reduction of greenhouse-gas emissions, waste-heat recovery, flexible yet efficient operation of fossil-fuelled energy systems, the adoption of cleaner fuels, the increase in the renewable-energy share are presently the cornerstone of every research effort in the energy and environmental field. Although the general agreement among governments, industries, and civil societies in the pursuit of sustainable growth, there is an urgent need of increasing the overall effort in this direction. The *World Energy Outlook* by the International Energy Agency (2019) foresees a slight increase of CO_2 emissions by 2050 due to the rise of energy demand, notwithstanding the current incentives and declared policy intentions (included within the *Stated Policies Scenario* in figure 1.1). To meet the long-term temperature goal set by the Paris Agreements, i.e. a temperature increase below 2 °C with respect to pre-industrial levels, more actions are required, as shown by the *Sustainable Development Scenario* in the same figure. Among the various solutions, the efficiency improvement accounts for almost 30% of the CO_2 emission reduction needed to comply with the above temperature limits. Moreover, the efficiency increase can also help to boost the competitiveness of the energy system from an economic standpoint, thus representing a valuable option that can conjugate both economic and environmental aspects.

Energy efficiency is a broad topic that can fit different fields, from transportation to buildings and power systems. In this work, the attention is posed on energy-conversion systems that convert thermal energy, which can come from combustion or from the waste heat of an energy-intensive process, to mechanical energy, which is then converted into electric energy. Historically, the conversion from thermal to electrical energy usually relied on closed Rankine cycles based on steam or open Joule-Brayton cycles based on air, where open and closed refer to whether the working fluid mixes with the hot gases or not. Although these technologies are well-established for fossil fuels, they can perform sub-optimally when the aim is to exploit other kinds of hot sources. A major step in efficiency improvement can be represented by developing tailored technologies for the specific energy-conversion problem without reworking existing solutions, which may be intrinsically limited from a thermodynamic perspective. Within this framework, organic Rankine cycles (ORCs) and supercritical carbon dioxide (sCO_2) cycles are promising solutions that can outperform conventional technologies based on steam and air for a variety of applications and temperature levels, as shown in figure 1.2.

As regards ORCs, the freedom to select a working fluid alternative to water is particularly

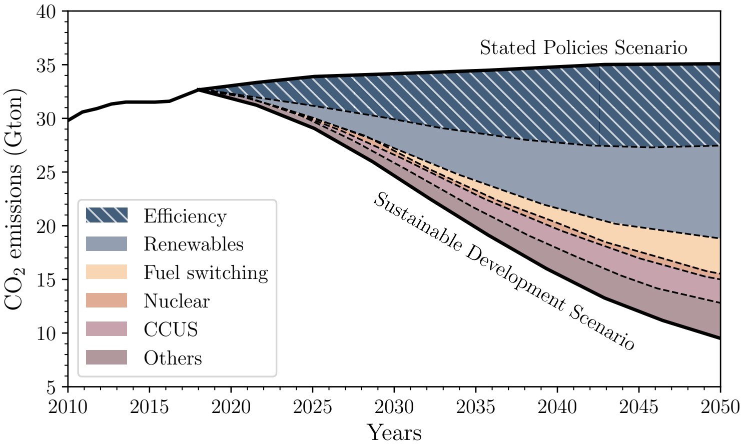

FIGURE 1.1. CO$_2$ emission reduction as foreseen by a *Sustainable Development Scenario* (i.e. to meet the temperature goal established by the Paris Agreement) relative to the *Stated Policies Scenario* (i.e. including existing policy framework and announced policy intentions) in the period 2010–2050 (International Energy Agency, 2019).

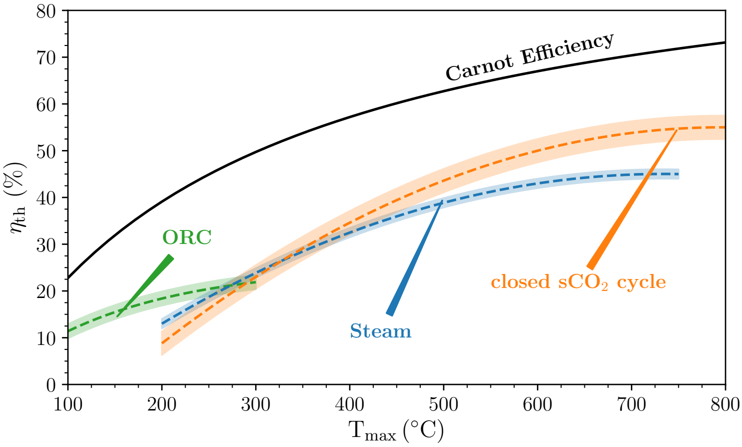

FIGURE 1.2. Potential efficiency improvement provided by ORC and sCO$_2$ power systems compared to conventional steam power plants for different temperature levels (reproduced from Ahn *et al.* (2015)). The Carnot efficiency assumes 15 °C as the minimum temperature.

attractive for low-temperature ($T_{max} \sim 150-300$°C) applications, such as geothermal (Astolfi *et al.*, 2014) and small biomass plants (Pantaleo *et al.*, 2017), industrial-scale waste-heat recovery (Yu *et al.*, 2016) and low-temperature solar-powered systems (Freeman *et al.*, 2015). The working fluid is generally an organic compound, which allows for an optimal design of the turbine and for a better match of temperature profiles between the hot source and the corresponding cycle heating (Macchi, 2017). As a drawback, organic fluids suffer from low thermal stability, preventing their usage for high-temperature applications ($T_{max} > 300$°C). Several technical options are discussed in literature (see, e.g., Astolfi, 2017, for a review); among them, the transcritical (or supercritical) layout can

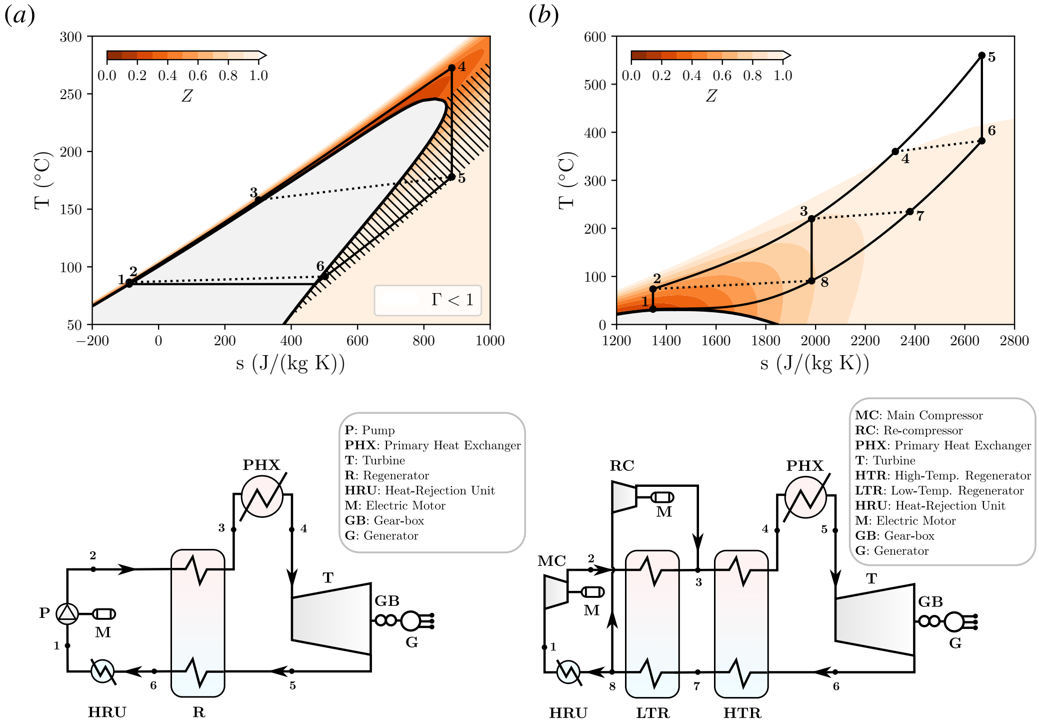

FIGURE 1.3. Two potential solutions to boost the efficiency of energy-conversion systems: (*a*) the transcritical organic Rankine cycle (regenerative layout) with MM (hexamethyldisiloxane, $C_6H_{18}OSi_2$) as working fluid and (b) the supercritical CO_2 cycle (recompressed layout). The ideal thermodynamic cycles are represented on the temperature–specific entropy plane in the top panels, while the corresponding components and their relative arrangements are reported in the bottom panels.

achieve higher efficiency than its subcritical counterpart at the expense of a higher investment cost (Colonna *et al.*, 2008; Schuster *et al.*, 2010; Lai *et al.*, 2011). In particular, heating the fluid at pressure larger than the critical one produces a temperature profile that generally matches better the temperature profile of a variable hot source. As a consequence, the second-law efficiency is expected to increase with respect to the conventional subcritical cycle. This is particularly relevant in the field of renewable sources and waste-heat recovery, in which the second-law efficiency is a better measure of the overall conversion process as it also takes into account the utilization of the available source (as opposed to the first-law efficiency, which just considers the quality of the power block by itself). An example of transcritical ORC is shown in figure 1.3(*a*), in which the ideal transformations that constitute the thermodynamic cycle along with a sketch of the main components are reported.

On the other hand, sCO_2 power systems are gaining popularity to exploit high-temperature thermal sources ($T_{max} \sim 400 - 700$°C), ranging from nuclear (Dostal, 2004) to concentrating solar power (Neises & Turchi, 2014) and waste heat recovery (Poerner & Rimpel, 2017; Marchionni *et al.*, 2020). The core idea behind this cycle, which is rooted in the pioneering work of Angelino (1968), is to have the compression process close to the thermodynamic critical point of CO_2 ($T_c = 30.98$ °C, $P_c = 73.77$ bar), wherein the critical temperature is in the order of ambient conditions. This process allows for a considerable saving of the compression work owing to the liquid-like fluid properties, thus increasing the overall conversion efficiency. As a result, sCO_2 plants exhibit overall higher conversion efficiency, simpler plant layout, and smaller turbomachinery sizes with respect to advanced steam power cycles (Musgrove & Wright, 2017). Moreover, the flexibility and off-design performance can benefit from the overall smaller equipment sizes and plant footprint. Several cycle arrangements are also proposed for sCO_2 power systems (see, e.g., Crespi *et al.*, 2017*b*, for a review). For illustrative purposes, the recompressed layout is reported in figure 1.3(*b*) in terms of thermodynamic transformations and main constitutive components.

Notwithstanding their theoretical potential, the lack of consolidated design experience has hindered the widespread of these power systems in the energy market. On the one hand, ORCs are well-established in geothermal power systems but struggle to succeed in other attractive fields, such as low-temperature waste-heat recovery from the industrial sector. On the other hand, sCO_2 power cycles are characterized by a technology readiness level that has not achieved market maturity yet. For both technologies, the overall plant efficiency is strongly related to the achievable efficiency of the turbomachinery components (Colonna *et al.*, 2015; Allison *et al.*, 2017), whose design practices cannot rely on several decades of experimental activities and in-field operation. A straightforward reworking of design criteria established in other fields may lead to shortcomings, owing to the unconventional gas dynamics underlying ORCs and sCO_2 turbomachinery, which considerably differs from the one based on the ideal-gas thermodynamics. Therefore, the understanding of such peculiar gas dynamics and its implication on turbomachinery design and performance becomes mandatory to boost the competitiveness of novel power cycles such as ORCs and sCO_2 systems.

1.2 The role of non-ideal compressible fluid dynamics

The non-ideal compressible fluid dynamics (NICFD) is established as a branch of fluid mechanics that deals with the motion of compressible fluids not obeying the ideal-gas thermodynamics. NICFD encompasses fluid flows in the two-phase (vapour-liquid) region and in what is often referred to as the dense-gas region, by contrast with the dilute-gas region where the ideal-gas approximation provides satisfactory results.

Although there is not a clear boundary between ideal and non-ideal gas dynamics, two thermodynamic parameters can be conveniently used to quantify the deviation from the ideal-gas model. The first parameter is the compressibility factor Z

$$Z = \frac{v}{v_{id}} = \frac{Pv}{\mathcal{R}T} \tag{1.1}$$

where v is the specific volume, $v_{id} = (\mathcal{R}T)/P$ is the specific volume predicted by the ideal-gas law, P is the pressure, T is the temperature and $\mathcal{R} = R/\mathcal{M}$ is the specific gas constant, where $R = 8314\,\mathrm{J/(kmol\,K)}$ is the universal gas constant and $\mathcal{M}$ is the molar mass. Z explicitly measures the deviation with respect to the thermal equation of state $P = P(T, v)$ of an ideal gas (Callen, 1985). In dilute-gas conditions, i.e. lower pressures and higher temperatures than their respective critical values, the ideal-gas behavior is recovered and $Z = 1$. By progressively increasing the pressure, Z reduces because the attractive intermolecular forces yield a specific volume lower than the ideal one. Values of Z below the unity are typically found close to the vapour-liquid saturation curve. In this thermodynamic region, the ideal-gas model is not accurate anymore and more sophisticated equations of state should be used (see, e.g., Peng & Robinson, 1976; Martin & Hou, 1955; Span & Wagner, 2003*a*,*b*). At extremely high pressure, the repulsive intermolecular forces become predominant and Z exceeds the unity.

A second thermodynamic parameter that can be used to discriminate between an ideal and non-ideal behaviour is the so-called fundamental derivative of gas dynamics Γ

$$\Gamma = \frac{v^3}{2c^2}\left(\frac{\partial^2 P}{\partial v^2}\right)_s = 1 + \frac{c}{v}\left(\frac{\partial c}{\partial P}\right)_s \tag{1.2}$$

where s is the specific entropy and $c = \sqrt{(\partial P/\partial \rho)_s}$ is the speed of sound, in which $\rho = 1/v$ is density. Γ is a non-dimensional measure of the curvature of isentropes in the (P, v)–plane or, equivalently, of the sound speed variation with pressure in isentropic processes. If $\Gamma > 1$, the speed of sound increases upon isentropic compressions; this is the typical behaviour of ideal gases with constant specific heats for which $\Gamma_{id} = (\gamma + 1)/2$, where $\gamma > 1$ is the ratio of specific heats. It follows that $1 < \Gamma \leqslant 1.33$ for an ideal gas with constant specific heats. Thermodynamic states exhibiting $\Gamma < 1$ are found in the single-phase vapour region of molecularly complex fluids for pressures and temperatures of the order of their critical-point values (see, e.g., Thompson & Lambrakis, 1973; Cramer, 1989; Colonna & Guardone, 2006) and in the near-critical two-phase region of most substances (Nannan *et al.*, 2013). As opposed to the ideal gas dynamics, the speed of sound decreases following an isentropic compression if $\Gamma < 1$. Based on the sound-speed evolution in isentropic processes, i.e. on the sign of $\Gamma - 1$, it is convenient to distinguish between the *ideal gas-dynamic regime* if $\Gamma > 1$, whereby the usual ideal-gas behaviour is recovered, and the *non-ideal gas-dynamic regime* if $\Gamma < 1$. Fluid-dynamic effects associated with thermodynamic states featuring $\Gamma < 1$ include the non-monotonic variation of the Mach number across isentropic expansions (Cramer & Best, 1991; Cramer & Crickenberger, 1992), the discontinuous increase of the Mach number across oblique shocks (Gori *et al.*, 2017; Vimercati *et al.*, 2018). If the fluid is composed of sufficiently complex molecules, then it may exhibit negative values of Γ in a narrow vapour region close to the critical point, thus yielding non-classical phenomena (Thompson, 1971; Thompson & Lambrakis, 1973; Cramer & Kluwick, 1984; Menikoff & Plohr, 1989; Kluwick, 2001; Zamfirescu *et al.*, 2008; Guardone *et al.*, 2010). As the region $\Gamma < 0$ has a limited extent and requires operating conditions not of practical interest for ORC applications, the present thesis only deals with flows of substances exhibiting $\Gamma > 0$, thus excluding non-classical phenomena from the dissertation.

For the archetypal ORC and sCO$_2$ cycles in figure 1.3, a map of the compressibility factor is superposed, besides highlighting the region with $\Gamma < 1$. Both applications have to deal with compressible-fluid flows operating in the NICFD regime. Firstly, the ORC turbine ($4 \mapsto 5$ in figure 1.3(*a*)) expands in a region characterized by both $Z < 1$ and $\Gamma < 1$, depending on the complexity of the working fluid. Moreover, as a consequence of low values of the speed of sound for organic compounds, the flow regime is eventually supersonic (Persico & Pini, 2017), enhancing the differences with respect to paradigmatic turbine vanes adopted in steam and air applications. Supersonic flow regimes with $\Gamma < 1$ pave the way for the occurrence of peculiar gas-dynamic phenomena, which are not foreseen by the ideal-gas theory, e.g. oblique shocks that feature an increase in the Mach number. Secondly, the sCO$_2$ main compressor ($1 \mapsto 2$ in figure 1.3(*b*)) operates in the neighbourhood of the thermodynamic critical point, whereby $Z < 1$. Furthermore, excursions in the two-phase domain can occur (Rinaldi *et al.*, 2015; Hosangadi *et al.*, 2019) owing to local flow accelerations around the compressor blades. In simple fluids such as carbon dioxide, $\Gamma > 1$ in the single-phase region, but $\Gamma < 1$ in the two-phase region (even exhibiting $\Gamma < 0$ in the near-critical two-phase domain (Nannan *et al.*, 2013)). Again, any conventional design criterion can hardly yield optimized efficiencies in such peculiar contexts without explicitly accounting for the above non-ideal effects.

1.3 Research objectives and outcomes

Notwithstanding the significant theoretical efforts to describe non-ideal compressible flows, the technical implications on turbomachinery design and operation are largely unknown. The extension of classical design criteria to turbomachinery operating in the NICFD regime can lead to shortcomings or sub-optimal performance. The difficulties in measuring high-temperature and high-pressure flows close to the saturation curve or the thermal-stability limit of the working fluid restrict experimental activities to simplified nozzle geometries (Head *et al.*, 2016; Lettieri *et al.*, 2017; Spinelli *et al.*, 2019), hindering the establishment of tailored design rules for turbomachinery.

To circumvent this lack of information, automated shape-optimization techniques based on high-fidelity computational fluid-dynamic (CFD) simulations can provide high-efficient turbomachinery profiles while inherently coping with non-ideal thermodynamics. To this end, the first part of this work is devoted to the formulation of a surrogate-based shape-optimization framework. The optimization tool is then applied to a variety of test cases, involving stator and rotor cascades, transonic and supersonic flow regimes, ideal-like and significantly non-ideal flows, and accounting for single and multiple operating conditions. The increase in efficiency for all reported cases indicates that shape-optimization techniques can be effectively used in designing turbomachinery for which well-established design rules are presently not available.

Alongside the development of shape-optimization techniques, the understanding of the underlying physics and its implications on turbomachinery flow fields is of paramount importance to control the performance. Up to the date of this thesis, many non-ideal phenomena are only predicted in simplified configurations and whether such non-ideal effects can also occur in turbomachinery flows is still unclear. An original contribution of this thesis is the first-ever assessment of non-ideal phenomena in supersonic turbine flows, such as the non-monotonic variation of the Mach number against the pressure along an expansion process and non-ideal oblique shocks/rarefaction fans featuring an increase/decrease of the Mach number. The occurrence of these phenomena is connected with the thermodynamic region identified by $\Gamma < 1$. As such, an uncertainty-quantification strategy combined with CFD simulations is devised to evaluate the turbine performance in presence of operational uncertainty that may cause a departure from the NICFD domain. This analysis elucidates the role of Γ on the part-load behaviour of the turbine, providing valuable information to the designer and minimizing the risk of potential pitfalls induced by non-ideal operation.

The above non-ideal effects are not observed in single-phase simple-fluid flows such as carbon dioxide. Nonetheless, the large volumetric departure from the ideal-gas model still poses some challenges on the aerodynamic design of the centrifugal compressor for sCO_2 power systems. To this end, a comprehensive analysis of the maximum achievable efficiency in presence of such non-ideal effects is performed, and the subsequent impact on the power cycle is quantified. It is shown that competitive efficiencies can be obtained when accounting for the real volumetric flow evolutions in the early design phase. The analysis only involves single-phase sCO_2 flows, but local flow accelerations can also promote two-phase flows in the near-critical region. The challenges connected with the simulation of two-phase compressible non-ideal flows are tackled in the last part of the manuscript. CFD strategies are ultimately developed to simulate such two-phase flows, conjugating the need for a reduced computational cost with an adequate solution accuracy. Finally, one of the developed methods is used to simulate the flow within a centrifugal compressor, purposely designed for realistic sCO2 applications. Particular emphasis is devoted to the understanding of the influence of variable intake thermodynamic conditions on the compressor performance and operability. As a result, marked deviations are encountered when applying the classical similitude to scale performance maps. Combining CFD simulation with analytic development and physical insight, an extended similitude theory that explicitly accounts for both non-ideal and two-phase effects is ultimately illustrated.

1.4 Outline of the thesis

The thesis is structured as follows.

Chapter 2 delineates the surrogate-based shape-optimization framework. First, the optimization strategy is discussed and a number of parametric studies are reported to tune the main hyperparameters of the surrogate model. To illustrate the optimizer potentialities, several optimization tasks are considered: single- and multi-point constrained optimizations of a converging-diverging nozzle cascade and a coupled stator-rotor constrained optimization of a transonic centrifugal stage. Besides improving the performance, detailed aerodynamic analyses unveil the rationale that stands behind the optimized configurations, laying the foundation for physics-based design criteria of such unconventional cascades.

Chapter 3 discusses non-ideal phenomena in the context of supersonic cascades for ORC applications. After recalling the ground theory of non-ideal steady supersonic flows, a number of converging-diverging turbine profiles are optimized for ideal-like and non-ideal conditions. The boundary conditions are selected to observe non-ideal effects that include the non-monotonic variation of the Mach number across expansions and the discontinuous increase of the Mach number across oblique shocks. The advantages and disadvantages of operating in non-ideal conditions are clearly stated, generalizing the specific findings by virtue of theoretical and analytical considerations. An uncertainty-quantification strategy that exploits a polynomial-chaos representation of the flow solver is also devised to quantify the departure from the upstream total state on the cascade performance. Gas-dynamic phenomena contributing to the change in cascade losses are thoroughly discussed and several recommendations are provided to make the designer aware of potential pitfalls associated with non-ideal flows.

Chapter 4 outlines non-ideal features in the context of centrifugal compressors for sCO_2 power systems. At first, preliminary designs are performed coupling mean-line analyses with evolutionary optimization algorithms to explore the sensitivity of the maximum achievable efficiency on the degree of non-ideality. A further step is done to quantify the impact of turbomachinery efficiency on the corresponding power cycle. Finally, with the intent of simulating the flow evolution within sCO_2 centrifugal compressors, two CFD strategies that can handle two-phase non-ideal compressible flows are developed and validated against experimental data available in the scientific literature. Thanks to such computational methods, the sCO_2 flow within a centrifugal compressor operating in near-critical conditions is examined and the main implications on compressor performance and operability are exhaustively discussed.

Chapter 5 summarizes conclusions and draws recommendations for future research activities.

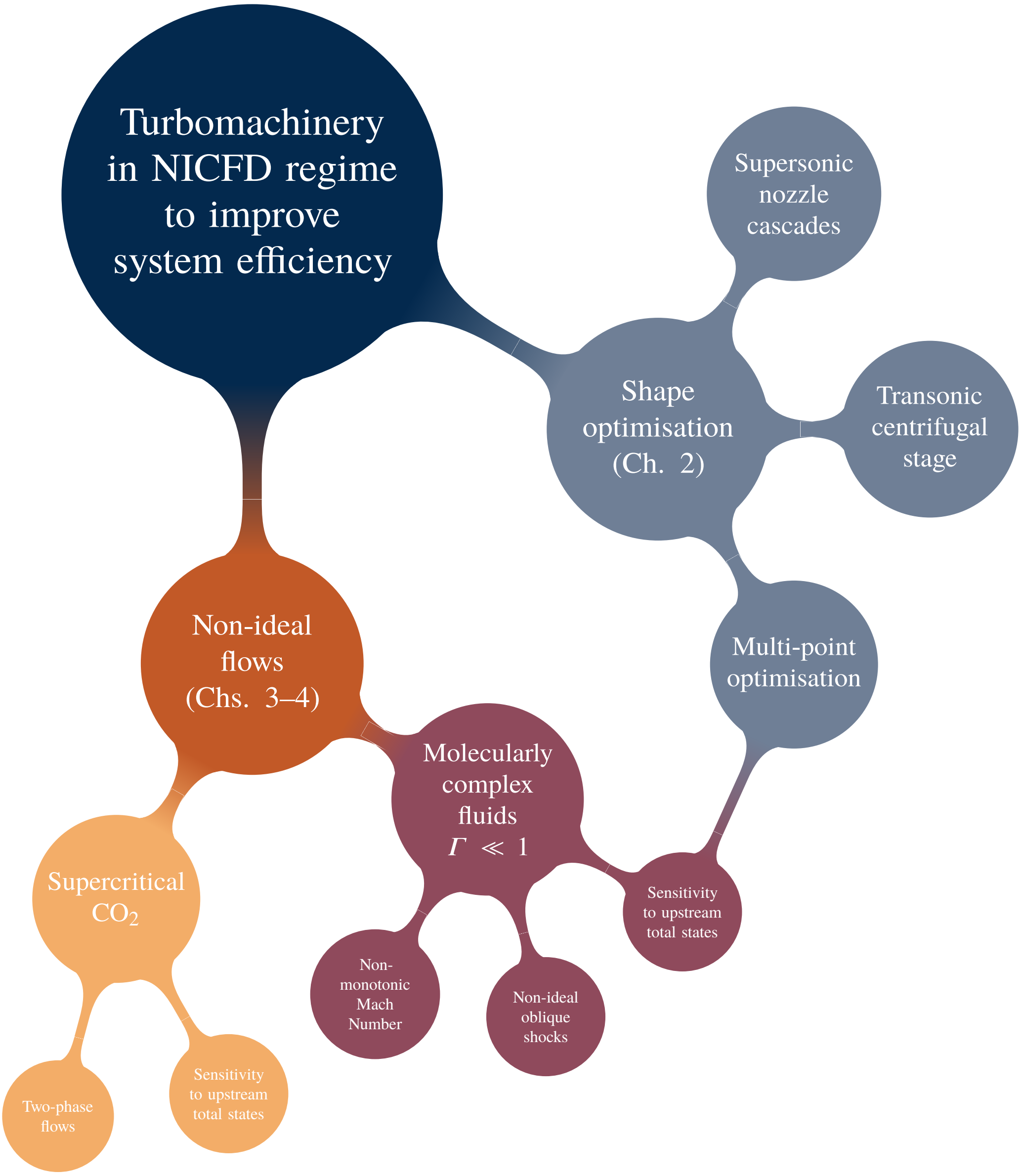

FIGURE 1.4. Structure of the thesis.

CHAPTER 2

SURROGATE-BASED SHAPE OPTIMIZATION OF TURBOMACHINERY PROFILES

This chapter illustrates a surrogate-based shape-optimization strategy for the design of turbomachinery blade profiles. In novel energy conversion systems, such as ORCs and sCO_2 *power systems, the non-conventional turbomachinery layout, as well as the non-ideal thermodynamics of the working fluid, significantly complicate the blade aerodynamic design. For such applications, well-established design rules are not available, and the design of turbomachinery may considerably benefit from the use of systematic optimization methods, especially in combination with high-fidelity CFD simulations, which inherently account for all salient flow features. Three shape optimizations are undertaken to showcase the optimizer capability, including single- and multi-point operating conditions, supersonic and transonic flow regimes, ideal-like and non-ideal flows, and stationary and rotating cascades.*

Some contents of this chapter are also discussed in:

Persico, G., Fernandez-Rodriguez, P., & Romei, A., (2019) High-fidelity shape optimization of non-conventional turbomachinery by surrogate evolutionary strategies, *Journal of Turbomachinery*, vol. 141(8): 081010 (11 pages), doi: 10.1115/1.4043252

Persico, G., Romei, A., Dossena, V., & Gaetani, P., (2018) Impact of shape-optimization on the unsteady aerodynamics and performance of a centrifugal turbine for ORC applications, *Energy*, vol. 165(A), pp. 2–11, doi: 10.1016/j.energy.2018.09.044

2.1 Aerodynamic shape optimization

The relevance of non-ideal effects in thermodynamic conditions of interest for ORC and sCO_2 power systems poses new and intriguing challenges in the aerodynamic design of the turbomachinery components. Empirical design rules, coming from the experience gained in steam- and air-based applications, and applied to this novel class of turbomachinery, can yield sub-optimal performance as many aerodynamic features are usually neglected in the process. The set-up of a dedicated experimental campaign to devise new design rules that include non-ideal effects is complicated by some practical difficulties, namely the thermal stability limit for organic compounds and the required high pressure for carbon dioxide in the near-critical region. Moreover, the similarity theory may not be accurate in presence of variable thermo-physical properties, thus constraining the thermodynamic conditions for an experimental campaign. Although experimental measurements in these peculiar thermodynamic conditions are still mandatory for a comprehensive validation of computational tools, the increase in computational resources has made possible the routine use of CFD simulations to perform dedicated optimization tasks, hence inherently including the above non-ideal effects within the design process of the machine.

The shape of a blade is crucial for its aerodynamic performance. Therefore, it is natural to imagine an optimization procedure that can maximize the aerodynamic performance by manipulating the blade geometry. One of the merits of including shape optimization in a design process is that its usage cuts across different applications, as opposed to empirical rules that hold only in those contexts from which they are also derived. Moreover, the application of rigorous optimization algorithms produces ’better’ solutions than considering just a few potential candidates, because a larger portion of the design space is explored during the optimization. Recalling that CFD simulations are time and computationally expensive, two classes of shape optimizations are customarily defined, depending on whether the gradient is available:

- *Adjoint method*: the gradient is available by solving the adjoint system of the governing equations (Giles & Pierce, 2000). As such, the optimization is carried out with gradient-based methods, which usually converge in few iterations.

- *Surrogate-based method*: the gradient is not available, hence the optimization has to be performed with gradient-free methods, which take many iterations to converge. A surrogate of the flow solver is usually employed to reduce the computational cost, which becomes otherwise unaffordable when multiple design variables are considered.

Each method has its own advantages and disadvantages, and one strategy can be preferable to the other depending on the application. As for the adjoint method, it requires the work-out of the CFD source code to solve the adjoint system of governing equations, which becomes more computationally expensive to be solved. However, this extra cost is compensated by the smaller number of iterations required by the optimization. The adjoint method can easily handle multi-dimensional problems, whose only additional cost is the potential higher number of iterations to converge. Examples of adjoint optimizations are thoroughly documented in literature, see, e.g., Walther (2012); Mueller & Verstraete (2017); Ntanakas *et al.* (2018); Vitale *et al.* (2020) only related to the turbomachinery field. The main disadvantage is that the optimization is based on gradient methods, hence the process can get stuck in local optima. The presence of multi-modal functions is not rare in aerodynamic design problems (Chernukhin & Zingg, 2013) and any alternative strategy that aims at mitigating this problem (e.g. multiple starting points) has to face a considerable increase in the computational cost.

In surrogate-based optimizations, meta-heuristic optimization algorithms, which allow scanning the entire design space, can be selected for the optimization loop. Moreover, constrained and multi-objective versions of meta-heuristic algorithms, such as evolutionary algorithms, can be straightforwardly formulated (Coello, 2000). Nonetheless, although such global algorithms have the potential to find the global optimum, they require many function evaluations to converge. The problem is solved by resorting to a surrogate of the computationally expensive simulation, which can be interrogated many times at a negligible computational cost. In this context, the initial training of the surrogate represents the major computational burden, which also scales with the dimensionality of the problem (only partially alleviated by the fact that the initial training can be easily parallelized). Although computational resources are getting increasingly more powerful, the initial surrogate interpolation is the main hurdle that may prevent including a large number of design variables in surrogate-based optimization. Moreover, the surrogate has to be reliable in representing the original flow solver in order to achieve the actual global optimum. To this end, many surrogate strategies that increment the surrogate accuracy during the optimization process are documented in the literature. The most popular surrogates are neural networks (Pierret & Van den Braembussche, 1999; Verstraete *et al.*, 2010) and Gaussian processes (Laurenceau & Sagaut, 2008; Reisenthel *et al.*, 2010). Usually, initial samples are generated with an appropriate sampling method, properly filling the design space, and are then evaluated with the high-fidelity solver. To reduce the computational burden in this phase, multi-fidelity approaches are also available, see, e.g., Han *et al.* (2013, 2017). Then, a first surrogate interpolation is performed on these solver responses. The way in which the surrogate is updated to increase its reliability is also subject to different choices. One possibility is to add the optimum individual to the initial pool of samples, recomputing each time the surrogate model. This strategy means that the user trusts that the initial surrogate interpolation is able to identify the zone where the global optimum is located and decides to locally increase the reliability of the surrogate to better exploit that region. Alternatively, in the context of Bayesian optimizations, the surrogate accuracy can be inferred and this information can be used during the update. With these methods, instead of directly minimizing the objective function, the optimization tries to maximize the so-called expected improvement (Jones *et al.*, 1998), which takes into account both the surrogate accuracy and the predicted value. In this way, the exploration of the design space is balanced with the exploitation of the optimal region. Finally, it is worth mentioning that the flexibility provided by a surrogate framework can be also used in conjunction with robust optimization tasks (Sabater & Goertz, 2019; Razaaly *et al.*, 2020), in which an additional surrogate representation approximates the function response in the stochastic space.

In this research work, a surrogate-based evolutionary shape-optimization methodology, named FORMA (Fluid-dynamic OptimizeR for turboMachinery Aerofoils), is developed and applied to different test cases. The optimization technique is constructed as a combination of (i) a flexible blade parameterization based on B-spline interpolation, (ii) a commercial compressible solver, including turbulence effects and a generalized thermodynamic treatment based on a look-up table (LUT) approach, and (iii) a gaussian-based surrogate model to reduce the overall computational cost. After detailing the main concepts behind the surrogate strategy in §2.2, FORMA is applied to single- and multi-point constrained optimizations of a supersonic turbine cascade for ORC applications in §2.3 and §2.4, respectively. Finally, the optimization of a centrifugal stage that includes both the stator and the rotor is carried out in §2.5, including aerodynamic and geometrical constraints.

2.2 Surrogate-based optimization

Before detailing the overall surrogate strategy, the mathematical foundations of the blade parametrization and of the surrogate model are recalled and the main assumptions are highlighted. The aim is to make the reader aware of the main modelling choices and their influence on the final outcome. Moreover, a clear overview of mathematics can also help to justify the need for parametric studies aiming at optimally setting the hyperparameters that stand behind these concepts.

On the contrary, the sampling and the optimization technique are not discussed in detail, because their optimal settings are nearly independent of this specific application. In the present manuscript, the Latin hypercube sampling (LHS) is selected as a space-filling technique, as it allows for uniform sampling in the prescribed design space (Ye, 1998). Other sampling techniques, such as quasi-Monte Carlo methods, can be employed as well, but the ability to uniformly filling the design space possesses the same aleatory component that also characterizes LHS. Likewise, there are many available alternatives for the meta-heuristic optimization algorithm. Nonetheless, the major weakness shared by all these methods lies in the lack of any mathematical proof for the convergence, in terms of both existence and rate, which prevents the identification of a superior optimization algorithm. As the optimization cost is not of concern, because the optimization is carried out on the surrogate, the well-known genetic algorithm (GA) (Mitchell, 1996) made available by the java engine for genetic algorithms (JEGA) library (Eddy, 2009) is used.

The entire surrogate strategy is built on top of the DAKOTA® environment (Adams *et al.*, 2017), whose correct implementation was verified on a large number of benchmark cases (see the associated user's guide). Several Python scripts automatize the whole shape-optimization process, interconnecting dedicated macros for the meshing and CFD solver with object-oriented shape parametrization code and with surrogate interpolations and optimizations.

2.2.1 Geometrical parametrization

The blade profile is an arbitrary curve, hence containing an infinite number of points. Therefore, the first step, represented in figure 2.1, involves the parametrization of the blade curve with a finite number of control points (CPs), whose orthogonal displacements d can be conveniently used as design variables in the optimization routine. Finding a compromise between the number of parameters and accuracy when reconstructing profiles is critical, bearing in mind that the choice of parameters has also to provide local effects on the final shape of the curve for the optimization aim. In this work, B-spline curves are shown to be a fair compromise to achieve this goal. A B-spline can be defined as a piecewise curve with components of degree n that provide local support, whose smoothness and continuity can be adjusted (Farin, 2006). As a result, the B-spline interpolation can be described as a weighted sum of basis functions as follows:

$$\mathbf{x}(u) = \sum_{j=0}^{L} \mathbf{CP}_j N_j^n(u) \tag{2.1}$$

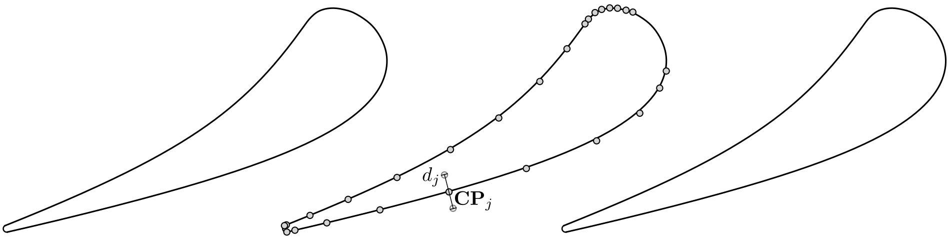

FIGURE 2.1. B-spline interpolation of a generic turbomachinery profile.

where $\mathbf{CP}_j$, with $j = 0, \dots, L$, are the control points, and $N_j^n(u)$ are the corresponding n-degree B-spline bases. For all cases showed in the following, the degree of B-spline bases is always set to $n = 3$. These bases can be defined recursively in the form:

$$N_j^n(u) = \frac{u - u_{j-1}}{u_{j+n-1} - u_{j-1}} N_j^{n-1}(u) + \frac{u_{j+n} - u}{u_{j+n} - u_j} N_{j+1}^{n-1}(u) \tag{2.2}$$

$$N_j^0(u) = \begin{cases} 0, & \text{if } u_{j-1} \leqslant u < u_j \\ 1, & \text{otherwise} \end{cases} \tag{2.3}$$

where $\{u_j\}_0^K$ is called the knot sequence, u is the mapping parameter used to build the curve, and $K = L + n - 1$. Knots can have different multiplicities inside the sequence, which define how many intertwined fundamental curves are included in each section of the B-spline. In this way, the shape is modified locally without changing neither the degree nor the continuity. In order to generate a B-spline curve whose CPs can be used as input parameters of the optimization algorithm, the baseline blade geometry needs to be interpolated. In this work, a least squares interpolation is used to find $L + 1$ CPs (L decided by the user), which entirely define the approximate B-spline curve $\mathbf{x}(u)$ of degree 3, given $P + 1$ data points and $K + 1$ knots. As in any other least squares minimization problem, the aim is to minimize the error in the form of:

$$\varepsilon = \sum_{i=0}^{P} ||\mathbf{p}_i - \mathbf{x}(w_i)||^2 \tag{2.4}$$

where $\{\mathbf{p}_i\}_0^P$ are the data points and $\{w_i\}_0^P$ are called the data parameters of the interpolation problem. Plugging the B-spline definition of equation 2.1 into equation 2.4, an expression for the error as a function of the CP positions is found, $\varepsilon = \varepsilon\left(\{\mathbf{CP}_j\}_0^L\right)$.

$$\varepsilon = \sum_{i=0}^{P} ||\mathbf{p}_i - \sum_{j=0}^{L} \mathbf{CP}_j N_j^3(w_i)||^2 \tag{2.5}$$

A classic least squares minimization is applied to the error, ending up with an expression of the form:

$$\sum_{j=0}^{L} \mathbf{CP}_j \sum_{i=0}^{P} N_j^3(w_i) N_k^3(w_i) = \sum_{i=0}^{P} \mathbf{p}_i N_k^3(w_i) \tag{2.6}$$

This is a linear set of equations that can be written as $\Theta \cdot \mathbf{CP} = \mathbf{b}$ and solved using any method of linear algebra. Given that Θ is positive definite, the Cholesky decomposition is used to solve the system, i.e. $\Theta = \mathrm{L} \cdot \mathrm{L}^\mathrm{T}$. A set of data parameters, $\{w_i\}_0^P$, must be provided to the algorithm. In FORMA, the sequence is built using a centripetal parametrization following the recursive implementation described in Lee (1989), which reads as

$$w_i = w_{i-1} + \frac{\sqrt{||\mathbf{p}_i - \mathbf{p}_{i-1}||_2}}{\sum_{i=0}^{P} \sqrt{||\mathbf{p}_i - \mathbf{p}_{i-1}||_2}} \tag{2.7}$$

$$w_0 = 0 \tag{2.8}$$

The knot sequence must also be assigned beforehand and it can be devised to break the symmetry of CP positions. In this way, a different number of CPs can be assigned in specific blade regions (see, for example, the cluster of CPs close to the leading edge in figure 2.1). In FORMA, the pressure and suction sides of the blade are generated with a single B-spline curve. The B-spline curve is then constrained to pass through the first and last data points using a multiplicity of $m = n$ in the ends.

In the definition of the blade parametrization, the trailing edge (TE) deserves separate consideration. As it is one of the thinnest parts of the blade, and structural and technological aspects may be predominant in its definition, the trailing edge is modelled with a fixed geometrical shape. Specifically, two alternatives are implemented in FORMA: circular and ellipsoidal shape. In the shape definition, two constraints must be strictly satisfied, i.e. the TE must pass through the first and the last point of the B-spline curve. Moreover, additional two constraints are highly desirable in this context, namely the TE has to be tangent to the first and to the last point of the B-spline curve to ensure smoothness and regularity in the overall blade shape. These four constraints have to match with the degree of freedom provided by the two above geometrical shapes. The circular geometry only features three degrees of freedom (center of the circle and radius), hence it is not possible to satisfy all the constraints. Therefore, the circular TE is forced to pass through the first and the last B-spline point, while the user can select the side (either suction side or pressure side) on which the first derivative is equalized. The ellipsoidal shape presents instead five degrees of freedom (the center of the ellipse, the two semi-axes and the rotation angle with respect to the x-axis), hence another condition has to be supplied along with the above four constraints. To comply with this requirement, the ellipse with the minimum eccentricity is considered. It means that the ellipsoidal shape closer (in $\mathcal{L}^2$ sense) to a circle is eventually selected among the infinite number of ellipses that fulfill the four constraints to ensure $\mathcal{C}^1$ continuity at the extremities.

Within the shape optimization strategy, the design variables are the displacement of CPs. In most cases, only a subset of the CPs provides consistent advantages in the fitness (anyhow such fitness is defined). In FORMA, the movable CPs are usually displaced along the local orthogonal direction with respect to the blade surface. The only exception involves the TE: as previously mentioned, the TE shape usually comes from technological and mechanical considerations, hence any change in this blade zone should be carefully evaluated. To favor a feasible design from a technological and mechanical perspective, the TE can only move rigidly, preserving the baseline thickness and shape. It means that only one CP out of four (unequivocally determining the TE shape) is allowed to move in the optimization process. The remaining control points will follow the movement through a rigid translation. To compute the local orthogonal direction, the first derivative of equation 2.1 has to be computed:

$$\frac{d}{dx}\mathbf{x}(u) = \sum_{j=0}^{L} \mathbf{CP}_j \frac{d}{dx} N_j^n(u), \tag{2.9}$$

where the problem consists in differentiating the B-spline bases, obtaining what follows:

$$\frac{d}{dx} N_j^n(u) = \frac{n}{u_{j+n-1} - u_{j-1}} N_j^{n-1}(u) - \frac{n}{u_{j+n} - u_j} N_{j+1}^{n-1}(u) \tag{2.10}$$

Merging the last two equations into a single expression and rearranging the terms, the following expression is found:

$$\frac{d}{dx}\mathbf{x}(u) = \sum_{j=0}^{L-1} \mathbf{Q}_j N_j^{n-1}(u) \tag{2.11}$$

The previous expression can be interpreted as a new B-spline curve of degree $n - 1$, with the same knot sequence but different control points $\mathbf{Q}_j$, defined as:

$$\mathbf{Q}_j = \frac{n}{u_{j+n} - u_j} \left(\mathbf{CP}_{j+1} - \mathbf{CP}_j \right) \tag{2.12}$$

As a consequence that the derivative of a B-spline curve is still a B-spline with the same knot sequence, the same algorithms that are used to generate the B-spline in a first-place can be also used to compute its first derivative in each point. In this way, the direction along which the movable CPs are displaced as well as the tangents at the B-spline extremities needed for the TE definition are computed in a straightforward way and at a negligible computational cost.

2.2.2 Kriging predictor

To tackle the high computational cost required by the optimization process, a surrogate of the flow response is introduced. The surrogate approximates the output response $y \in \mathbb{R}$ of the target quantity that is sought to be minimized (e.g., entropy production) or, equivalently, any non-linear constraint with respect to the design variables. Given $N \subseteq L$ movable CPs, the vector $\mathbf{d} = (d_1, d_2, \ldots, d_N) \in \mathbb{R}^N$ is the vector containing the corresponding orthogonal displacement that are involved in the optimization process. It is worth recalling that, given a generic vector $\mathbf{d}$, a unique blade design is identified by considering the displaced control points and the fixed ones. The surrogates can be then expressed in general terms as a map between the input parameters to the output quantity, $\mathbf{d} \mapsto y$.

To build this functional map, many surrogate models are currently available (the interested reader is referred to the review paper of Simpson *et al.* (2001)). After preliminary trials with different surrogates, the Kriging model (Martin & Simpson, 2005) is eventually selected in FORMA to approximate objective functions and non-linear constraints. A Kriging model states that any realization of the quantity of interest y comes from a distribution Y:

$$Y = \boldsymbol{\beta}^T \mathbf{f}(\mathbf{d}) + \varepsilon, \qquad \varepsilon \sim \mathcal{N}(\mathbf{0}, \boldsymbol{\Sigma}) \tag{2.13}$$

The first term $\boldsymbol{\beta}^T \mathbf{f}(\mathbf{d})$ incorporates the mean trend of the process, where $\mathbf{f}(\mathbf{d}) = (f_1(\mathbf{d}), f_2(\mathbf{d}), \ldots, f_h(\mathbf{d})) \in \mathbb{R}^H$ are functional bases that have to be decided a priori and $\boldsymbol{\beta} = (\beta_1, \beta_2, \ldots, \beta_h) \in \mathbb{R}^H$ are the regression coefficients. In the field of deterministic computer approximation, the choice of the mean trend is usually aleatory, based on the user's experience and the data available. Generally, the mean trend is not easily recognizable in high-dimensional space; if there is a clear correlation among the data, it is probably better to directly exploit this information as a surrogate rather than resorting to a Kriging modeling. For a general functional form, such as in equation 2.13, the model is usually known as *universal Kriging*. In absence of any information, the easiest choice is to use a simple constant as a regressor, then relying on the second term to pull the surface response through the observed data. In these circumstances, the general model in Equation 2.13 can be then simplified as:

$$Y = \beta_0 + \varepsilon, \qquad \varepsilon \sim \mathcal{N}(\mathbf{0}, \boldsymbol{\Sigma}) \tag{2.14}$$

which is known as *ordinary Kriging*. Finally, the constant μ can be provided by the user. Under this condition, the model takes the name of *simple Kriging*. In FORMA, the simple Kriging is not considered; different functional forms are discussed in §2.3.3 for a specific test case, including both the ordinary and the universal Kriging formulation, this latter built with linear and quadratic terms.

The second term $\varepsilon \sim \mathcal{N}(\mathbf{0}, \boldsymbol{\Sigma})$ represents the error of the linear regression and is modelled as a Gaussian and stationary random process, with zero mean and covariance:

$$\boldsymbol{\Sigma} = \sigma^2 R(\mathbf{d}_1, \mathbf{d}_2, \boldsymbol{\vartheta}) \tag{2.15}$$

where $\mathbf{d}_1$ and $\mathbf{d}_2$ represents two generic sets of movable control points, while $\boldsymbol{\vartheta} \in \mathbb{R}^N$ is a hyperparameter of the model. The process variance is the scalar σ^2 (unknown), whereas R identifies the spatial correlation function. If $y \sim Y$ is assumed to be continuous, also the error must be continuous since it is given by the difference of the output and its regressed prediction. It follows that, if $\mathbf{d}_1$ and $\mathbf{d}_2$ are two design variables that are close together, the relationship between them should be somehow stronger, corresponding to a larger covariance of the couple $(\mathbf{d}_1, \mathbf{d}_2)$, whilst the correlation between these two points is expected to be lower when they are far apart. There are different ways to model the spatial correlation function; the most common choice (which is the one implemented in FORMA) is to rely on a Gaussian function, which provides a relatively smooth and infinitely differentiable surface (Martin & Simpson, 2005). Since the problem is n-dimensional, after assuming that two generic sets $\mathbf{d}_1, \mathbf{d}_2$ are independent, a multivariate correlation function given by the product of each univariate correlation function is used.

$$R(\mathbf{d}_1, \mathbf{d}_2) = \prod_{i=1}^{N} e^{-\vartheta_i \left(d_{1_i} - d_{2_i}\right)^2} \tag{2.16}$$

Bearing in mind the ground assumptions of the Kriging model discussed so far, the next step is to build the predictor that realizes the desired map $\mathbf{d} \mapsto y$. Let $\{\tilde{\mathbf{d}}_1, \tilde{\mathbf{d}}_2, \ldots, \tilde{\mathbf{d}}_k\}$ be a set of k designs that are properly sampled in the design space (e.g. with LHS) and $\tilde{\mathbf{y}} = (\tilde{y}_1, \tilde{y}_2, \ldots, \tilde{y}_k) \in \mathbb{R}^K$ the corresponding responses evaluated through the CFD solver. This training set makes possible to build a linear predictor of the quantity of interest $\hat{y}$ at a future design $\mathbf{d}$, taking the general form:

$$\hat{y}(\mathbf{d}) = \boldsymbol{\lambda}(\mathbf{d})^T \, \tilde{\mathbf{y}} + \lambda_0 \tag{2.17}$$

Among various linear predictors, two features are selected: (i) the predictor is unbiased (the expected value matches the true value), and (ii) it minimises the mean square error (MSE) of the prediction:

$$\min_{\boldsymbol{\lambda}, \lambda_0} \quad \mathbb{E}\left[\boldsymbol{\lambda}(\mathbf{d})^T \tilde{\mathbf{y}} + \lambda_0 - y(\mathbf{d})\right]^2 \tag{2.18}$$

subject to the unbiasedness constraint, $\mathbb{E}\left[\boldsymbol{\lambda}(\mathbf{d})^T \tilde{\mathbf{y}} + \lambda_0 - y(\mathbf{d})\right] = 0$, which will just give $\lambda_0 = 0$. This interpretation (as opposed to the Bayesian perspective) clearly explains why Kriging models are also called best linear unbiased predictors (BLUP), where *best* is meant in $\mathcal{L}^2$ sense. By solving the minimization problem (the interested reader can find all the mathematical details in Stein (1999)), the universal Kriging predictor assumes the following expression:

$$\boxed{\hat{y}(\mathbf{d}) = \mathbf{f}(\mathbf{d})^T \hat{\boldsymbol{\beta}} + \mathbf{r}(\mathbf{d})^T \mathbf{R}^{-1} \left(\tilde{\mathbf{y}} - \mathbf{F}\hat{\boldsymbol{\beta}}\right)} \tag{2.19}$$

In the above expression, $\mathbf{F} \in \mathbb{R}^{K \times H}$, with generic element $f_{ij} = f_j(\tilde{\mathbf{d}}_i)$, with $i = 1, \ldots, k$ and $j = 1, \ldots, h$, represents the j-th basis function evaluated at the i-th sample. $\mathbf{R} \in \mathbb{R}^{K \times K}$ is the correlation matrix, which is composed by the spatial correlation function as defined in the equation 2.16 evaluated for all possible pairs of sampled designs:

$$\mathbf{R} = \begin{bmatrix} R(\tilde{\mathbf{d}}_1, \tilde{\mathbf{d}}_1) & R(\tilde{\mathbf{d}}_1, \tilde{\mathbf{d}}_2) & \ldots & R(\tilde{\mathbf{d}}_1, \tilde{\mathbf{d}}_k) \\ R(\tilde{\mathbf{d}}_2, \tilde{\mathbf{d}}_1) & R(\tilde{\mathbf{d}}_2, \tilde{\mathbf{d}}_2) & \ldots & R(\tilde{\mathbf{d}}_2, \tilde{\mathbf{d}}_k) \\ \vdots & \vdots & \ddots & \vdots \\ R(\tilde{\mathbf{d}}_k, \tilde{\mathbf{d}}_1) & R(\tilde{\mathbf{d}}_k, \tilde{\mathbf{d}}_2) & \ldots & R(\tilde{\mathbf{d}}_k, \tilde{\mathbf{d}}_k) \end{bmatrix}$$

The matrix $\mathbf{R}$ is positive semidefinite owing to the functional form of the adopted spatial correlation function. It is also symmetric because $R(\tilde{\mathbf{d}}_i, \tilde{\mathbf{d}}_j) = R(\tilde{\mathbf{d}}_j, \tilde{\mathbf{d}}_i)$ and the diagonal consists of all ones as $R(\tilde{\mathbf{d}}_i, \tilde{\mathbf{d}}_i) = 1$. The vector $\mathbf{r}(\mathbf{d}) \in \mathbb{R}^K$ contains the spatial correlation evaluated between the new design $\mathbf{d}$ and the k samples used in the regression process:

$$\mathbf{r}(\mathbf{d}) = \left[R(\mathbf{d}, \tilde{\mathbf{d}}_1), R(\mathbf{d}, \tilde{\mathbf{d}}_2), \ldots, R(\mathbf{d}, \tilde{\mathbf{d}}_k)\right] \tag{2.20}$$

Finally, $\hat{\boldsymbol{\beta}} \in \mathbb{R}^H$ is the generalised least squares estimate, i.e.

$$\hat{\boldsymbol{\beta}} = \left(\mathbf{F}^T\mathbf{R}^{-1}\mathbf{F}\right)^{-1}\mathbf{F}^T\mathbf{R}\tilde{\mathbf{y}} \tag{2.21}$$

It can be proved that the Kriging predictor in Equation 2.19 interpolates exactly the observations that are used in the model regression. In fact, $\mathbf{r}(\tilde{\mathbf{d}}_i) = \mathbf{R}(i,:)$ and $\mathbf{r}(\tilde{\mathbf{d}}_i)^T\mathbf{R}^{-1} = \mathbf{R}(i,:)^T\mathbf{R}^{-1} = \mathbf{e}_i$ where $\mathbf{e}_i$ is the the i-th unit vector, therefore:

$$\hat{y}(\tilde{\mathbf{d}}_i) = \mathbf{f}(\tilde{\mathbf{d}}_i)^T\hat{\boldsymbol{\beta}} + \mathbf{e}_i(\tilde{y} - \mathbf{F}\hat{\boldsymbol{\beta}}) = \mathbf{f}(\tilde{\mathbf{d}}_i)^T\hat{\boldsymbol{\beta}} + (y(\tilde{\mathbf{d}}_i) - \mathbf{f}(\tilde{\mathbf{d}}_i)^T\hat{\boldsymbol{\beta}}) = y_i \tag{2.22}$$

However, such attractive property has to cope with a numerical issue related to the correlation matrix $\mathbf{R}$, which is usually ill-conditioned[1]; the inversion of an ill-conditioned matrix can lead to significant numerical inaccuracies. A possible remedy to this problem is to add a small nugget effect, which improves the conditional number of the matrix. Therefore, instead of taking the inverse of the correlation matrix $\mathbf{R}^{-1}$, $(\mathbf{R} - \lambda_n\underline{\mathbf{I}})^{-1}$ is inverted, where λ_n is a small positive value ($\lambda_n = 10^{-6}$ in this work). As a consequence, the Kriging predictor does not exactly interpolate the observed data, but the process that leads to the identification of the Kriging predictor is less prone to numerical errors.

As a last feature, the mean-square error of the linear predictor $\hat{y}(\mathbf{d})$ can be also computed, and it results

$$\boxed{s^2(\mathbf{d}) = \hat{\sigma}^2\left[1 - \mathbf{r}(\mathbf{d})^T\mathbf{R}^{-1}\,\mathbf{r}(\mathbf{d}) + \left(\mathbf{F}^T\mathbf{R}^{-1}\mathbf{r}(\mathbf{d}) - \mathbf{f}(\mathbf{d})\right)^T\left(\mathbf{F}^T\mathbf{R}^{-1}\mathbf{F}\right)\left(\mathbf{F}^T\mathbf{R}^{-1}\mathbf{r}(\mathbf{d}) - \mathbf{f}(\mathbf{d})\right)\right]} \tag{2.23}$$

in which $\hat{\sigma}^2$ is the least squares estimate:

$$\hat{\sigma}^2 = \frac{(\tilde{y} - \mathbf{F}\hat{\boldsymbol{\beta}})^T\mathbf{R}^{-1}(\tilde{y} - \mathbf{F}\hat{\boldsymbol{\beta}})}{K} \tag{2.24}$$

s^2 turns out to be 0 for the sampled designs, $s^2(\tilde{\mathbf{d}}_i) = 0$, as a consequence of the fact that Kriging model (almost) exactly interpolates them. Finally, it is worth highlighting that, because of the Gaussian assumption, the distribution Y defined in Equation 2.13 is also normally distributed, with mean $\hat{y}$ and variance s^2, i.e. $Y \sim \mathcal{N}(\hat{y}, s^2)$.

The Kriging predictor $\hat{y}(\mathbf{d})$ in equation 2.19 can be used in place of demanding high-fidelity simulation. The reliability of the predictor can be increased by adding more observations in the region of the design space in which $s^2(\mathbf{d})$ is high. However, both the above expressions rely on the assumption about the shape of the correlation function, modelled as Gaussian function in equation 2.16, and on the corresponding hyperparameters $\boldsymbol{\vartheta} = (\vartheta_1, \ldots, \vartheta_N) \in \mathbb{R}^N$. One can get an estimate of $\boldsymbol{\vartheta}$ by maximizing the associated likelihood $L(y|\beta, \sigma^2, \boldsymbol{\vartheta})$. Notice that a closed solution for this optimization problem does not exist, hence it must be solved numerically. By plugging the least-squares estimate $\hat{\sigma}^2$ as a function of $\boldsymbol{\vartheta}$ into the likelihood expression and, instead of maximizing $L(y|\beta, \sigma^2, \boldsymbol{\vartheta})$, the equivalent minimization of $-\log\left(L(y|\beta, \sigma^2, \boldsymbol{\vartheta})\right)$ is considered, the following optimization problem comes out:

$$\hat{\boldsymbol{\vartheta}} = \arg\min_{\boldsymbol{\vartheta}}\left(\frac{1}{2}\log\left(\det\left(\mathbf{R}\right)\right) + \frac{K}{2}\log\left(2\pi\hat{\sigma}^2\right) + \frac{K}{2}\right) \tag{2.25}$$

in which both $\mathbf{R}$ and $\hat{\sigma}$ are functions of $\boldsymbol{\vartheta}$.

---

[1] The condition number of a matrix is defined as: $k(\mathbf{A}) = ||\mathbf{A}^{-1}|| \cdot ||\mathbf{A}||$. As a rule of thumb, a matrix is considered ill-conditioned if the logarithm of the condition number is greater than the computer precision.

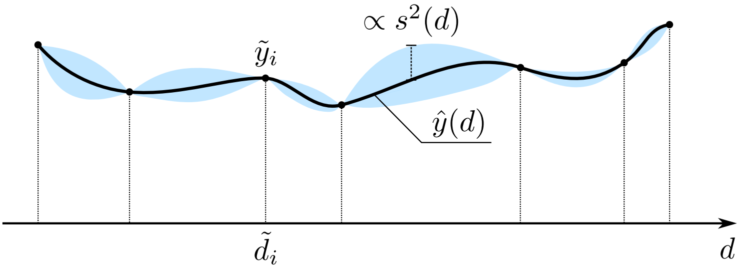

FIGURE 2.2. Exemplary Kriging predictor $\hat{y}(d)$ alongside its mean-square error $s^2(d)$ for a one-dimensional problem ($d \in \mathbb{R}$) starting from high-fidelity samples ($\tilde{d}_i, \tilde{y}_i$).

The optimization problem is solved by DAKOTA® using DIRECT, which is a gradient-free global optimization algorithm based on a Lipschitzian approach (Jones *et al.*, 1993). In practice, the algorithm subdivides the design space in hyper-rectangles and evaluates the objective function at their centers. The most promising rectangles are further subdivided and the process is repeated until convergence. Once $\hat{\boldsymbol{\vartheta}}$ is computed, the Kriging predictor $\hat{y}(\mathbf{d})$ and its mean-square error $s^2(\mathbf{d})$ can be readily computed from equations 2.19 and 2.23, respectively.

For illustrative purposes, figure 2.2 shows an exemplary Kriging predictor for a one-dimensional problem ($d \in \mathbb{R}$), highlighting how the mean-square error affects the predictor. Specifically, as the Kriging interpolates (almost) exactly the observations ($\tilde{d}_i, \tilde{y}_i$), the mean-square error is there (almost) zero, while it increases away from them.

2.2.3 Surrogate strategy

The surrogate strategy is illustrated in figure 2.3 by referring to a minimization problem, e.g. the minimization of the entropy production. Before starting the shape optimization, the baseline blade profile is parametrized in accordance with §2.2.1, choosing the movable CPs whose orthogonal displacements will be used as design variables in the optimization. Then, an appropriate number of blade geometries are sampled with the LHS technique within the identified design space. The number of samples has to be decided beforehand by the user and it will be the object of a dedicated parametric study later in this chapter. The performance of the so-identified blades is evaluated via CFD simulations. Input geometries and corresponding output response produce the so-called design of experiments (DoE), on which an initial surrogate is built. Distinct universal Kriging predictors are built on top of the DoE for the objective function $\hat{y}_{of}(\mathbf{d})$ and any non-linear constraint $\hat{y}_{cns}(\mathbf{d})$ imposed in the specific optimization task. Several alternatives for the mean trend of the Gaussian process (first term in equation 2.13) are tested and results are discussed in terms of convergence rate and optimization outcome later in the chapter. Once all first estimates of Kriging predictors (objective function and constraints) are obtained, the new blade that has to be assessed with the CFD to improve the surrogate reliability depends on the selected infilling criterion. The two most popular alternatives are:

I) Infilling at $\mathbf{d}^*$ for which $\hat{y}(\mathbf{d}^*)$ is minimum. Following this procedure, the surrogate accuracy is increased in the optimal region found by the first surrogate interpolation. The infilling strategy is polarised towards the *exploitation* of that optimal zone, trusting that the initial surrogate (built from the DoE) is capable of capturing the overall trend of the objective function and correctly identifying the optimal region.

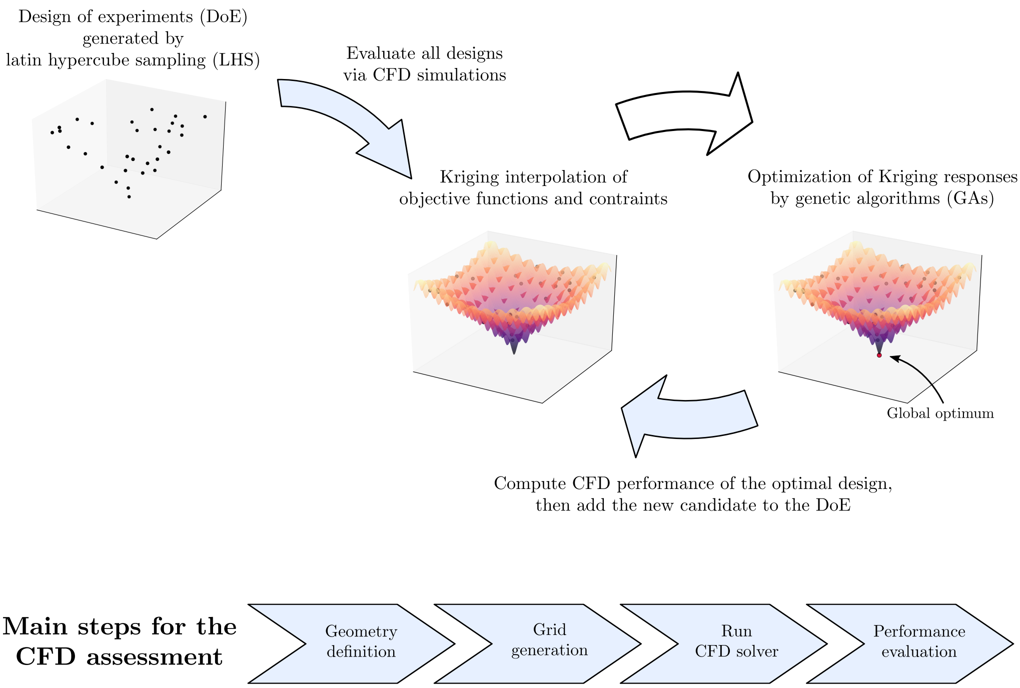

FIGURE 2.3. General flow chart of the surrogate-based shape-optimization tool. The light-blue arrow in the top frame stands for a complete CFD assessment, whose main steps are summarized in the bottom frame.

II) Infilling at $\mathbf{d}^*$ for which the expected improvement is maximized. The improvement of the objective function can be interpreted as $I(\mathbf{d}) = \max(y_{min} - Y(\mathbf{d}), 0)$, where y_{min} is the minimum value among all CFD results included in the analysis so far and $Y(\mathbf{d}) \sim \mathcal{N}(\hat{y}(\mathbf{d}), s^2(\mathbf{d}))$ is the Gaussian process followed by the new blade $\mathbf{d}$. Therefore, the improvement $I(\mathbf{d})$ is an utility function that returns either $(y_{min} - Y(\mathbf{d}))$ if a further minimization of the objective function for $\mathbf{d}$ is expected or zero otherwise. As Y is a random variable, I is a random variable as well, then it cannot be directly maximized. For this reason, the expected value of the improvement is taken (Jones *et al.*, 1998):

$$\mathbb{E}\left[I(\mathbf{d})\right] = (y_{\mathrm{min}} - \hat{y}(\mathbf{d}))\Phi\left(\frac{y_{\mathrm{min}} - \hat{y}(\mathbf{d})}{s(\mathbf{d})}\right) + s(\mathbf{d})\,\phi\left(\frac{y_{\mathrm{min}} - \hat{y}(\mathbf{d})}{s(\mathbf{d})}\right) \tag{2.26}$$

where $\phi(\cdot)$ and $\Phi(\cdot)$ represent the probability density function (PDF) and the cumulative density function (CFD) of a standard normal distribution, respectively. The blade $\mathbf{d}^*$ that has to be assessed via CFD is the one that maximizes the expected improvement $\mathbb{E}\left[I(\mathbf{d})\right]$. Such infilling strategy privileges the *exploration* of the design space in which the surrogate is not accurate (large mean-square error). It follows that the new candidate $\mathbf{d}^*$ is not necessary the one which returns the minimum objective function predicted by the surrogate $\hat{y}(\mathbf{d})$, but $\mathbf{d}^*$ may also be the one for which the surrogate accuracy $s^2(\mathbf{d})$ is larger. Moreover, to avoid infilling in the region out of interest, the surrogate error has to be sufficiently large that there are some probabilities that the minimum value may be actually located there.

This latter strategy, as implemented in the built-in `ego` model in DAKOTA®, was preliminarily tested but later abandoned in favor of the first infilling criterion, which was found more effective in presence of constrained optimizations. In FORMA, the constrained minimization of the surrogate prediction $\hat{y}_{of}(\mathbf{d})$ is carried out with GA. After a preliminary study focused on the impact of the GA parameters, an effective set-up was found, featuring a population size of 300 individuals, a crossover rate of 0.8, and a mutation rate of 0.02. The selection technique classifies the optimal individuals following the elitism scheme, giving a higher rank to those individuals that satisfy all imposed constraints (computed from $\hat{y}_{cns}(\mathbf{d})$). Following this procedure, candidate blades that do not satisfy all constraints will disappear as long as the population keeps evolving. As a result, the individuals that belong to the final population are expected to meet all constraints. The infilling process is stopped after a fixed number of iterations (200 in this case) depending on the availability of computational resources and time. In the following, the surrogate-based shape optimization strategy is applied in order to the single- and multi-point constrained optimization of a supersonic cascade in §§2.3-2.4, respectively, and to the single-point constrained optimization of a transonic centrifugal stage (both stator and rotor) in §2.5. The first optimization task has also the scope to illustrate the effect of different modelling choices, such as the mean trend of the Kriging predictor, and hyperparameters, e.g. the DoE size. The optimal settings are derived from these parametric studies and retained for the subsequent optimization tasks.

2.3 Single-point constrained optimization of a supersonic turbine cascade

2.3.1 Description of the test case

The first test case involves a converging-diverging blade, which acts as a first-stage stator for axial turbomachinery operating in an ORC for combined heat and power applications (Colonna *et al.*, 2008). The flow is expanded from superheated conditions ($P^t_0 = 8.0\,\mathrm{bar}$, $T^t_0 = 272.5\,\mathrm{K}$) with a total-to-static expansion ratio of 7.3 ($P_1 = 1.1\,\mathrm{bar}$). Such a large expansion ratio with respect to usual values for gas and steam turbine stages is made possible by the large molecular weight of the organic compound, which requires a smaller enthalpy drop than light fluids at a given pressure ratio (Macchi & Perdichizzi, 1981). As opposed to the original application, which features the siloxane MDM (octamethyltrisiloxane, $C_8H_{24}O_2Si_3$), the present cascade expands the siloxane MM (hexamethyldisiloxane, $C_6H_{18}OSi_2$). This choice is motivated by the possibility of exhibiting severe non-ideal effects by MM below its thermal stability limit. Therefore, to keep a common thread with the following chapter, which focuses on non-ideal effects in supersonic cascades, the optimization is carried out by considering the thermodynamic properties of MM. For the expansion of interest for the present optimization, non-ideal effects are limited ($Z \approx 0.9 - 1.0$, see figure 2.4) and the gas-dynamic evolution, summarized by the ratio of specific heats, is nearly the same for the two fluids. As a further proof of that, the isentropic Mach number at the outlet remains constant ($M = 2.0$) despite the fluid modification. The resulting isentropic expansion is reported in figure 2.4(a).

Another feature prompted by the large molecular weight is the comparatively small speed of sound, which easily induces supersonic flows within the blade channel. To accomplish the supersonic expansion, a converging-diverging blade shape is needed, featuring a large leading-edge that also acts as a converging section upstream of the throat. The diverging section downstream of the throat is designed by applying the theory of characteristics. The baseline blade is reported in the original contribution of Colonna *et al.* (2008) and has been already utilized in diverse optimization tasks (Pini *et al.*, 2015*a*; Vitale *et al.*, 2017), therefore it is intended as a benchmark to illustrate the potentialities of the present shape-optimization tool. The resulting flow field is displayed in figure 2.4(b). From the reported pressure field, a classical fish-tail shock pattern is recognized at the trailing edge. Such flow configuration steams from the finite thickness of the trailing edge: the supersonic flow from both the suction and the pressure side has to turn around the trailing edge.

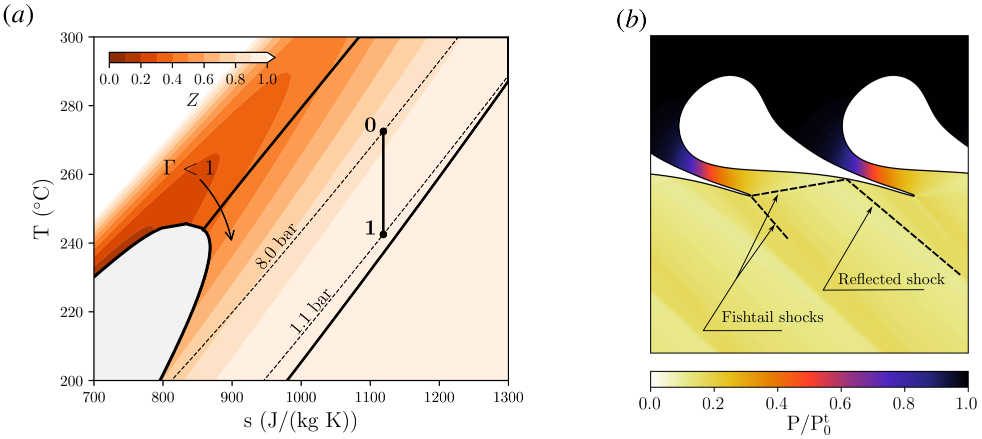

FIGURE 2.4. Boundary conditions (*a*) and flow field (*b*) of the supersonic nozzle cascade, which serves as a baseline for a dedicated shape-optimization task. The region $\Gamma < 1$ is contained within the two tick black lines.

The only way to accomplish such supersonic rotation is by means of expansion waves. Then, the two flow streams meet and turn towards a shared direction. As opposed to the previous situation, this additional flow turning requires the onset of compression shocks. The fish-tail branch that originates from the pressure side reflects on the rear suction side of the adjacent blade. The shock reflection combined with the ongoing flow acceleration on the suction side prompts the onset of an additional strong shock, which smears out downstream of the cascade while mixing with the surrounding flow.

2.3.2 Formulation of the optimization problem

It is evident that the flow field produced by the supersonic cascade is rather complex and there is a large room for performance improvement, e.g. by reducing the strength of the shock waves as they are mainly responsible for the performance deterioration. In this context, the shape optimization can represent an effective solution to boost cascade performance.

As already mentioned, the success of the shape optimization also depends on the blade parametrization. The pressure and the suction side of the blade are parametrized with a single B-spline as described in §2.2.1. The blade curve is closed by the trailing edge, which is modelled as an ellipsoidal curve to ensure $\mathcal{C}^1$-continuity at the merging nodes. To have an adequate representation of the baseline blade (with a geometrical error less than 10^{-6} m), a larger number of CPs is used where the blade curvature is high. Surface gradients computed with inviscid adjoint simulations showed that the rear part of the blade (especially the suction side) is the most critical region for the performance (Pini *et al.*, 2015*a*). An analysis of variance in combination with viscous simulations came to the same conclusion (Romei & Persico, 2018). Therefore, only those CPs placed on the rear part of the blade (6 along the suction side and 2 along the pressure side) are displaced and included in the optimization, represented by the blue dot in figure 2.5. Moreover, an additional CP is included in the optimization to account for the rigid movement of the TE (solid orange dot in figure 2.5), resulting in 9 moveable CPs. The associated symmetric orthogonal displacements, varying from a minimum of ±0.2 mm close to the TE up to a maximum of ±2.0 mm in the central part of the blade, establish the design variables for the optimization, i.e. $\mathbf{d} = (d_1, \ldots, d_9) \in \mathbb{R}^9$. The overall design space is represented in figure 2.5.

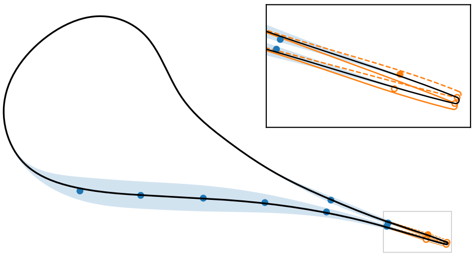

FIGURE 2.5. Design space for the shape optimization of a supersonic nozzle cascade; ● moveable CPs on the blade profile; ● moveable CP at the trailing edge; ○ CPs at the trailing edge that move rigidly with the moveable CP.

Having identified the design variables and their effect on the blade shape, a first optimization is undertaken by targeting the minimization of the entropy production Δs at design conditions. In this way, all kinds of losses are considered throughout the optimization. Alternative objective functions that have been historically selected for the optimization of supersonic cascades are related to the disuniformity of the flow at the cascade outlet, see, e.g., Pasquale *et al.* (2013) and Pini *et al.* (2015*a*). This choice is rigorous in the context of inviscid simulations, in which the only source of losses is given by the onset of shocks, which alters the flow field as well. However, entropy production (or, equivalently, total loss coefficients) should be preferred in viscous simulations as it also incorporates trailing-edge losses that could vary in accordance with the base-pressure value. While minimizing the entropy production, a direct constraint on the mass-flow rate is imposed, accepting a variation in the baseline value limited to ±1%. The introduction of such constraint is motivated by the fact that the supersonic cascade is choked, therefore it directly sets the mass-flow rate in the corresponding power system. The optimization problem reads as follows:

$$\begin{aligned} \min_{\mathbf{d}} \quad & \Delta s \\ \text{subject to:} \quad & 0.99 \leqslant \dot{m}/\dot{m}_{nom} \leqslant 1.01 \end{aligned} \tag{2.27}$$

To evaluate both the objective function and the constraint, CFD simulations are performed by meshing each time the candidate blade geometries without modifying the boundary conditions. Numerical simulations are carried out with ANSYS-CFX 18.1®. No-slip and adiabatic conditions are imposed on the blade surface. Axial flow is prescribed at the inlet along with total pressure and temperature (P_0^t, T_0^t), as detailed in the previous section. At the outlet, an average static pressure P_1 is imposed; local pressure differences of 5% are allowed at the outlet domain. This latter is placed at around 8 axial chords downstream of the trailing edge to promote the flow mixing, thus avoiding spurious pressure wave reflections. Since only blade-to-blade effects are of interest, quasi-three-dimensional simulations are carried out by considering a straight stream tube around the midspan (free-slip conditions at the hub and shroud surface). A single-blade passage is considered by exploiting periodic boundary conditions. The employed turbulence model is $k-\omega$ SST (Menter, 1994), whose boundary conditions are set as turbulence intensity ($T = 5\%$) and eddy viscosity ratio ($\mu_t/\mu = 10$). The CFD solver converts the above turbulent conditions in suitable values of k and ω by means of algebraic correlations. Note that the effect of turbulent boundary conditions on the present cascade is practically negligible (Romei *et al.*, 2019).

The thermodynamic model (multi-parameter equation of state of MM by Thol *et al.* 2016) is implemented using LUTs to speed up the evaluation of the thermodynamic properties (see, e.g., Pini *et al.*, 2015*b*). Pressure and temperature are used as primitive variables to build the

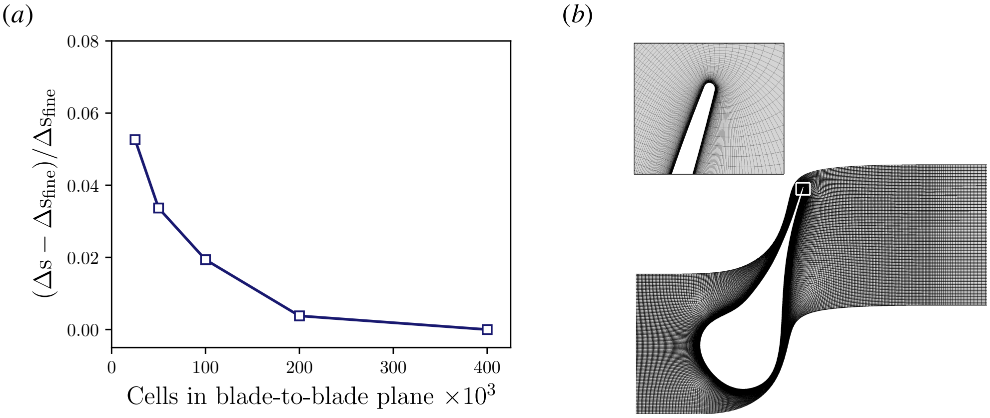

FIGURE 2.6. Grid convergence assessment (*a*) in terms of entropy production for the baseline cascade. The selected grid for the optimization task is reported in frame (*b*), consisting in approximately 100,000 cells in the blade-to-blade plane and providing the best compromise between accuracy (error < 2% in the entropy production) and computational cost.

thermodynamic tables via the NIST REFPROP® database (Lemmon *et al.*, 2013), which also provides dedicated correlations for transport properties (Meier *et al.*, 2004; Perkins *et al.*, 2013). The table ranges are taken large enough to avoid any clip or extrapolation which may make critical the convergence process, with an accuracy of approximately 0.1 K and 0.1 bar for temperature and pressure, respectively. A finer thermodynamic discretization did not lead to any substantial variation in solution. High-resolution total variation diminishing (TVD) schemes (Barth & Jespersen, 1989) are employed in the discretization of both flow and turbulence equations. A central difference scheme is instead adopted for the diffusive flux.

Hexahedral meshes are generated with ANSYS-TURBOGRID®. A proper cell clustering near blade walls is imposed to ensure $y^+ \lesssim 1$, thus avoiding the introduction of wall functions in the solution. Several grid refinements were produced to estimate the effect of the geometrical discretization. The results from this study are reported in figure 2.6(*a*) in terms of relative error in the entropy produced, which is the objective function of the present optimization problem. A clear asymptotic trend is observed by increasing the number of cells in the blade-to-blade plane. Ultimately, the mesh consisting in $100,000$ cells in the blade-to-blade plane is selected, as it provides the best compromise between accuracy (geometrical error less than 2%) and computational cost (~ 8 minutes on an Intel® Xeon® CPU E5-2630 v3 @ 2.40GHz equipped with 16 cores). The computational mesh is displayed in figure 2.6(*b*). The mesh is regenerated whenever the blade geometry is modified. The mesh generation and saving take around 1 additional minute on the previous machine.

2.3.3 Sensitivity of the optimization outcome to surrogate hyperparameters

As stated in §2.2.3 and throughout the mathematical description of the Kriging predictor, there are some choices and parameters that have to be decided a priori. In this section, a number of parametric studies devoted to establishing an optimal set-up for the surrogate strategy are presented.

Before illustrating these studies, an exemplary convergence process is reported in figure 2.7 to illustrate the main trend. It is worth highlighting that the convergence is monitored after the first surrogate interpolation, which requires to simulate all blades in the DoE. At each iteration, a new CFD simulation is carried out following the infilling-technique described in §2.2.3 (in this

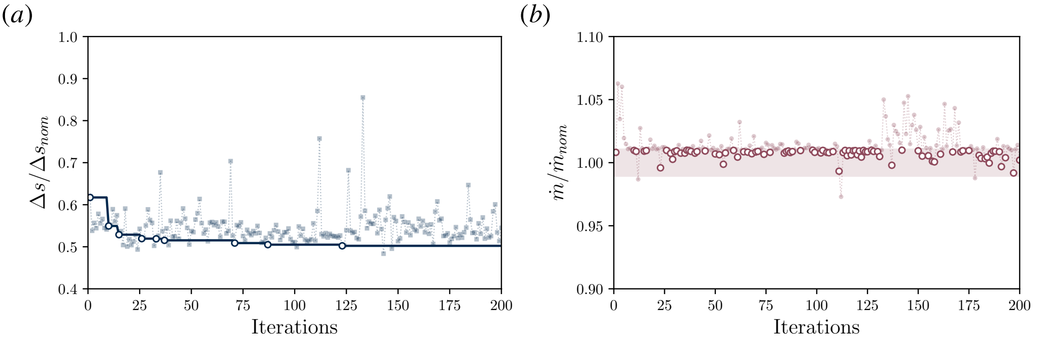

FIGURE 2.7. Exemplary convergence history for the supersonic cascade optimization. The thick line in (*a*) monitors the minimum objective function that satisfies the constraint. The filled band in (*b*) represents the acceptable deviation of the constraint.

case, based on the minimization of the Kriging predictor for the objective function accounting for the constraint fulfilment). For the following studies, the convergence history will be expressed as the solid line in figure 2.7(*a*), which is updated whenever a blade produces a smaller entropy while coping with the constraint on the mass-flow rate. A common feature is shared by all the optimizations that were carried out for this specific cascade: the largest reduction in the objective function is achieved in less than 20 iterations (around 50% of reduction in the entropy produced), then only marginal improvements are observed (few percentage points). Moreover, at a certain point (around the 125^{th} iteration for the specific convergence of figure 2.7), the blade performance, both in terms of the objective function and constraint, arguably departs from the optimal value. As a consequence of sampling in a neighborhood of the expected optimal region, surrogate predictors suffer from overfitting. However, the convergence does not blow up: as long as blades outside the optimal region are evaluated, the localized overfitting reduces and the surrogate predictors recover their accuracy.

Bearing in mind the underlying evolution of the surrogates, a first parametric study is conducted to evaluate the mean trend $\boldsymbol{\beta}^T\mathbf{f}(\mathbf{d})$ of the Kriging predictor in equation 2.13. Actually, one can imagine whatever functional shapes when modelling this term and there is not mathematical evidence of any superior choice. For the present work, simple yet effective polynomial functions are considered to model the mean trend: (i) constant (reducing the surrogate to the so-called *ordinary* Kriging), (ii) linear in the design variables, and (iii) quadratic in the design variables (excluding mixed terms $d_i d_j$ for $i \neq j$). The corresponding analytical functions reads as follows:

$$\boldsymbol{\beta}^T\mathbf{f}(\mathbf{d}) = \beta_0 \qquad \text{constant} \qquad (2.28)$$

$$\boldsymbol{\beta}^T\mathbf{f}(\mathbf{d}) = \beta_0 + \sum_{i=0}^{9} \beta_i d_i \qquad \text{linear} \qquad (2.29)$$

$$\boldsymbol{\beta}^T\mathbf{f}(\mathbf{d}) = \beta_0 + \sum_{i=0}^{9} \beta_i d_i + \sum_{j=0}^{9} \beta_j d_j^2 \qquad \text{quadratic} \qquad (2.30)$$

The parametric study is undertaken by considering the same DoE for the first surrogate interpolation. The DoE size includes 90 blade geometries, i.e. ten times the number of the design variables. As with any space-filling technique, LHS also has a pseudo-random component in the sampling generation. To fully account for this inherent variability, three independent DoEs are

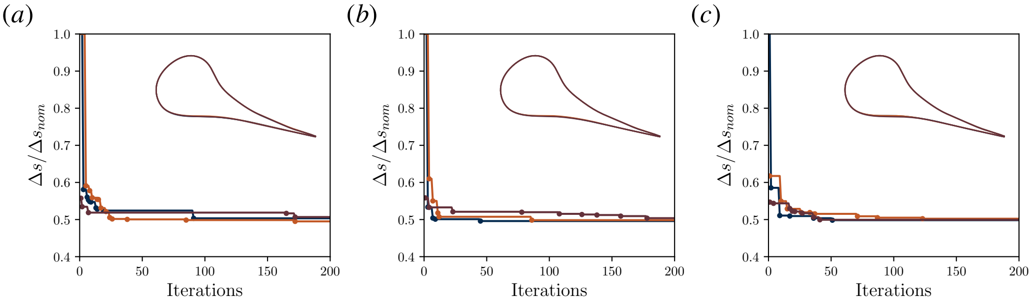

FIGURE 2.8. Convergence histories by accounting for different trend functions in the Kriging formulation: (*a*) constant (ordinary Kriging), (*b*) linear, and (*c*) quadratic. Each case is run three times with a different DoE initialization.

generated by imposing different `random seed`.

The convergence histories for this study are reported in figure 2.8 alongside the resulting optimal blades. The variation in the trend functions produces neither an increase in the computational cost/time to train the Kriging predictors nor any stability issue from the numerical perspective. All optimizations converge to the same blade shape regardless of the trend function and the DoE initialization. By a careful inspection of the trends, the optimizations that exploit the quadratic mean trend are the ones that achieve convergence earlier. In particular, two out of three optimizations find the optimal profiles within 50 surrogate updates. Although optimizations performed with the constant and linear trend for the Kriging predictors still produce the same optimal blade, the last reduction in the objective function is achieved later in the convergence processes. Moreover, the convergence rate seems more dependent on the DoE initialization for these trends, but more independent runs are needed to make a final statement from a statistical standpoint. Gathering all this information, the quadratic mean trend as in equation 2.30 is arguably the most appropriate choice for the present surrogate strategy and, hence, it is selected as a default option hereinafter (unless otherwise noted).

A second parametric study is conducted to assess the effect of the DoE size on the optimization convergence and outcome. Three increasing DoE sizes are tested, including 45 (five times the number of design variables), 90 (ten times) and 180 (twenty times) blade geometries, respectively. It is worth highlighting that LHS is not a nested space-filling technique. In other words, the intermediate DoE size does not contain the blade geometries included in the smallest DoE size, but the two sets are independent. As before, for each case the optimization is run three times by changing the `random seed`, hence considering different blade geometries distributed in the prescribed design space. In accordance with the previous study, the quadratic mean trend is assumed for the Kriging predictors.

Figure 2.9 illustrates the optimization outcomes for the three DoE sizes. As for the previous analysis, all optimizations share approximately the same reduction in the objective function and optimal blade shapes. Again, the main difference lies in the number of iterations required to achieve the optimal result and the sensitivity to the variability of DoE composition. Surprisingly, the initialization with 90 samples seems to be more robust to the DoE variability; one would expect that the larger the dimension of DoE, the better the design space is filled. As a matter of fact, three independent runs are not sufficient to make any claim on this point from a statistical perspective. Still, the analysis seemingly suggests that the convergence process is not largely sensitive to the DoE initialization: at the end, the optimization converges approximately to the same blade. The proper choice of the DoE has to ultimately consider the cost of the single CFD simulation: if

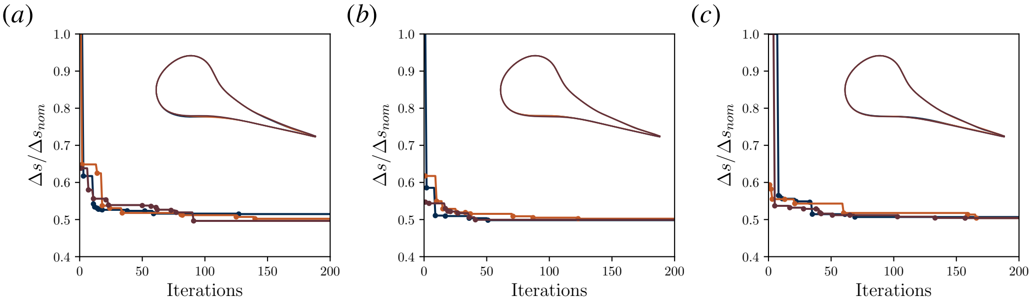

FIGURE 2.9. Convergence histories by varying the DoE size: (*a*) $5 \cdot$ #CPs (45 samples), (*b*) $10 \cdot$ #CPs (90 samples), and (*c*) $20 \cdot$ #CPs (180 samples). Each case is run three times with a different DoE initialization.

on one hand a larger DoE size is expected to accelerate the convergence, on the other a larger computational cost is needed for the first surrogate interpolation.

In an effort of quantifying the deviations between the different set-ups, the average entropy value out of the fifteen optimizations is 3.46 J/(kg K), with a net decrease of 50.2% from the baseline level. The worst optimization leads to an entropy value 2.5% higher than the average value, while the best optimization produces an entropy value 1.4% lower than the average one. Considering the magnitude involved, the main conclusion from this analysis is that even the smallest size, which consists of five times the number of design variables, is able to provide a consistent reduction in the objective function. Therefore, if the single CFD cost is comparably large, a small DoE size combined with a number of surrogate updates can be preferable to spending most of the computational resources in completing a larger DoE evaluation.

2.3.4 Aerodynamic analysis

The optimization outcome is now analyzed from an aerodynamic perspective in order to infer the mechanism that leads to an optimized blade. As a result of the optimization, the entropy produced by the cascade is almost halved. By introducing a total-pressure loss coefficient that conveniently summarizes the blade performance in dimensionless form, namely

$$Y = \frac{P_0^t - P_1^t}{P_0^t - P_1}, \tag{2.31}$$

the mixed-out value is reduced from 15.7% (baseline) to 8.6% (optimized), while complying with the constraint on mass-flow rate.

Figure 2.10 compares the optimal blade with the baseline. The optimization changes the shape of the blade in the rear part while keeping unaltered the throat size, acting as a geometric constraint assigned to the throat. This is fully consistent with the application of the constraint on the mass-flow rate: as a consequence of the choked operation, the mass-flow rate only depends on the throat size. This behaviour is illuminating the capability of the evolutionary strategy in learning through surrogate interpolation, producing a physically sound optimal configuration.

As previously mentioned, the main responsible for performance degradation in the baseline cascade is the main shock that generates on the rear suction side, see also figure 2.11(*a*). Previous inviscid simulations (Colonna *et al.*, 2008; Pini *et al.*, 2015*a*) performed on a similar cascade but making use of a sharp trailing edge, thus nearly eliminating the fish-tail flow structure, show that the leading shock remained almost unaltered and similar to the one observed in the present viscous simulation. As a result, it is highly probable that the shock onset is generated by the shape of the

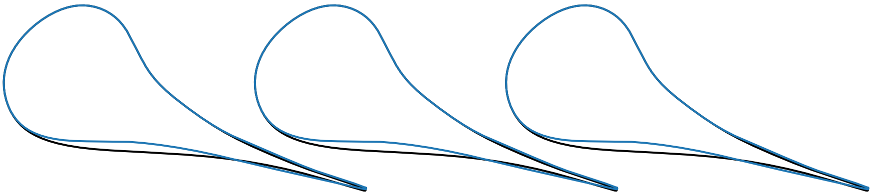

FIGURE 2.10. Comparison between the baseline (——) and the optimal (——) blade profile.

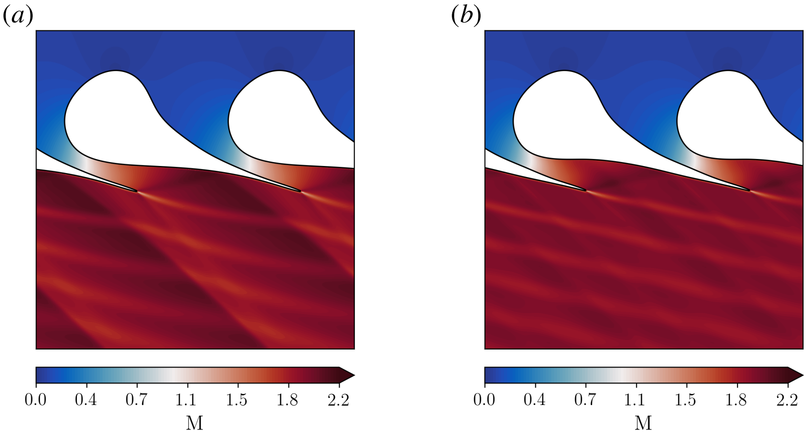

FIGURE 2.11. Mach number field for the baseline (*a*) and the optimal (*b*) cascade.

rear region of the blade, which is not able to accomplish an adapted supersonic expansion. The onset of shocks in the cascade-exit flow, associated to local flow deflections, is also responsible for the waving character of the wake appearing from the entropy distribution, as clearly visible in figure 2.12(*a*). The entropy fields also illustrate the severe loss generation due to the mixing of the shock-induced gradients downstream of the cascade, which overcomes the contribution of entropy rise across the shock. It is worth underlying that no classic empirical or analytical method can guarantee to avoid these effects when designing a highly supersonic cascade, thus further motivating the application of a systematic optimization tool to generate highly efficient profiles. The action of the optimization can be clearly understood considering the flow configuration obtained for the optimal cascade, reported in figure 2.11(*b*). The optimizer generates an optimal blade with a higher curvature in the diverging channel and an almost straight shape downstream of the cascade opening, thus nearly nullifying the unguided turning. As a result, the pressure gradients in the rear suction side of the blade are drastically minimized, eliminating the main shock observed in the baseline case. Consequently, the flow released by the cascade features a much more uniform direction, as marked by the straight wake avenues leaving the optimal cascade, see 2.12(*b*).

By looking at the pitchwise pressure distribution half axial chord downstream of the trailing edge in figure 2.13(*a*), it is evident that the optimal blade manages to strongly reduce the pressure variability at the cascade exit, eliminating the sharp pressure gradients induced by the shocks characterizing the baseline cascade aerodynamics. Moreover, the pressure distribution on the blades, reported in figure 2.13(*b*) in terms of isentropic Mach number along the non-dimensional curvilinear abscissa, supports the above interpretation of the optimization effect. The shape of the optimal blade anticipates the flow acceleration on the suction side, just downstream of the sonic

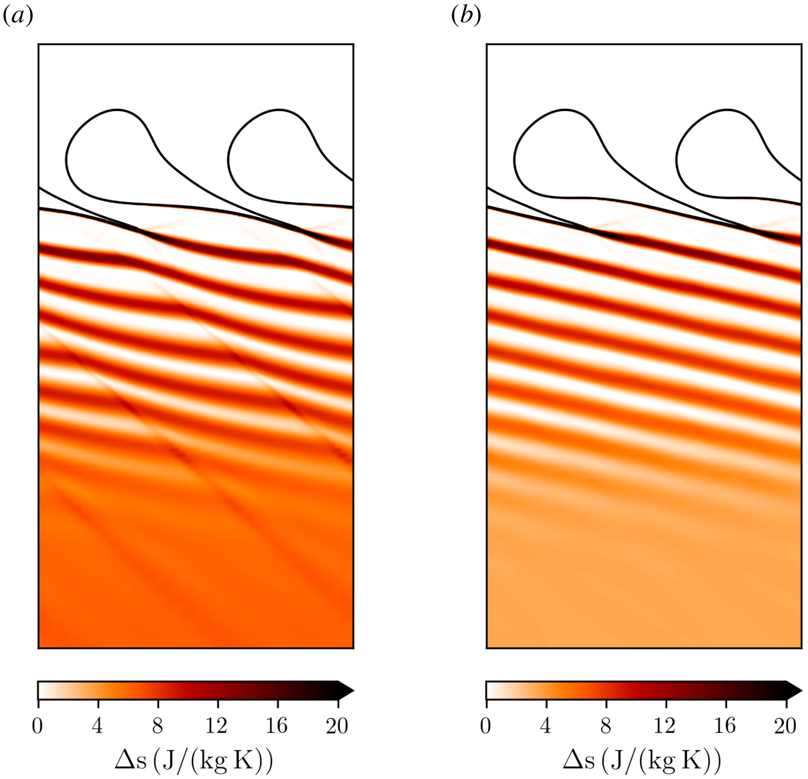

FIGURE 2.12. Entropy field for the baseline (*a*) and the optimal (*b*) cascade.

throat and still within the bladed channel; consequently, the over-speed on the rear suction side is limited and the subsequent deceleration is mostly reduced, as testified by the almost constant M_{is} for $0.8 \leqslant s_{norm} \leqslant 1.0$.

The indirect outcome of these flow features on the cascade performance is best summarized by figure 2.13(*c*), which reports the evolution of the total-pressure loss coefficient along the axial direction for the two cascades. First, the two configurations exhibit similar loss levels at the TE. In this region, the loss is mainly caused by the boundary layers on the blade sides. Moving downstream, the onset of the shock has a dramatic impact on the loss coefficient of the baseline blade; in particular, the entropy production connected to the mixing of the shock gradients makes rise the loss coefficient from 9.0% at the TE to 15.7% seven axial chords downstream, where the flow is completely mixed-out. In the case of the optimal blade, the elimination of the main shock greatly reduces the mixing loss to less than 2 percentage points. This leads to a mixed-out loss coefficient equal to 8.6%, almost halved with respect to the one of the baseline blade, and to a much faster mixing, with evident advantages for the aerodynamics of the subsequent rotor.

2.4 Multi-point constrained optimization of a supersonic turbine cascade

The major shortcoming involving converging-diverging cascades is represented by their drastic efficiency drop at pressure ratios different from the design one (Goldman, 1972). As future power systems have to be as flexible as possible to allow for a larger penetration of renewable sources in

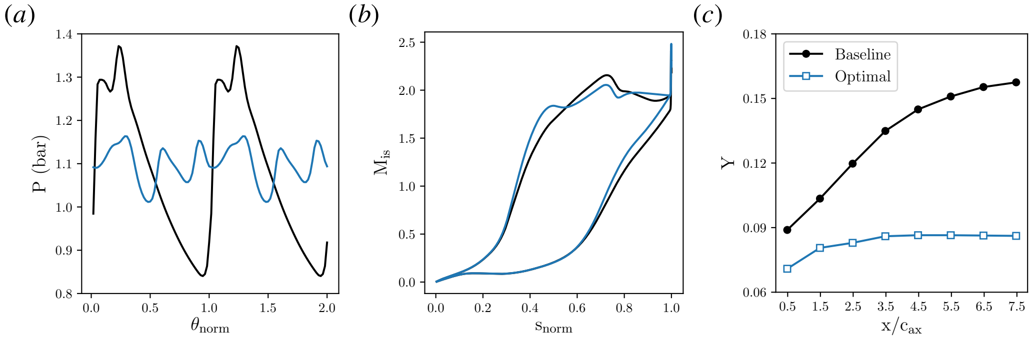

FIGURE 2.13. Aerodynamic comparison between the baseline and the optimal profile: (*a*) pitchwise pressure distribution half of axial chord downstream of the trailing edge, (*b*) isentropic Mach number distribution on the normalized blade surface, and (*c*) streamwise evolution of the total-pressure loss coefficient downstream of the cascade.

TABLE 2.1. Operating conditions included in the multi-point optimization.

	P_0^t (bar)	T_0^t (°C)	P_1 (bar)	P_0^t/P_1	$M_{is,1}$
OP1	8.0	272.5	1.1	7.3	2.0
OP2	8.0	272.5	1.4	5.7	1.8
OP3	8.0	272.5	0.7	10.0	2.2

the energy market, one possibility is to account for a number of representative operating conditions during the blade design. The goal is then to maximize the performance not on a specific operating point, but on a number of potential conditions that can be representative of system operation. Such a problem is tackled in this second optimization task, in which multiple operating conditions are accounted for in the objective function formulation.

2.4.1 Formulation of the optimization problem

The baseline cascade used for this optimization is the same presented in the previous section. The parametrization also follows the one previously outlined, so that the number of design variables (nine) and the resulting design space is identical to the one displayed in figure 2.5. As the main effect on the efficiency of a supersonic cascade is represented by a change in the pressure ratio, three different scenarios are considered by varying the outlet static pressure. This latter modification can be representative of seasonal variations of the ambient temperature, which directly affects the condensation temperature of the ORC system and, hence, the back-pressure at the turbine outlet. Three realistic boundary conditions are identified, as in Table 2.1: the operating point OP1 recalls the design conditions for the previous single-point optimization. The other two operations point OP2 and OP3 feature a smaller and a larger pressure ratio than OP1, respectively.

When formulating the optimization problem, several choices are possible to incorporate all operating conditions into a single objective function. In general terms, a weighted average can be considered, assigning different weights based on the likelihood for which a condition can occur. If a specific operating condition is predominant during field operation, then it is desirable to give a high priority to the maximization of the blade performance in that condition at the expense of the others. A general formulation based on a probabilistic description of operating conditions is provided later in §3.5 for shape optimization in the context of severe non-ideal flows. For the present optimization task, equal weights are assigned to all operating conditions, i.e. the underlying probability to observe one out of three conditions is the same. The resulting optimization problem can be formulated as:

$$\begin{aligned} \min_{\mathbf{d}} \quad & \left(\varDelta s_{OP1} + \varDelta s_{OP2} + \varDelta s_{OP3} \right) / 3 \\ \text{subject to:} \quad & 0.99 \leqslant \dot{m}_{OP1} / \dot{m}_{OP1,nom} \leqslant 1.01 \end{aligned} \tag{2.32}$$

Besides equally including the entropy generation by the three operating conditions in the objective function, a non-linear constraint on the mass-flow rate is imposed relatively to OP1. In analogy with the previous optimization, the optimized cascade has to provide a well-defined mass-flow rate in design conditions, as resulting from cycle analyses. The objective functions and the constraint are evaluated by means of CFD simulations with the settings outlined in the previous section. The computational domain is generated for each blade geometry in accordance with the grid-convergence study previously reported, resulting in meshes with 100,000 cells in the blade-to-blade plane while preserving $y^+ \lesssim 1$ along the blade surface. The computational cost is roughly three times compared to the single-point optimization, as the evaluation of the objective function for the single blade geometry requires three separate CFD simulations, one for each set of boundary conditions in Table 2.1.

As a consequence of the larger computational cost, the first surrogate interpolation is carried out on a DoE that includes 45 blade geometries, uniformly sampled in the design space by means of LHS. Based on previous results, the quadratic formulation is employed in the modelling of the Kriging mean trend.

2.4.2 Optimization outcome

The convergence history is reported in figure 2.14. On the left frame, the evolution of the entropy production is reported for each operating condition whenever the surrogate is updated; apparently, a clear trend cannot be recognized. This should not surprise the reader as the optimization does not directly act on the three entropy productions, but it tries to minimize their sum. On the right frame, the filtered trends, following the criterion mentioned in the previous section, elucidate the optimization behaviour. The largest drop in the objective function is brought by minimization of losses in OP1; this result is achieved after few surrogate updates. Then, the optimization tries to improve the performance by acting mainly on the other two operating conditions. As a matter of fact, if the blade performs optimally in OP1 (with performance similar to the one achieved for the single-point optimization), then the performance deteriorates when either increasing or decreasing the pressure ratio. After the 25^{th} iteration, the optimum is found and there is no additional progress in the objective function for the remaining surrogate updates.

The optimal blade profile is illustrated in figure 2.15, where it is compared against the optimal profile obtained with the single-point optimization. The two blades look very similar, recalling that the main modification with respect to the baseline is related to the rear part of the blade. The multi-point optimal profile is characterized by a slightly larger thickness on the suction side; however, this is compensated by a similar reduction in the pressure side. In this way, the throat size remains approximately unaltered between the two configurations, as deemed by the combination of the constraint on the mass-flow rate and choked operation.

By analyzing the corresponding performance for the three operating conditions, only a slight improvement is achieved by performing a multi-point optimization over the investigated range, as clearly illustrated by figure 2.16, which reports the mixed-out loss coefficient for the three operating points and the corresponding average (dashed lines). A similar multi-point optimization performed with an adjoint solver has revealed a larger improvement of the overall performance (Pini *et al.*,

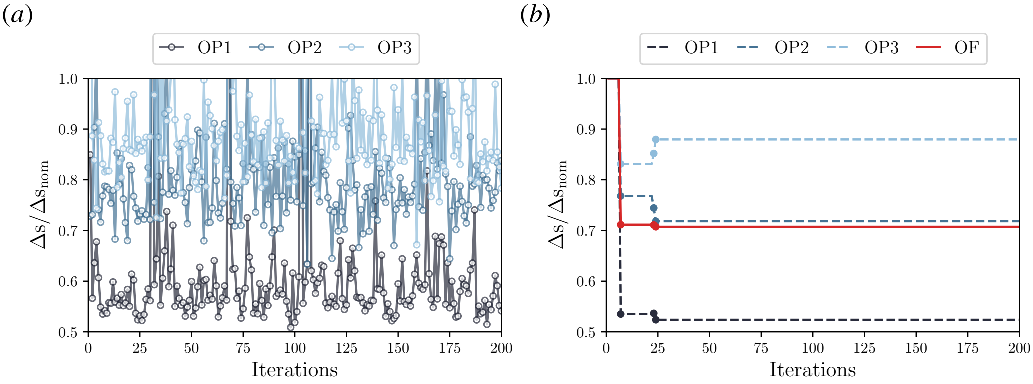

FIGURE 2.14. Convergence history for the multi-point constrained optimization of the supersonic blade cascade: (*a*) entropy production for the three operating conditions throughout the optimization, and (*b*) monitor of the minimum objective function that satisfies the constraint alongside corresponding entropy produced in each operating condition.

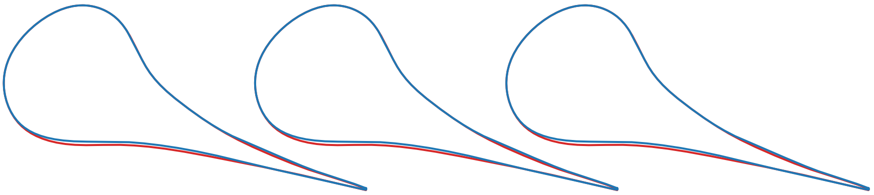

FIGURE 2.15. Comparison between the single-point (——) and multi-point (——) optimal blade profile.

2014). The main explanation for this discrepancy is that the present optimization also features a constraint on the mass flow rate, which limits the feasible design space. As previously discussed, such constraint has a direct influence on the throat size, which has to be preserved to fulfill the constraint. Despite the similar averaged performance, this is achieved in different ways by the two cascades. Such evidence has a first implication on the optimization strategy: as the objective function includes the performance of multiple conditions in a single coefficient, this latter may be more subject to multi-modal behaviour, for which gradient-based algorithms are not suitable. Multi-modal objective functions are instead not a concern for the present surrogate-based strategy, in which the surrogate is built on the entire design space and optimized with global optimization algorithms such as GA. In overall terms, the multi-point optimal profile features smaller losses in OP2 than the single-point blade, compensated by larger losses in OP1 and OP3. Finally, it must be recalled that the multi-point optimization requires a larger computational cost than the single-point formulation, hence the user has to evaluate whether the additional cost is justified.

The flow fields produced by the two optimal cascades in the three operating conditions are reported in figure 2.17 in terms of Mach number. The multi-point optimization produces a converging-diverging profile adapted for the condition OP1, which is intermediate in terms of pressure ratio between OP2 and OP3. Therefore, the reduction in the objective function for the multi-point optimization is pursued by following the same path delineated by the single point, i.e. producing an adapted nozzle cascade in OP1 conditions. This explanation clarifies the similarity between the flow fields produced by the two optimal cascades, notwithstanding different optimization processes. In both cases, by reducing the pressure ratio (OP2), a shock onsets on

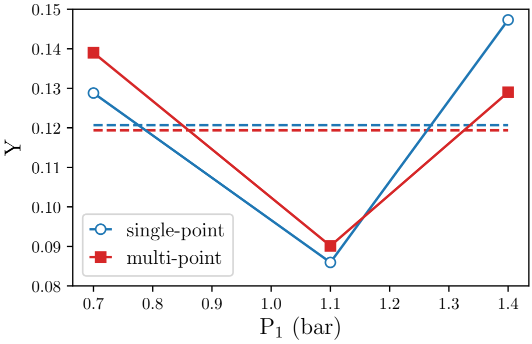

FIGURE 2.16. Mixed-out total-pressure loss coefficient for single-point and multi-point optimal cascade against variations in the downstream static pressure.

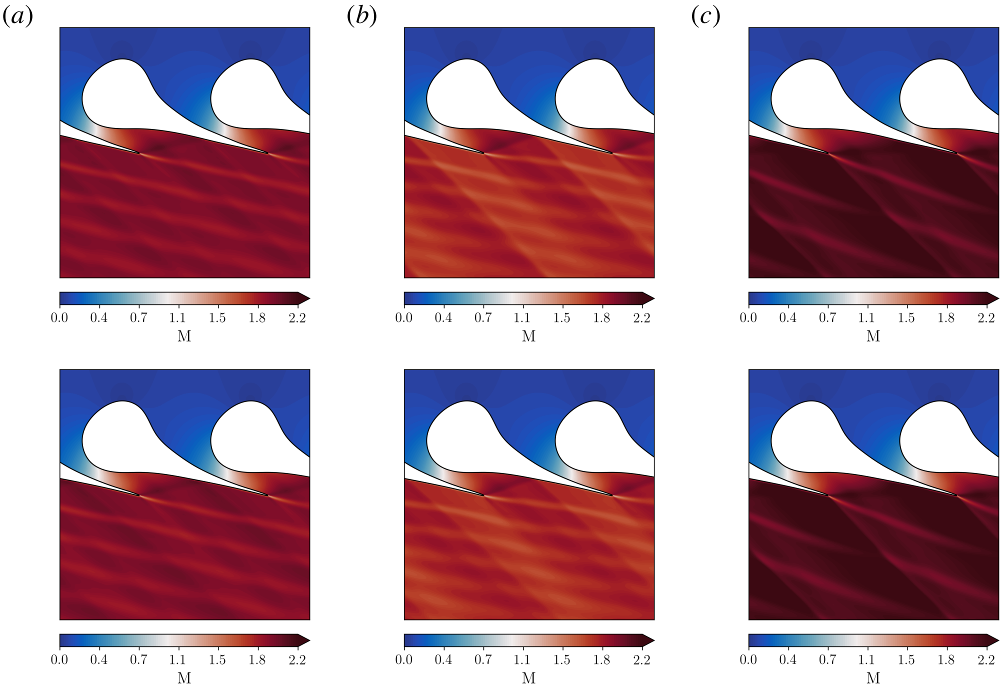

FIGURE 2.17. Mach number fields for the single-point (top frames) and multi-point (bottom frames) optimal cascades: (*a*) OP1, (*b*) OP2, and (*c*) OP3.

the rear suction side because, as the geometry is adapted for a larger expansion, the flow must be recompressed to match the larger back pressure at the stator outlet. On the other hand, when the pressure ratio increases (OP3), the flow acceleration on the suction side increases to comply with the larger expansion. Ultimately, the flow terminates in a shock at the trailing edge, which is mainly responsible for entropy production due to the mixing process occurring downstream.

The blade loadings expressed in terms of isentropic Mach number are reported in figure 2.18 for the three operating conditions. The slight variations between the two distributions are strictly correlated with the blade profiles reported in figure 2.15. In general, the flow accelerates less

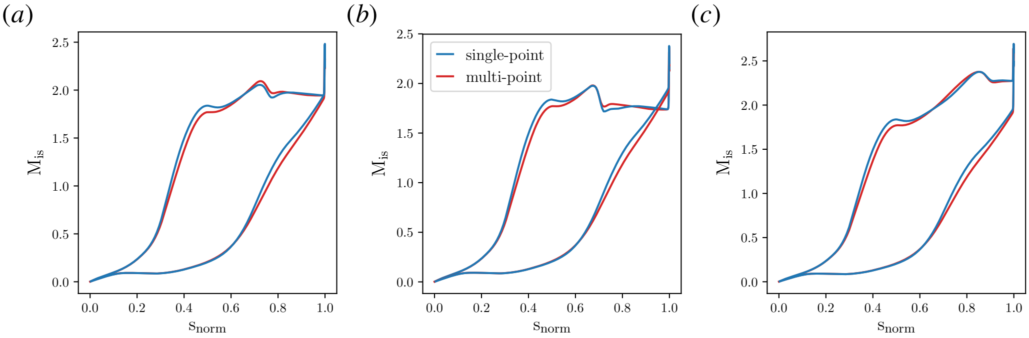

FIGURE 2.18. Isentropic Mach number distributions on the normalized blade surfaces for the three operating conditions: (*a*) OP1, (*b*) OP2, and (*c*) OP3.

within the multi-point optimized blade as a consequence of the smaller area in the diverging channel. The superior performance of the profile obtained through the multi-point optimization in OP2 conditions can be clearly understood by observing the corresponding shock reduction at $s_{norm} = 0.65$. A similar interpretation cannot be provided for the opposite situation in OP3, in which the single-point optimized blade performs better. As discussed before, in these conditions the main responsible for the efficiency reduction is the shock originating at the trailing edge, which will propagate downstream. Therefore, the observed variations in the cascade performance can be attributed to a different strength of this shock, which does not explicitly appear in the blade loading distribution.

2.5 Single-point constrained optimization of a transonic centrifugal turbine stage

Heavy organic compounds are characterized by a relatively small enthalpy drop along with the expansion, laying the ground for compact turbine configurations even in large-scale ORC systems made by few stages and characterized by supersonic flow regimes. To accomplish the supersonic expansion in an efficient way, the first stage usually relies on a converging-diverging shape, such as the one introduced and optimized in the earlier sections. The previous analysis shed light on the current limitations of supersonic cascades in off-design conditions, whose performance cannot be proficiently improved even by resorting to multi-point shape optimizations. As the flexibility of the power system is becoming as important as its efficiency, the present-day paradigm for ORC turbine is shifting towards a higher number of stages, accepting an increased size of the machine. With the aim of preserving compactness while increasing the number of stages, the novel radial-outflow or centrifugal turbine represents a valid alternative to conventional layouts, receiving scientific (Pini *et al.*, 2013) as well as industrial (Spadacini *et al.*, 2011) recognition. The centrifugal layout allows disposing of many stages in a relatively compact device, reducing the cascade expansion ratios and, hence, avoiding supersonic flow conditions. Furthermore, centrifugal turbines can properly accomplish the large volumetric flow ratio thanks to the inherent increase of passage area along the flow path, thus limiting the flaring angle without a significant increase in meridional flow component. For these reasons, this set-up has the potential for achieving high aerodynamic performance as well as wide power control capability. Due to the novelty of this configuration, there are no tailored design criteria, which can provide efficient turbomachinery profiles. Within this framework, shape optimization methods can represent effective strategies to deal with the design of this turbomachinery. To this end, a complete centrifugal stage (stator and rotor) optimization is undertaken in the following to showcase the potentialities of the present surrogate-based shape-optimization strategy.

2.5.1 Description of the test case

The centrifugal blade rows studied in this work are conceived for application in the six-stage ORC centrifugal turbine proposed in Pini *et al.* (2013) operating with MDM as working fluid. The layout of the original turbine consists of six 0.5 reaction stages, each of them featuring the same discharge flow angle (66.7°, opposite in sign between stators and rotors), and the same blade meridional chord (26 mm). The six-stage arrangement allows limiting the flow regime to transonic conditions, despite the large pressure ratio. The through-flow analysis conducted by the authors highlights the smooth flow evolution in the meridional channel. The axisymmetric distribution of the Mach number confirms that the flow is transonic or weakly supersonic. In the present work, the focus is on the stator and rotor that compose the first stage.

The flow is expanded from $P_0^t = 10.0\,\mathrm{bar}$ and $T_0^t = 274.0\,\mathrm{K}$ with an overall total-static expansion ratio of approximately 2 across the first stage ($P_2 = 5.37\,\mathrm{bar}$). The corresponding isentropic expansion is conveniently reported in a $T - s$ plane in figure 2.19(a), in which the map of Z is superposed, highlighting the relevant role of non-ideal effects ($Z = 0.6 - 0.8$). Both the stator and the rotor cascade are expected to be transonic but their outlet Mach number does not exceed unity, hence converging blade channels are considered for the baseline configurations. These baselines are designed by applying the technique proposed in Persico *et al.* (2013), who suggests using profiles featuring an elliptic-arc mean line to induce a sufficiently smooth acceleration of the flow along the blade channel. Then, a conventional distribution of thickness is applied to the mean-line to construct the blade. The resulting profiles, originally designed in cartesian coordinate systems, are finally mapped into polar coordinates using a conformal transformation, in order to maintain the geometric angles of the blade.

The stator blade is designed to deflect the flow from radial outward flow to 66.7°; the blade number, selected using the Zweifel criterion (Zweifel, 1945), resulted equal to 27. The thickness distribution is taken from that of a lightly loaded low-pressure axial turbine. The rotor blade is designed to deflect the (relative) flow from about 50.0° to −66.7°; for such a high aerodynamic loading, the application of the Zweifel criterion led to 52 blades. Moreover, the slender profile shape used for the stator was found to be not suitable for a blade with turning larger than 90 deg, as flow detachment might occur in the central part of the profile. For this reason, an alternative thickness distribution is assigned, taken from that of a high-pressure turbine blade, resulting in a more advantageous configuration also from the structural point of view. The blade geometries and the resulting pressure field are reported in figure 2.19(b). Alongside non-ideal effects, transonic flow regimes are established, prompting compression shocks in the rear part of both blades.

2.5.2 Formulation of the optimization problem

The general parametrization procedure recalls the steps outlined in §2.2.1 and already explained for the parametrization of the supersonic cascade. Nonetheless, depending on the specific blade aerodynamics, a different CP distribution is identified as follows.

As for the stator blade, the shape optimization is focused on the rear part of the profile. However, as discussed in detail by Persico (2017), also the front suction side is critical, as adverse pressure gradients can be established in this area. For these reasons, the stator geometry is parametrized with 21 CPs, 14 of those are movable by ±0.4 mm along the direction normal to the local blade surface, as reported in figure 2.20(a). Moreover, one additional CP is varied by ±0.5 mm to account for the

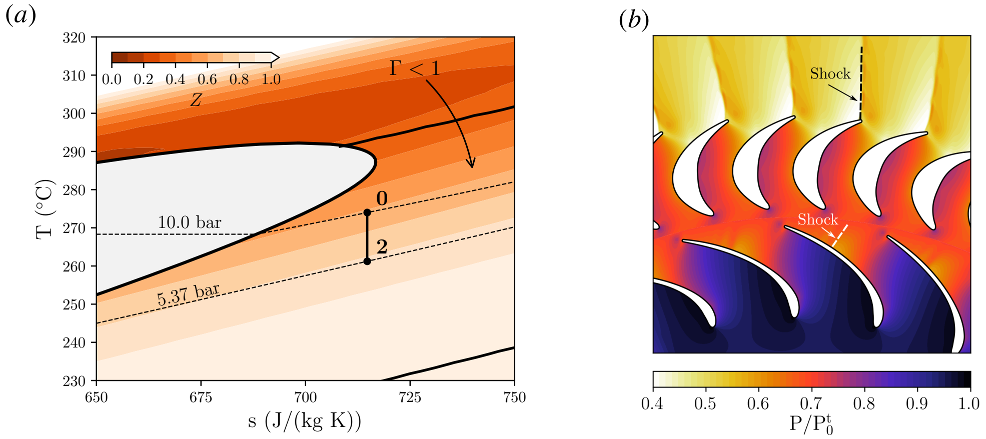

FIGURE 2.19. Boundary conditions (*a*) and flow field (*b*) of a transonic centrifugal stage, which serves as a baseline of a dedicated shape-optimization task. The region $\Gamma < 1$ is contained within the two tick black lines.

rigid displacement of the TE, which is modelled with an ellipsoidal shape. As a result, 15 design variables, i.e. $\mathbf{d}_{stat} \in \mathbb{R}^{15}$, are considered for the optimization of the stator alone.

As for the rotor parametrization, although the baseline exhibits very different features with respect to the stator, it shares with this latter some design difficulties. The significant curvature in the rear region, required to regularly distribute the very high turning along the whole blade, complicates the design, especially on the suction side. The central section of the blade, which features the largest camber and thickness, is also critical, especially for the blade loading control. These considerations lead to parametrize the blade with 20 CPs, assembled as follows: 4 on the leading edge, 7 on the suction side, 5 on the pressure side and 4 on the trailing edge; as highlighted in figure 2.20(*b*), 9 CPs are movable along the direction normal to the local blade surface by a displacement increasing from ±0.5 mm in the trailing edge region to ±0.8 mm in the central part of the blade. Out of these 9 movable CPs, 5 are placed on the suction side and 4 are placed on the pressure side, while the front part of the blade is kept fixed within the optimization process. Analogously to previous parametrizations, one additional moveable CP is placed in the trailing-edge region to permit a rigid movement of this latter within ±0.6 mm while preserving the baseline shape and thickness. Such rotor parametrization asks for additional 10 design variables $\mathbf{d}_{rot} \in \mathbb{R}^{10}$ to be included in the optimization problem.

As the optimization is carried out for the whole stage simultaneously, the overall number of design variables includes both design variables for the stator and the rotor, resulting in 25 design variables, $\mathbf{d} = \mathbf{d}_{stat} \bigcup \mathbf{d}_{rot} \in \mathbb{R}^{25}$. Having identified the design variables, the optimization problem is formulated as follows:

$$\begin{aligned} \min_{\mathbf{d}=\mathbf{d}_{stat} \bigcup \mathbf{d}_{rot}} \quad & \Delta s = s_2 - s_0 \\ \text{subject to:} \quad & -0.5^\circ \leqslant \beta_2 - \beta_{2,nom} \leqslant 0.5^\circ \\ & A_{rot}/A_{rot,nom} \geqslant 0.95 \end{aligned} \tag{2.33}$$

While minimizing the entropy produced by the entire stage (stator and rotor), some constraints have to be satisfied. In particular, the rotor outlet flow angle is constrained to vary within $\Delta\beta_2 = \pm 0.5^\circ$. Such constraint copes with the request to keep a correct incidence on the subsequent nozzle cascade, besides constraining the specific work in accordance with the Euler equation for

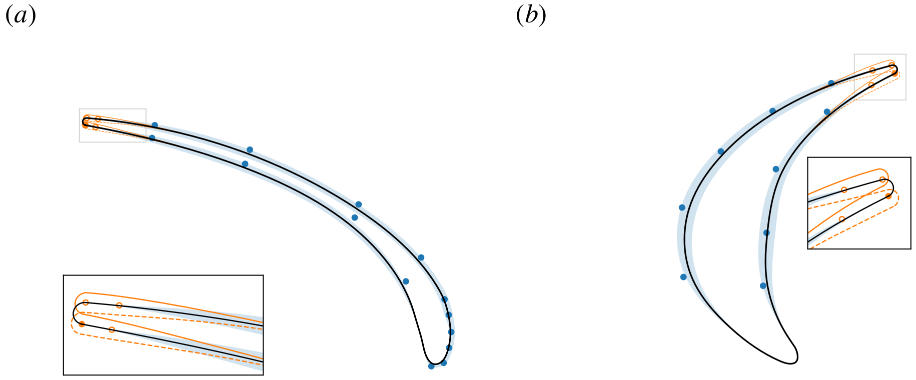

FIGURE 2.20. Design space for the shape optimization of a transonic stator and rotor for a centrifugal turbine stage; ● moveable control points on the blade profile; ● moveable control point at the trailing edge; ○ control points at the trailing edge that moves rigidly with the adjustable control point.

the work exchange. Conversely to the previous optimization test-case, the mass-flow rate is not directly constrained. However, the constraint on the outlet flow angle has also a side effect on the mass-flow rate because the cascade is not choked. More specifically, the mass-flow rate is likely to marginally increase as a consequence of the expected efficiency improvement. Furthermore, a geometrical constraint on the area of the rotor profile is also imposed to preserve the mechanical feasibility of the optimized profile.

The entropy production and the rotor flow angle at the outlet are estimated from dedicated CFD simulations, with settings similar to the ones detailed in §2.3.2. As the present optimization involves both the stator and the rotor, steady-state simulations are performed by introducing a mixing plane between the stationary and the rotating ($\omega = 3000\,\text{RPM}$) domain. The mixing-plane interface averages velocity components along the circumferential direction, thus enabling the simulation of a single periodic blade passage for both the stator and rotor. Quasi three-dimensional simulations are undertaken by considering two straight layers along the spanwise direction and considering free-slip boundary conditions at the endwalls. The thermodynamic model for MDM relies on the multi-parameter equation of state as formulated by (Thol *et al.*, 2017) and made available by REFPROP® (Lemmon *et al.*, 2013), and it was introduced via LUTs. The table ranges are taken large enough to avoid any clip or extrapolation which may make critical the convergence process, with an accuracy of approximately 0.1 K and 0.1 bar for temperature and pressure, respectively. A finer thermodynamic discretization did not lead to any substantial variation in solution.

Hexahedral meshes are generated with ANSYS-TURBOGRID®. A proper cell clustering near blade walls is imposed to ensure $y^+ \lesssim 1$, thus avoiding the introduction of wall functions in the solution. The grid assessment is carried out separately for the stator and rotor. The results are reported in figure 2.21(*a*) in terms of relative error in the entropy produced, which is the objective function of the present optimization problem. A clear asymptotic trend is observed by increasing the number of cells in the blade-to-blade plane, with a faster convergence rate for the stator. The relative flow angle at the outlet rotor is found to converge faster than the entropy, therefore this latter guides the selection of a suitable mesh for the rotor. Ultimately, both stator and rotor grids consist of 150,000 cells in the blade-to-blade plane, which returns a geometrical error of less than 1% in both cases. The computational meshes are displayed in figure 2.21(*b*)–(*c*) for the stator and rotor, respectively. The resulting computational cost required for the overall stage simulation is ~ 30 minutes on an Intel® Xeon® CPU E5-2630 v3 @ 2.40GHz equipped with 16 cores.

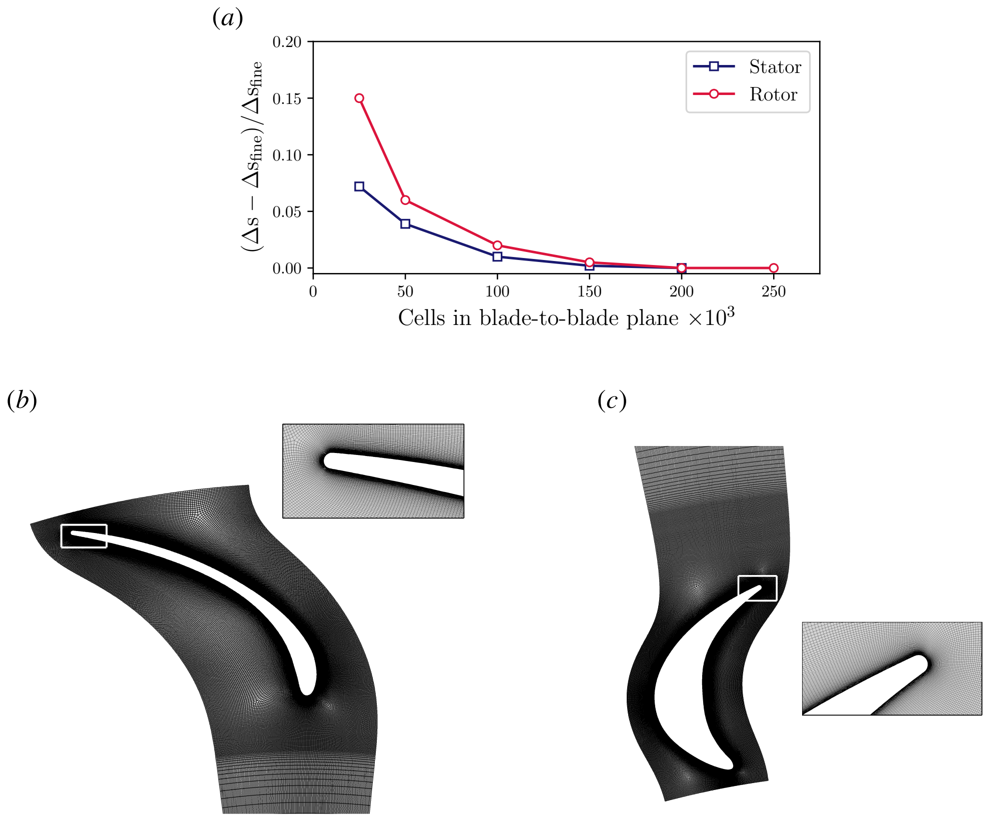

Figure 2.21. Grid convergence assessment (*a*) in terms of entropy production for the baseline stator and rotor. The selected grids for the optimization task are reported in frame (*b*) and (*c*), respectively, each grid consisting in approximately 150,000 cells in the blade-to-blade plane and providing the best compromise between accuracy and computational cost.

The first surrogate interpolation is carried out on a DoE that includes 125 blade geometries, i.e. five times the number of design variables. Based on previous results, the quadratic formulation is employed in the modelling of the Kriging mean trend.

2.5.3 Optimization outcome

The convergence history is illustrated in figure 2.22. Analogously to previous optimization tasks, the larger reduction in the objective function occurs after few iterations (approximately 25% with respect to the baseline value), then subsequent improvements are obtained, though to a lesser extent (further decreases up to 5 percentage points after 200 iterations). As a consequence of the larger design space compared to previous optimizations, there might be still room for improvements if the optimization could have kept going after the 200^{th} iteration. Nonetheless, the reduction of 30% in the entropy produced by the stage is considered satisfactory, and no additional surrogate updates are run.

The two optimized blades are compared against the baselines in figure 2.23. The optimal stator features a larger curvature right after the leading edge, while the trailing-edge region is slightly modified. As for the rotor, the optimization mainly alters the central region of the blade, reducing

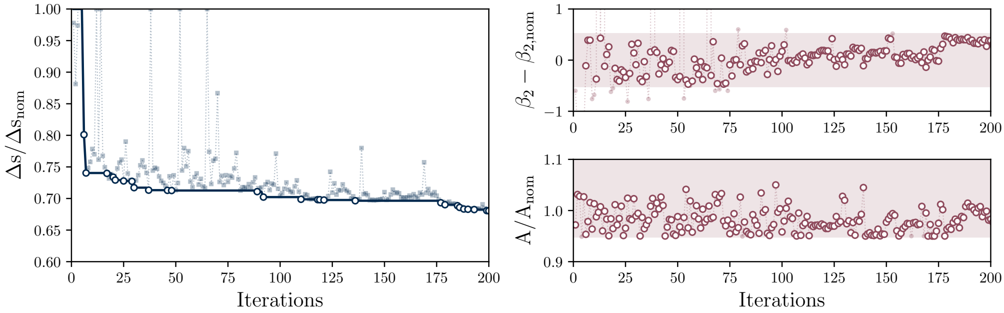

FIGURE 2.22. Convergence history of the transonic centrifugal stage optimization. On the left frame, the thick line monitors the minimum objective function that satisfies the constraint. The filled band in constraint histories represents the acceptable deviation of the constraint.

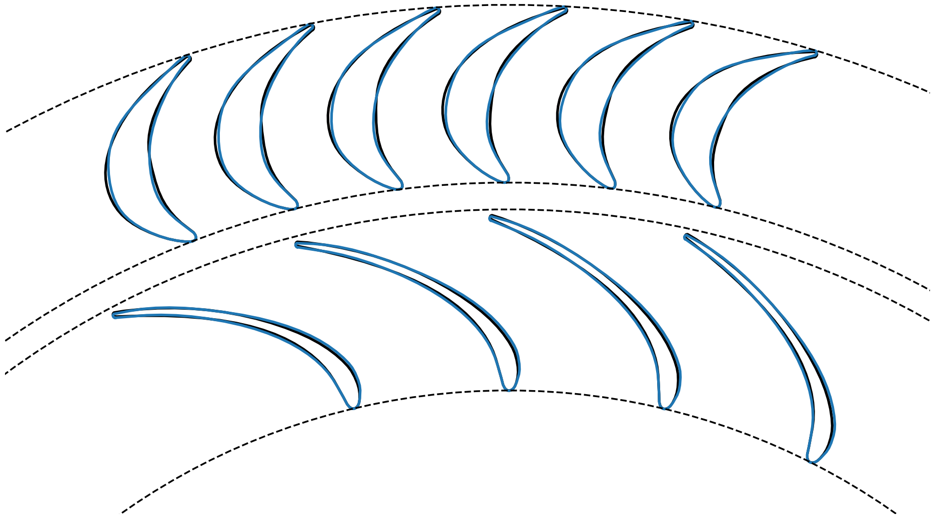

FIGURE 2.23. Comparison between the baseline (——) and the optimal (——) stator and rotor profile.

the thickness on both blade sides. The rear region of the rotor is also altered, as the trailing edge is moved azimuthally in such a way as to limit the curvature in the final part of the blade.

To understand the effect of the optimization, a loss breakdown is carried out to separate the effect of the stator and of the rotor on the stage efficiency. This latter is quantified in terms of total-to-total efficiency, defined as:

$$\eta_{TT} = \frac{h_0^t - h_2^t}{h_0^t - h_{2,is}^t} = 1 - \underbrace{\frac{h(P_1^t, s_1) - h(P_1^t, s_0)}{h_0^t - h_{2,is}^t}}_{\mathit{\Delta}\eta_{\text{stat}}} - \underbrace{\frac{h(P_2^t, s_2) - h(P_2^t, s_1)}{h_0^t - h_{2,is}^t}}_{\mathit{\Delta}\eta_{\text{rot}}} \tag{2.34}$$

where $\mathit{\Delta}\eta_{\text{stat}}$ and $\mathit{\Delta}\eta_{\text{rot}}$ are conveniently defined to isolate the loss contribution form the stator and the rotor, respectively. Table 2.2 reports these values for the baseline and the optimized stage, highlighting the predominant role of the rotor in the determination of the stage efficiency. Based

TABLE 2.2. Stage-efficiency variations between baseline and optimal blades.

	$\Delta\eta_{\text{stat}}$ (%)	$\Delta\eta_{\text{rot}}$ (%)	η_{TT} (%)
Baseline	1.2	7.0	91.8
Optimal	1.5	4.2	94.3

on these results, the optimization mainly acts on improving the rotor performance, whose loss contribution decreases from 7.0% to 4.2%. Meanwhile, the stator losses slightly increase, passing from 1.2% to 1.5%. Overall, the total-to-total efficiency rises by 2.5 percentage points. On a strictly quantitative ground, the improvement in stage efficiency is sufficiently high for being estimated reliably by the CFD solver; as a matter of fact, comparison against experiments showed that the CFD model here used provides performance estimates within 1% of the experimental value, as reported in Persico *et al.* (2012).

Finally, it is interesting to understand how such improvements are obtained from an aerodynamic standpoint. To this end, the flow fields expressed in terms of Mach number are reported in figure 2.24 for the two configurations. The severe shock that onsets at the trailing edge of the baseline rotor is split into two minor shocks in the optimized configuration. The combination of the two shocks has a lower impact on the overall entropy produced compared to the original shock, as shown in figure 2.25 in which the entropy increase across the shocks is barely visible in the optimized cascade. As for the stator, the loss increase is mainly given by the onset of multiple shocks on the rear part of the optimized configuration, although they do not significantly contribute to entropy production. Apart from the efficiency, however, the presence of multiple shocks can promote unsteady interactions with the subsequent rotor cascade. Such undesired effect observed in the stator is strictly correlated with the employed parametrization techniques based on B-splines. As widely explained in §2.2.1, the more CPs, the more the piecewise curves that provide the local support. In these circumstances, a straight shape in localized blade regions to accomplish a regular loading distribution is harder to achieve. Such requirement is even more attractive in transonic blades, in which the presence of small bumps can provoke the onset of small shocks, as observed for the present stator. However, such shape regularity is difficult to be ascribed within the optimization as a constraint. One possibility is to reduce the number of control points, but this action would limit the design space and the achievable improvement. An alternative could be represented by the development of a regularization step right after the parametrization, trading a part of the B-spline flexibility with more regular blade-loading distributions. This idea sets the ground for future research activities to enhance the capability of the present shape-optimization tool.

2.6 Concluding remarks and key findings

A technique for the shape optimization of turbomachinery blade profile is developed and tested on several design tasks. At first, the blade parametrization based on a B-spline interpolation is introduced. It enables the accurate reproduction of the baseline blade with a limited number of control points. Moreover, the B-spline interpolation can be carried out with a non-uniform knot sequence, allowing for the specification of more/fewer control points in localized blade regions. The local modification of the blade shape is accomplished with the displacement of a subset of control points. Therefore, movable control points and their associated displacements constitute the design variables of the optimization problem.

The optimization is carried out with genetic algorithms, which can easily deal with constraints and multi-modal objective functions. To tackle the large number of function evaluations needed

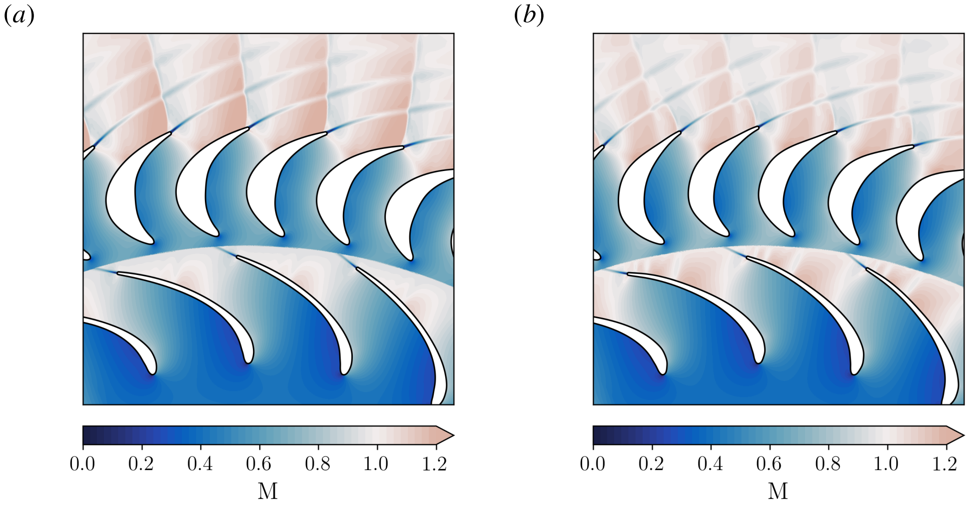

FIGURE 2.24. Mach number field for the baseline (*a*) and the optimal (*b*) transonic stage.

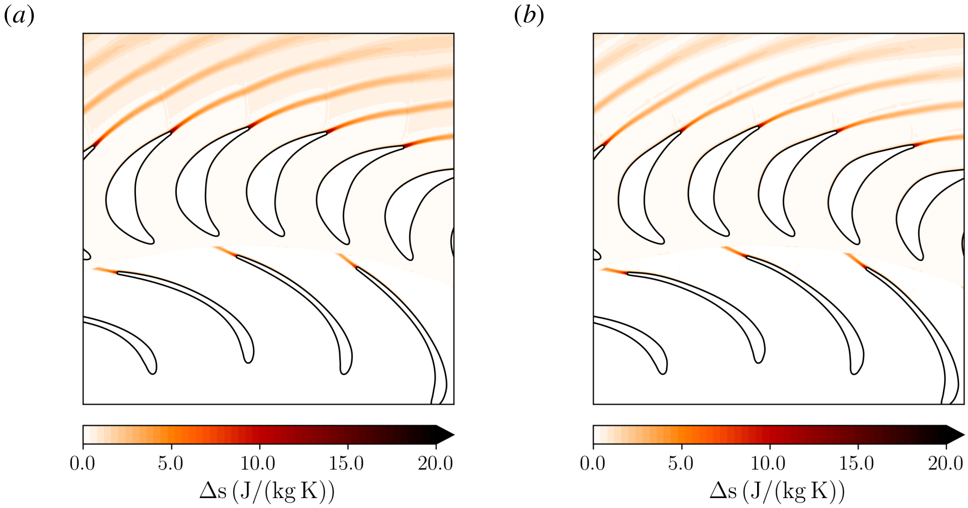

FIGURE 2.25. Entropy field for the baseline (*a*) and the optimal (*b*) transonic stage.

by genetic algorithms to converge, computationally expensive CFD simulations are replaced by Kriging predictors for both objective functions and constraints. A number of blades are identified within the prescribed design space with a space-filling algorithm and simulated via CFD. The blade designs and associated output responses are collected to generate the first surrogate interpolation. The optimization with genetic algorithms is then performed on such surrogates, which can be interrogated many times at a negligible computational cost. The reliability of surrogates is progressively increased throughout the optimization by adding samples to the initial design pool.

The surrogate-based shape-optimization strategy is used to design different turbine cascades, which differ in terms of flow regimes, non-ideal effects, target performance, system constraints, and turbine layout. The first optimization task was used as a reference to assess some modelling choices related to the surrogate and to evaluate the sensitivity of the final outcome on the initial design pool on which the first surrogate interpolation is performed. As a result of these parametric studies, the proper set-up of surrogate parameters is identified and used for the remaining cases. In the following, a summary of the design cases and optimization outcomes illustrates the effectiveness of the present optimization strategy:

1. The first design task involved an axial-turbine converging-diverging cascade for ORC applications. The baseline cascade faced a supersonic flow regime ($M > 2$) and ideal-like conditions ($Z \sim 0.9 - 1.0$). The requirement was the maximization of the performance at design conditions while accepting a deviation of $\pm 1\%$ in the datum mass-flow rate. The optimal blade exhibits a total-pressure loss coefficient halved with respect to the baseline value while coping with the mass-flow rate constraint.

2. The previous cascade was subject to further optimization by including multiple operating conditions in the definition of the objective function. However, minor improvements are obtained with respect to the previous optimization, which only accounted for the design conditions.

3. The shape optimization is then applied to the re-design of a transonic centrifugal stage for ORC applications. The expansion is characterized by significant non-ideal conditions ($Z \sim 0.6 - 0.8$). Both stator and rotor profiles are optimized with the aim of reducing the overall entropy generation while preserving the outlet flow angle and satisfying a minimum area requirement for mechanical reasons. The optimal cascades produce an increase of 2.5 percentage points in the stage efficiency while coping with all prescribed constraints.

Especially in the context of supersonic turbines, whose performance is largely determined by shock losses, the shape optimization is expected to provide consistent improvement compared to analytical methods, e.g. based on the method of characteristics, which inherently assume inviscid flow and do not consider the interaction of trailing edge shock with the rear suction side in the blade design.

CHAPTER 3

NON-IDEAL FLOWS IN SUPERSONIC TURBINES

Flows in the close proximity of the vapour-liquid saturation curve and critical point are examined for supersonic turbine cascades, where an expansion occurs through a converging-diverging blade channel. The present chapter illustrates potential advantages and drawbacks if turbine blades are designed for operating conditions featuring a non-monotonic variation of the Mach number across the expansion, and non-ideal oblique shocks and Prandtl-Meyer waves downstream of the trailing edge. In contrast to ideal-gas flows, for a given pressure ratio across the cascade, the flow field and the turbine performance are found to be highly dependent on the thermodynamic state at the turbine inlet, in both design and off-design conditions. As a consequence, an uncertainty quantification study clearly indicates that a significant non-ideal expansion leads to an amplification of the operational uncertainty. Although the study focuses on a specific fluid, the agreement with the general isentropic steady flow theory arguably extends the present results to most molecularly complex fluids featuring $\Gamma < 1$ *in the single-phase vapour region.*

Some contents of this chapter are also discussed in:

Romei, A., Vimercati, D., Persico, G., & Guardone, A., (2020) Non-ideal compressible flows in supersonic turbine cascades, *Journal of Fluid Mechanics*, vol. 882: A12 (26 pages), doi: 10.1017/jfm.2019.796

Romei, A., Vimercati, D., Guardone, A., & Persico, G., (2020) Amplification of operational uncertainty induced by non-ideal flows in supersonic turbine cascades, *Journal of Engineering for Gas Turbines and Power*, vol 142(8):081006 (15 pages), doi: 10.1115/1.4047770

3.1 Introduction to non-ideal flows in molecularly complex fluid

Flows of molecularly complex fluids in the neighborhood of the vapour-liquid saturation curve and critical point depart significantly from the ideal-gas-like behaviour typical of dilute thermodynamic states. As commented in the introduction, this discrepancy emerges from the analysis of the sound speed variation along with isentropic transformations, which can be conveniently reduced to the evaluation of the fundamental derivative of gas dynamic $\mathit{\Gamma}$ (Thompson, 1971), that can also be expressed as:

$$\mathit{\Gamma} = 1 + \frac{\rho}{c}\left(\frac{\partial c}{\partial \rho}\right)_s \tag{3.1}$$

Recall that if $\mathit{\Gamma} > 1$, the speed of sound increases upon isentropic compression; this is the typical behaviour of dilute, ideal gases with constant specific heats for which $\mathit{\Gamma}_{id} = (\gamma + 1)/2$, where $\gamma > 1$ is the ratio of the specific heats. As opposed to the ideal gas dynamics, the speed of sound decreases following an isentropic compression if $\mathit{\Gamma} < 1$. Thermodynamic states exhibiting $\mathit{\Gamma} < 1$ are found in the single-phase vapour region of molecularly complex fluids for pressures and temperatures of the order of their critical-point values (see, e.g., Thompson & Lambrakis, 1973; Cramer, 1989; Colonna & Guardone, 2006) and in the near-critical two-phase region of most substances (Nannan *et al.*, 2013). Based on the sound-speed evolution in isentropic processes, i.e. on the sign of $\mathit{\Gamma} - 1$, it is convenient to distinguish between the *ideal gasdynamic regime* if $\mathit{\Gamma} > 1$, in which the usual ideal-gas behaviour is recovered, and the *non-ideal gasdynamic regime* if $\mathit{\Gamma} < 1$. Fluid-dynamic effects associated with thermodynamic states featuring $\mathit{\Gamma} < 1$ include the non-monotonic variation of the Mach number across isentropic expansions (Cramer & Best, 1991; Cramer & Crickenberger, 1992), the discontinuous increase of the Mach number across oblique shocks (Gori *et al.*, 2017; Vimercati *et al.*, 2018) and non-classical phenomena in the regime $\mathit{\Gamma} < 0$ (Thompson, 1971; Thompson & Lambrakis, 1973; Cramer & Kluwick, 1984; Menikoff & Plohr, 1989; Kluwick, 2001; Zamfirescu *et al.*, 2008; Guardone *et al.*, 2010). The present discussion is limited to single-phase flows of substances exhibiting $\mathit{\Gamma} > 0$, thus excluding non-classical phenomena.

Fluids evolving in the non-ideal classical gasdynamic regime $0 < \mathit{\Gamma} < 1$ are encountered in several industrial applications, including the flow in the turbo-expander of ORC power systems (see, e.g., Colonna *et al.*, 2008). At present, the majority of ORC plants feature cycles with relatively mild maximum pressures and temperatures (subcritical cycles). In these conditions, even if the expansion through the turbine may partly occur in the non-ideal gasdynamic regime, non-ideal effects such as those mentioned above are, in fact, not observed (Hoffren *et al.*, 2002; Persico, 2017).

Several studies indicate that a potential gain in efficiency may be achieved by employing high-temperature ORCs, in particular transcritical cycles (Schuster *et al.*, 2010; Lai *et al.*, 2011). Within this framework, the occurrence of non-ideal effects cannot be excluded. An example can be found in the work of Colonna *et al.* (2008), where some numerical simulations display a non-monotonic Mach number in the blade channel. This result, however, was not commented on in light of its potential influence on the aerodynamic performance of the cascade. Whether non-ideal effects in the expansion process can affect the turbine performance and design is still unclear.

The present study contributes to the understanding of non-ideal flows evolving in supersonic nozzle cascades, by showing the role of non-ideal effects in turbine performance and discussing their design implications. To this end, exemplary flows of siloxane MM in nozzle cascades are considered and compared. MM is a molecularly complex fluid currently employed in ORC power plants (Colonna *et al.*, 2015) and is chosen here as a representative of the class of fluids where non-ideal effects can be observed. In fact, several studies (Cramer & Best, 1991; Cramer & Crickenberger, 1992; Guardone & Vimercati, 2016; Vimercati *et al.*, 2018) indicate that qualitatively similar behaviour is expected between different fluids exhibiting $0 < \mathit{\Gamma} < 1$. Therefore, although conducted on a specific fluid, the present analysis is arguable of more general validity and thus its outcomes may be extended to other fluids relevant to the ORC field.

In the cases analyzed here, the turbine vanes always operate in the non-ideal gas-dynamic regime. Nonetheless, non-ideal effects are found only in a smaller domain of the entire non-ideal gas-dynamic regime. Depending on the upstream total conditions, two very different operating regimes can establish: one mirrors the ideal-gas scenario and is obtained with relatively dilute conditions at the cascade inlet; the other one, obtained for high-pressure inlet conditions, is characterized by non-ideal effects. To account for this difference, a further distinction based on the value of Γ is made hereinafter: the operating conditions are classified as *ideal-like operating regime* whenever $\Gamma \sim 1$ in the supersonic expansion, yielding turbine aerodynamics qualitatively similar to its ideal-gas counterpart. On the other hand, $\Gamma \ll 1$ in the supersonic expansion identifies the *non-ideal operating regime*, whereby non-ideal effects may play a significant role in the cascade operation. Even so, it is worth highlighting that the threshold between the two operating regimes is not a well-defined boundary and further fundamental studies aiming at developing a comprehensive theory are still needed. For convenience, turbine cascades operating in the ideal-like and non-ideal operating regime are referred to as *ideal-like cascade* and *non-ideal cascade*, respectively. The same designations will be also used to distinguish the corresponding flow features.

Finally, since non-ideal effects can only occur in specific thermodynamic conditions, whether an operational uncertainty in the power cycle affects the turbine operation in a non-ideal gas-dynamic regime also deserves a proper answer. To this end, a comparative analysis between an ideal-like and a non-ideal supersonic nozzle cascade is performed by introducing uncertainties in the values of maximum temperature and pressure of the power cycle, as well as in the condensation temperature. Cycle uncertainties are properly converted into an operational uncertainty of the first-stage stator, enabling their formulation in CFD simulations in the form of variations in flow boundary conditions. A surrogate-based uncertainty-quantification analysis is combined with CFD simulations to propagate the above operational uncertainty on the cascade aerodynamics. Similar procedures of uncertainty quantification were successfully applied to estimate ORC turbomachinery performance in what we called ideal-like conditions (Bufi *et al.*, 2015; Razaaly *et al.*, 2019). In the present work, the methodology is applied to both ideal-like and non-ideal cascades, comparing their probabilistic performance in terms of cascade losses, alteration of the flow field delivered to the first rotor, and implications on the corresponding power cycles. Since the underlying gas-dynamic physics greatly changes between the two cases, the subsequent impact of an operational uncertainty is expected to differ as well.

3.2 Non-ideal effects in expanding flows

The onset of anomalous compressibility-related effects for flow variables close to the corresponding critical values is anticipated and explained here by recalling available theoretical results. Specifically, well-known results from the theories of quasi-one-dimensional flows and oblique waves (Prandtl-Meyer waves and oblique shock waves) are briefly reported to demonstrate the relevant qualitative and quantitative differences that emerge when the flow evolution occurs in the non-ideal gasdynamic regime, rather than in dilute-gas conditions. The fluid considered hereafter, namely the siloxane MM, is modelled using the state-of-the-art multi-parameter equation of state formulated by Thol *et al.* (2016). The states selected for the theoretical studies of this section are reported in the well-known T–s (temperature–entropy) and P–v (pressure–specific volume) diagrams of figure 3.1.

Firstly, steady quasi-one-dimensional flow (Thompson, 1988) is used as representative of the expansion process through a variable-area duct (inviscid and with constant total enthalpy h^t). Figure 3.2 shows the distribution of the Mach number M with the pressure, for different total conditions chosen along the same isobaric line, which is $P^t = 0.5\,P_c$ in figure 3.2(a) and $P^t = 2\,P_c$

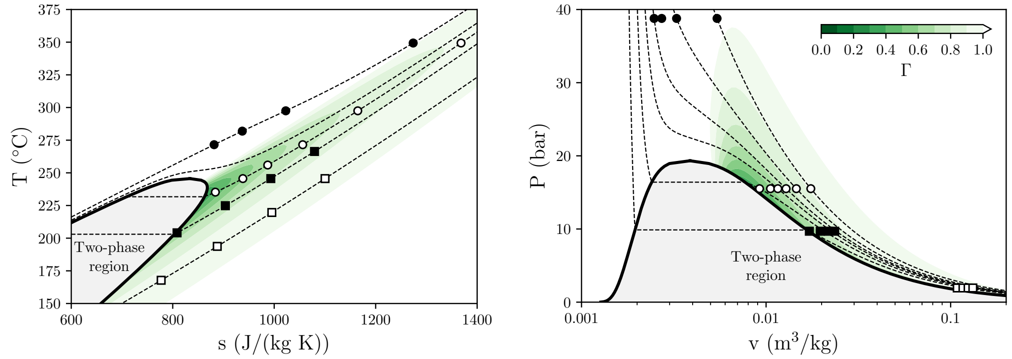

FIGURE 3.1. Thermodynamic diagrams for MM showing the states used in the parametric studies: ■ total conditions for isentropic nozzle flows in figures 3.2(*a*) and 3.3(*a*); ● total conditions for isentropic nozzle flows in figures 3.2(*b*) and 3.3(*b*); □ upstream thermodynamic state for Prandtl-Mayer waves of figure 3.4(*a*) and for oblique shock waves of figure 3.5(*a*); ○ upstream thermodynamic state for Prandtl-Mayer waves of figure 3.4(*b*) and for oblique shock waves of figure 3.5(*b*). A map of the fundamental derivative of gas dynamic Γ is superposed. The gray area identifies the two-phase region. Dotted lines ($\cdots$) represent isobars (left figure) or isotherms (right figure).

in figure 3.2(*b*).

Despite $\Gamma < 1$ at the selected total states, at relatively low total pressures and high temperatures (figure 3.2(*a*)), most of the expansion occurs in dilute-gas conditions. Thus, the distributions of the Mach number are qualitatively identical and also quantitatively very similar to that computed from the ideal-gas model, which depends on the pressure ratio P^t/P only. The ideal-gas limit curves hereafter are all obtained by setting $\gamma = c_{p,\infty}(T_c)/c_{v,\infty}(T_c)$, where $c_{p,\infty}$ and $c_{v,\infty}$ are the specific heats in the ideal-gas limit and T_c is the critical temperature. In the present case, $\gamma = 1.026$.

The effects of the non-ideal thermodynamic behaviour of the fluid can be fully appreciated by selecting thermodynamic states in the proximity of the critical point or in the supercritical region. The scenario observed in figure 3.2(*b*) is representative of the flow evolution in the non-ideal gas-dynamic regime and involves not only a marked quantitative difference with respect to its ideal-gas counterpart but also important qualitative differences. Indeed, extrema in the Mach number may possibly occur, see for example case $T^t = 1.05\,T_c$ in figure 3.2(*b*), where T^t is the total temperature. As a result, the Mach number is no longer monotonic across the isentropic expansion. This follows immediately from the analysis of Cramer & Best (1991), in which the parameter

$$J = 1 - \Gamma - \frac{1}{M^2} = \frac{\rho}{M}\frac{dM}{d\rho} \tag{3.2}$$

is introduced as a dimensionless measure of the Mach number derivative with the density (or pressure, after straightforward manipulation) and condition $J > 0$ is recognized as the necessary condition for the Mach number to decrease across isentropic expansions.

Figure 3.3 reports the distribution of the area ratio A/A^* with the pressure, where A^* is the critical area (at which $M = 1$), for different total conditions chosen along the same isobaric lines as above, namely $P^t = 0.5\,P_c$ in figure 3.3(*a*) and $P^t = 2P_c$ in figure 3.3(*b*). In both cases, the distribution of the area ratio is qualitatively similar to that of the ideal-gas limit. However, significant quantitative differences can be appreciated in the exemplary non-ideal case depicted in figure 3.3(*b*). As an example, expansion from total conditions up to $A/A^* = 2$ corresponds to an expansion ratio $\beta = P^t/P = 2.76$ from $T^t = 1.05\,T_c$ and to $\beta = 6.78$ in the ideal-gas limit ($T^t \to \infty$ at fixed P^t). This should be compared to the case $P^t = 0.5\,P_c$, for which the same

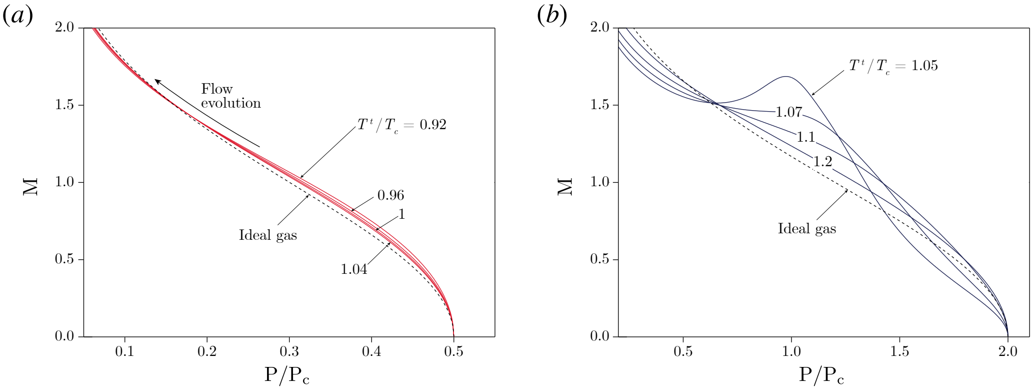

FIGURE 3.2. Mach number distribution for quasi-one-dimensional flow of fluid MM with total pressure (*a*) $P^t = 0.5\,P_c$ and (*b*) $P^t = 2\,P_c$; each solid line corresponds to a different value of the total temperature T^t, while dotted lines are obtained from the ideal-gas model of MM.

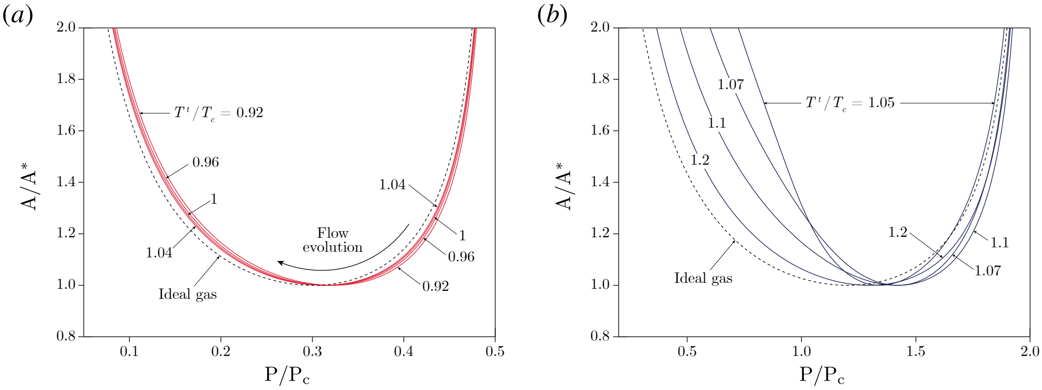

FIGURE 3.3. Area ratio distribution for quasi-one-dimensional flow of fluid MM with total pressure (*a*) $P^t = 0.5\,P_c$ and (*b*) $P^t = 2\,P_c$; each solid line corresponds to a different value of the total temperature T^t, while dotted lines are obtained from the ideal-gas model of MM.

area ratio $A/A^* = 2$ corresponds to $\beta = 6.15$ from $T^t = 1.05\,T_c$. An alternative interpretation is connected with the design of the diverging portion of a nozzle aimed at realizing a given outlet pressure. The same outlet pressure is attained with a considerably larger exit-to-throat area ratio if expanding from high total-pressure conditions, thus involving severe non-ideal gas-dynamic effects.

Next, oblique waves are examined, as representative of the turning processes of a supersonic stream that can possibly occur at the trailing-edge of the turbine blades and in the rear blade section. Figure 3.4(*a*) reports the downstream Mach number against the flow deflection angle ϑ across Prandtl-Meyer waves, computed for a fixed upstream pressure $P_A = 0.1\,P_c$ and Mach number $M_A = 2$, and different values of the upstream temperature T_A. Each curve is computed using the definition of the Prandtl-Meyer function given by Cramer & Crickenberger (1992) and valid for arbitrary equations of state. At the selected upstream states, $\Gamma_A = 0.96 \div 0.98$. In this range, the level of non-ideality is sufficiently low that the actual features of Prandtl-Meyer waves are qualitatively similar to those computed from the ideal-gas model, despite a slight quantitative difference is still observed. Note, also, that across centered Prandtl-Meyer fans the fluid is isentropically expanded

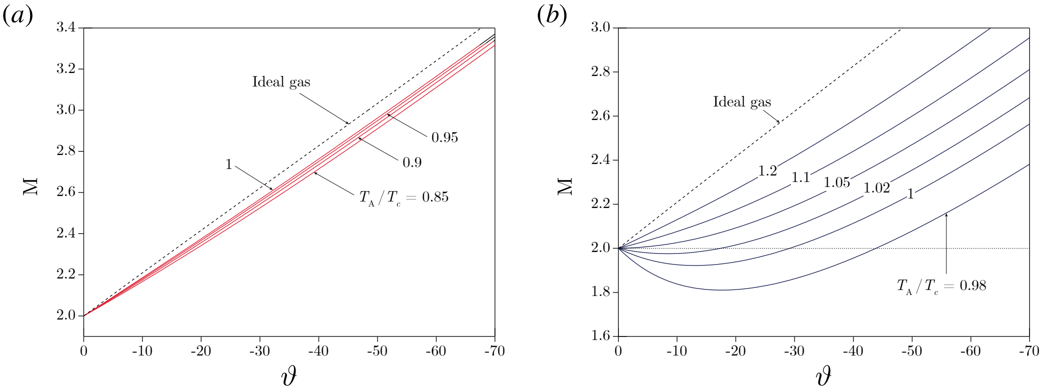

FIGURE 3.4. Variation of the Mach number with the wave deflection angle across Prandtl-Meyer waves in fluid MM with upstream Mach number $M_A = 2$ and pressure (*a*) $P_A = 0.1\,P_c$ and (*b*) $P_A = 0.8\,P_c$; each solid line corresponds to a different value of the total temperature T_A, while dotted lines are obtained from the ideal-gas model of MM.

and therefore driven towards more dilute thermodynamic conditions. The non-ideal turning of a supersonic stream across Prandtl-Meyer waves is depicted in figure 3.4(*b*), which is obtained by setting the state upstream of the wave to $P_A = 0.8\,P_c$ and $M_A = 2$, while different values of T_A are considered. Remarkable quantitative and qualitative differences can be observed, most importantly the possibility that the Mach number decreases across the rarefaction wave, which is in contrast with the ideal-gas behaviour. For later convenience, Prandtl-Meyer waves featuring a decrease of the Mach number are referred to as non-ideal Prandtl-Meyer waves. The non-monotonic variation of the Mach number within the wave stems from thermodynamic states satisfying $J > 0$ during the expansion (Cramer & Crickenberger, 1992). Indeed, the flow field corresponding to Prandtl-Meyer waves is isentropic and with constant total enthalpy, so that the same considerations of the one-dimensional case apply (Wheeler & Ong, 2013; Galiana *et al.*, 2016).

Finally, an analogous study is performed for oblique shock waves, see figure 3.5. Figures 3.5(*a*) and 3.5(*b*) are generated using the same upstream states of figures 3.4(*a*) and 3.4(*b*), respectively. Although the compression across the shock brings the flow towards more dense and therefore non-ideal thermodynamic conditions, at relatively low upstream pressures such as in figure 3.5(*a*), non-ideal effects are in fact not observed, except at the quantitative level and to a limited extent. On the contrary, in figure 3.5(*b*) a non-ideal discontinuous increase of the Mach number is observed across oblique shocks. This phenomenon is the compression counterpart of the decrease of the Mach number in Prandtl-Meyer waves depicted in figure 3.4(*b*). Following Gori *et al.* (2017) and Vimercati *et al.* (2018), oblique shocks producing an increase in the Mach number will be referred to as non-ideal oblique shocks afterward. It was demonstrated by Vimercati *et al.* (2018) that weak oblique shocks from upstream states featuring $J_A > 0$ are necessarily non-ideal oblique shocks. Moreover, due to non-isentropic effects, non-ideal oblique shocks can possibly occur from upstream states $J_A < 0$, though it is still required that $J > 0$ along the shock adiabat connecting the upstream and downstream states.

3.3 Gasdynamics of nozzle cascades in the non-ideal regime

In this section, the flow field within a linear nozzle cascade operating in the non-ideal gas-dynamic regime is examined by means of numerical simulations. While the previous discussion focused

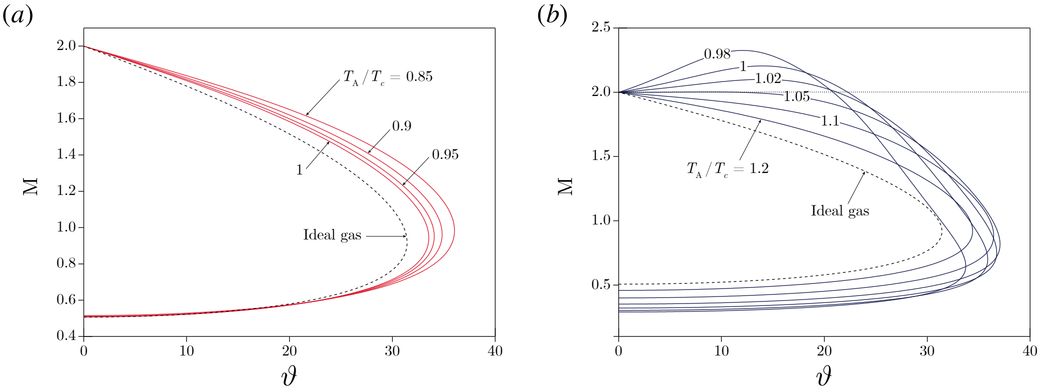

FIGURE 3.5. Variation of the Mach number with the wave deflection angle across oblique shock waves in fluid MM with upstream Mach number $M_A = 2$ and pressure (*a*) $P_A = 0.1\,P_c$ and (*b*) $P_A = 0.8\,P_c$; each solid line corresponds to a different value of the total temperature T_A, while dotted lines are obtained from the ideal-gas model of MM.

on non-ideal effects in the inviscid limit, the correct modelling of the flow through the cascade should account for viscous effects (e.g. boundary layers). In this regard, a comparison between viscous and inviscid losses for the same class of turbine blades was presented by Pini *et al.* (2015*a*). This study shows the large impact of thermo-viscous effects on the shock wave formation and on the mixing process downstream of the cascade, pointing to the need of performing a viscous computation to predict such losses in a turbine cascade. To this end, RANS simulations are carried out.

The computational flow solver is described in §3.3.1. The blade configurations used in this study are presented in §3.3.2 and the grid-convergence assessment in §3.3.3. Expansion through states featuring $\Gamma < 1$ can possibly present very different behaviours, according to the occurrence of diverse non-ideal effects. Three exemplary operating conditions (each consisting of a design point and selected off-design cases) are presented in §3.3.4 and §3.3.5 to illustrate the larger variability and diversity of the flow evolution offered by the non-ideal thermodynamics.

3.3.1 Computational flow model

Numerical simulations are carried out with ANSYS-CFX 18.1®. No-slip and adiabatic conditions are imposed on the blade surface. Axial flow is prescribed at the inlet along with total pressure and temperature (P_0^t, T_0^t). At the outlet, an average static pressure P_1 is imposed; local pressure differences of 5% are allowed. The outlet domain is placed at 8 axial chords downstream of the trailing edge to avoid spurious pressure wave reflections. Since only blade-to-blade effects are of interest, quasi-three-dimensional simulations are carried out by considering a straight stream tube around the midspan (free-slip conditions at the end walls). A single-blade passage is considered by exploiting periodic boundary conditions. The employed turbulence model is $k - \omega$ SST, whose boundary conditions are set as Turbulence Intensity ($T = 5\%$ for all simulations) and eddy viscosity ratio ($\mu_t/\mu = 10$ for all simulations). Note that these boundary conditions have very limited influence on the cascade performance for moderate values of the upstream total pressure (P_0^t up to $0.6P_c$), see Romei *et al.* (2019); the same considerations are expected to hold for a larger range of total pressures. The cascade Reynolds number, based on the blade chord and computed using the mass flow-averaged density, dynamic viscosity, and velocity, is $Re \simeq 2 \cdot 10^6 \div 10^7$ for the simulations involving an expansion far from the thermodynamic critical point. For the simulations close to the critical point, the comparatively larger thermodynamic variations result in a significant variation of the Reynolds number through the blade passage, from $Re \simeq 5 \cdot 10^6$ (based on inlet quantities) to $Re \simeq 10^8$ (outlet quantities). Therefore, the cascade Reynolds number is large enough to assume fully turbulent boundary layer along the entire blade in all examined conditions.

The turbulent Prandtl number is set to $Pr_t = 1$ in all simulations, consistently with other studies (e.g. Otero *et al.*, 2018). With reference to the peculiar dependence of thermodynamic properties on the temperature in the non-ideal gas dynamic regime, it is still unclear whether a specific choice of the turbulent Prandtl number impacts the flow field and consequently the aerodynamic performance of the cascade. A sensitivity analysis on Pr_t, in the range $Pr_t = 0.1 \div 1.5$, was conducted and reveals negligible influence of this parameter on the flow fields (e.g., a maximum temperature variation of 0.05% downstream of the cascade).

The thermodynamic model (multi-parameter equation of state of MM by Thol *et al.* 2016) is implemented using a LUT approach, which allows to speed up the evaluation of the thermodynamic properties (see, e.g., Pini *et al.*, 2015*b*). Thermodynamic tables are built by referring to the NIST REFPROP® database (Lemmon *et al.*, 2013), which also provides dedicated correlations for transport properties (Meier *et al.*, 2004; Perkins *et al.*, 2013). The thermodynamic discretization recalls the one introduced in §2.3.2 for moderate pressure levels, whereby non-ideal effects are weak, while the step in temperature and pressure is reduced by one order of magnitude close to the critical point to comply with the larger gradients in thermo-physical properties. High-resolution TVD schemes (Barth & Jespersen, 1989) are employed in the discretization of both flow and turbulence equations. A central difference scheme is instead adopted for the diffusive flux. The suitability of the present computational set-up for simulations of non-ideal compressible flows near the saturation curve and critical point is discussed and confirmed in the study of Pini *et al.* (2017).

3.3.2 Blade configuration and operating conditions

The turbine cascades used in the following study result from the shape optimizations of the baseline cascade shown in figure 2.4(*b*) by applying the procedure widely described in chapter 2.

The unconstrained optimization aimed at minimizing the entropy production is performed for three exemplary design conditions, namely I-DES, N̂-DES and Ň-DES, reported in table 3.1and depicted in the *T*–*s* diagram in figure 3.6. The design case labeled I-DES recalls the same application, in terms of inlet and outlet thermodynamic conditions of the nozzle cascade, examined in the previous chapter. For these thermodynamic conditions, the flow evolution is similar to that of an ideal gas, thus the expansion inside the nozzle depends almost only on the expansion ratio and on the ratio between specific heats. On this basis, I-DES and related off-design conditions I-OFF-*i*, $i = \left\{\beta_+, \beta_-, T^t_+, P^t_-\right\}$, are referred to as the *ideal-like* operating regime of the nozzle cascade.

Operating conditions N̂-DES and Ň-DES are chosen to highlight non-ideal effects on the flow features arising in the proximity of the blade trailing edge, which are highly influential on the overall cascade performance. Two peculiar operating conditions can be identified in which the Mach number at the trailing edge is close to a local maximum (N̂-DES) or to a local minimum (Ň-DES). For convenience, these operating conditions along with the related off-design cases N̂-OFF-β_+ and Ň-OFF-*i*, $i = \left\{\beta_-, T^t_+, P^t_-\right\}$, are referred to, in the following, as the *non-ideal* operating regime of the nozzle cascade.

The blades optimized for I-DES, N̂-DES and Ň-DES are shown in figure 3.7. All optimal blades feature a higher curvature in the diverging channel and an almost straight profile in the rear part of the blade. In this way, the main compression shock wave is almost eliminated, adapting the nozzle cascade geometry to the expansion process on which the optimization is performed in an analogous way to what is discussed in 2. In the non-ideal gas-dynamic regime, relatively small expansion ratios can generate large outlet Mach numbers, due to the low values of the speed of sound. As an example, operating condition N̂-DES features $M \approx 1.8$ at the nozzle exit with

TABLE 3.1. Boundary conditions for numerical simulations. P_0^t and T_0^t are the total upstream pressure and the total upstream temperature, respectively, P_1 is the downstream static pressure and $\beta = P_0^t/P_1$.

Case Label	P_0^t [bar]	T_0^t [°C]	P_1 [bar]	β
I-DES	8.00	270	1.07	7.3
I-OFF-β_+	8.00	270	0.70	11.4
I-OFF-β_-	8.00	270	1.50	5.3
I-OFF-T_+^t	8.00	290	1.07	7.3
I-OFF-P_-^t	7.00	270	0.96	7.3
N̂-DES	40.0	270	18.5	2.2
Ň-DES	40.0	270	12.5	3.2
N̂-OFF-β_+	40.0	270	16.0	2.5
Ň-OFF-β_-	40.0	270	15.0	2.7
Ň-OFF-T_+^t	40.0	290	12.5	3.2
Ň-OFF-P_-^t	35.0	270	10.9	3.2

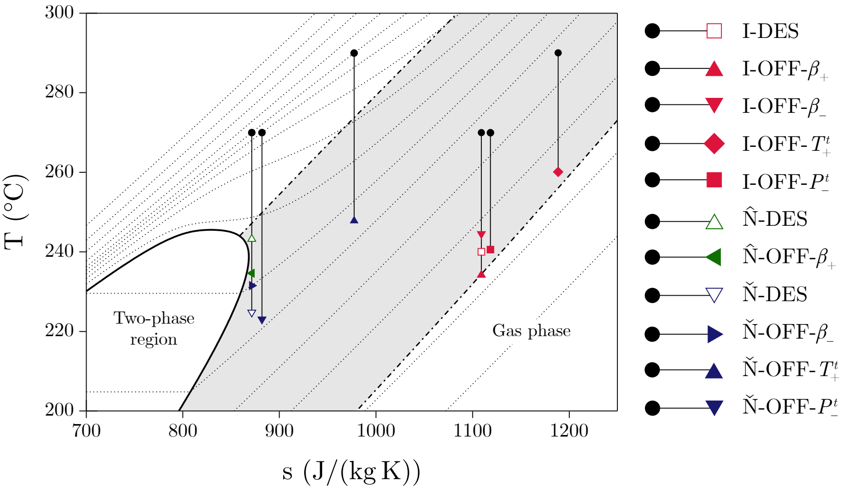

FIGURE 3.6. Temperature versus specific entropy diagram for MM, showing the expansion processes considered in the present work. Dotted lines (· · ·) represent different isobars. Dash-dotted lines (· – ·) identify $\Gamma = 1$.

$\beta = 2.2$. Thus, converging-diverging shapes are mandatory to cope with the supersonic expansion albeit with a comparatively small pressure ratio. The resulting geometries produced by shape optimizations are consistent with the quasi-one-dimensional theory. The selected design conditions are such that $A/A^* = 2.2$ for I-DES, $A/A^* = 1.4$ for N̂-DES and $A/A^* = 2.2$ for Ň-DES. Note that the optimized blades for I-DES and Ň-DES are very similar, despite the significantly different expansion ratios. On the other hand, the optimal blade for N̂-DES differs significantly from all the others due to the much smaller exit-to-throat area ratio.

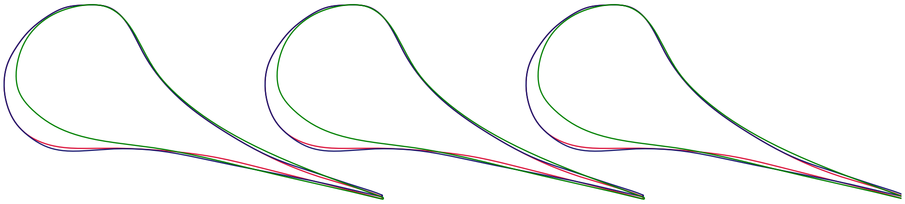

FIGURE 3.7. Optimised nozzle cascades for I-DES (——), N̂-DES (——) and Ň-DES (——).

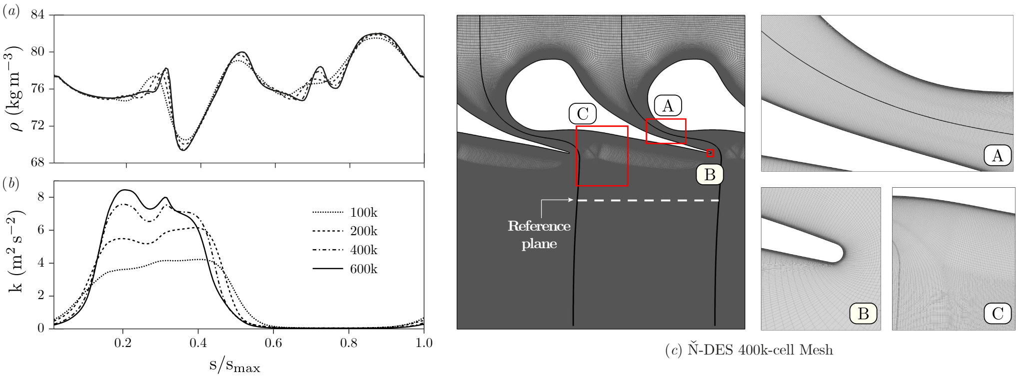

(c) Ň-DES 400k-cell Mesh

FIGURE 3.8. Grid-convergence assessment on Ň-DES: azimuthal distributions of (*a*) density and (*b*) turbulent kinetic energy evaluated on a reference plane located at half axial chord downstream of the cascade; (*c*) details of the 400k-cell mesh (convergence achieved). The cell count refers to the single-blade passage.

3.3.3 Grid assessment and near-wall resolution

Mesh sensitivity analysis is carried out on four different grid refinements, consisting of approximately 100k, 200k, 400k, 600k cells in the blade-to-blade plane (single-blade passage). Grid convergence is assessed on operating condition Ň-DES, detailed in §3.3.2, which involves the highest Reynolds numbers and the most significant non-ideal effects among the other cases.

Figure 3.8(*a*) shows the density distribution along a reference plane located at half axial chord downstream of the cascade, for the different levels of refinements. Grid convergence is achieved starting from the 400k-cell mesh. Other thermodynamic quantities such as pressure, temperature, entropy, and speed of sound show trends very similar to that of figure 3.8(*a*). The same is observed for the velocity and Mach number distributions.

In figure 3.8(*b*), the turbulent kinetic energy profiles are plotted. Higher deviations, with respect to mean-flow quantities, are observed between the different grids. It should also be noticed that the turbulence fields may not achieve a grid-independent state in the presence of shock waves (Sinha *et al.*, 2003). Nevertheless, the 400k-cell and 600k-cell meshes show comparable values of the peak and average turbulent kinetic energy. The distribution of the turbulent kinetic energy is relevant for the prediction of the mixing process downstream of the blades and its evaluation is indeed critical if the stator-rotor axial gap is very small. However, in the present study we are concerned with the performance of the stator alone, thus mixed-flow conditions downstream of the cascade are always achieved by virtue of the wide fluid domain employed in all simulations (see §3.3.1). Similar considerations apply to the turbulence frequency distribution on the different grids. Thus, the 400k-cell mesh, illustrated in figure 3.8(*c*), is chosen as the most suitable for the purpose of the present investigation. The simulation of operating conditions different from the

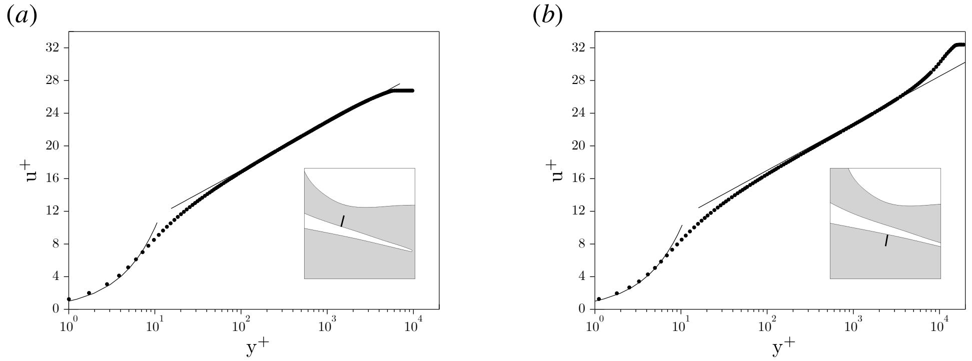

FIGURE 3.9. Velocity profiles in wall units (*a*) in proximity of the channel throat and (*b*) in the rear part of the suction side, downstream of the point of shock reflection. Markers denote the computed u^+ values at grid nodes; solid lines correspond to $u^+ = y^+$ and to the log-law $u^+ = 2.5 \ln y^+ + 5.5$.

Ň-DES is performed on grids with similar topology and refinement.

The total pressure loss coefficient Y, introduced in equation 2.31 and evaluated at two axial chords downstream of the trailing edge, is used to evaluate the cascade performance. This coefficient accounts for all loss sources such as shock (and related shock-boundary layer interaction), mixing, and viscous losses, thus giving an overall indication of the cascade performance. It is found that the maximum difference with respect to the finest-grid value ($Y = 6.7\%$) is 0.4 percentage points (100k-cell grid).

In the above grid assessment, the near-wall grid resolution has been kept constant among the various levels of refinement. Velocity profiles in the boundary layer at selected locations are shown in figure 3.9, specifically in the proximity of the throat and in the rear part of the blade suction side, downstream of the point where the fishtail shock is reflected. The distributions shown in this figure are computed using the 400k-cell mesh. The computed velocity profiles are qualitatively similar to each other, consistently with the fact that there is no shock-induced boundary layer separation. Relatively small deviations are observed with respect to the incompressible, zero-pressure-gradient laws for the viscous sublayer and logarithmic region. This is not surprising in fluids having large heat capacities, due to the very small values of the Eckert number (see Kluwick, 2004; Cinnella & Congedo, 2007; Sciacovelli *et al.*, 2017). Moreover, the computed temperature and density distributions in the boundary layer are nearly constant. Analogous considerations apply to other operating conditions listed in table 3.1.

3.3.4 Ideal-like operating regime of nozzle cascades

In this section we establish the general framework for the analysis of flows in nozzle cascades by focusing on the ideal-like operating regime. Concepts familiar to ideal-gas flows in nozzle cascades are reviewed and extended to the non-ideal thermodynamic description of the flow. The converging-diverging nozzle optimized for the design condition I-DESis considered. In addition to the design condition, cascade performance are also analysed by considering four different off-design expansions I-OFF-i, $i = \left\{\beta_+, \beta_-, T^t_+, P^t_-\right\}$. Each of these processes is detailed in table 3.1 and shown graphically in the T–s thermodynamic plane of figure 3.6. Note that total temperature values used throughout this work lie within the thermal stability limit of the working fluid (Preissinger & Bruggemann, 2016; Keulen *et al.*, 2018).

Pressure and Mach number distributions for I-DES are reported in figure 3.10. The optimization, performed in such conditions, generates a nozzle cascade that features a smooth expansion process,

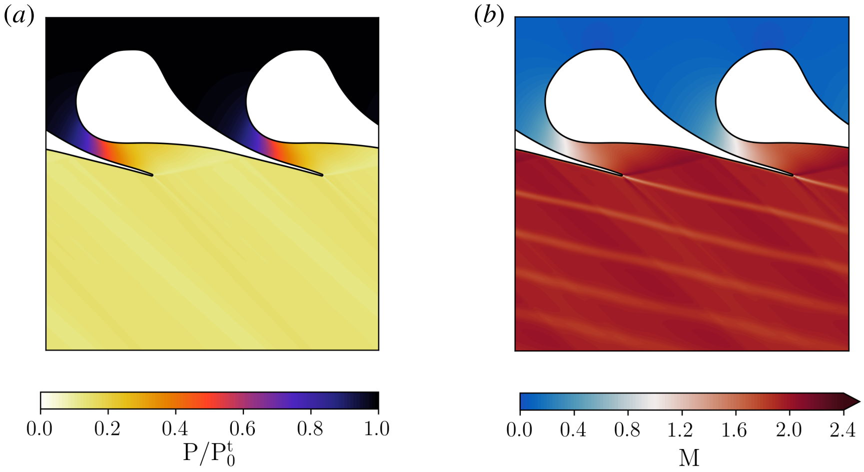

FIGURE 3.10. Pressure field (*a*) and Mach number field (*b*) for I-DES.

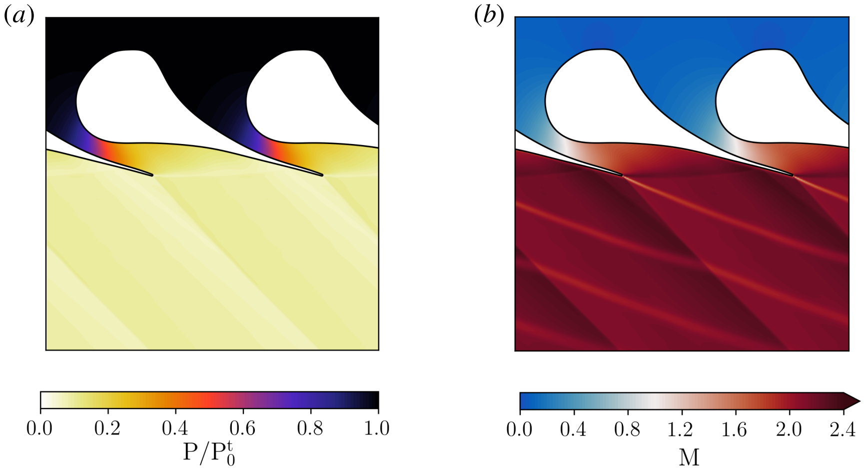

FIGURE 3.11. Pressure field (*a*) and Mach number field (*b*) for I-OFF-β_+.

characterized by a nearly uniform pressure field downstream of the cascade. A weak fishtail shock stems from the trailing edge. More details on the cascade aerodynamics are reported in §2.3.4. Quantitatively, the nozzle cascade exhibits a kinetic energy loss coefficient $Y = 8.2\%$. This value is used as a reference to quantify the impact of off-design conditions on the blade performance within the ideal-like operating regime. Furthermore, I-DES displays a mass-flow-averaged Mach number measured at half axial chord downstream of the trailing edge (representing a plausible stator-rotor gap) equal to $M_{05} = 1.94$.

Off-design cases I-OFF-β_+ and I-OFF-β_- expand from the design superheated conditions to lower and higher outlet pressures, respectively, with respect to the design value. These conditions are very common in power systems due to the seasonal variation of ambient temperature, which directly affects the temperature of condensation and hence the turbine outlet pressure.

I-OFF-β_+ imposes to the flow an expansion characterized by a higher pressure ratio. According to quasi-one-dimensional theory, in the blade channel the flow expands as in the design condition

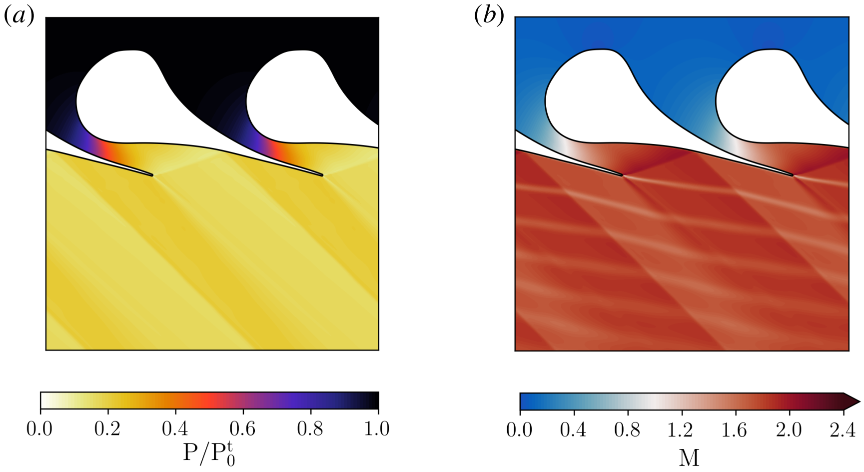

FIGURE 3.12. Pressure field (*a*) and Mach number field (*b*) for I-OFF-β_-.

and a post-expansion is required to match the lower outlet pressure. This behaviour can be qualitatively recognized in figures 3.11. The main contribution to the post-expansion is given by the wider Prandtl-Meyer fan generated on the pressure side of the trailing edge. However, the cascade loss coefficient increases to $Y = 9.7\%$ due to the formation of a stronger shock wave on the opposite side of the trailing edge. For the selected upstream total conditions, the additional expansion provides a higher Mach number ($M_{05} = 2.15$) at the outlet.

The effect of a reduced pressure ratio is illustrated by case I-OFF-β_-, shown in figures 3.12. The pressure distribution shown in figures 3.12(*a*) is strongly affected by the onset of a strong shock wave, especially where the fishtail shock reflects. As a consequence, cascade losses increase showing a net increment of the kinetic energy loss coefficient to $Y = 12.3\%$. Note that the entropy increase across the shocks is only a small share of the overall entropy production. In this regard, the analysis of the entropy fields in figure 3.13 reveals that (i) the entropy jump across shock waves is negligible if compared to the entropy increase generated in the boundary layer and in the mixing downstream of the cascade even in presence of comparatively strong shock waves and (ii) the mixing losses increase with higher non-uniformities caused by stronger shocks in off-design operation. Moreover, the rotor will experience a higher aerodynamic forcing induced by the presence of shock waves. Stronger shock waves lead to a reduction of the Mach number downstream of the nozzle cascade ($M_{05} = 1.75$), as expected in ideal-like conditions.

The following off-design cases I-OFF-T_+^t and I-OFF-P_-^t feature the design pressure ratio, but the fluid is expanded from different upstream total temperatures and pressures, respectively, with respect to I-DES. These conditions may be representative of different part-load control strategies in the context of ORC power systems.

I-OFF-T_+^t corresponds to an increase of the upstream total temperature. In this case, quasi-one-dimensional theory of ideal gases predicts no differences with respect to the design flow evolution, as the expansion process is governed only by the expansion ratio and the ratio of the specific heats, which remains fairly constant by increasing the inlet temperature of 20 °C. The flow field distributions reported in figures 3.14 confirm qualitatively this behaviour, showing no appreciable differences with respect to the ones presented in figure 3.10 for the design condition. Quantitatively, both the outlet Mach number ($M_{05} = 1.94$) and the kinetic energy loss coefficient ($Y = 8.2\%$) are very close to the design values.

Finally, I-OFF-P_-^t features a lower upstream total pressure. The outlet pressure is also reduced

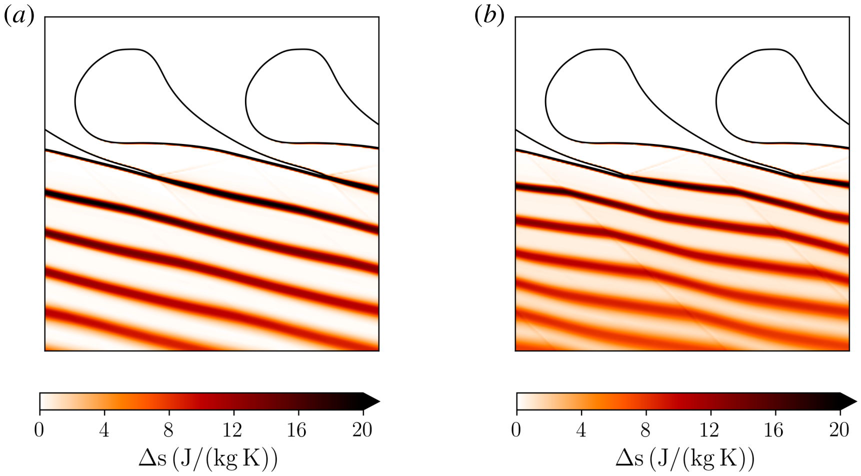

FIGURE 3.13. Entropy fields for I-DES (a) and I-OFF-β_- (b).

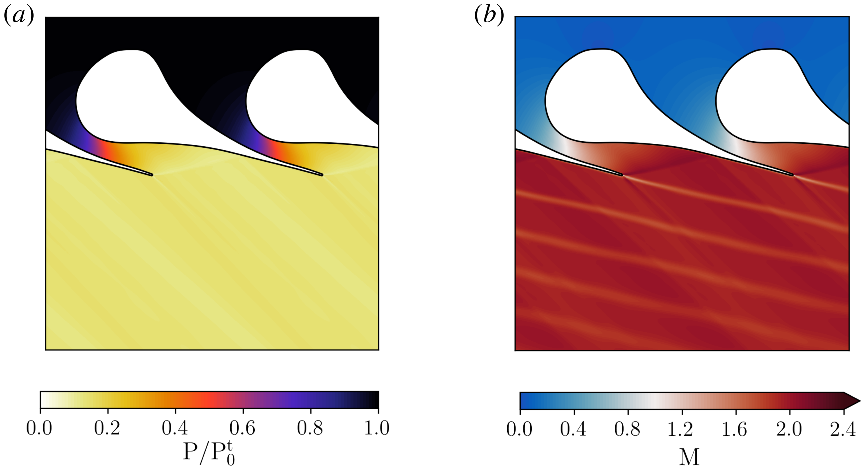

FIGURE 3.14. Pressure field (a) and Mach number field (b) for I-OFF-T_+^t.

to maintain the design pressure ratio. Similarly to I-DES and I-OFF-T_+^t, the same pressure ratio entails qualitatively similar flow fields, see figures 3.15, and in turn analogous values of the outlet Mach number ($M_{05} = 1.94$) and of the loss coefficient ($Y = 8.2\%$).

To sum up, the performance of a supersonic converging-diverging cascade operating in the non-ideal gas-dynamic regime ($\Gamma < 1$) is reported but qualitatively showing ideal-gas behaviour. In the ideal-like operating regime, four off-design conditions were analyzed: (i) an increase of the pressure ratio delivers a larger outlet Mach number with a slight increase of cascade losses; (ii) reducing the pressure ratio, the nozzle cascade features significantly lower performance due to the onset of a strong shock wave to match the higher outlet pressure; (iii) variation of the upstream total state at the same pressure ratio has practically no effect on the cascade performance.

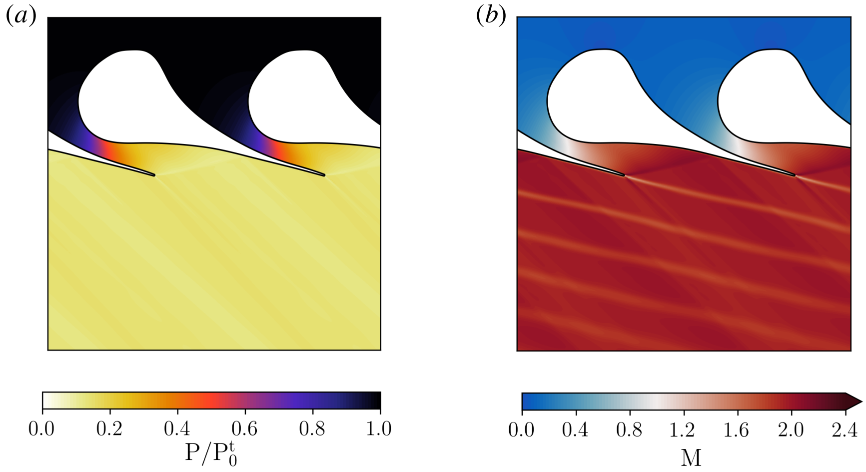

FIGURE 3.15. Pressure field (*a*) and Mach number field (*b*) for I-OFF-P^t_-.

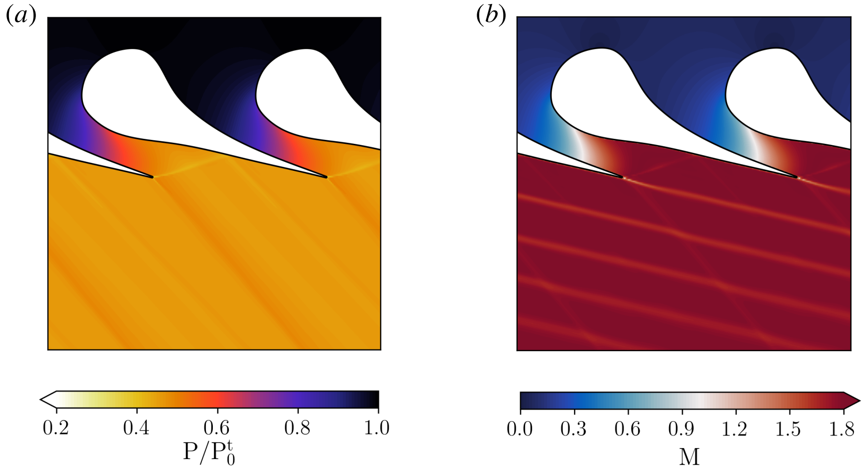

FIGURE 3.16. Pressure field (*a*) and Mach number field (*b*) for N̂-DES.

3.3.5 Non-ideal operating regime of nozzle cascades

In order to investigate the performance of representative nozzle cascades working in the non-ideal operating regime, two different blades are considered, which are designed for expansions N̂-DES and Ň-DES. Off-design behaviour is assessed on four cases labelled N̂-OFF-β_+ and Ň-OFF-i, $i = \left\{\beta_-, T^t_+, P^t_-\right\}$. Each of these cases is detailed in table 3.1 and the corresponding expansion processes are reported in the T–s thermodynamic plane of figure 3.6.

The present choice of the upstream total state for both design conditions offers the possibility to observe and examine effects associated with the non-ideal evolution of the Mach number. According to quasi-one-dimensional theory, the isentropic expansion from $P^t_0 = 40\,\text{bar}$ and $T^t_0 = 270\,°\text{C}$ features a non-monotonic Mach number (see figure 3.2(*b*)) with a remarkable difference ($\Delta M \approx 0.26$) between the two stationary points. Moreover, if $J > 0$ in the neighborhood of the trailing edge (i.e. the expansion through the blade channel end between the two extrema), non-ideal Prandtl-Meyer fans and oblique shocks might be established. This scenario is clarified

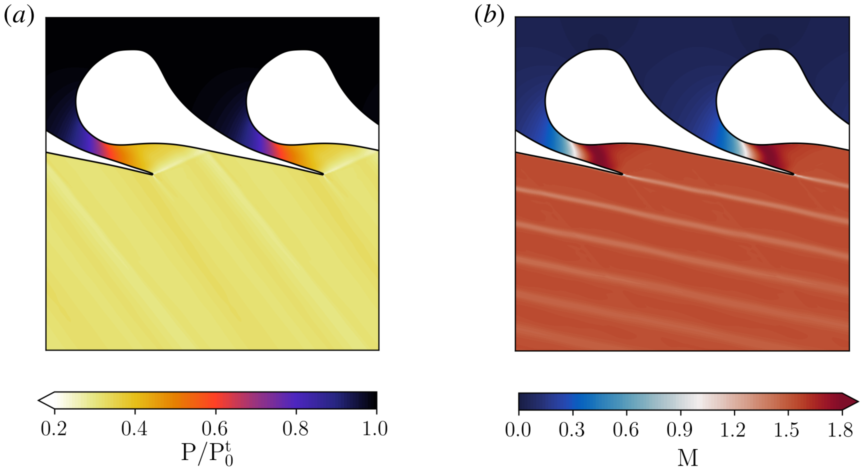

FIGURE 3.17. Pressure field (*a*) and Mach number field (*b*) for $\check{\mathrm{N}}$-DES.

using two specific examples in which the expansion through the blade channel ends near a stationary point of the Mach number (local maximum for $\hat{\mathrm{N}}$-DES and local minimum for $\check{\mathrm{N}}$-DES). Note that a possible advantage deriving from this situation is the enhanced uniformity of the Mach number distribution within the stator-rotor axial gap, due to the relatively low sensitivity of the Mach number to perturbations in the outlet pressure ($J \approx 0$).

Pressure and Mach number distributions for $\hat{\mathrm{N}}$-DES and $\check{\mathrm{N}}$-DES are shown in figures 3.16–3.17. For both cases, a pattern of weak oblique waves occurs downstream of the trailing edge, evidenced in the pressure contours. Inspection of the Mach number fields reveals that no appreciable variation of the Mach number is observed across the oblique wave patterns, owing to very small values of J. Quite distinct values of the outlet Mach number are observed, namely $M_{05} = 1.77$ for $\hat{\mathrm{N}}$-DES and $M_{05} = 1.51$ for $\check{\mathrm{N}}$-DES. As a matter of fact, the comparatively lower value observed in $\check{\mathrm{N}}$-DES, which features instead an increased pressure ratio, is a consequence of the fact that $J > 0$ along with the expansion (indeed the local maximum of the Mach number moves within the blade channel). Cascade performance, used in the following to assess the off-design behaviour, amount to $Y = 4.8\%$ for $\hat{\mathrm{N}}$-DES and $Y = 6.7\%$ for $\check{\mathrm{N}}$-DES.

$\hat{\mathrm{N}}$-OFF-β_+ and $\check{\mathrm{N}}$-OFF-β_-, analogously to I-OFF-β_+ and I-OFF-β_-, respectively, aim at determining the impact of different pressure ratios on the cascade performance. The upstream total conditions are instead kept constant. As the nomenclatures suggest, the blades used in the off-design cases $\hat{\mathrm{N}}$-OFF-β_+ and $\check{\mathrm{N}}$-OFF-β_- are those optimized for $\hat{\mathrm{N}}$-DES and $\check{\mathrm{N}}$-DES, respectively.

The larger pressure ratio in $\hat{\mathrm{N}}$-OFF-β_+ is achieved by means of post-expansion, see figure 3.18. The actual features of the Mach number field downstream of the trailing edge differ significantly from those observed in the ideal-like operating regime. The Prandtl-Meyer fan generated on the pressure side of the trailing edge, and subsequently reflected on the suction side of the neighboring blade, produces a non-ideal decrease of the Mach number. Past the trailing edge, the matching of pressure and flow direction across the wake is accomplished by a non-ideal oblique shock which increases the Mach number. Note that similar flow features can be observed also in $\hat{\mathrm{N}}$-DES, albeit to a much lower extent. The high amount of post-expansion of $\hat{\mathrm{N}}$-OFF-β_+ can be further appreciated from the waviness of the wake. Overall, the prevailing effects is the Mach number decrease across the expansion waves downstream of the trailing edge, which ultimately results in $M_{05} = 1.66$ (while $M_{05} = 1.77$ in the design condition $\hat{\mathrm{N}}$-DES). The total pressure loss coefficient instead increases to $Y = 6.5\%$, as expected, due to the onset of the relatively strong shock generated

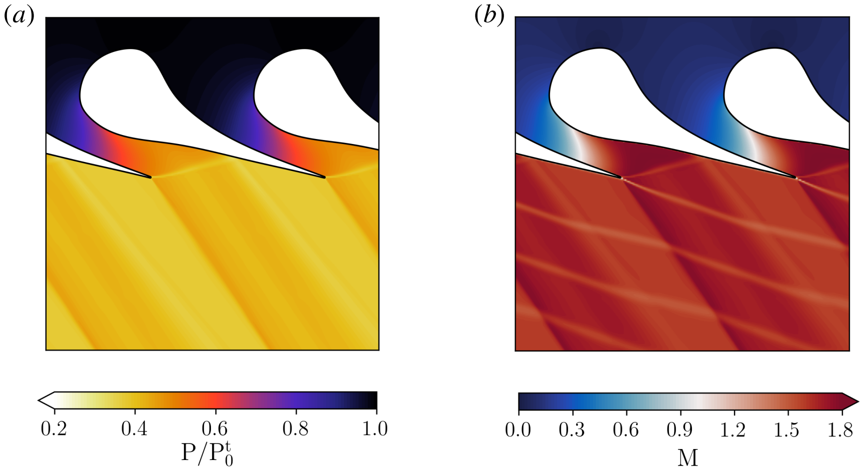

FIGURE 3.18. Pressure field (*a*) and Mach number field (*b*) for N̂-OFF-β_+.

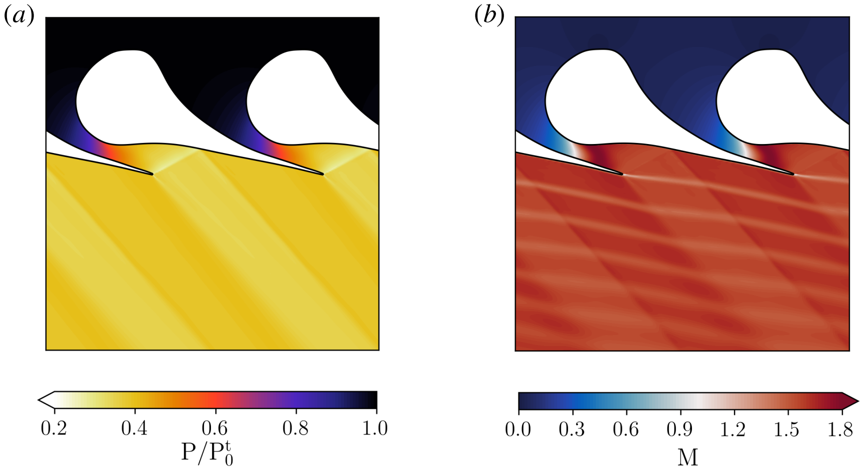

FIGURE 3.19. Pressure field (*a*) and Mach number field (*b*) for Ň-OFF-β_-.

at the trailing edge.

Configuration Ň-OFF-β_- features a decreased pressure ratio. To accommodate the higher outlet pressure, a stronger oblique shock stems from the pressure side of the trailing edge and is reflected on the suction side of the neighboring blade, whereas a rarefaction fan is generated on the opposite side of the trailing edge, as shown in figure 3.19. For both waves, a non-ideal variation of the Mach number is observed, namely the Mach number decreases across the Prandtl-Meyer expansion and increases across the oblique shock wave. The overall Mach number variation follows the non-ideal character of the compression process, resulting in $M_{05} = 1.57$ (while $M_{05} = 1.51$ in Ň-DES). The question arises whether the contribution of shock losses to the overall entropy production is influenced by non-ideal effects; inspection of the entropy fields in figure 3.20 for the design field and the representative off-design condition represented by Ň-OFF-T_+^t shows that there is no substantial difference with the entropy fields reported for the ideal-like operating regime in figure 3.13. Upon careful inspection, a wider wake can be appreciated for the ideal-like scenario.

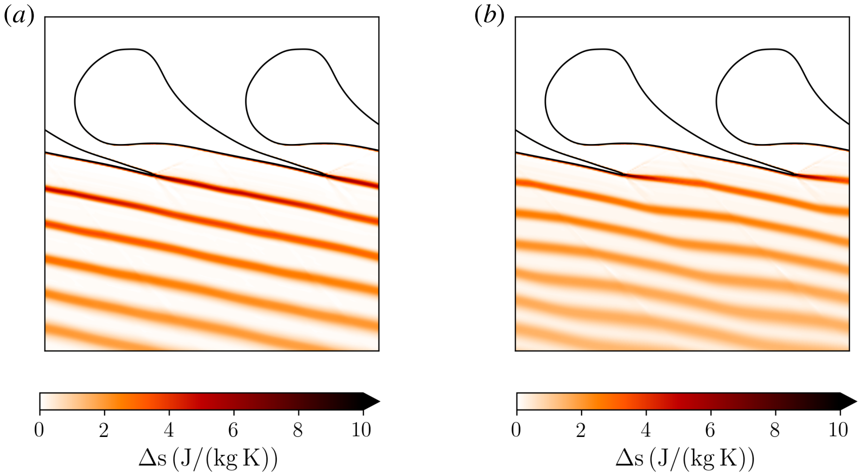

FIGURE 3.20. Entropy fields for $\check{\text{N}}$-DES (*a*) and $\check{\text{N}}$-OFF-β_- (*b*).

In agreement with other works Galiana *et al.* (2016, 2017), the most accredited explanation is that a higher value of the Prandtl-Meyer function, characterizing non-ideal flows $\mathit{\Gamma} \ll 1$, induces higher turning angles, thus a reduced separation region behind the trailing edge.

The situation depicted above for $\hat{\text{N}}$-OFF-β_+ and $\check{\text{N}}$-OFF-β_- is opposed to the ideal-like scenario. The non-ideal variation of the outlet Mach number with the outlet pressure might have remarkable consequences on the operation of the entire turbine. As a matter of fact, the present supersonic cascades are prototypes of the first stators of ORC turbines. The nozzle is commonly followed by a transonic rotor, whose operational characteristics and performance are crucially dependent on the flow regime (whether subsonic or supersonic) associated with the relative flow at the inlet. The rotor-inlet flow is indeed proportional to the (absolute) Mach number at the outlet of the stator, modulated by the rotational speed. Supersonic relative flows at the rotor inlet are detrimental to the turbine flexibility and performance mainly due to the so-called unique-incidence phenomenon (Starken *et al.*, 1984). Within this supersonic flow regime, the rotor leading edge behaves as a bluff body, enabling the formation of a bow shock upstream of the leading edge. Both the shock strength and its distance from the rotor leading edge are a function of the inlet relative Mach number and the leading edge radius. Under this condition the inlet flow angle is no longer a free parameter but is given by the bow-shock interaction among adjacent rotor cascades. It can be proved that, for a given rotor geometry, a unique pattern of characteristic lines is feasible, thus admitting a unique inlet flow angle (Starken, 1993). Therefore, the flow is chocked in the rotor cascade and it is not possible to adjust the mass flow by varying the upstream flow angle. Besides, supersonic rotor cascades may present a complex pattern of shock waves and shock-boundary layer interactions, which is likely to result in a lower stage efficiency as the Mach number at the rotor inlet increases (Rinaldi *et al.*, 2016). A proper design of the rotor cascade allows mitigating the aforementioned phenomena (see, e.g., Bufi & Cinnella, 2018), even though such design is valid only for a specific operating condition. From this point of view, operating conditions similar to $\hat{\text{N}}$-DES, i.e. tuned to obtain a local maximum of the Mach number near to the trailing edge, are advantageous against the unique incidence phenomenon. Indeed, both an increase and a decrease of the outlet pressure would reduce the outlet Mach number, thus increasing the safety margin for unique incidence. On the contrary, for design conditions analogous to $\check{\text{N}}$-DES, a Mach number increase is expected for whatever pressure-ratio variation in the neighborhood of the design point. In particular, a non-ideal effect that unexpectedly increases the stator-outlet/rotor-inlet Mach number for different pressure

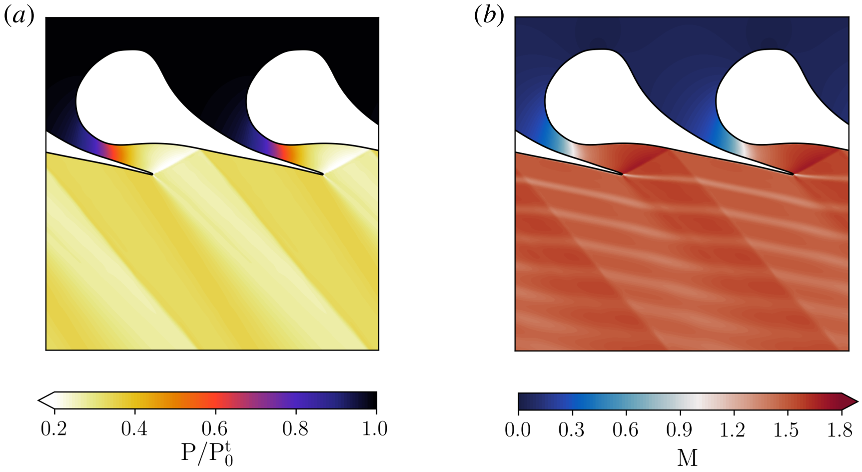

FIGURE 3.21. Pressure field (a) and Mach number field (b) for Ň-OFF-T^t_+.

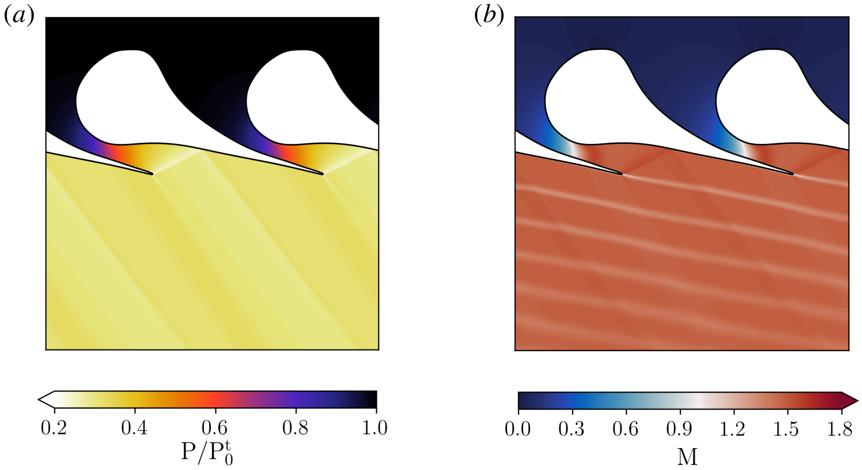

FIGURE 3.22. Pressure field (a) and Mach number field (b) for Ň-OFF-P^t_-.

ratios (e.g. Ň-DES → Ň-OFF-β_-) might drive the rotor in unique-incidence condition, with severe detrimental effects on the turbine operation and performance. It is worth highlighting that in the ideal-like operating regime a decrease/increase of the outlet pressure always increases/decreases the Mach number.

As anticipated in §3.2, the upstream total quantities play a key role in the expansion process for non-ideal flows. The last two examples Ň-OFF-T^t_+ and Ň-OFF-P^t_- aim at demonstrating the effect of a variation in the total upstream conditions, at a fixed pressure ratio. In the same spirit as I-OFF-T^t_+ and I-OFF-P^t_-, the total temperature, and pressure are varied independently. The reference condition for this study is Ň-DES.

We first consider the impact of an increase of the upstream total temperature on the cascade performance (Ň-OFF-T^t_+). As a consequence of the total temperature increase, the adapted pressure ratio (across the blade channel only) increases as well, see figure 3.3(b) for expansions with a similar value of the total pressure. In the present case, since the pressure ratio is fixed, the increase of total temperature triggers a strong shock wave downstream of the cascade where the fish-tail shock reflects, see figure 3.21. The total pressure loss coefficient dramatically increases to $Y = 16.1\%$, resulting in more than two times the design loss coefficient. As a result of the strong shock wave formation, the Mach number decreases to $M_{05} = 1.47$. Non-ideal oblique shocks are not observed in the present configuration because the shock adiabat centered on the thermodynamic state at the trailing edge no longer contains the $J > 0$ region necessary for the Mach number increase (Vimercati *et al.*, 2018). Note that in the case of ideal-like operating conditions, the cascade loss coefficient remains nearly constant through an increase of the upstream total temperature (I-DES → I-OFF-T^t_+), thus highlighting a severe distinction between the ideal and non-ideal operating conditions. Considering that inherent fluctuations of the set-point temperature are unavoidable, such turbines will most likely oscillate from strong shocks to shock-free conditions, compromising the stability, performance, and mechanical integrity of the stage.

Finally, Ň-OFF-P^t_- illustrates the consequences of a decrease in the upstream total pressure. The pressure and Mach number fields, see figures 3.22, are qualitatively similar to the design ones. On a quantitative level, the Mach number peak in the blade channel and the outlet Mach number ($M_{05} = 1.45$) are both reduced and a stronger shock-wave pattern is generated at the trailing edge, confirmed by the increase of the loss coefficient ($Y = 8.8\%$). Compared to the variation in the upstream total temperature (Ň-OFF-T^t_+), the variation of the total upstream pressure affects the flow field and the cascade performance to a lower extent.

It is worthwhile to underline that the flow-field dependence on the upstream total quantities is not limited to a specific thermodynamic range, differently from the non-monotonic variation of the Mach number or the onset of oblique shocks featuring an increase of the Mach number.

3.4 Uncertainty quantification

The above off-design cases Ň-OFF-T^t_+ and Ň-OFF-P^t_- clearly show the large influence of the upstream total state on the cascade aerodynamics. In this context, an operational uncertainty is expected to promote significant departures from nominal conditions when the turbine is expanding in the non-ideal regime. Therefore, a rigorous uncertainty quantification (UQ) is performed by accounting for realistic uncertainty affecting the corresponding power cycles. The upstream total conditions recall the one reported in table 3.1, but the total temperature is raised to $T^t_0 = 272.5\,^\circ\mathrm{C}$ to avoid two-phase flows when uncertainties are included. The corresponding design expansion processes are reported in figure 3.23, where the turbine outlet pressure is set as the saturation pressure at $T_{cond} = 85\,^\circ\mathrm{C}$ (combined power and heat application). The I-DES and Ň-DES expansion ratios are considered as nominal conditions for the ideal-like and non-ideal scenario, respectively. As a result of the total temperature increase, the design loss coefficient for the non-ideal cascade is $Y = 7.3\%$, i.e. slightly higher than what was found for Ň-DES. Consistently with the discussion in §3.3.4, the design loss coefficient for the ideal-like cascade remains unaltered despite the total temperature rise.

Alongside nominal conditions, the definition of uncertainties has to be addressed. The data reported in Zanellato *et al.* (2018) is the only source of operational variability in running ORC power plants that is available in the open literature. Specifically, field measurements of temperature and pressure at the outlet of the evaporator (T_{eva}, P_{eva}) and temperature in the condenser (T_{cond}) are there reported for two-level saturated cycles. Although system layouts and working fluids are considerably different from the ones employed in this work, a similar variability in controlling an ORC power plant can be expected. Based on the published data, the following relative variations from nominal and/or average conditions are derived: $\Delta T_{eva}/T_{eva} \approx 1.25\%$, $\Delta P_{eva}/P_{eva} \approx 1.25\%$, $\Delta T_{cond}/T_{cond} \approx 1\%$ with temperatures expressed in degrees Celsius. Whilst outlet evaporator pressure and temperature can be directly prescribed as boundary conditions at the inlet of the

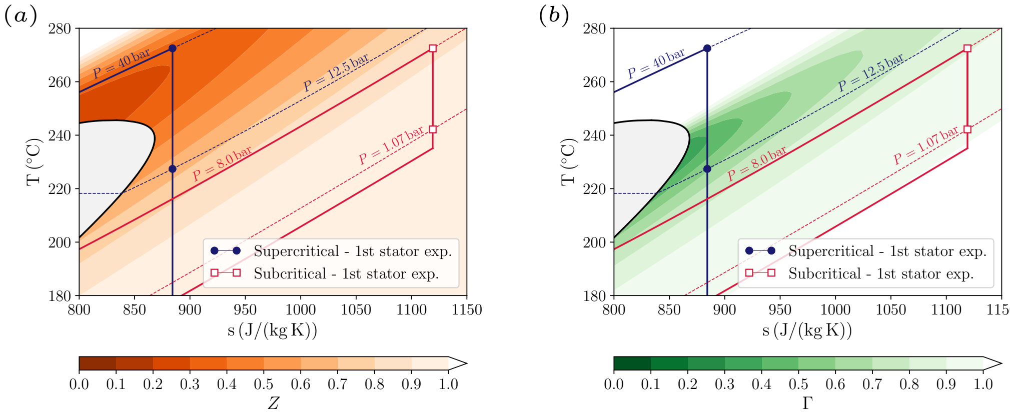

FIGURE 3.23. Design expansion processes for the ideal-like (subcritical) and non-ideal (supercritical) expansion process. A map of the compressibility factor Z and fundamental derivative of gas dynamics Γ are superposed in frames (*a*) and (*b*), respectively.

TABLE 3.2. Summary of uncertainties accounted in this work along with their probabilistic distributions ($\mathcal{B}$: beta distribution; $\mathcal{N}$: normal distribution, μ, σ: mean and standard deviation of the normal distribution, α, β: shape parameters of the beta distribution).

Uncertainty		Ideal-like	Non-ideal
T_0^t (°C)	$\sim$	$\mathcal{N}(\mu = 272.5, \sigma = 1.175)$	$\mathcal{N}(\mu = 272.5, \sigma = 1.175)$
P_0^t (bar)	$\sim$	$\mathcal{B}(\alpha = 2, \beta = 4.5)$ on $[7.9, 8.1]$	$\mathcal{B}(\alpha = 2, \beta = 4.5)$ on $[39.5, 40.5]$
P_1 (bar)	$\sim$	$\mathcal{N}(\mu = 1.075, \sigma = 0.007)$	$\mathcal{N}(\mu = 12.5, \sigma = 0.024)$

turbine, the uncertainty in the condensation temperature must be propagated to the first-stator outlet pressure. The pressure level at the stator outlet, given the overall expansion ratio dictated by the cycle, depends on the number of stages arranged in the machine and their specific reaction degrees. The enthalpy drops are distributed among cascades with the following rationale (Persico & Pini, 2017): the first stage provides the highest enthalpy drop ($r \leqslant 0.25$, where $r = \Delta h_{rot,is}/\Delta h_{stat,is}$ is the isentropic reaction degree and $\Delta h_{rot,is}$, $\Delta h_{stat,is}$ are the isentropic enthalpy drop across the rotor and the stage, respectively), while the remaining stages operate at the maximum efficiency point ($r \approx 0.5$). As far as the number of stages is concerned, on the one hand, a single-stage axial turbine is selected for the ideal-like cascades, while five stages are required to efficiently accomplish the non-ideal expansion. As a matter of fact, for the non-ideal scenario a higher number of stages was dictated by overall lower values of the speed of sound, which lead to a highly supersonic Mach number for comparatively lower pressure ratios. Given $\Delta T_{cond}/T_{cond} \approx 1\%$, a sampling strategy is applied to derive the corresponding variations in the static pressure $\Delta P_1/P_1$ at the stator outlet. Preliminary calculations show that no qualitative differences emerge neither in the ideal-like nor in the non-ideal case when changing input distributions (e.g. assuming uncertainties as uniformly distributed). Gathering all this information, the operational uncertainties are formulated to be independently distributed as in table 3.2.

3.4.1 Surrogate-based uncertainty quantification strategy

To derive statistically relevant information about turbine operation, one should sample from the input probability distributions a large number of boundary conditions, say $\mathcal{O}(10^6 - 10^8)$, and process each of them via CFD simulations to compute several realizations of the cascade performance. However, this methodology cannot be applied as it is because of the high computational cost required by the single CFD evaluation. To circumvent this problem, a surrogate-based strategy is devised. First, a smaller number of CFD cases are run to build a surface response of selected quantities that are indicative of the nozzle-cascade performance. Then, the surface response is used as a surrogate of the flow solver to process the large number of evaluations needed to derive statistically relevant indications. In this work, polynomial-chaos (PC) representations (Le Maître & Knio, 2012) are used as surrogates of the flow model with respect to three operational parameters, namely T_0^t, P_0^t and P_1. Distinct PC expansions are computed for each output response, e.g. the cascade loss coefficient Y, the mass flow rate $\dot{m}$ processed by the cascade, besides others. The PC representation allows expressing an output random variable in a series of polynomials ψ mutually orthogonal to the probability measure ρ associated with the input uncertainties. For standard probability measures, a convenient choice is to select ψ in according to the Askey scheme (Askey & Wilson, 1985), resulting in the Hermite and Jacobi polynomials for the normal and beta distributions assumed in this work, respectively. The implemented surrogate model, expressed in terms of cascade loss coefficient for illustrative purposes, can be then summarised by the following expression:

$$
\begin{aligned}
Y(T_0^t, P_0^t, P_1) &= \sum_{i=0}^{p} \sum_{j=0}^{p} \sum_{k=0}^{p} \xi_{ijk} \psi_i(T_0^t) \psi_j(P_0^t) \psi_k(P_1) \\
\xi_{ijk} &= \frac{1}{\langle \psi_i \psi_j \psi_k, \psi_i \psi_j \psi_k \rangle} \int_{\Xi} Y \, \psi_i \psi_j \psi_k d\rho_i d\rho_j d\rho_k
\end{aligned}
\tag{3.3}
$$

where, for the ease of readability, in Eq. (3.3) i, j, k indicate both the polynomial order p and the uncertainties which polynomials and probability measures refer to. The operator $\langle \cdot, \cdot \rangle$ expresses the inner product in the space $L^2(\Xi, \rho)$, where Ξ is the support of the probability density $\rho = \rho(T_0^t)\rho(P_0^t)\rho(P_1)$, see Tab. 3.2. The integrals to determine the PC coefficients ξ_{ijk} are solved by tensorization of the corresponding Gaussian quadrature rule of order q in each stochastic dimension, resulting in overall q^3 CFD evaluations. It is worth recalling that the numerical strategy integrates exactly all polynomials of orders up to $2q - 1$. It follows that to integrate exactly Y, modelled of order q, the order of polynomials in the PC expansions ψ has to be truncated at $p = q - 1$. Once the PC representation is settled, statistics are computed by sampling the surrogate model, which can be effectively interrogated many times at an almost-free computational cost. A pointwise PC expansion is used when processing trends and flow fields.

Differently from the above analyses, the grid size with 200×10^3 elements in the blade-to-blade plane is selected hereinafter for both the ideal-like and non-ideal case, accepting in the computation of the cascade loss coefficient a difference with respect to the finest value of 0.08 and 0.17 percentage points (pp), respectively, as highlighted in Figure 3.24(a). Such grid refinement represents the best compromise between computational cost and accuracy, accepting a higher discretization error in the non-ideal scenario because of the expected larger variabilities. Three quadrature orders are investigated in Figure 3.24(b) in terms of cascade-loss distributions for the non-ideal case, which ought to represent the most challenging stochastic problem in light of the expected larger variability. All quadrature orders produce very similar Gaussian distributions, whose minor differences are attributable to the sampling error. The difference in mean estimates is 0.002 pp between the PC representation built with $q = 4$ and $q = 5$. Since the same quadrature order is also preserved for other output variables, a conservative $q = 4$ is employed to produce

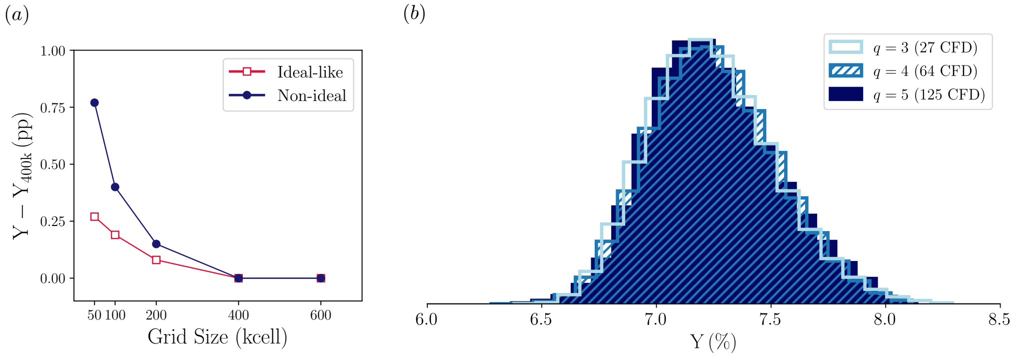

FIGURE 3.24. Computational tool verification in terms of (*a*) grid convergence for CFD calculations and (*b*) statistic convergence for PC representations. The grid size indicates the number of cells in the blade-to-blade plane. The statistic convergence is assessed on the non-ideal stochastic problem.

all the following results. A complete uncertainty-quantification study consisting in 64 CFD runs required approximately 16 hours on an Intel® Xeon® CPU E5-2630 v3 @ 2.40GHz equipped with 16 cores. One advantage of resorting to a PC representation over other surrogate methods is that the polynomial coefficients β_{ijk} can be directly used to estimate the total Sobol indices S^T, which quantify the global contribution of each uncertainty to the total variance of the quantity of interest (Crestaux *et al.*, 2009).

3.4.2 Probabilistic performance of supersonic nozzle cascades

In this section, the effects of operational uncertainty on the stator aerodynamics are discussed. From an integral perspective, the most significant indicator is the cascade-loss coefficient (following the definition provided in the equation 2.31) and the processed mass flow rate. This latter quantity is particularly relevant because it directly establishes the mass flow rate within the power cycle if the supersonic cascade is choked, as in the present situation. To this end, the joint probability distributions in terms of normalized mass flow rate (with respect to the nominal value) and loss coefficient are reported in Figure 3.25 for the two cascades. At a first glance, substantial differences between the ideal-like and non-ideal cascade operation can be appreciated from both a quantitative and qualitative perspective. On a quantitative ground, the non-ideal loss distribution is characterized by nearly symmetrical support that amounts to 1.5 pp (measured as a difference between the maximum and minimum value), which is six times larger than its ideal-like counterpart. Besides, the mass-flow-rate support is four times larger as well. On the other hand, an inspection of the joint-distribution shapes unveils different kinds of correlation between the two observed quantities, suggesting peculiar gas-dynamic evolutions under uncertainty. In particular, a significant negative dependence correlates the mass flow rate and loss coefficient for the non-ideal case. Instead, the joint distribution does not suggest any clear correlations between variables in the ideal-like scenario.

A classification of the importance of uncertainties on the cascade performance can help to understand these fundamental differences. Figure 3.26 reports a sensitivity analysis based on total Sobol indices S^T, which quantifies the contribution of each uncertainty (i.e. T_0^t, P_0^t and P_1) to the total variance of mass flow rate in Figure 3.26(*a*) and cascade losses in Figure 3.26(*b*).

For what concerns the mass flow rate, the resulting zero contribution of the downstream pressure indicates that both supersonic cascades are choked. Nonetheless, the predominant variable contributing to the mass-flow-rate uncertainty varies between the two cases. For the

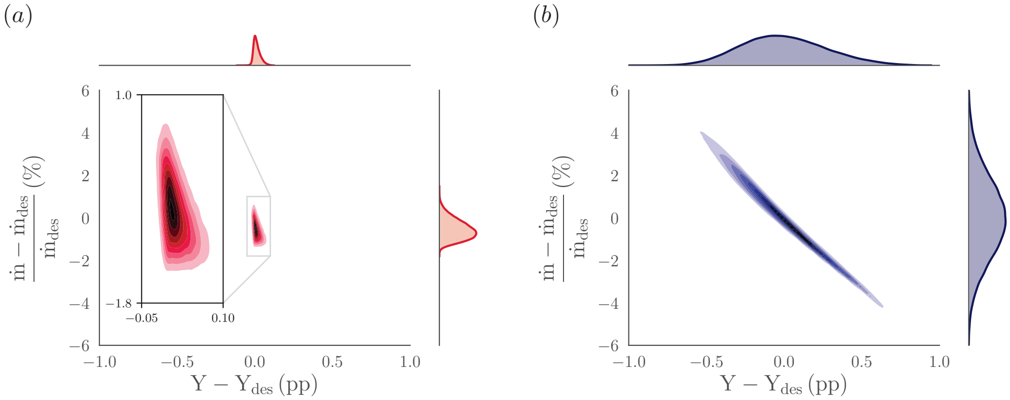

FIGURE 3.25. Joint probability distributions of the normalized mass flow rate and cascade-loss coefficient in the ideal-like (*a*) and non-ideal (*b*) operating regime.

ideal-like regime, the total pressure overcomes the contribution of the total temperature, while roles are reversed in the non-ideal regime. Recalling that the mass flow rate under choked operation exclusively depends on the thermodynamic properties at the throat section, indicated with superscript * hereinafter, via the relationship $\dot{m} = \rho^* c^* A^*$, where the throat area A^* is geometrically fixed, a variation in the upstream total state defines different isentropes along with the expansion in the converging part occurs. In an ideal-like operation, the total pressure has a larger influence on the density while the speed of sound is more sensitive to variations in the total temperature. To support this last statement, a parametric study imposing a separate increase in the total pressure and total temperature is considered under the assumptions of the quasi-one-dimensional approach described in §3.2. The magnitude of these increases mirrors the maximum variations imposed in the stochastic analysis, i.e. +1.25% of the corresponding total variables. A resulting increase of 0.1 bar in the nominal total pressure affects more the density value ($\Delta\rho^*/\rho^*_{des} = +1.4\%$) than a separate increase of 3.5 °C in the nominal total temperature ($\Delta\rho^*/\rho^*_{des} = -1.0\%$). Furthermore, an opposite but comparable-in-magnitude variation in the speed of sound ($\Delta c^*/c^*_{des} = +0.6\%$) is prompted by the total temperature rise, while a significant lower sensitivity is found against the total-pressure increase ($\Delta c^*/c^*_{des} = -0.1\%$). Since the mass flow rate is ultimately provided by the product $\rho^* c^*$, the total pressure contribution overall prevails over the total temperature as reported in Figure 3.26(*a*). Nonetheless, the smooth variation of density and speed of sound along ideal-like isentropes leads to a quantitatively small departure from the mass-flow-rate nominal value, as evidenced in the corresponding distribution of Figure 3.25(*a*).

An analogous parametric study is conducted for the non-ideal case, where similar relative increases with respect to the upstream total variables are applied, resulting in 0.5 bar and 3.5 °C for the total pressure and total temperature, respectively. The total temperature rise at fixed total pressure provides a variation in the density and speed of sound equal to $\Delta\rho^*/\rho^*_{des} = -4.5\%$ and $\Delta c^*/c^*_{des} = -0.8\%$, respectively. The opposite, i.e. an increase in total pressure at fixed total temperature, produces $\Delta\rho^*/\rho^*_{des} = +0.8\%$ and $\Delta c^*/c^*_{des} = +1.1\%$. These quantitative variations explain why and how total temperature mostly contributes to the mass-flow-rate uncertainty.

Analogous physical considerations based on loss-variance decomposition, see Figure 3.26(*b*), can explain the differences observed in the loss distributions of Figure 3.25. The underlying expansion process, to which the cascade aerodynamics is strictly correlated, depends on both the prescribed expansion ratio, given by the combination of upstream and downstream pressure, and on its evolution with respect to the upstream total quantities, as explained in §3.2 for simplified

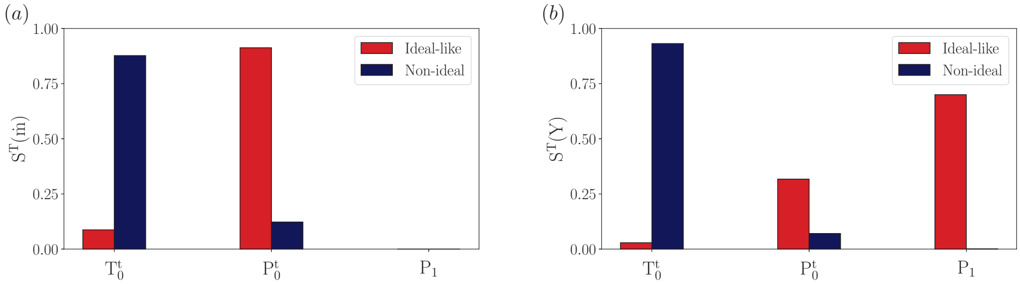

FIGURE 3.26. Total Sobol indices of (*a*) mass flow rate and (*b*) cascade loss for the ideal-like and non-ideal operating regime.

expanding flows. In the limit of polytropic-gas flows, the expansion ratio uniquely determines the expansion evolution. This behaviour is partially recovered in the ideal-like cascade, where the expansion process is almost entirely determined by the expansion ratio, as highlighted in Figure 3.26(*b*) by the larger contributions of the pressure upstream and downstream of the cascade. If the expansion ratio varies, the flow must adjust downstream of the blade opening to match the prescribed expansion process, resulting in a different oblique-shock/post-expansion pattern at the trailing edge and a subsequent variation of aerodynamic losses. A non-negligible contribution of the total temperature copes with the small degree of non-ideality characterizing ideal-like operation.

On the contrary, non-ideal cascade losses are completely dominated by a variation in the upstream total temperature, which overcomes the contribution given by a variation in the expansion ratio, in terms of either upstream total pressure or downstream static pressure. As a matter of fact, the adapted expansion process, which can be conveniently represented by A/A^*, exhibits a significant sensitivity to total-temperature variations, see §3.2. Therefore, as a result of a change in the total temperature, the desired area ratio to have a shock-free expansion changes while the area ratio across the cascade is geometrically imposed, thus inducing off-design conditions that are more severe than those triggered by a change in the pressure ratio.

Finally, the hierarchy of uncertainties established from the variance decomposition also clarifies the shape morphology of the joint distributions found in Figure 3.25. For the non-ideal case, the prevailing uncertainty is the total temperature for both the cascade loss and mass flow rate, acting in an opposite sense (e.g. whenever the total temperature increases, the mass flow rate decreases while the cascade loss increases). Alongside a reduction of mass flow rate as described in the parametric study conducted before in this section, an increase in the total temperature leads to a decrease of A/A^* at a given outlet pressure. Therefore, when A/A^* becomes lower than the design one, the cascade is expanding more than the requested in the blade channel, then forcing the flow to adjust itself at the trailing edge via compression shocks to match the prescribed outlet pressure with a consequent rise in the aerodynamic losses. The deviation from a limiting linear joint distribution is given by the smaller effect provided by the total pressure on both the mass flow and losses. The absence of a key uncertainty shared by both quantities in the ideal-like operating regime conceals the underlying structure of the corresponding joint distribution.

So far, the analysis focuses on integral parameters which are explanatory of the cascade aerodynamics. Nevertheless, such large performance variations should be followed by as many changes in the local flow field. To this end, the coefficient of variation, $CoV = \sigma/\mu$, where σ and μ represent the standard deviation and the mean, respectively, of pressure, Mach number, and total pressure fields is computed in Figure 3.27. It is worth recalling that a stochastic field does not have a physical meaning, per se, i.e. there is not a proportional relationship between a peak in the CoV and the actual value of the corresponding quantity.

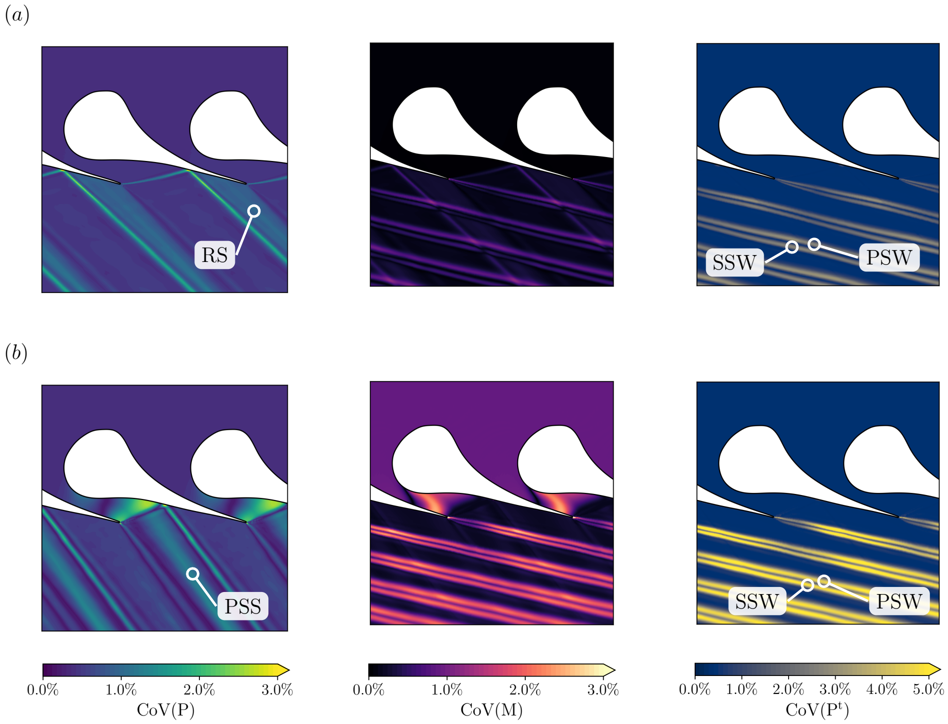

FIGURE 3.27. Pressure (P), Mach number (M) and total pressure (P^t) coefficient-of-variation (CoV) fields for the ideal-like (a) and non-ideal (b) cascade. *RS* indicates the peak of variation induced by a reflected-shock intensity change, while *PSS* refers to the uncertainty induced by a modification in the pressure-side shock strength. *PSW* and *SSW* highlight the uncertainty in the pressure-side and suction-side branch of the wake, respectively. The white dashed lines indicate three axial traverses at x/c_{ax} = 1.15, 1.45, 1.75, where pitchwise distributions are extracted..

As expected, ideal-like and non-ideal fields exhibit significant dissimilarities. In supersonic turbines, the supersonic flows from the pressure and suction side meet at the trailing edge. In turning around the trailing edge to a shared direction, they first expand via rarefaction fans and, subsequently, they possibly generate shock waves which will propagate into the flow field. As evidenced by figures 3.10–3.17, for both nominal cases only the flow coming from the pressure side generates a shock to accomplish the turning process. This shock reflects on the suction surface of the adjacent blade, interacting with the suction-side boundary layer, running downstream of the cascade afterward.

Operational uncertainty in the ideal-like case will only affect the intensity of the shock reflection and the subsequent interaction with the adjacent-blade suction side, without considerably modifying the shock strength that stems from the pressure side (pressure values across the shock are unaltered). This behaviour can be again explained by referring to A/A^*. In ideal-like conditions, A/A^* is almost constant under operational uncertainty, hence the expansion process in the blade channel remains unaltered, not affecting the shock pattern at the blade opening. On top of that, the outlet pressure is also varied, imposing a flow adjustment downstream of the blade opening, i.e. in the shock reflection, to match the prescribed boundary condition. Indeed, given a nearly constant pressure value upstream of the reflected shocks, the highly uncertain value of the pressure downstream, as illustrated by the marker *RS* in Figure 3.27(a), is a clear indication of the shock-strength change. The periodicity is restored by a subsequent variation in the shock pattern at the trailing edge on the

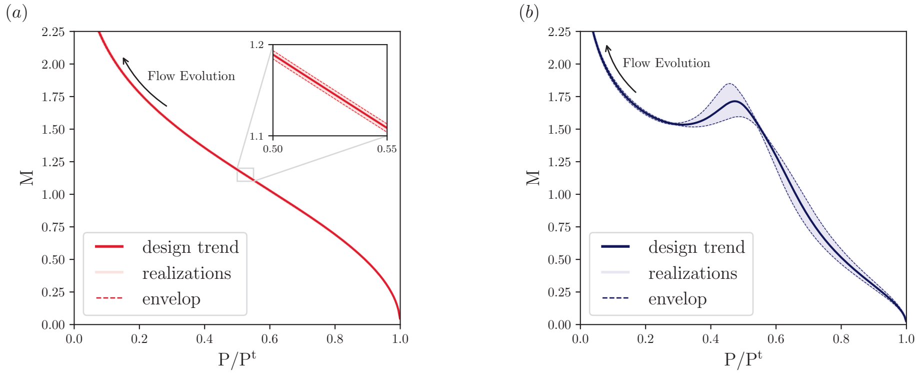

FIGURE 3.28. Design Mach number distributions predicted by the quasi-one-dimensional theory for an ideal-like expanding flow (with total states $P^t = 8\,\text{bar}$ and $T^t = 272.5\,°\text{C}$) and a non-ideal expanding flow (with total states $P^t = 40\,\text{bar}$ and $T^t = 272.5\,°\text{C}$) of fluid MM, along with 200 independent uniformly distributed realizations assuming ±1.25% uncertainty in both the design total pressure and temperature.

suction side, i.e. given a lower/higher value of pressure as a consequence of the reflected-shock modification, the flow will turn less/more accordingly. A variation in the trailing-edge shock pattern will also affect the wake formation and evolution. In this regard, two distinct effects combine in the generation of the wake: (i) a variation in the turning process, strictly connected with the shock-strength modification, will induce a different wake width, and (ii) a variation in the pressure-gradient downstream of the cascade will produce a change in the outlet flow angle (Mee *et al.*, 1992). As a result, a bulk of an unaltered wake splits into two peaks of uncertainty (named *PSW* and *SSW* in Figure 3.27), which include both the direction and width change. The wake changes in depth (i.e. minimum total pressure) as well, due to the base-pressure variation to comply with the prescribed turning process, thus altering the nominal cascade losses (Denton & Xu, 1990) as quantitatively discussed in the first part of the section.

On the other hand, a predominant uncertainty in the trailing-edge shock strength on the pressure side emerges from the analysis of non-ideal stochastic fields in Figure 3.27(*b*). By virtue of the aforementioned variations in A/A^*, it is not surprising that the shock at the cascade opening is the flow structure most affected by uncertainties. As long as the geometrical ratio is fixed, the variation in A/A^* triggered by non-ideal gas dynamics can impose smaller or larger recompression than the one in design conditions. For example, let me assume that A/A^* reduces compared to the design value, which fixes the geometrical ratio in turn. Then, the larger diverging area imposed by the geometry forces the flow to expand more in the blade channel, requiring stronger recompression via shock at the blade opening to match the outlet boundary condition. Although the highest variation is found upstream of the shock, a noteworthy pressure field variation is also found downstream of it, marked as *PSS* in Figure 3.27(*b*), which will run away orthogonally. Besides, the modification in the shock strength at the trailing edge will induce a change in the wake development downstream of the cascade, qualitatively similar to what we described for the ideal-like scenario, albeit to a larger quantitative extent. Lower but still significant variations also affect the reflected shock and the fish-tail flow pattern that arises from the suction side, revealing a flow field highly altered by operational uncertainty.

Furthermore, a peculiar evolution of the Mach number uncertainty can be observed in the blade channel of the non-ideal cascade. A zero variation is calculated at the throat, where a sonic Mach number ($M = 1$) always onsets. Then, Mach number values are affected by a large uncertainty, which cannot be prompted by area-ratio variation alone. The inspection of the

Mach number distribution with pressure in Figure 3.28, obtained with the quasi-one-dimensional approach detailed §3.2, can elucidate on this matter. Negligible variations are found in Figure 3.28(a) for the ideal-like case, consistently with the $CoV(M)$ field in Figure 3.27(a). As for the non-ideal expansion, a non-monotonic trend of the Mach number against the pressure is predicted in Figure 3.28(b), in accordance with the corresponding flow field in figure 3.17. In this context, the local minimum and maximum are strongly altered by operational uncertainty, thus justifying the significant uncertain region within the blade channel detected in the Mach number field but absent in the pressure field.

As a final comment, the operational uncertainty largely perturbs cascade nominal operation within a non-ideal framework, presumably affecting the overall cycle performance as well. The combination of quasi-one-dimensional analyses with stochastic analyses sheds light on the physical nature of these variations, which are found to be mainly related to the large sensitivity of the A/A^* on the upstream total temperature. Alongside the large performance deviations found in the supersonic stator, the operational uncertainty induces a highly uncertain flow delivered to the first rotating-blade row, which may further amplify the efficiency variation of the overall turbine. The estimate of this additional non-ideal implication will be the core of the next section.

3.4.3 Consequences on the rotor aerodynamics

The previous analysis shows that the first rotating cascade has to operate with a highly variable incoming flow when the stator expansion occurs in the non-ideal regime ($\Gamma \ll 1$). Although the rotor experiences higher values of Γ (e.g., in the present case, the minimum value is $\Gamma = 0.5 - 0.6$ at the inlet, becoming $\Gamma = 0.9 - 1.0$ as long as the expansion proceeds), a variation in the incoming flow might still provoke a departure from its nominal conditions. Two main issues may arise: (i) a variation in the relative Mach number field, inducing supersonic flow regime at the rotor inlet and, consequentially, unique-incidence operation (Bufi & Cinnella, 2018); (ii) a variation in the flow angle, yielding a positive or negative incidence at the rotor leading edge, thus affecting both the work extracted and the stage reaction degree and efficiency.

As for the first point, the inspection of Mach number uncertainty in Figure 3.27 reveals that only the wake (low Mach number region) is altered by operational uncertainty, while the free-stream Mach number is practically constant. In fact, variations occurring in the ideal-like nozzle cascade are not enough large to have a perceivable effect on the value of the free-stream Mach number. For the non-ideal cascade, the operational uncertainty does entail large variations, but operation in the neighborhood of a stationary point (i.e. the local minimum) makes the Mach number robust to perturbations in the pressure field (e.g. given by modifications in the shock strengths). Moreover, the non-monotonic trend of the Mach number in Figure 3.28 shows that the sensitivity of the Mach number on the upstream total state attenuates when approaching the local minimum.

On the contrary, variations in the incidence angle require a deeper investigation, as many thermodynamic variables are involved in a complex way. To do so, some preliminary considerations on the rotating cascade are needed. As a design criterion, $\alpha_2 = 0°$ is assumed. It means that the flow leaving the rotor is completely axial, thus minimizing the outlet kinetic energy. A straightforward manipulation of the rothalpy balance ($h + (w^2 - u^2)/2 = \text{const.}$ across the rotor, where w and u are the relative and peripheral velocity, respectively) combined with the velocity-triangle relationship $\vec{v} = \vec{u} + \vec{w}$, and assuming $v_0^2 \ll v_1^2$ ($v_0^2/v_1^2 < 0.05$ for both supersonic stators), yields the following equation:

$$\frac{u}{v_1} = \frac{r}{2(1-r)\sin\alpha_1} + \frac{\sin\alpha_1}{2}, \tag{3.4}$$

Plugging into Eq. (3.4) the pitchwise mass-flow averages of v_1 and α_1 that are extracted from the nominal flow fields at half axial chord downstream of the trailing edge $x/c_{ax} = 1.50$ (as plausible stator-rotor gap), the peripheral speed is estimated for the two cases. Next, prescribing

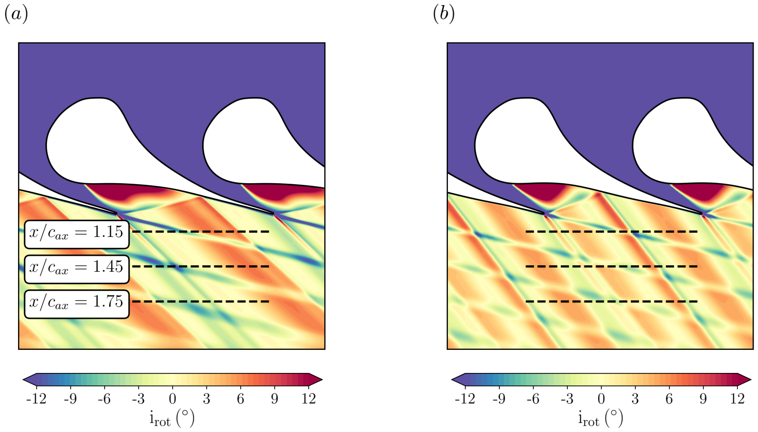

FIGURE 3.29. Rotor incidence angle downstream of the ideal-like (*a*) and non-ideal (*b*) stator cascade. The black dashed lines indicate three axial traverses at $x/c_{ax} = 1.15, 1.45, 1.75$, where pitchwise distributions are extracted.

a zero incidence at design conditions, the blade angle at the rotor inlet is determined for the ideal-like and non-ideal case. In Figure 3.29, rotor incidence distributions i_{rot} downstream of the stator trailing edge are reported. It is clear that the average value of zero-incidence at nominal conditions is obtained by balancing the negative peaks (provided by the wake) with the positive peaks (provided by shock waves). Nonetheless, large pitchwise deviations of incidence from the average value might substantially increase the stator-rotor interaction, with a further burden on the overall stage performance (Gaetani *et al.*, 2010).

These incidence fluctuations are related to the non-uniform flow field delivered by the first-stator cascades; as previously discussed, in strongly non-ideal conditions this flow field is highly affected by operational uncertainty. In this context, two points need to be addressed: first, quantifying the corresponding uncertainty on the rotor incidence, thus assessing whether the rotor departs from nominal conditions; second, establishing an optimal stator-rotor gap (if any) such that the superposition of the two competitive effects (wake and shocks) reduces the overall incidence variations. For illustrative purposes, pitchwise distributions of pressure, total pressure and incidence are reported in Figure 3.30 and Figure 3.31 for the ideal-like and non-ideal case, respectively, at three selected downstream axial traverses, namely $x/c_{ax} = 1.15, 1.45, 1.75$. Pressure distributions allow visualizing the modification in shock strength, while total pressure distributions highlight the evolution of the wake under uncertainty. From these trends, it is possible to better appreciate the relationship between the stochastic fields, described in the previous section, with the corresponding physical values. The same designations previously devised are here adopted to outline the uncertainty peaks in the corresponding distributions.

In the ideal-like scenario, the main uncertainty is the pressure value behind the reflected shock. While the shock is smeared moving downstream as a consequence of the mixing process, the induced uncertainty just slightly changes. On the other hand, the uncertainty in the wake morphology, both in terms of width and depth, is almost negligible for the ideal-like case. A noticeable variation is only found in the distribution at $x/c_{ax} = 1.75$, as shown in the central frame of Figure 3.30(*c*). In this case, there is an amplification of the wake uncertainty when the reflected shock intercepts the wake coming from the suction side. Moreover, the shock-induced uncertainty in the pressure field seemingly rises the corresponding uncertainty in the pressure-side branch of the wake. Connected to this combination of uncertainties that arises from the shock-wake

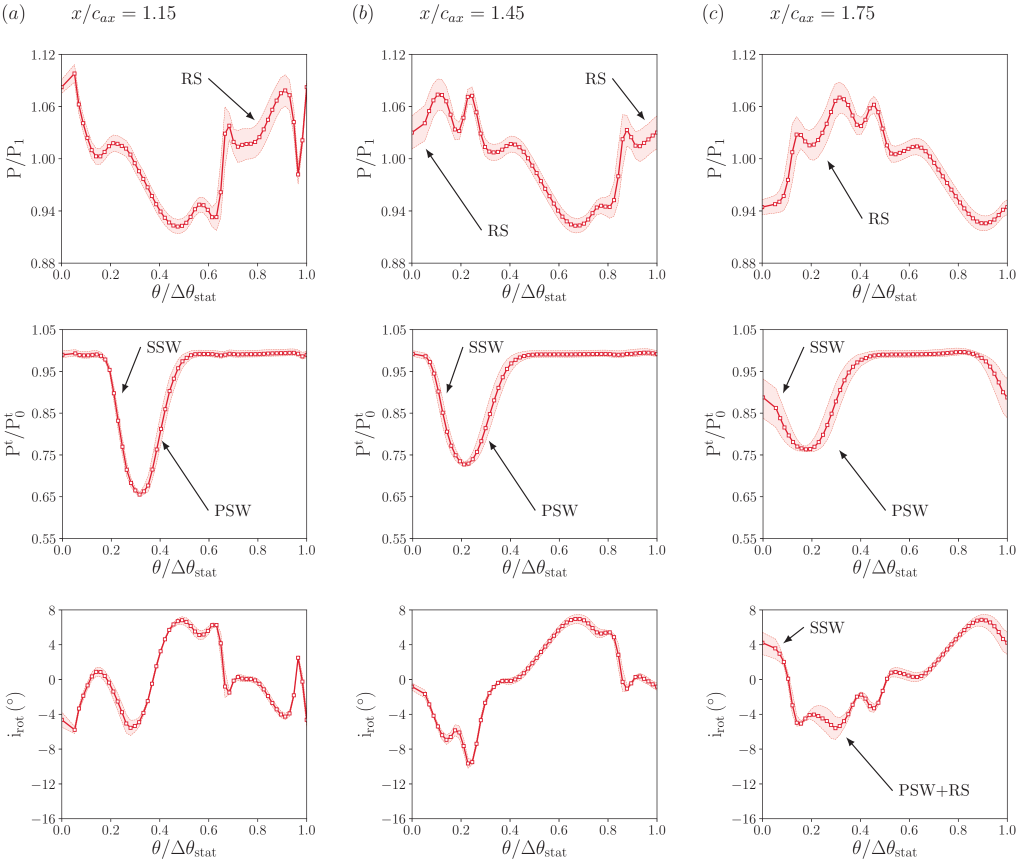

FIGURE 3.30. Pitchwise distributions of pressure, total pressure and rotor incidence angle at different axial transverse downstream of the stator trailing edge for the ideal-like cascade. The nomenclature of the uncertainties is reported in Figure 3.27.

interactions, the incidence distribution becomes locally uncertain as well, notwithstanding the small extent of such variations in terms of both the region and magnitude. For the other cases, in which the shock-induced uncertainty runs into the free stream, see Figure 3.30(*a*)-(*b*), variations in the incidence nominal trend can be barely recognized.

A more complex situation is depicted by the non-ideal scenario in Figure 3.31. Consistently with the stator analysis, uncertainties are overall more significant. From pressure trends, it can be noticed that the main variation is right before the reflected shock, opposed to the ideal-like case; as explained above, this uncertainty arises from the shock modification at the blade opening, propagating downstream orthogonally to the shock front. Pressure trends at different measurement planes are nearly identical, while the wake evolution in the total-pressure fields shows that its uncertainty increases as long as the mixing process occurs. The combination of these effects directly impacts the determination of the incidence uncertainty. At $x/c_{ax} = 1.15$, the uncertainty that is induced by the pressure-side shock (PSS) couples with the uncertainty in the suction-side branch of the wake (SSW); the superposition of these two uncertainties yields a sharp incidence drop ($i_{rot} - i_{rot,des} = -10°$). While moving downstream, the main pressure uncertainty progressively intercepts the pressure-side branch of the wake and its associated uncertainty (PSW). Differently from the previous case, the superposition of these two effects does not produce an appreciable

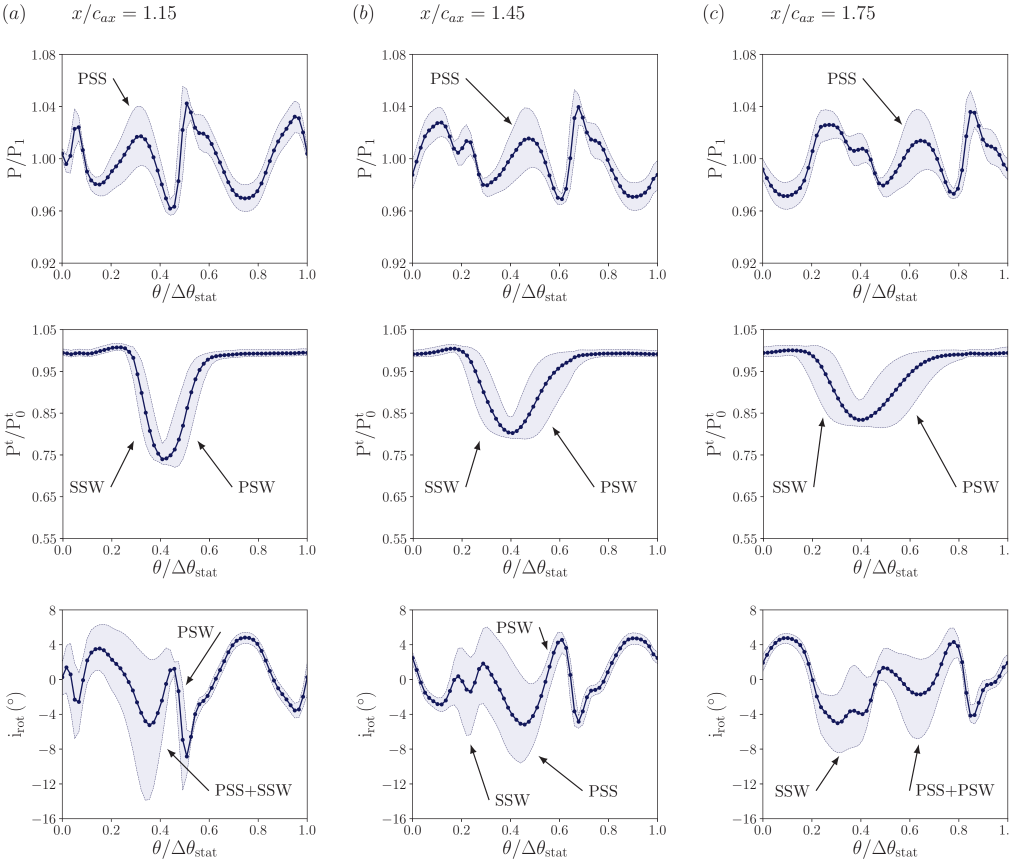

FIGURE 3.31. Pitchwise distributions of pressure, total pressure and rotor incidence angle at different axial transverse downstream of the stator trailing edge for the non-ideal cascade. The nomenclature of the uncertainties is reported in Figure 3.27.

increase in the incidence uncertainty. As a matter of fact, only PSS and SSW seem to affect the incidence trend, while PSW only provides a negligible contribution.

The evident alteration of the pitchwise incidence distribution under operational uncertainty confirms that a non-ideal gas-dynamic regime in the supersonic stator may also trigger off-design operation in the subsequent rotor cascade. As further proof of that, Figure 3.32 reports the pitchwise-averaged incidence angle $\overline{i_{rot}}$ at different axial transverse downstream of the stator cascade. The averaged incidence varies ±0.3° and ±3.0° as a consequence of an ideal-like and non-ideal gas dynamics, respectively. The quantitative impact of such variations on the rotor aerodynamics will depend on the specific 3D blade design, operating conditions, and flow regime. As a general guideline, design criteria that make the rotor more robust against incidence variations, e.g. privileging a rotor design with a larger leading-edge radius, should be applied in the context of non-ideal flows. Moreover, there seems not to be an advantageous axial location where the rotor can be conveniently placed without incurring such large incidence variations. Therefore, the classical criteria for determining the stator-rotor axial gap also apply in the non-ideal scenario.

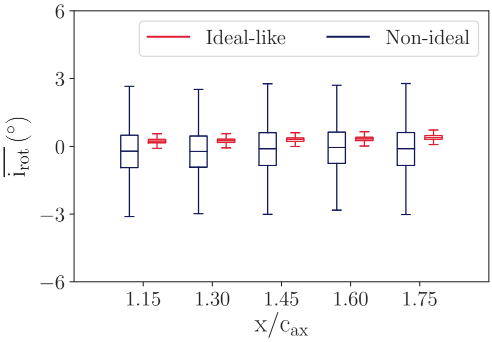

FIGURE 3.32. Evolution of the pitchwise-averaged rotor incidence angle along the axial coordinate for the ideal-like and non-ideal cascade.

3.5 Multi-point optimization of the non-ideal cascade

The previous analysis points out the significant departure in cascade and stage performance as the upstream total state changes. Specifically, the main responsible for these departures is found to be the upstream total temperature, as highlighted in Figure 3.26(*b*) by decomposing the total variance. Such information sets the ground for a dedicated multi-point optimization aiming at reducing the performance variability within the expected range of variations, i.e. $T_0^t \sim \mathcal{N}(\mu = 272.5, \sigma = 1.175)$, distributed in accordance with the previous assumption. Differently from what was established in §2.4, in which uniform weights were assigned when combining multiple operating conditions in the determination of a single objective function, the probabilistic characterization of the dependent variable T_0^t makes the choice of the objective function more complicated. As a matter of fact, as the input variable is a random variable, any objective function, namely, e.g., the entropy production Δs (as an alternative to Y to indicate the cascade performance), is a random variable as well. The straight minimization of a random variable is meaningless because a random variable by itself is not measurable. Therefore, it is convenient to first introduce a measure of Δs, e.g. the expected value:

$$\mathbb{E}[\Delta s(T_0^t)] = \int_{-\infty}^{\infty} \Delta s(T_0^t) d\rho_{T_0^t} = \int_{-\infty}^{\infty} \frac{1}{\sqrt{2\pi}\sigma} \exp\left(-\frac{(T_0^t - \mu)^2}{2\sigma^2}\right) \Delta s(T_0^t) dT_0^t \tag{3.5}$$

in which, as a simplification, the cascade performance under operational uncertainty is expressed as a function of T_0^t only, thus neglecting the marginal contribution of P_0^t (valid at least in these thermodynamic conditions, see Figure 3.26(*b*)). The integral in equation (3.5) can be solved only numerically. Analogously to §3.4.1, an effective quadrature rule is represented by the Gaussian quadrature rule associated with the input probability function. For normal distributions, the weights and the quadrature nodes are computed with respect to Hermite polynomials $\mathcal{H}$. In this way, the above integral can be approximated as:

$$\mathbb{E}[\Delta s(T_0^t)] \approx \frac{1}{\sqrt{\pi}} \sum_{i=0}^{n} w_i \Delta s\left(\sqrt{2}\sigma x_i + \mu\right) \tag{3.6}$$

where x_i are the roots of Hermite polynomials of degree n, while w_i are the associated weights computed as $w_i = \dfrac{2^{n-1} n! \sqrt{\pi}}{n^2 \left[\mathcal{H}_{n-1}(x_i)\right]^2}$. It can be proved that Gauss-Hermite quadrature is able to

TABLE 3.3. Weights and corresponding total-temperature boundary conditions for the multi-point optimization.

w	$\widehat{T}$ (°C)
0.1667	270.46
0.6667	272.50
0.1667	274.54

provide an exact solution of the integral in (3.5) whenever $\Delta s(T_0^t)$ can be modelled as a polynomial of degree $2n-1$. For the present optimization, $n = 3$, therefore the resulting numerical accuracy is of the same order of magnitude as a quadrature order $q = 5$ for the resolution of the integral in equation 3.3. As shown in §3.4.1, $q = 5$ is more than sufficient to compute the expected value of the output response, therefore the same level of accuracy is expected for the present estimate. Table 3.3 reports the weights and the values of upstream total temperature $\widehat{T} = \sqrt{2}\sigma x + \mu$ at which the entropy production has to be computed.

The optimization problem can be formulated as:

$$\min_{\mathbf{d}} \qquad w_1 \Delta s(\widehat{T}_1) + w_2 \Delta s(\widehat{T}_2) + w_3 \Delta s(\widehat{T}_3) \tag{3.7}$$

in which the design variables **d** are identical to those identified in §2.3.2. The entropy production at a given upstream total state is computed with the computational model detailed in §3.3.1. To balance accuracy and computational cost, the mesh topology employed for the UQ study in §3.4.1, consisting of 200×10^3 elements in the blade-to-blade plane with $y^+ < 1$ at the blade walls, is also selected for the optimization. Non-linear constraints are not considered as the scope of the present optimization is to assess whether inherent variabilities arising from a non-ideal gas dynamic can be mitigated by a proper blade design. The surrogate initialization and modelling strategy recall the ones employed in the previous multi-point optimization, see 2.4.

The resulting optimal blade profile is reported in Figure 3.33(a) and compared with the previous non-ideal cascade. The most relevant modification involves a reduction in the diverging channel of the cascade. Such result is not surprising, as the Ň-DES cascade was originally optimized for $T_0^t = 270$ °C; hence, as a result of the increase in the design total temperature to avoid the penetration in the two-phase domain during the UQ study, the original cascade features an A/A^* larger than the optimal value. The expected value of the total pressure loss coefficient decreases by 0.2 percentage points after the multi-point optimization, as illustrated by the dashed lines in Figure 3.33(b). This improvement is rather limited, as it is included in the range of performance variability of the original cascade outlined in Figure 3.25(b). Moreover, by inspecting the trend of loss coefficient against the total temperature, it can be observed that this trend is no longer linear as for the original cascade, but losses diminish less when the upstream total temperature is reduced. On the other hand, the performance deterioration by increasing the upstream total temperature is almost the same. The unaltered sensitivity to the total temperature is coherent with the prescribed objective function (expected value), which does not include anything related to the spread of the target output response. An alternative to the expected value can be represented by the minimization of the α-quantile ($\alpha > 0.5$) (Razaaly *et al.*, 2020). Such a choice would demand an increase in the computational cost, as the quantile estimate would generally require a larger number of simulations. However, a more robust blade profile against variations in total temperature (i.e., smaller standard deviation) can be obtained only by trading a part of the performance (i.e., higher expected value) and, given the modest improvement obtained by the present multi-point unconstrained optimization (minimum expected value), any additional attempt in this direction is arguably not worth. The conventional blade channel produced by this optimization, despite the

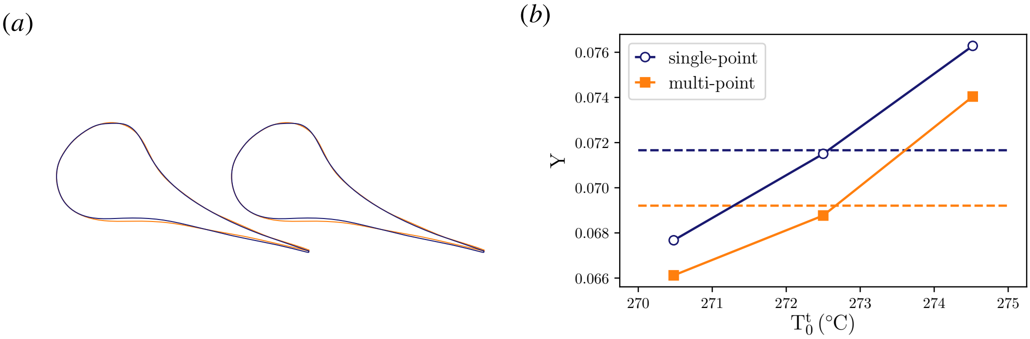

FIGURE 3.33. Multi-point unconstrained optimisation with respect to the prescribed variation in the total temperature for the non-ideal cascade. (a) Ň-DES (——) and optimised (——) blade profile, (b) variation in the cascade loss coefficient with total temperature for the two blade profiles.

unconventional flow character triggered by severe non-ideal effects, seemingly suggests that the performance variabilities are entirely due to the underlying non-ideal gas dynamic rather than to a sub-optimal blade geometry.

3.6 Generalization to other organic fluids

Until now, the analysis was limited to specific thermodynamic conditions of MM expanding flows. In this section, the findings are arguably generalized to a wider class of organic fluids. The amplification of operational uncertainty was mainly due to the significant sensitivity of throat thermodynamic properties with respect to the upstream total state. It was shown that a variation in the throat thermodynamic conditions, namely in the density and speed of sound, has paramount importance both in the mass flow rate processed by the (choked) cascade and in its aerodynamic losses, as a consequence of A/A^* modification. Specifically, the variation in the nominal trend of A/A^* is recognized as the main contributor to the change in the cascade performance. Based on this physical backbone, the A/A^* trend can be conveniently used to predict whether non-ideal gas-dynamic regimes amplify small departures from nominal conditions.

To this end, Figure 3.34 reports area-ratio evolutions against the pressure, along with Γ and Z fields, for three expanding flows of exemplary classes of fluids, namely a refrigerant (R1234yf, $C_3H_2F_4$), an aromatic hydrocarbon (Toluene, C_7H_8) and a linear siloxane (MDM, $C_8H_{24}O_2Si_3$). The selected fluids are representative of both low temperature (refrigerants) and high temperature (aromatic hydrocarbons and siloxanes) ORC applications. The choice of these fluids is also motivated by their comparatively different molecular complexity, which can be defined according to Harinck *et al.* (2009) as:

$$N = \frac{2c_{v,id}(T_c)}{\mathcal{R}} \tag{3.8}$$

N is equal to 25.9, 44.8 and 115.9 for R1234yf, toluene and MDM, respectively. For sake of comparison, MM has $N = 78.4$. The molecular complexity is closely linked with the achievable minimum Γ (Colonna & Guardone, 2006), while most substances feature low values of the compressibility factor Z in the proximity of the critical point regardless of the molecular complexity. Different fluids that belong to the same class (refrigerants, hydrocarbons, siloxanes) are expected to share comparable values of Γ close to the critical point, thus behaving similarly from a non-ideal gas-dynamic perspective. The reduced total temperatures for the three expansions are $T^t/T_c = 1.13, 1.08, 1.04$, respectively. The reduced total pressure is $P^t/P_c = 2$ for all expansions.

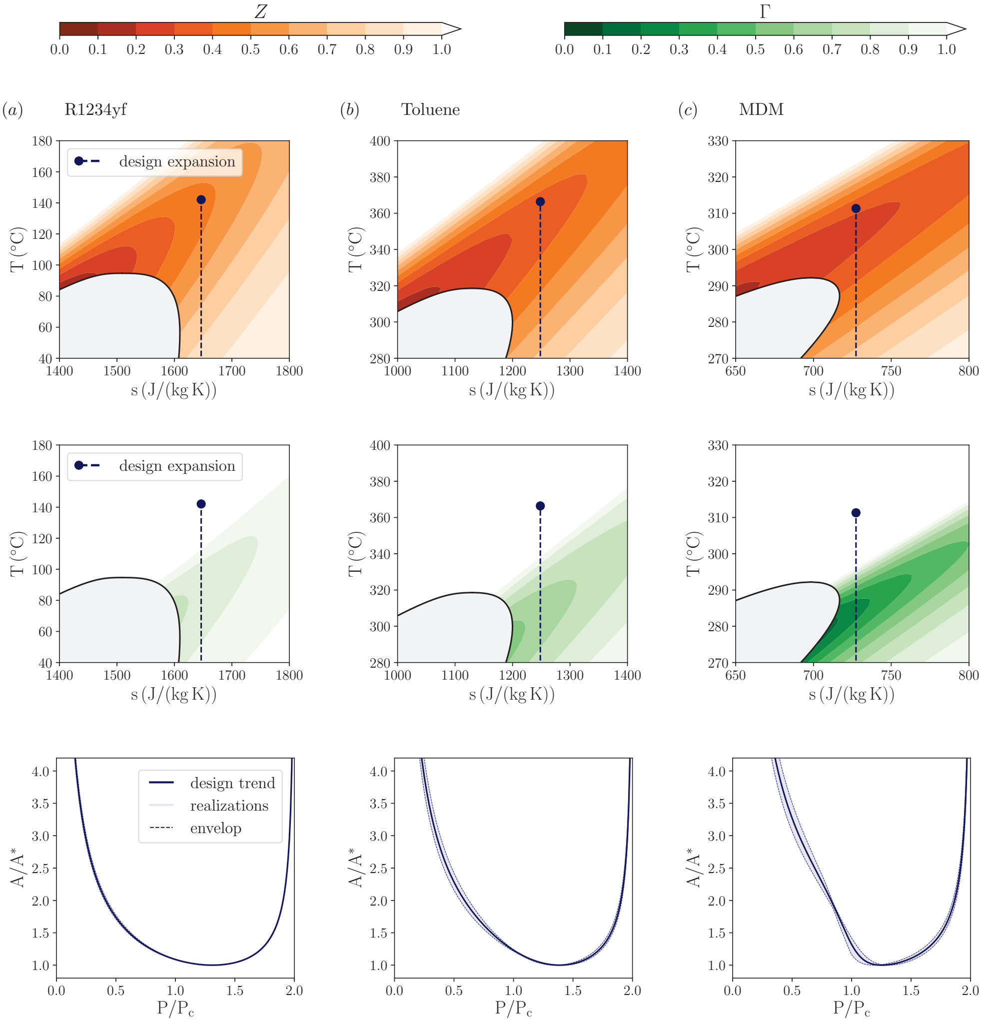

FIGURE 3.34. Design area-ratio distributions (bottom frames) predicted by the quasi-one-dimensional theory for (*a*) the refrigerant R1234yf (with total states $P^t/P_c = 2$ and $T^t/T_c = 1.13$), (*b*) the aromatic hydrocarbon Toluene (with total states $P^t/P_c = 2$ and $T^t/T_c = 1.08$) and (*c*) the linear siloxane MDM (with total states $P^t/P_c = 2$ and $T^t/T_c = 1.03$), along with 200 independent uniformly distributed realizations assuming ±1.25% uncertainty in both the design total pressure and temperature (measured in Celsius degree). Maps of the compressibility factor Z (top frames) and fundamental derivative of gas dynamics Γ (central frames) are superposed to the design expansion process in the T–s plane.

The total states are selected to achieve very low values of Γ and Z along with the expansions while avoiding two-phase flows when uncertainties are introduced. To be consistent with the above UQ study, a variation of ±1.25% in both total quantities (with temperature measured in Celsius degrees) is here considered. Within this framework, 200 independent realizations are reported in Figure 3.34 along with the A/A^* nominal trend.

The inspection of the area-ratio evolution (bottom panels) reveals that the amplification of the operational uncertainty increases with the molecular complexity. Similar tests performed with other fluids (consisting of linear, cyclic, and aromatic hydrocarbons, refrigerants, and linear and cyclic siloxanes) seemingly confirm this conjecture. As previously noted, the thermodynamic properties mostly contributing to performance variations were the density and the speed of sound at the throat and their associated gradients. The departure of both density and speed of sound from the ideal-gas behaviour is accounted in either Z or Γ, hence one might question whether one out of these two parameters can better describe the sensitivity of the expansion on the upstream stagnation state. It is worth underlining that neither Γ nor Z can be linked to a single property variation (whether density or speed of sound) without altering the other from the ideal-gas behaviour. From Figure 3.34, Γ, which is strictly related to the molecular complexity of the fluid, seems to discriminate the quantitative variation in A/A^* and, implicitly, in the cascade performance, notwithstanding low values of Γ and Z share a large portion of the thermodynamic region in molecularly complex fluids. As a matter of fact, all expansion processes feature very low values of Z, i.e. $Z_{min} = 0.47, 0.34, 0.27$ along the isentropic expansions of R1234yf, toluene and MDM, respectively, but comparatively different levels of Γ, whose minimum values are $\Gamma_{min} = 0.82, 0.63, 0.27$, respectively. Moreover, it seems that variations triggered by non-ideal flows are quantitatively limited up to $\Gamma_{min} \approx 0.8$ while becoming progressively more significant for lower values of Γ.

To conclude, in addition to qualitative non-ideal effects that exclusively depend on Γ, e.g. the non-monotonic trend of the Mach number against the pressure or the increase of the Mach number across an oblique compression shock, also quantitative departures from the nominal trend, mostly given by the dependency of the expansion process on the upstream stagnation state, seem to be mainly linked to Γ. Following the results of this analysis, when dealing with molecularly complex fluids the inspection of the Γ evolution along the isentropic expansion should be carefully evaluated to be aware of the potential performance variability triggered by non-ideal operation.

3.7 Concluding remarks and key findings

Non-ideal flows of siloxane MM in converging-diverging nozzle cascades were investigated numerically. Steady-state numerical solutions were obtained by employing a Reynolds-averaged Navier-Stokes flow solver, featuring a k-ω SST turbulence model along with state-of-the-art thermodynamic treatment. By examining representative design points along with selected off-design conditions, two opposite scenarios were recognized within the non-ideal gas-dynamic regime $\Gamma < 1$. In the range of inlet pressures approximately up to the critical pressure, the expansion process in the nozzle cascade is qualitatively similar to that observed in the ideal-gas limit. In other words, despite the nozzle expansion occurs in the non-ideal gas-dynamic regime, non-ideal effects do not play a major role and ideal-gas considerations can be applied in the design and performance analysis of the cascade (ideal-like scenario). Quantitative differences with respect to the dilute-gas flow field are arguably negligible at relatively low pressures (e.g. $\Gamma \sim 1$) and increase approaching the supercritical regime. Expansion from supercritical conditions can instead exhibit strong non-ideal effects which determine a quantitative and qualitative deviation from the flow features characterizing subcritical expansions (non-ideal scenario).

The main implications for nozzle-cascade flows in their non-ideal operating regime are:

(I) a potentially advantageous design, involving stationary points of the Mach number in the proximity of the blade trailing edge, leads to a nearly uniform outlet Mach number distribution in the stator-rotor axial gap with low sensitivity to slight variations in the outlet pressure;

(II) if the above-mentioned stationary point is the local maximum/minimum, a decrease/increase in the outlet Mach number is observed with decreasing/increasing outlet pressure, achieved by means of non-ideal Prandtl-Meyer waves/oblique shocks;

(III) the cascade performance is highly sensitive to variations in the upstream total pressure and temperature, at constant pressure ratio. The present analysis suggests a larger influence of total temperature variations over the total pressure.

The performance of nozzle cascades operating in the non-ideal gas-dynamic regime is found to be largely sensitive to departure from the design conditions. To this end, a probabilistic framework that accounts for small operational uncertainty is formulated, combining an uncertainty-quantification strategy based on a polynomial-chaos representation of the flow solver. The mass flow rate and the cascade losses are found to change four and six times more than their ideal-like counterparts, respectively, given the same relative variations in the boundary conditions. The physical reasons behind these variations were illustrated by means of the general steady isentropic quasi-one-dimensional flow theory. It is shown that a change in the upstream total temperature largely affects the density and the speed of sound at the throat, therefore: (i) the mass flow rate directly changes as a consequence of turbine choked operation, (ii) the area-ratio A/A^* evolution severely changes when $\Gamma \ll 1$, thus triggering off-design operation in the turbine vane. As a matter of fact, a variation in A/A^* modifies the adapted pressure ratio across the cascade, which has to rely on a modification of the shock pattern at the trailing edge to fulfill the prescribed expansion with a consequent alteration of nominal losses. Such variability is inherently connected with the sudden change in the gas-dynamic evolution when changing the upstream stagnation state. Aligned with this interpretation, shape optimization including multiple operating conditions confirms that limited improvements can be obtained (included in the former range of variations), while the performance variability persists regardless of the specific blade geometry.

On top of that, the entire flow field in non-ideal conditions is found to be highly affected by operational uncertainty. As a result, the subsequent rotor cascade has to deal with a variable incoming flow. As such, the rotor incidence angle varies both locally (up to 10°) and in average (±3°), opposed to a nearly null variation in the ideal-like scenario.

Numerical results are found to be consistent with the predictions of the quasi-one-dimensional flow and oblique-wave theories, which are of general validity and mainly depend on the behaviour of the fundamental derivative of gas dynamics. From the qualitative point of view, the conclusions of this study are not limited to specific blade geometries but generally apply to supersonic expansions of MM in converging-diverging blade channels with comparable inlet and outlet conditions. Moreover, the present findings can arguably be extended to most molecularly complex fluids featuring $\Gamma \ll 1$ in the single-phase vapour region.

As a final comment, non-ideal flows through nozzle cascades are also expected to influence other cycle components in several ways. Following the results of this study, stator and rotor aerodynamic losses are largely sensitive to operational uncertainty, as a consequence of shock-pattern and incidence-angle modifications, respectively. The two effects couple in the determination of the first-stage and, hence, turbine isentropic efficiency η^t_{is}. Many studies advocate that the ORC plant efficiency considerably depends on the turbine-efficiency value, thus qualitatively linking the observed turbine variations to as many variations in the cycle efficiency.

The turbine efficiency also enters into the power output, via the relationship $\dot{W} = \dot{m}\,\Delta h_{is}\,\eta^t_{is}$, where Δh_{is} is the isentropic enthalpy drop associated with the turbine expansion. In the above expression, the powers drained by the pump and auxiliaries are neglected as a first approximation. Moreover, significant variations in the mass flow rate are found to characterize the non-ideal scenario (up to ±4% with respect to the design value). Nonetheless, a negative correlation between the mass flow rate and the isentropic enthalpy drop is noticed for these thermodynamic conditions. It follows that the product $\dot{m}\,\Delta h_{is}$ changes less compared to the mass-flow-rate variation alone.

A change in the mass flow rate may also trigger off-design operation in the heat exchangers, affecting both heat-transfer coefficients and thermal powers. Preliminary off-design analyses of the transcritical cycle, accounting directly for the observed mass-flow-rate variations, have reported that the pinch-point temperature at the regenerator can change up to ±2.5 K.

Most of the variations in the non-ideal regime are associated with the high sensitivity of the expansion process to the upstream turbine total temperature, i.e. the maximum temperature of the cycle. Although the system dynamics may hinder some of these effects, careful control of the maximum temperature becomes mandatory to ensure proper plant operation in these conditions.

CHAPTER 4

NON-IDEAL FLOWS IN TURBOMACHINERY FOR SUPERCRITICAL CARBON DIOXIDE POWER SYSTEMS

This chapter discusses the challenges connected with turbomachinery for sCO$_2$ *power systems. The importance of modelling turbomachinery components is highlighted by incorporating simplified mean-line representations in power-system analyses. This general framework prepares the ground for the three-dimensional design of the main compressor and the subsequent performance analyses at off-design conditions. Computational fluid dynamic simulations, intentionally devised to tackle compressible non-ideal two-phase flows, reveal the significant influence of both non-ideal and two-phase effects on the compressor aerodynamics and performance.*

Some contents of this chapter are also discussed in:

Romei, A., Gaetani, P., Giostri, A., & Persico, G., (2020) The role of turbomachinery performance in the optimization of supercritical carbon dioxide power systems, *Journal of Turbomachinery*, vol. 142(7): 071001 (11 pages), doi: 10.1115/1.4046182

Romei, A., & Persico, G., (2021) Computational fluid-dynamic modelling of two-phase compressible flows of carbon dioxide in supercritical conditions, *Applied Thermal Engineering*, vol. 190: 116816 (20 pages), doi: 10.1016/j.applthermaleng.2021.116816

4.1 Challenges connected with sCO_2 turbomachinery

sCO_2 power systems represent a promising cost-effective solution for several technologies, ranging from nuclear (Dostal, 2004) to concentrating solar power (Neises & Turchi, 2014) and waste heat recovery (Poerner & Rimpel, 2017). In these fields of applications, sCO_2 plants may prevail over conventional power systems based on steam as working fluid thanks to the overall higher conversion efficiency, simpler plant layout, and smaller turbomachinery sizes (Musgrove & Wright, 2017). As opposed to ORC systems, whose standard layout already features the highest technology readiness level (TRL), sCO_2 systems still need significant development to enable their penetration in the market, both at the system and at the component level. Presently, there are only a few examples of pilot plants aiming at demonstrating the feasibility of the technology, such as the US-funded project STEP and the EU-funded projects sCO_2-Hero and sCO_2-flex to name a few.

Until the date of this thesis, the interest for the sCO_2 technology is mainly justified by potential advantageous performance based on techno-economic analyses of the thermodynamic cycle, which usually rely on simplified models for the main components (heat exchangers and turbomachinery). Unfortunately, these analyses may be biased by reworking paradigms derived from conventional technologies, for which consolidated data and results are available. The aleatory decision to assume specific values for some parameters may determine on paper the success of a sCO_2 power system over a traditional one. An example is given by the common tendency to assume constant values for the turbomachinery efficiencies, whose choice greatly affects the overall cycle performance (Allison *et al.*, 2017). Besides, the arbitrary root of this choice may lead to significantly different, sometimes contradictory, results published in the open literature (a clear example is illustrated by the survey conducted in Crespi *et al.* (2017*a*)). Systematic and tailor-made rules for this specific field have yet to be devised in order to enable fair comparisons with well-established technologies.

Therefore, the first part of this chapter will tackle the integration of preliminary turbomachinery design, purposely performed for sCO_2 cycles, within a broader system analysis. As the main centrifugal compressor is recognized as one of the most critical components of the entire technology (Wright *et al.*, 2010), a larger effort is focused on its preliminary design on the basis of a purposely developed mean-line tool, highlighting the role of non-ideal flows due to the near-critical compression. The general expectation is that the compressor may be less efficient or may exhibit more stability issues if compared to its air-breathing counterpart, resulting from operation close to the thermodynamic critical point, where a sharp variation in the thermodynamic properties and local two-phase flows may possibly occur. This statement was questioned by Noall & Pasch (2014), who provided a preliminary analysis of a full-scale compressor featuring a comparatively high efficiency ($83 \div 85\%$).

Alongside the compressor mean-line design, preliminary designs of the axial turbine (suitable for a larger range of plant capacities than the radial-inflow counterpart (Musgrove & Wright, 2017)) are carried out as well. All preliminary designs, which feature different stagnation conditions, aerodynamic loading, and dimension, are collected to devise consistent polynomial correlations (separately for the compressor and for the turbine). In doing so, realistic variations of the turbomachinery efficiencies are included within the framework of cycle analysis and optimization. These tailored correlations make it possible to properly infer the evolution of optimal cycle parameters, such as overall pressure ratio and cycle efficiency, for different temperature levels and target plant capacities. As the last point of this combined turbomachinery-cycle analysis, the investigation is also extended to the preliminary design of multi-stage turbomachinery, revealing again the paramount importance of integrating turbomachinery design, albeit at a preliminary level, in the overall power cycle analysis.

The main problem associated with the mean-line formulation is that it neglects an important feature of sCO_2 compressors operating in near-critical conditions, namely the potential occurrence of two-phase flow due to local flow accelerations. Presently, the effect of two-phase flows on compressor performance for sCO_2 applications is in practice unknown: the main hurdle is represented by the lack of suitable computational tools that are able to deal with high-speed non-ideal two-phase flows interacting with compressor blades. To solve this issue, two CFD models are developed and validated against experiments of cavitating and condensing sCO_2 flows in §4.6. Both models describe the two-phase flow in terms of mixture properties, hence single-phase governing equations are recovered and expressed in terms of proper averaged properties.

The development of CFD models that are capable of handling compressible two-phase non-ideal flows sets the ground for high-fidelity performance analyses of sCO_2 flows within a centrifugal compressor, which are carried out in §4.7. At first, the three-dimensional compressor design is undertaken by considering a reference compression process, coming from the optimization of the power cycle. Particular attention is devoted to the design of the impeller, in which many competing geometrical parameters can promote the establishment of phase transition. Moreover, when it comes to compressors operating in near-critical conditions, the classical similitude theory can present shortcomings due to: (i) non-ideal effects that largely affect the compressor aerodynamics (Baltadjiev *et al.*, 2015; Ameli *et al.*, 2018*b*) and (ii) two-phase flows that can originate from local flow accelerations (Pecnik *et al.*, 2012; Hosangadi *et al.*, 2019). As opposed to conventional air-breathing compressors, whose performance remains unaltered regardless of the upstream conditions, the above effects are highly sensitive to the intake thermodynamic conditions. As a consequence of the compression close to the critical point, a small change in the upstream total state induces large variations in most of the thermo-physical properties (Hacks *et al.*, 2019). To a certain extent, one can imagine that every time the intake thermodynamic state is perturbed, the compressor has to deal with a different fluid. However, the large departure from the ideal-gas thermodynamics prevents using γ to account for this fluid difference when the performance maps are expressed in their dimensionless form. Moreover, because of the vicinity to the saturation curve, a change in the intake thermodynamic conditions will also affect the extent of the two-phase region within the blade channel. The influence of these parameters on compressor performance maps is widely discussed, shedding light on the way they act in the modification of the ideal similarity based only on the flow coefficient and the peripheral Mach number.

4.2 Mean-line formulation for preliminary turbomachinery design

In this section, the mean-line tools are presented and the main assumptions are clearly pointed out. In order to explore a wide range of design conditions at a reasonable computational cost, the mean-line representation is selected as a simulation tool for both turbomachinery components, namely centrifugal compressors and axial turbines. The mean-line representation assumes uniform and unidirectional flow in each relevant section at midspan, hub, and tip. Thanks to these simplifications, it allows determining a preliminary machine layout in terms of size, angular speed, blade heights, and velocity triangles at a low computational cost. Moreover, it also provides a realistic representation of the flow path along the machine. As both codes (turbine and compressor) are conceived as direct simulation tools (geometrical parameters as input, performance as output), they need an external optimization routine for design applications. Carbon dioxide properties are computed by calling the external thermodynamic library RefProp® (Lemmon *et al.*, 2013), which features a multi-parameter equation of state expressed in terms of Helmholtz fundamental relation (Span & Wagner, 1996).

4.2.1 Centrifugal compressors

The mean-line code for the design of centrifugal compressors operating with sCO_2 is based on several loss models, formulated as enthalpy variations, which account for the sources of entropy generation usually occurring in centrifugal compressors. The calculations are run by assigning the compressor geometry along with upstream total quantities and mass-flow rate. The main components and geometrical parameters considered in the code are sketched in figure 4.1, where only the volute, placed after the vaned diffuser, is not explicitly reported. For sake of brevity, the detailed description of the code is not reported, however it follows standard mean-line implementations reported in the literature (Schiffmann & Favrat, 2010; Meroni *et al.*, 2018*b*).

The impeller loss model is rooted in the pioneering work of Oh *et al.* (1997), which was validated for sCO_2 compressor (Lee *et al.*, 2014; Ameli *et al.*, 2018*a*; Meroni *et al.*, 2018*b*) against experimental results (Wright *et al.*, 2010). Five sources of losses (causing a decrease in the total pressure rise), namely incidence, blade-loading, tip clearance, mixing, and skin-friction losses, were formulated to derive the impeller efficiency. Moreover, three external losses (only contributing to an increase of the machine total enthalpy) were also considered, i.e. recirculation, disc-friction, and leakage losses. The present design tool recovers the full set of losses, whose analytical expressions are reported in table 4.1 for the reader's convenience. The deviation angle at the impeller outlet is estimated with the slip factor formulation provided by Wiesner (1967). Whenever splitter blades are introduced, the effective number of blades is assumed as $N_{\text{eff}} = N_{bl} + 0.75N_{spl}$, where N_{bl} represents the number of full blades and N_{spl} is the number of splitter blades, if not specified otherwise.

In an effort of improving the predictive capabilities, realistic losses for the diffuser and volute, as well as their preliminary sizing, are also implemented. Two kinds of losses are considered for the vaned diffuser, namely incidence and skin-friction losses, recalling the formulations available for the impeller. The skin-friction loss occurring in the vaned diffuser includes an additional factor δ_{BL}, accounting for the development of the boundary layer in the impeller channel (Aungier, 2000). A constant skin-friction coefficient, $c_f = 0.006$, is considered in the computation of skin-friction losses for both the impeller and the vaned diffuser. This value was suggested for air-breathing compressors (Jansen, 1967), whose operating conditions feature significantly lower Reynolds numbers with respect to the typical values found in sCO_2 compressors (Lettieri *et al.*, 2014). Besides, a dedicated analysis of the skin-friction coefficient was performed by Ameli *et al.* (2018*a*), showing that $c_f = 0.006$ is reasonably acceptable for sCO_2 centrifugal compressors. Finally, the radial component of the velocity at the diffuser outlet is dissipated to account for the volute loss. A skin-friction loss for the volute might be formulated as well, however the kinetic energy involved in

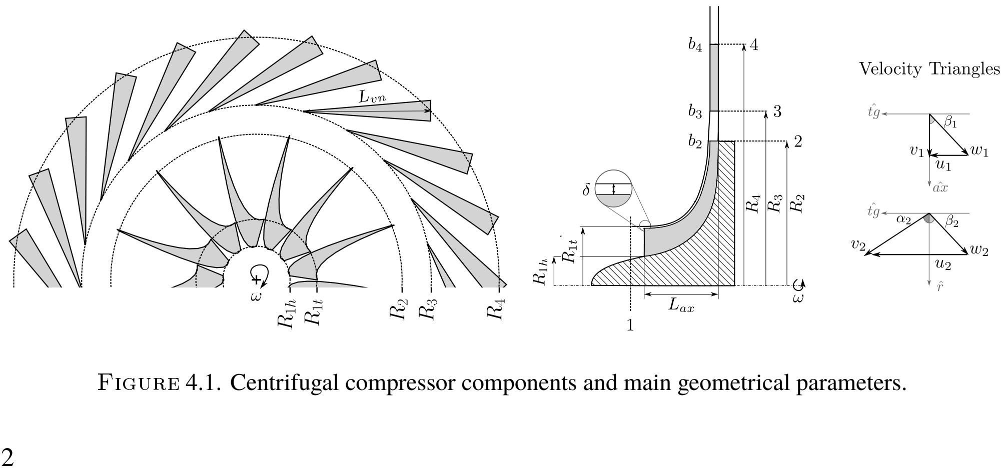

FIGURE 4.1. Centrifugal compressor components and main geometrical parameters.

TABLE 4.1. Loss correlations implemented in the centrifugal-compressor mean-line design tool.

Loss Mechanism	**Loss Model**	
Impeller incidence	$\Delta h_{in} = f_{inc}\, w_1^2 \sin^2(\beta_1 - \beta_{1,bl})/2$	$f_{inc} = 0.5 \div 0.7$
Impeller blade loading	$\Delta h_{bl} = 0.05 D_f^2 u_2^2$	$D_f = 1 - \dfrac{w_2}{w_1} + \dfrac{0.75\Delta h_{TT}/u_2^2}{\dfrac{w_{1t}}{w_2}\left[\left(\dfrac{N_{\text{eff}}}{\pi}\right)\left(1 - \dfrac{D_{1t}}{D_2}\right) + 2\dfrac{D_{1t}}{D_2}\right]}$
Impeller clearance	$\Delta h_{cl} = 0.6\dfrac{\delta}{b_2} v_{2,tg}\sqrt{\dfrac{4\pi(R_{1t}^2 - R_{1h}^2)\, v_{2,tg}\, v_{1,m}}{b_2\, N_{\text{eff}}(R_2 - R_{1t})(1 + \rho_2/\rho_1)}}$	
Impeller mixing	$\Delta h_{mx} = 0.5\dfrac{v_2^2}{1 + \tan^2\alpha_2}\left(\dfrac{\varepsilon}{1-\varepsilon}\right)^2$	$\varepsilon = 0 \div 0.35$
Impeller friction	$\Delta h_{sf} = 2c_f\dfrac{L_b}{D_h}\overline{w}^2$	$\overline{w} = \dfrac{v_{1,tg} + w_{1,tg} + v_2 + 2w_{1h} + 3w_2}{8}$ $L_b = \dfrac{\pi}{8}(2R_2 - (R_{1t} + R_{1h}) - b_2 + 2L_{ax})\left(\dfrac{2}{(\cos\beta_{1t} + \cos\beta_{1h})/2 + \cos\beta_{2,g}}\right)$ $L_{ax} = D_2(0.014 + 0.023\, D_2/D_{1h} + 2.012\, \dot{V}_{T1}/(u_2 D_2^2))$ $D_h = \dfrac{\pi(D_{1t}^2 - D_{1h}^2)}{2\pi D_1 + N_{\text{eff}}(D_{1t} - D_{1h})}$
Recirculation	$\Delta h_{rc} = 8 \times 10^{-5} \sinh(3.5\alpha_2^3)\, D_f^2\, u_2^2$	
Disc friction	$\Delta h_{df} = c_f\dfrac{\overline{\rho}\, R_2^2\, U_2^3}{4\dot{m}}$	$\overline{\rho} = (\rho_2 + \rho_1)/2$
Leakage	$\Delta h_{lk} = \dfrac{\dot{m}_L\, u_L\, u_2}{2\dot{m}}$	$\dot{m}_L = \rho_2\, u_L\, \delta\, L_{ax}\, N_{\text{eff}}, \quad u_L = 0.816\sqrt{\dfrac{2\Delta P_L}{\rho_2}}$ $\Delta P_L = \dfrac{\dot{m}(R_2 v_{2,tg} - R_{1t} v_{1t,tg})}{N_{\text{eff}}\, \overline{R}\, \overline{b}\, L_{ax}}, \quad \overline{R} = (R_2 + R_{1t})/2, \quad \overline{b} = (b_1 + b_2)/2$
Diffuser incidence	$\Delta h_{in,d} = f_{inc}\, v_3^2 \sin^2(\alpha_3 - \alpha_{3,bl})/2$	$f_{inc} = 0.5 \div 0.7$
Diffuser friction	$\Delta h_{sf,d} = 2c_f\dfrac{L_{vn}}{D_{h,vn}\delta_{BL}^{0.25}}\overline{v}^2$	$\overline{v} = \sqrt{v_3^2 + v_4^2}/2$ $L_{vn} = D_3(D_4/D_3 - 1)/(\cos\alpha_{3,g} + \cos\alpha_{4,bl})$ $\delta_{BL} = 5.142\, c_f\, L_{vn}/D_{h,vn}$ $D_{h,vn} = (D_{3h} + D_{4h})/2$ $D_{3h} = \dfrac{2\, b_2(2\pi\, R_3/N_{vn} - t_3)}{(\pi\, R_3/N_{vn} - t_3) + b_2/\cos\alpha_{3,bl}}, \quad D_{4h} = \dfrac{2\, b_2(2\pi\, R_4/N_{vn} - t_4)}{(\pi\, R_4/N_{vn} - t_4) + b_2/\cos\alpha_{4,bl}}$
Volute loss	$\Delta h_{vol} = \dfrac{v_{4,r}^2}{2}$	

this component is rather low so that this source of loss is not expected to significantly affect the compressor performance.

The mean-line code is validated against experimental data provided by Sandia Laboratories (Wright *et al.*, 2010) at three different rotational speeds, namely 45000 rpm, 50000 rpm, and 55000 rpm. The introduction of vaned-diffuser losses requires to supply its main geometrical parameters, i.e. outlet and inlet diffuser angles ($\alpha_{3,g}$, $\alpha_{4,g}$), vane length and vane number (L_{vn}, N_{vn}), inlet and outlet vane thicknesses (t_3, t_4) and diffuser radial extensions (R_3, R_4). Although very detailed information about impeller geometry can be found in Wright *et al.* (2010), only $\alpha_{3,g} = 71.5°$ and $N_{vn} = 17$ are there clearly reported for the vaned diffuser. The missing geometrical information is retrieved from (Wright *et al.*, 2009) (fig. 2, p. 3) by graphical extrapolation. Values adopted in the validation are: $t_3 = 1\,\text{mm}$, $t_4 = 6\,\text{mm}$, $R_3 \approx R_2$, $D_4 = 65.2\,\text{mm}$, $L_{vn} = 22.8\,\text{mm}$ and $\alpha_{4,g} = 31.5\,°$. A relatively small outlet diffuser angle, measured from the radial direction, is consistent with the large volute size reported in Wright *et al.* (2010). Within this mean-line framework, the vaned diffuser and the volute are sized mainly according to Aungier (2000); for the volute, a circular external shape is assumed.

To foster the tool validity, an uncertainty-quantification analysis is also presented along with the validation. The scope is to prove that comparatively small variability in the input parameters does not produce large uncertainties in compressor performance, thus boosting the tool fidelity when different cases are compared. Moreover, unavoidable approximations in the derivation of the diffuser geometry are properly accounted for in this way. A Monte Carlo sampling is performed for each rotational speed, including seven independent uncertainties as reported in table 4.2. A uniform distribution is prescribed for all uncertainties. In addition to the geometrical data of the vaned diffuser, which were inferred from images reported in Wright *et al.* (2009, 2010), thus inherently

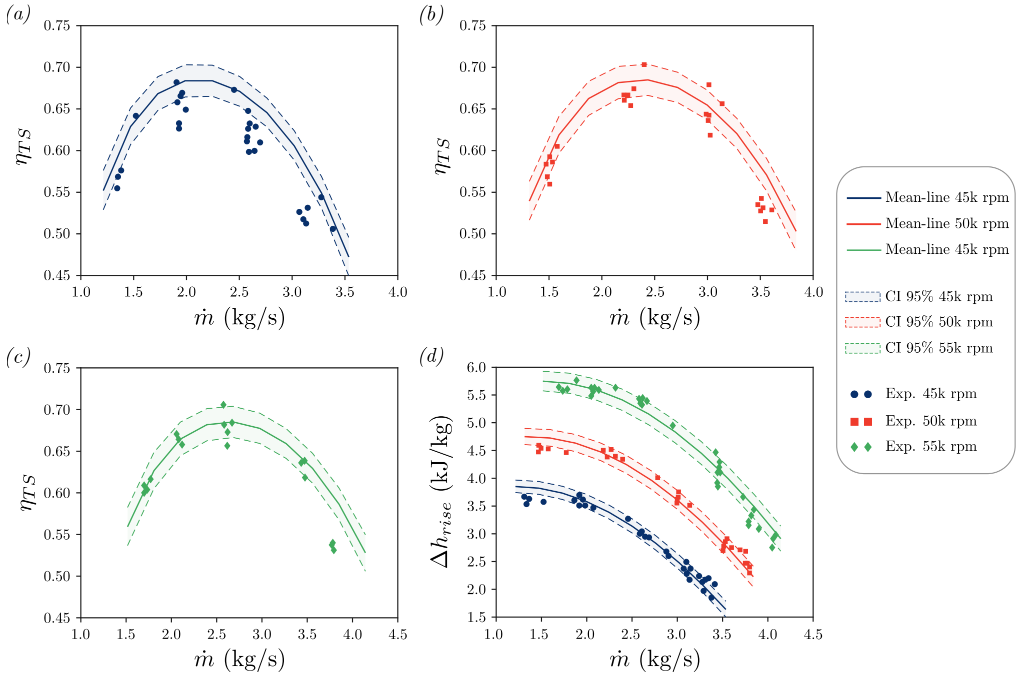

FIGURE 4.2. Compressor mean-line predictions along with 95% confidence intervals compared against experimental data (Wright *et al.*, 2010). Efficiency maps for (*a*) 45000 rpm, (*b*) 50000 rpm and (*c*) 55000 rpm. Enthalpy-rise map at different speedlines in subfigure (*d*).

TABLE 4.2. Uncertainties included in the validation process.

Uncertainty	**Range**
k_μ	$\mathcal{U}([0.98, 1.02])$
c_f	$\mathcal{U}([0.005, 0.007])$
C_P	$\mathcal{U}([0.6, 0.7])$
$\alpha_{4,g}$	$\mathcal{U}([30, 35])\,^\circ$
L_{vn}	$\mathcal{U}([22.4, 23.2])$ mm
t_3	$\mathcal{U}([0.75, 1.25])$ mm
t_4	$\mathcal{U}([5.75, 6.25])$ mm

uncertain, the following uncertainties are also included: the skin friction coefficient c_f, a coefficient k_μ which evaluates the effect of variations up to ±2% in the slip-factor estimation, and the design pressure-recovery coefficient for the vaned diffuser, defined as $C_P = (P_4 - P_3)/(P^t_3 - P_3)$.

Figure 4.2 reports the mean trend along with the extended confidence intervals for performance maps expressed in terms of total-to-static efficiency and enthalpy rise. This latter is intended as the equivalent enthalpy rise associated to the real increase in total pressure across the compressor, accordingly expressed as:

$$\Delta h_{rise} = h(P^t_5, s_1) - h(P^t_1, s_1) = l_{eul} - \Delta h_{imp} - \Delta h_{diff} - \Delta h_{vol} \tag{4.1}$$

where l_{eul} is the eulerian work, Δh_{imp} is the sum of all impeller losses, Δh_{diff} and Δh_{vol} includes all losses in the diffuser and volute, respectively. On the other hand, the compressor efficiency is generally defined in the code as

$$\eta^c_{T\chi} = \frac{h(P^t_5, s_1) - h(P^t_1, s_1) - \chi\, v_5^2/2}{l_{eul} + \Delta h_{ext}}, \tag{4.2}$$

where Δh_{ext} contains all external losses, while the definition of the parameter χ allows for different efficiency formulations. If $\chi = 1$, the expression returns the total-to-static efficiency η^c_{TS} (as in the present validation case), while if $\chi = 0$, then it returns the total-to-total efficiency η^c_{TT}.

The validation shows that most of the experimental data fall in the predicted 95% confidence intervals. A slightly higher discrepancy ($\approx$ 1 pp) is found in the efficiency maps for the lowest rotational speed. Moreover, upon examination of figures 4.2(a)–(c), the mean-line code overpredicts the efficiency at higher flow coefficients. The enthalpy-rise map, on the other hand, remarkably matches experimental data for all rotational speeds and flow coefficients. The combination of efficiency and enthalpy-rise maps suggests that the overprediction in the efficiency curves at higher flow coefficients can be attributed either to the outlet kinetic energy or to the external losses, by comparison of their associated formulations (see equations (4.1) and (4.2)). Nonetheless, future analysis based on the mean-line model only involves the peak (design) efficiency; accordingly, the overprediction at higher flow coefficients does not undermine the validity of the results presented in the following. Finally, the uncertainty in the efficiency prediction is around ±1.5 pp for peak values, which is satisfactory in light of the large uncertainties characterizing the diffuser geometry.

4.2.2 Axial turbines

The design of sCO$_2$ turbines is performed by using the in-house mean-line code zTurbo (Persico & Pini, 2017). The main geometrical parameters for a single-stage configuration are sketched in figure 4.3. zTurbo was conceived for the design of different turbine architectures, operating in subsonic, transonic, or supersonic flow regimes. Like any mean-line model, zTurbo inherently ignores the detailed shape of the turbine blades, but it relies on correlations for losses whose reliability determines the fidelity of the performance estimates. Few studies document a good agreement between the mean-line calculations and performance measurements (Craig & Cox, 1970; Wilson, 1984).

Within the framework of zTurbo, the calculation is run assigning total quantities at the turbine inlet, the static pressure at the outlet, and the mass-flow rate along with the main geometrical parameters. The code contains several loss correlations, e.g. Ainley & Mathieson, Traupel, and

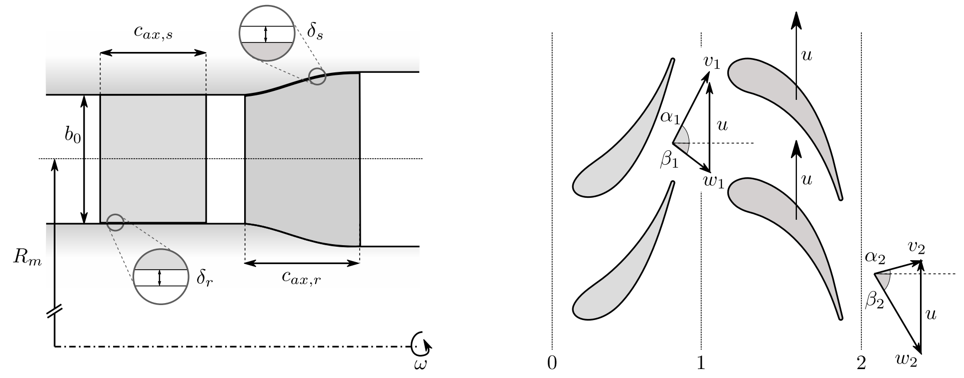

FIGURE 4.3. Single-stage axial turbine components and main geometrical parameters.

Craig-Cox for axial turbines, complemented by specific corrections for supersonic flows and post-expansions downstream of the throat. In this work, Traupel loss correlations are employed. The outflow angle is estimated by applying a proper deviation correlation (Sawyer, 1972), while the blade number is evaluated with the standard loading criterion of Zweifel (1945).

In the last five years, zTurbo was applied to axial (Casati *et al.*, 2014; Bahamonde *et al.*, 2017), radial-outflow (Pini *et al.*, 2013; Bahamonde *et al.*, 2017), and radial-inflow (Bahamonde *et al.*, 2017) turbines. Casati *et al.* (2014) reports a validation against a four-stage axial turbine, showing prediction capabilities similar to what documented in Meroni *et al.* (2018*a*) (namely, errors of ≈ 2 pp with respect to the experiments). Up to the date of the present thesis, there are no reliable data of sCO_2 axial turbines for validation. However, contrarily to the compressor, the turbine operates in a thermodynamic region whereby the ideal-gas behaviour is recovered, therefore past validations of the mean-line tool are deemed sufficient for the purposes of the present analysis.

4.3 Optimized compressor designs at variable operating conditions

The aim of this section is to assess the implication of the non-ideal effects, depending on the upstream stagnation state, on the achievable compressor efficiency η_{TT}^{c} for different sizes and pressure ratios. To this end, several optimizations are carried out in order to generate optimized compressor designs (in terms of highest total-to-total efficiency) by varying the inlet thermodynamic states and, consequentially, the departure from the ideal-gas approximation. Representative 26 compressor-intake conditions are recognized in the plane T–s (identified by black dots in figure 4.4) in the range of $33\,°C < T_1^t < 150\,°C$ and $70\,\text{bar} < P_1^t < 100\,\text{bar}$. The lower temperature limit is chosen to avoid local two-phase flows in the compressor (at least in design conditions), while the upper limit eventually includes realistic inlet conditions for a recompressor. Pressure limits are based on preliminary cycle considerations for different minimum temperatures, retaining a large range to widen the study. This analysis is limited to single-stage compressors for sake of compactness and costs, but an extension to multi-stage configurations is reported later in §4.5.1.

Several assumptions for the compressor design are made: (i) the impeller blade number is computed as in Eckert & Schnell (1961); (ii) splitter blades are included; (iii) zero incidence is assigned at the impeller inlet; (iv) the inducer is always included; (v) the vaned-diffuser is designed (L_{vn}, N_{vn}, R_3, R_4) according to Aungier (2000); (vi) the diffuser inlet flow angle is not corrected for the diffusion in the vaneless space; (vii) the pressure-recovery coefficient C_P is set at 0.7, which is representative of a fair diffusion process in design conditions; (viii) blade and vane thicknesses are proportionally scaled from the Sandia's main compressor; (ix) clearances are proportionally scaled from the Sandia's main compressor, considering a maximum cap of 1 mm.

The user cannot arbitrarily impose the target pressure ratio, but this latter results from the mean-line calculations (only inlet total conditions are imposed). Therefore, a penalty formulation is embedded in the objective function (η_{TT}^{c}) to drive the optimization towards designs satisfying the prescribed pressure ratio, accepting an absolute error of 0.01. Moreover, since the aim of the designer is to avoid choked-flow operation at least in the design condition, neither in the impeller nor in the diffuser, both relative Mach number at the impeller inlet and absolute Mach number at the impeller outlet are constrained, $M_{w,1t} < 1.3$ and $M_2 < 1.1$ respectively. This latter parameter is still consistent with unchoked operations since the vaneless gap between the impeller and the vaned diffuser can be properly sized to avoid the onset of sonic throats within the vaned-diffuser channel. Design variables for the optimizations are reported in table 4.3. The lower and upper bounds are based on aerodynamic and rotordynamic considerations, whose explanation can be found in several textbooks (see, e.g., Whitfield & Baines (1990); Ludtke (2004)). Preliminary optimization tests unveiled the presence of multiple local optima, thus excluding gradient-based optimization methods. Therefore, optimization problems are solved with genetic algorithms available in the

TABLE 4.3. Design variables for the optimization of centrifugal compressors.

Design Variable	**Lower bound**	**Upper bound**
$\phi = \dot{V}_1^t/(u_2\,D_2^2)$	0.02	0.09
ω	2000 rpm	100 000 rpm
$1 - D_{1h}^2/D_{1t}^2$	0.5	0.95
$\beta_{2,g}$	-70°	-10°
$\alpha_{3,g}$	65°	75°
b_2/D_2	0.03	0.08
D_{1t}/D_2	0.3	0.7
$[R_4\cos(\alpha_{4,g})]/[R_3\cos(\alpha_{3,g})]$	1	3

Optimization Toolbox of Matlab®. As these algorithms are meta-heuristic, five optimizations are performed for each inlet condition. The compressor design with the maximum objective-function value out of the five trials is ultimately selected.

Two compressor sizes are considered, induced by two representative values of the ingested mass-flow rate. According to Crespi *et al.* (2017*a*), the net specific work for a recompression cycle is typically in the range of 75 ÷ 175 kJ/kg. Considering as a spectrum of power 5 ÷ 50 MW, the turbine mass-flow rate is in the range of 70 ÷ 300 kg/s. As long as both the main compressor and the recompressor elaborate only a part of the total mass-flow rate, the analysis is performed for $\dot{m} = 50$ kg/s and $\dot{m} = 250$ kg/s. Mass-flow rates below $\dot{m} = 50$ kg/s are not considered, because the resulting compressor size would be so small to make the rotordynamics, sealing, and bearing features dominate over the aerodynamics. Finally, three representative pressure ratios $\beta_{TT} = P_5^t/P_1^t$ are investigated, namely 2, 3.5 and 5. Higher pressure ratios are excluded from the analysis because they lead to technically not-relevant maximum pressure (> 450 bar).

The maximum compressor efficiencies for the combination of selected pressure ratios, mass-flow rates, and inlet thermodynamic conditions are conveniently reported in the T–s diagram in figure 4.4. The efficiency fields indicate that a specific pattern connected to the inlet thermodynamic conditions cannot be easily recognized. Although at low pressure ratios a difference between low and high temperature is present, see figures 4.4(*a*) and 4.4(*d*), the variation is relatively low ($\approx$ 1 pp) and included in the computational uncertainty. Still, an opposite trend is observed in figure 4.4(*e*), where the compressor presumably works less efficiently when the inlet thermodynamic conditions are far from the critical ones. The present analysis, given the design assumptions, seems to suggest that the compressor-intake thermodynamic conditions have no relevant consequences on the achievable compressor efficiency, but comparable efficiencies can be obtained after a dedicated optimization task. The resulting optimized compressor layouts are shown for two representative intake conditions in figure 4.5, taking as a reference the smallest mass-flow rate. The first set of thermodynamic conditions ($T_1^t = 34$ °C, $P_1^t = 78.75$ bar, $\rho_1^t = 447.81$ kg/m^3) leads to a density which is approximately four times higher than the second one ($T_1^t = 145$ °C, $P_1^t = 74.00$ bar, $\rho_1^t = 105.4$ kg/m^3).

At first glance, the most evident geometrical difference lies in a bigger impeller-eye opening and volute to compensate for the overall lower density. However, a more careful inspection reveals that flow evolutions along the impeller meridional coordinate are relatively different. Compressors designed for upstream thermodynamic conditions far from the critical point show a sharper variation in the blade height across the impeller. In fact, when the volumetric variation ($\dot{V}_{5,is}/\dot{V}_1^t$) is considered, the first set of operating conditions shows 0.77 and 0.62 for $\beta_{TT} = 2$ and $\beta_{TT} = 5$, respectively. Conversely, the second set shows 0.59 and 0.32 for the same pressure ratios. The difference in the volumetric behaviour for the same pressure ratio can be explained

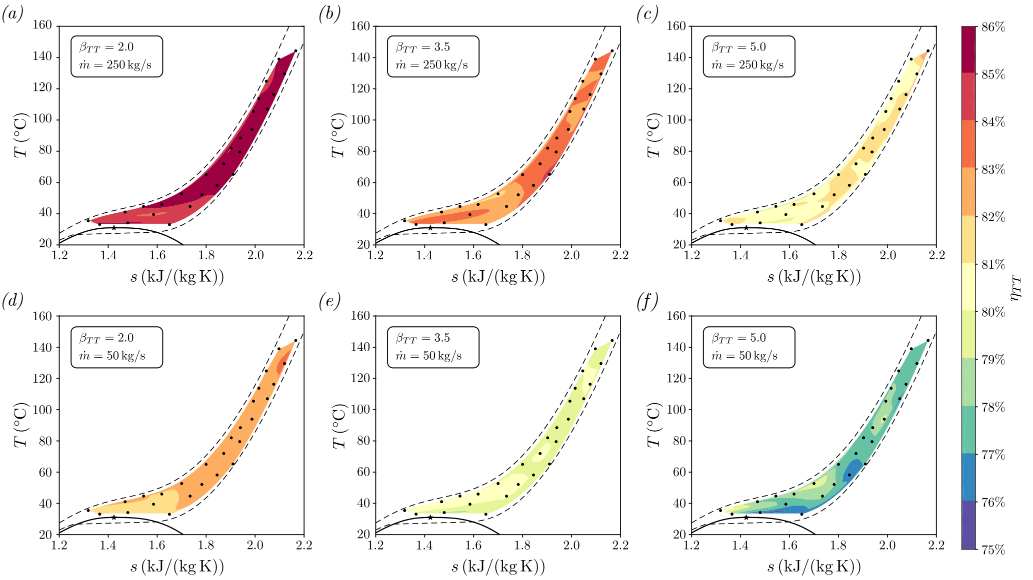

FIGURE 4.4. Compressor total-to-total efficiency η^c_{TT} contours on the T–s thermodynamic plane for different pressure ratios and mass flow rates. (- - -) minimum (70 bar) and maximum (100 bar) isobars; (•) inlet thermodynamic states on which the optimization is performed. (⋆) CO_2 critical point (T_c = 30.98 °C, P_c = 73.77 bar).

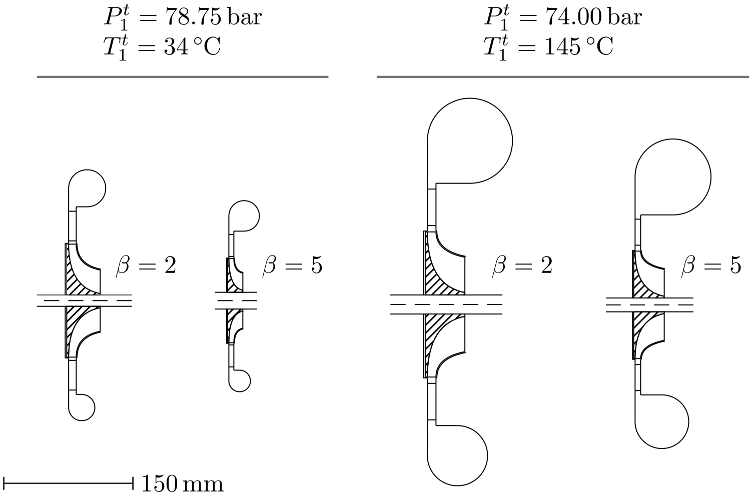

FIGURE 4.5. Optimal compressor layouts for different intake-fluid thermodynamic conditions. The mass-flow rate is 50 kg/s for all compressors represented in the figure.

only as a contribution of non-ideal effects, enhanced in the first case due to the proximity of the thermodynamic inlet conditions to the critical point. To be more specific, by comparing the previous results obtained for T^t_1 = 34 °C and P^t_1 = 78.75 bar with the ones obtained in the ideal-gas limit (i.e. low pressures and high temperatures), there is an underestimation of the volumetric variation of 24% for β_{TT} = 2, which increases to 53% for β_{TT} = 5. These errors have to be compared with the one made by using an ideal-gas model to estimate the flow evolution for the second set of inlet thermodynamic conditions, resulting in 0.7% for $\beta_{TT} = 2$ and 9% for $\beta_{TT} = 5$. It follows that accounting for non-ideal properties is crucial to obtain a reliable preliminary design of the machine when it operates in the neighborhood of the thermodynamic critical point. Moreover, this analysis demonstrates that the optimization of the mean-line code converges to the proper geometry by considering the meridional flow-path evolution. Finally, it is possible to achieve technically competitive compressor efficiencies, comparable to those obtained in more dilute conditions (where the ideal-gas behaviour is partially recovered), when designing representative full-scale compressors.

With reference to figure 4.4, the mass-flow rate (i.e. the compressor size) or the pressure ratio (i.e. the compressor loading) show larger effects on the compressor efficiency. On the one hand, the size reduction, e.g. from figure 4.4(a) to figure 4.4(d), causes a clear efficiency reduction ($\Delta\eta^{c}_{TT} \approx -2.5\,\mathrm{pp}$), due to the increase in the clearance- and leakage-loss relative weight. This efficiency decrement given by size effects ($\Delta\eta^{c}_{TT} \approx -2 \div 3\,\mathrm{pp}$) is found at each pressure ratio of the present analysis. On the other hand, by increasing the pressure ratio, hence the aerodynamic loading and its associated losses (e.g. blade loading and recirculation), the compressor efficiency drops about 2 pp as well. Moreover, the same qualitative behaviour given by a pressure-ratio variation is found for the two sets of mass-flow rates, not evidencing an explicit cross-dependency between aerodynamic loading and compressor size.

As far as optimal rotational speeds are concerned, they show a wide range of variation within the limits selected for the optimizations. To give an overview, the extreme cases are considered, i.e. the smallest highly-loaded compressor ($\dot{m} = 50\,\mathrm{kg/s}$, $\beta_{TT} = 5$) and the largest slightly-loaded compressor ($\dot{m} = 250\,\mathrm{kg/s}$, $\beta_{TT} = 2$). The former features optimal rotational speeds in the order of $60\,000 \div 80\,000$ rpm within the investigated thermodynamic ranges, while the latter shows comparatively smaller values and range ($10\,000 \div 20\,000$ rpm). The imposition of a lower rotational speed, for example employing a single-shaft configuration, would presumably result in a much smaller compressor efficiency with respect to those reported in this work. Finally, for all examined cases, the peripheral velocity is found to be lower than 500 m/s, thus limiting eventual issues related to the mechanical integrity.

4.4 Correlations for turbomachinery efficiency at design conditions

Based on mean-line estimates, efficiency correlations to be included in the cycle analysis are devised. The analysis is initially limited to single-stage turbomachinery, since the relatively limited pressure ratio of interest to sCO$_2$ cycles ($\sim 2 \div 5$) can be allocated efficiently in a single-stage configuration for both centrifugal compressors and axial turbines, thus guaranteeing a relevant technical simplification. If the cycle is intended for power capacity higher than approximately 100 MW, multi-stage turbomachinery becomes the only viable choice capable of elaborating the large flow rates while exhibiting comparatively higher component efficiencies. In the last section of the paper, an extension to multi-stage architectures is discussed, still focusing on relatively small power targets.

Recalling the approach of Macchi & Perdichizzi (1981), both compressor and turbine efficiencies are expressed as a function of two independent similarity parameters. The selected parameters are the pressure ratio β, which accounts for machine loading, and the size parameter SP, which includes the size effect. As a matter of fact, self-similarity in Reynolds number can be assumed, since the Reynolds number exceeds 10^7 for both the machines in the conditions of interest. Besides, the impact of the fluid thermodynamics on the design efficiency is neglected as the optimal turbomachinery efficiency was demonstrated not to depend on the intake conditions. Finally, as the correlations are calibrated on already optimized turbomachinery, a parameter accounting for the rotational speed is not needed (Macchi & Astolfi, 2017) (turbomachinery are supposed to work at their optimal rotational speed). It follows that the implementation of these correlations to estimate optimized turbomachinery efficiencies within cycle routines implicitly assumes that each turbomachinery rotates at its own optimal rotational speed on separate shafts. Size parameter SP and the pressure ratio β are declined differently whether they refer to the compressor or to the turbine:

$$\text{compressor:} \quad \beta_c = \frac{P^t_{out}}{P_{T,in}} \qquad SP_c = \frac{\sqrt{\dot{V}^t_{in}}}{\Delta h_{is}^{0.25}} \tag{4.3}$$

$$\text{turbine:} \quad \beta_t = \frac{P^t_{in}}{P_{out}} \qquad SP_t = \frac{\sqrt{\dot{V}_{out,is}}}{\Delta h_{is}^{0.25}} \tag{4.4}$$

where the superscript t stands for total quantities, while the subscript is indicates that the quantity is obtained through an isentropic process.

These two parameters allow for a straightforward implementation within cycle routines, without significantly increasing the computational cost. Different analytical formulations (exponential, cubic, quadratic, polynomial) were tried to properly interpolate the evolution of turbomachinery efficiencies when the size parameter and the pressure ratio are varied. Eventually, the simple yet effective polynomial formulation is selected,

$$\eta = a\, SP^b + c\, \beta^d + e, \tag{4.5}$$

where a, b, c, d, e are determined via a least-square regression of optimized turbomachinery designs. For both the correlations, the maximum deviation between the predicted and the actual (as provided by the mean-line optimization) value is reported. Moreover, the coefficient of determination R^2, whose standard definition is reported as follows, is evaluated for both cases.

$$R^2 = 1 - \frac{\sum_{i=1}^N (\eta_i - \hat{\eta}_i)^2}{\sum_{i=1}^N (\eta_i - \overline{\eta})^2}, \tag{4.6}$$

where N is the number of optimized designs considered for the correlation fitting, η_i are the efficiency values provided by the mean-line code optimization, $\overline{\eta}$ is their mean value and $\hat{\eta}_i$ are the values predicted by the correlation.

4.4.1 Compressor efficiency correlation

The centrifugal-compressor efficiency correlation is formulated by including all the optimal compressor designs presented in Section 4.3, consisting of overall $N = 156$ designs. About 8% of the optimal compressor pool exhibits a discrepancy of $1.0 \div 2.0$ pp with respect to the predicted efficiency value. These deviations are considered acceptable because they are within the uncertainty range of the mean-line tool. One outlier ($|\eta - \hat{\eta}| = 3$ pp) is noticed and excluded a posteriori from the fitting. The final compressor-efficiency correlation, reported graphically in figure 4.6, reads as:

$$\eta_c = 0.4649\, SP_c^{0.8033} - 0.0183\, \beta_c^{0.8870} + 0.8298 \tag{4.7}$$

The validity ranges for such correlation are $2 \leqslant \beta_c \leqslant 5$ and $0.020\,\text{m} \leqslant SP_c \leqslant 0.080\,\text{m}$. The coefficient of determination is $R^2 = 0.87$. Reasonably, the predicted efficiency can be clipped for $SP_c > 0.080\,\text{m}$, assuming that size effects are going to vanish as compressor size increases.

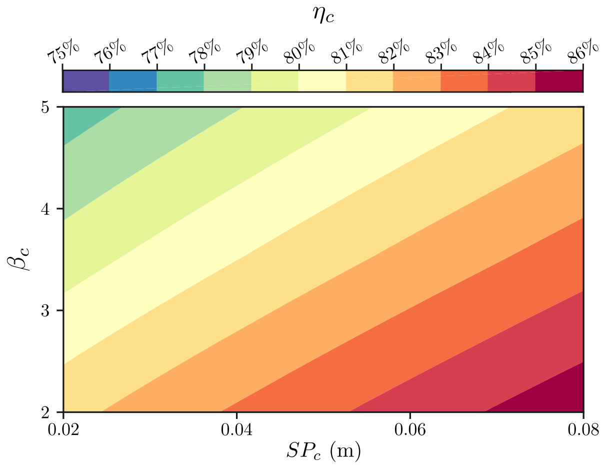

FIGURE 4.6. Compressor total-to-total efficiency η^c_{TT} as a function of size parameter SP_c and pressure ratio β_c.

TABLE 4.4. Design variables for the optimization of single-stage axial turbine.

Design Variable	**Lower bound**	**Upper bound**
ω	2000 rpm	100 000 rpm
$\alpha_{1,g}$	65 °	78 °
$c_{ax,s}$	20 mm	100 mm
$\beta_{2,g}$	65 °	78 °
$c_{ax,r}$	20 mm	100 mm
b_0	10 mm	50 mm
b_0/D_m	0.025	0.25
r	0	0.8

4.4.2 Turbine efficiency correlation

Before illustrating the turbine-efficiency correlation, the optimization set-up is discussed. Some design assumptions are made in this context: (i) axial flow at the stator inlet; (ii) constant mean diameter; (iii) the stator-rotor axial distance is set as 0.5 of the stator axial chord; (iv) trailing-edge thickness-to-throat opening ratio is set at 0.1 for both stator and rotor; (v) stator hub and rotor tip clearances are equal to 0.5 mm. Design variables are instead reported in table 4.4. As for compressor optimizations, lower and upper bounds are chosen accordingly to aerodynamic and mechanical considerations available in the open literature.

The objective function is the maximization of machine efficiency, which is generally coded in zTurbo as:

$$\eta^t_{T\chi} = \frac{l_{eul}}{h^t_1 - h_{3,is} - \chi v_3^2/2} \tag{4.8}$$

Depending on how much kinetic energy $v_3^2/2$ is recovered downstream of the turbine, different efficiency formulations are possible. It is assumed that a diffuser is installed downstream of the turbine, recovering 50% of the residual kinetic energy, hence $\chi = 0.5$ is used for the turbine efficiency hereinafter.

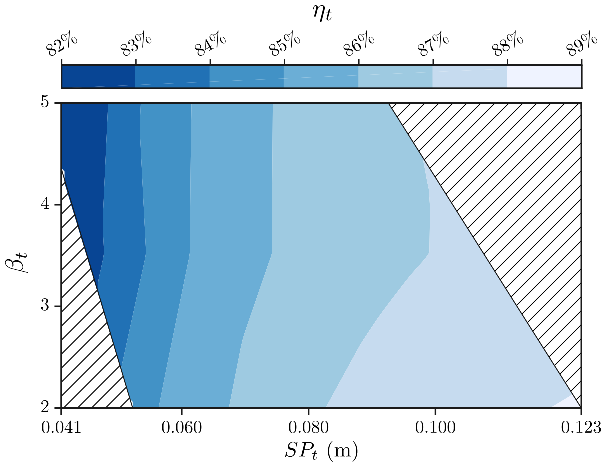

FIGURE 4.7. Turbine efficiency $\eta^t_{T\chi}$, with $\chi = 0.5$, as a function of size parameter SP_t and pressure ratio β_t. The correlation is not valid within dashed areas.

The objective function accounts for different penalties if some design constraints are not satisfied. In particular, the following constraints are imposed: (i) the flaring angle, both for the stator and the rotor, cannot exceed $\pm 15°$; (ii) the absolute Mach number downstream of the stator M_1 has to be lower than 1.35 (eventually relying on supersonic post-expansion, which becomes too inefficient for $M_1 > 1.4$); (iii) the peripheral speed at midspan cannot exceed 500 m/s. The expected presence of multiple local maxima drives the choice of the optimization algorithm towards meta-heuristic methods as for the compressor optimizations. To reduce the possible stochastic scatter given by meta-heuristic methods, each optimization is run twice and the best design in terms of highest turbine efficiency is selected.

As the turbine-intake thermodynamic conditions in the range of interest for sCO$_2$ power systems are not expected to trigger peculiar non-ideal effects, a comparatively lower number of optimizations is performed. $N = 36$ optimal designs are identified in the range of $\dot{m} = 50 \div 250$ kg/s, $T_{T0} = 550 \div 750$ °C and $\beta_t = 2 \div 5$. Additional optimizations are run for $\dot{m} > 250$ kg/s, evidencing no efficiency variations given the other two parameters constant. For all turbine designs, the reaction degree r, defined as in table 4.4, results in approximately 0.5. At the lowest mass-flow rate, i.e. $\dot{m} = 50$ kg/s, the rotational speed is found at its upper limit (100 000 rpm), suggesting that the optimal rotational speed may be beyond that value. All other optimal designs are characterized by rotational speeds between 20 000 ÷ 95 000 rpm, typically higher than their compressor counterparts. If a single-shaft compressor-turbine configuration is desired, a trade-off on the rotational speed should be made, compromising at least one out of two machine efficiency.

As in the previous section, the turbine-efficiency correlation is obtained by fitting the efficiency of these representative 36 optimal designs. The maximum deviation between the mean-line efficiency and the predicted value is below 1 pp for all examined cases. No outliers are found. The coefficient of determination is $R^2 = 0.96$. The analytical expression reads as:

$$\eta_t = -0.0003\, SP_t^{-1.7107} + 5.0665\, \beta_t^{-9.7428} + 0.8858 \tag{4.9}$$

whose validity range is reported in figure 4.7. The correlations can be clipped for size parameters SP beyond the upper limit, as optimization tests for higher flow rates demonstrated self-similarity for size effects.

4.5 SCO$_2$ cycle optimizations including tailored efficiency correlations

A dedicated analysis on sCO$_2$ cycle optimizations, including proper modelling of turbomachinery efficiencies, is now presented. The investigation is limited to the recompression sCO$_2$ cycle at full-load condition, whose layout is reported in figure 4.8. However, since the backbone of sCO$_2$ power cycles is invariant among different layouts, the present findings are expected not to be limited to the cycle arrangement here considered. Among the large number of cycle arrangements (see, for a review, Crespi *et al.*, 2017*b*), the recompression cycle provides high efficiency and a comparatively simple layout. The presence of an internal heat recuperation allows retrieving the residual thermal energy at the turbine outlet to preheat the compressed fluid, thus reducing both the heat input and the heat rejected to the environment. To cope with the strong variation of the fluid specific heat in the cold side, the recuperative process is split into two units operating with different mass-flow rates. In this way, it is possible to optimize the temperature profiles between hot and cold sides by acting on the thermal capacity of the cold side, so that the entropy generated by finite-temperature differences in the heat-transfer process is reduced. In this work, heat exchangers, both the primary heat exchanger and recuperators, are simulated with a one-dimensional approach, splitting the overall heat-transfer problem into several sub-problems whereby the fluid properties are assumed constant. A finite pinch-point temperature difference $\varDelta T_{pp}$ is provided for each heat exchanger, to avoid the occurrence of negative pinch-point temperature difference when the split factor, $SF = \dot{m}_{LTR}/\dot{m}$, i.e. the ratio between the mass flow in the low-temperature regenerator (LTR) and the overall mass flow, is varied. A dedicated routine checks where the pinch-point occurs within LTR, as the cooling process is strongly non-linear due to the significant variation of CO$_2$ specific heat in the range of interest. Based on previous works (Astolfi *et al.*, 2018), a 10 °C is imposed as a pinch-point temperature difference in the heat exchangers and a relative pressure drop $\varDelta p/p_{in} = 2\%$ is considered for all heat exchangers as well. The heat input is provided by a hot source at a constant temperature. Electric (both for generator and motors) and mechanical efficiencies are set at the constant value of 97% (Astolfi *et al.*, 2018). Turbomachinery components are implemented either at constant isentropic efficiency or with dedicated efficiency correlations, detailed in §4.4. For each cycle, maximum and minimum pressures, along with the split factor, are varied to obtain the highest electrical efficiency, defined as $\eta_{el} = \dot{W}_{el}/\dot{Q}$, where $\dot{W}_{el}$ is the electrical power and $\dot{Q}$ is the thermal power input. To this end, a hybrid optimization routine is used, combining a genetic-based algorithm to initialize a gradient-based method. Figure 4.8 also reports the typical transformations on temperature–specific entropy (T–s) thermodynamic plane, fixing the cycle minimum temperature $T_{min} = 35$ °C and the hot-source temperature $T_{max} = 550$ °C and assuming isentropic transformations for the turbomachinery in the cycle visualization.

Having identified the main assumptions behind the model of the power cycle, the main goal of this study is to analyze the impact of the turbomachinery efficiencies on cycle performance estimates; in particular, the proposed correlations are compared to the standard assumption of taking fixed turbomachinery efficiencies. The assessment is carried out in a parametric way, by changing the hot-source temperature (T_{max}), the cycle minimum temperature (T_{min}), and the net power output ($\dot{W}_{el}$). Varying the cycle pressure ratio (i.e. ratio between cycle maximum and minimum pressure) within the range of validity of the proposed correlations (i.e. $\beta = 2 \div 5$), the sCO$_2$ cycle is optimized in terms of cycle electrical efficiency, taking as design variables the minimum pressure and the split factor. Note that each turbomachinery features slightly different pressure ratios as a consequence of the pressure drops occurring in the heat exchangers.

Three turbomachinery models are tested: (i) constant-turbomachinery efficiencies $\eta_t = 0.90$ and $\eta_c = 0.86$; (ii) constant-turbomachinery efficiencies $\eta_t = 0.86$ and $\eta_c = 0.82$; (iii) turbomachinery-efficiency correlations $\eta = f(SP, \beta)$, as formulated in Section 4.4. The first set of constant efficiencies represents relatively optimistic designs and they are approximately comparable with

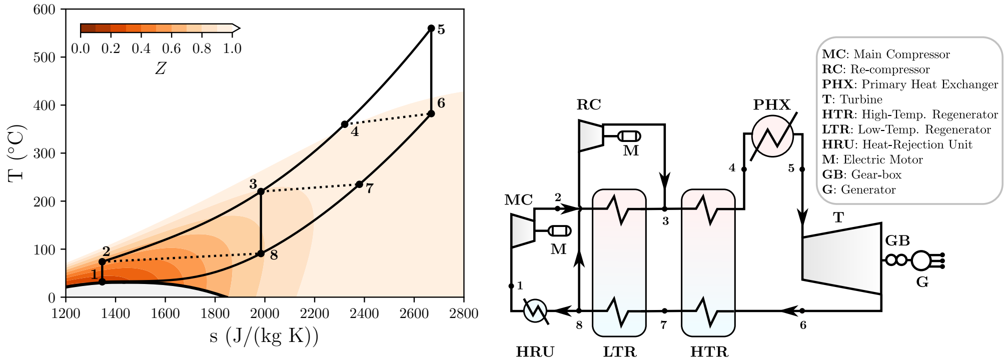

FIGURE 4.8. Recompression sCO_2 cycle layout and corresponding thermodynamic transformations on T–s plane. A map of the compressibility factor $Z = Pv/RT$ is superposed.

values presently adopted for gas-turbine applications. On the other hand, the second set exhibits more realistic values, taken approximately as the mean values provided by the correlations given in equations (4.7) and (4.9).

First, the hot-source temperature is changed and the associated variations on cycle performance are analyzed by employing different fidelity models for the turbomachinery components. The cycle minimum temperature and the power size are set constant at $T_{min} = 35\,°\text{C}$ and $\dot{W}_{el} = 25\,\text{MW}$, respectively. Two maximum temperature values are considered, namely $T_{max} = 550\,°\text{C}$ and $T_{max} = 750\,°\text{C}$. The results of this analysis are illustrated in figure 4.9(a). Qualitatively, the efficiency trends for both hot-source temperatures are similar. From a quantitative perspective, instead, there is ≈ 10 pp-difference in the efficiency value between the lowest and the highest hot-source temperature. This difference is expected as the maximum temperature has a significant influence on the overall cycle efficiency. When $\beta = 2$, the optimized electrical efficiency including turbomachinery-efficiency correlations is similar to the one predicted with the first set of constant-turbomachinery efficiencies (i.e. $\eta_t = 0.90$ and $\eta_c = 0.86$). Coherently, at low pressure ratio and moderate power size, the predicted turbomachinery efficiencies from the two models are found comparable. Nevertheless, as long as the pressure ratio increases, the discrepancy between the two models increases as well. Constant-efficiency models only show the thermodynamic impact of the pressure ratio on the cycle, without accounting for the impact of the increased aerodynamic loading on the turbomachinery performance. At about $\beta = 3.5$, turbomachinery efficiencies predicted via correlations are approximately equal to the second set of constant-efficiencies ($\eta_t = 0.86$ and $\eta_c = 0.82$). At a higher pressure ratio, the efficiency penalty increases, and the overall cycle efficiency starts decreasing, evidencing a maximum in the curve $\eta_{el}(\beta)$ for both the hot-source temperatures. In absence of proper correlations for the turbomachinery efficiency, the maximum is not captured at the highest hot-source temperature, while a slight reduction of electrical efficiency can be appreciated at the lowest maximum temperature. However, for this latter case, the reduction in the cycle performance is only given by the smaller fraction of residual heat available at the turbine outlet, which affects the recuperative process, and not also by the deterioration of turbomachinery performance. Indeed, the cycle efficiency drop is more pronounced when turbomachinery-efficiency correlations are employed, because two effects (lower turbomachinery efficiency and worse recuperative process) couple to decrease the cycle efficiency. An increase of the maximum temperature hides the second effect when $\beta < 5$, resulting not only in a quantitative overestimation of the overall cycle efficiency but also in a wrong trend prediction when constant efficiencies are assumed. At the highest pressure ratio, which represents the worst-case scenario

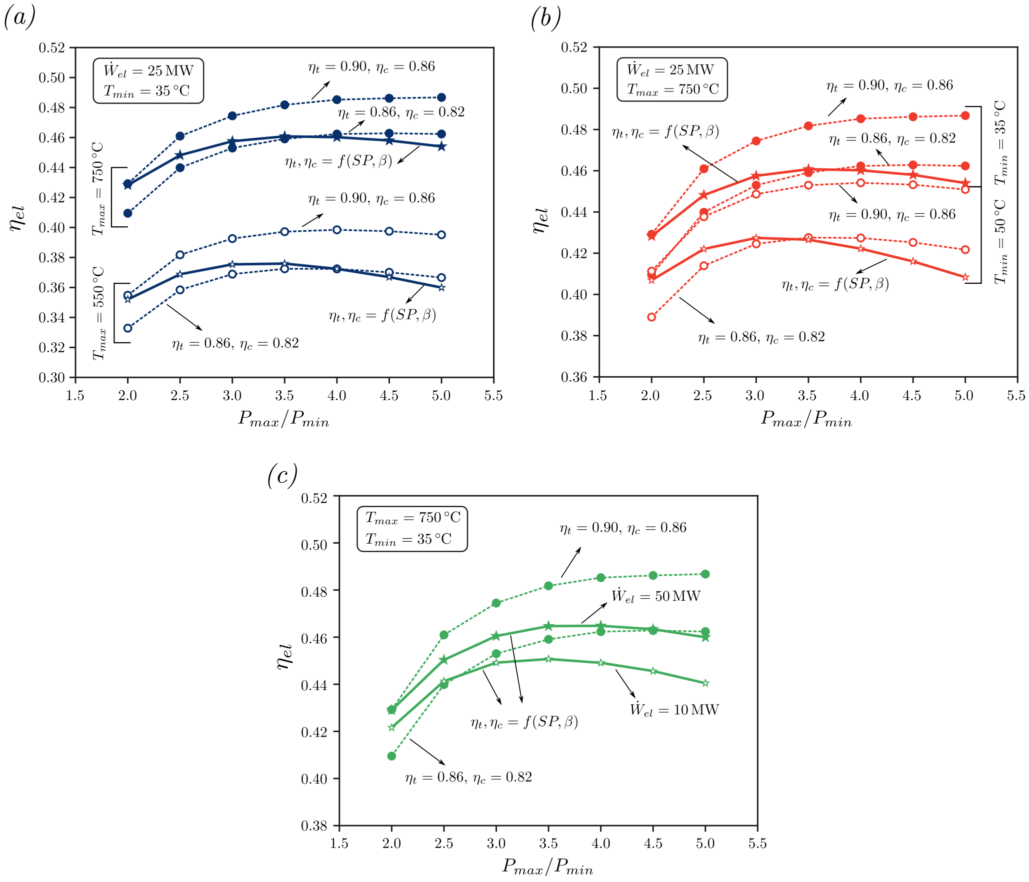

FIGURE 4.9. Parametric assessment of cycle efficiency η_{el} evolution as a function of the cycle pressure ratio P_{max}/P_{min} by changing the hot-source temperature (a), the minimum temperature (b) and the installed power capacity (c).

where larger efficiency differences are found, cycle efficiency is overestimated of about 1.0 pp and 4.0 pp by employing the two set of constant efficiencies with respect to the prediction provided by using correlations.

Figure 4.9(b) shows the effect of the minimum temperature, by keeping constant the hot-source temperature and the power capacity at $T_{max} = 750\,°\mathrm{C}$ and $\dot{W}_{el} = 25\,\mathrm{MW}$, respectively. The main trend of electrical efficiency is qualitatively similar to the ones observed in the previous analysis. When the minimum temperature increases, the overall lower cycle efficiency is associated with the higher compression work required by the main compressor. This latter evidence can also explain why the optimal pressure ratio is different for the two cases when the efficiency correlations are used. Indeed, the reduction of the main-compressor efficiency given an increase of the pressure ratio affects more the cycle efficiency, as a consequence of the larger work required to compress CO$_2$ far from the critical point.

Finally, the implications of a small power capacity on the cycle efficiency are illustrated in figure 4.9(c). It compares the variation of cycle efficiency with the pressure ratio for two representative plant capacities, namely 10 MW and 50 MW. The minimum and maximum temperature are equal to $T_{min} = 35\,°\mathrm{C}$ and $T_{max} = 750\,°\mathrm{C}$. By applying constant efficiency for the turbomachinery, the cycle performance is not dependent on the plant size; indeed, cycle routines can be equivalently formulated in terms of specific quantities. On the other hand, considering the performance of turbomachinery within the cycle routines, appreciable differences are found. The smaller plant size has an efficiency which is lower of around 1 pp at small pressure ratio up to 2 pp when $\beta = 5$ if compared to the larger plant capacity. This efficiency deviation between the two plant capacities is only related to the corresponding turbomachinery size, accounted in the size parameters within the correlations (see equations (4.7) and (4.9)).

In all these studies, the plant efficiency is found to be more sensitive to variations in the turbine efficiency rather than in the compressor ones (both main and recompressor), as already pointed out by Allison *et al.* (2017). This is due to the larger enthalpy variation that occurs within the turbine, which weights more in the overall efficiency estimate. Moreover, the more the compressor operates close to the critical point, the smaller the enthalpy rise, the less important the compressor efficiency from a cycle perspective.

To sum up, for all the investigated parametric cases, a noticeable difference is found in the prediction of cycle efficiencies and of optimal pressure ratios, when proper turbomachinery modelling is included in the cycle analyses. A set of constant efficiencies, which may be of general validity and can provide comparably accurate results (i.e. within 2 pp with respect to the correlations) for all examined ranges, i.e. $T_{max} = 550 \div 750\,°\mathrm{C}$, $T_{min} = 35 \div 50\,°\mathrm{C}$ and $\dot{W}_{el} = 10 \div 50\,\mathrm{MW}$, seems not to be available.

4.5.1 Potential efficiency gain employing multi-stage turbomachinery

Up to this point, the investigation on cycle performance was limited to single-stage turbomachinery. However, multi-stage arrangements might exhibit higher efficiencies as a consequence of the reduced aerodynamic loading at high cycle pressure ratio and/or in connection to technological constraints in terms of angular or peripheral speed. The aim of this subsection is to assess the potential efficiency gain achievable through multi-stage turbomachinery with respect to single-stage configurations.

To this end, several optimizations, for both two-stage centrifugal compressors and axial turbines, are performed for a discrete number of pressure ratios and size parameters. The optimization algorithm, as well as the optimization set-up in terms of objective functions, constraints, and design variables, recalls the one discussed for the optimizations of the corresponding single-stage layout. The geometrical design variables, see Tables 4.3 and 4.4 for compressors and turbines, respectively, are doubled (one group for each stage), while the same rotational speed is considered for both stages. Besides, the pressure-ratio distribution between the two stages is also optimized, retaining that their product must satisfy the overall prescribed pressure ratio. As far as the multi-stage centrifugal compressor is concerned, the crossover bend and the return vane channel, which deswirles the flow before entering into the next impeller, deserve appropriate considerations. Under the assumption of zero vane incidence, which is reasonable at design conditions, a total-pressure loss coefficient is considered, defined as $(P_{T,in} - P_{T,out})/(P_{T,in} - P_{in})$ equal to 0.25 for both components, and a pressure-recovery coefficient, i.e. $(P_{out} - P_{in})/(P_{T,in} - P_{in}) = 0.45$, for the return vane channel only (Ludtke, 2004). At the exit of the second stage, a volute is prescribed as in the single-stage configuration. On the other hand, the extension to a two-stage axial turbine is less complex and it does not require additional components to be modelled.

The optimized two-stage machine performance is reported in figure 4.10 for selected conditions of pressure ratio and size parameter in terms of efficiency deviation $\Delta\eta$; this latter is defined as the difference between the two-stage optimized efficiency and the value provided by the correlations given in equations (4.7) and (4.9) for single-stage compressors and turbines, respectively.

Upon examination of the figure 4.10(a), which reports the compressor-efficiency deviation, the application of two-stage compressors for $\beta_c < 3$ provides lower efficiency if compared to the

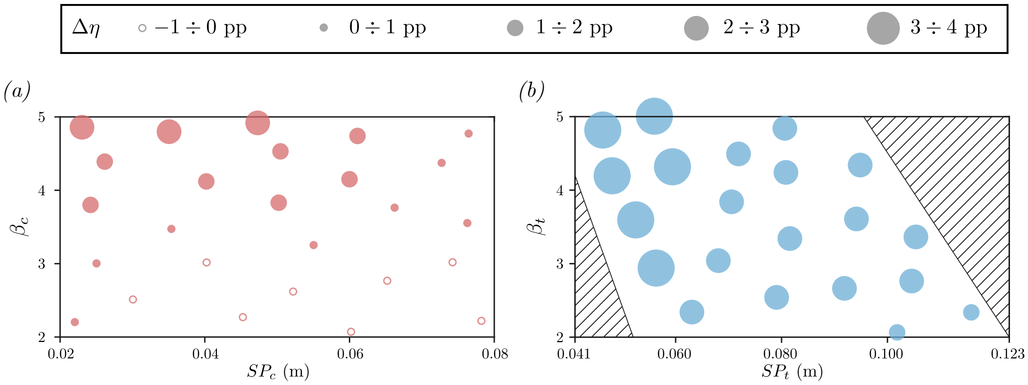

FIGURE 4.10. Efficiency deviation $\Delta\eta$ between dedicated optimizations of two-stage machines and predicted efficiencies by single-stage correlations for compressors (*a*) and turbines (*b*).

corresponding single-stage configuration. Indeed, for these values of pressure ratio, a reduction in the aerodynamic loading and in its associated losses does not compensate the additional losses introduced by the crossover bend and the return vane channel. Otherwise, as long as the pressure ratio increases ($\beta_c > 3$), a positive efficiency gain is provided by the multi-stage solution, achieving up to $\Delta\eta_c = 2.0 \div 2.5$ pp at small size parameters ($SP_c < 0.05$ m) and high pressure ratio ($\beta_c > 4.5$).

On the other hand, a two-stage turbine prevails over the single-stage layout for all the pressure ratios, as illustrated in figure 4.10(*b*). Moreover, the efficiency gain provided by a multi-stage turbine is comparatively higher than the efficiency gain achievable by multi-stage compressors. With the exception of few designs located at high size parameters ($SP_t > 0.10$ m) and low pressure ratio ($\beta_t < 2.5$), featuring an increase of about $\Delta\eta_t = 1.0 \div 1.5$ pp, the larger part of the mapped region exhibits a net increase of $\Delta\eta_t = 2 \div 3$ pp, which is extremely relevant as cycle performance are more affected by an increase in the turbine efficiency than that in the compressor (Allison *et al.*, 2017). Furthermore, for the lowest size-parameter values, i.e. $SP_t < 0.06$ m, the efficiency gain raises to $\Delta\eta_t = 3 \div 4$ pp. For such optimized designs, the single-stage configuration converges to high values of rotational speed, close to the upper bound imposed in the optimization routine (see table 4.4); the high peripheral speed required to obtain the work exchange combined with a limited angular speed result in relatively large mean diameter, thus implying a comparably small blade aspect ratio b/D_m. Relying on a multi-stage architecture, the aerodynamic loading on each stage is reduced, so that a smaller peripheral velocity is required. As a consequence, the optimization can find optimized machine designs which feature comparatively lower rotational speeds and higher blade aspect ratio, thus considerably reducing the weight of the secondary and, especially, of the leakage losses. A further increase in the number of stages, without additional constraints on the rotational speed, is expected to produce a significantly lower rise in the turbomachinery efficiency, as most of the losses, e.g. related to the blade loading and to the aspect ratio, are already minimized in the two-stage setup.

These optimized two-stage turbomachinery designs are used to formulate a correction for the correlations previously developed. To this end, a linear regression is used, exhibiting a coefficient of determination $R^2 = 0.75 \div 0.80$ for both the compressor $\Delta\overline{\eta}_c$ and the turbine $\Delta\overline{\eta}_t$ correction. The maximum deviation between the linear model prediction $\Delta\overline{\eta}$ and the actual deviation $\Delta\eta$ (as in the figure 4.10) is 0.75 pp and 0.50 pp for the compressor and the turbine, respectively, which are within the corresponding mean-line code errors. The analytical expressions for the linear

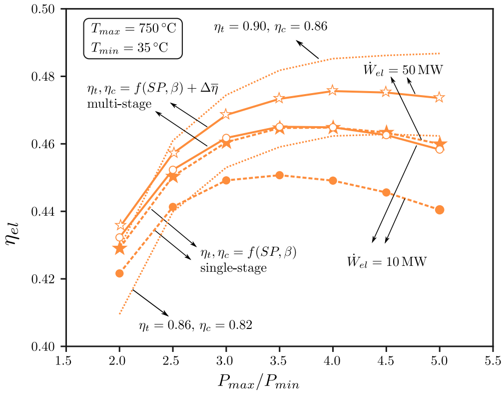

FIGURE 4.11. Cycle efficiency η_{el} evolution as a function of the cycle pressure ratio P_{max}/P_{min} for two installed power capacities by employing single- and multi-stage turbomachinery. Dotted lines: constant turbomachinery efficiencies. Dashed lines: efficiency correlations for single-stage turbomachinery. Solid Lines: efficiency correlations for multi-stage turbomachinery.

corrections are:

$$\Delta\bar{\eta}_c = -0.15172\,SP_c + 0.00577\,\beta_c - 0.00671 \tag{4.10}$$

$$\Delta\bar{\eta}_t = -0.20126\,SP_t + 0.00006\,\beta_t + 0.04447 \tag{4.11}$$

where the subscript c refers to the compressor, whilst the subscript t refers to the turbine. These corrections have to be added to the single-stage machine correlations (refer to equations (4.7) and (4.9) for compressor and turbine, respectively) to obtain the two-stage machine efficiency.

The corrected correlations are used to infer the potential cycle-efficiency gain brought by multi-stage turbomachinery, as illustrated in figure 4.11. If a multi-stage solution performs worse than the corresponding single stage, i.e. $\Delta\bar{\eta} < 0$, the single-stage layout is considered for the selected cycle pressure ratio even in the multi-stage calculations. Two power-capacity targets are considered, namely $\dot{W}_{el} = 10\,MW$ and $\dot{W}_{el} = 50\,MW$ at fixed minimum and hot-source temperature, i.e. $T_{min} = 35\,°C$ and $T_{max} = 750\,°C$, respectively. Even at the smallest pressure ratio $\beta = 2$, the turbine-efficiency increase given by the multi-stage solution induces a substantial rise in the cycle efficiency, which results in +0.6 pp and +1.0 pp for high and low power capacity, respectively. As long as the pressure ratio increases, the marginal cycle improvement increases as well, achieving +1.2 pp and +1.8 pp at $\beta = 5$ for high and low power capacity, respectively. However, the expected efficiency gain given by a multi-stage turbomachinery arrangement must deal with the capital-cost increase, thus a trade-off between the increase of cycle performance and the plant cost has to be found. An optimum pressure ratio in the range $\beta = 2 \div 5$ also exists for multi-stage configurations, conversely to what predicted by the constant-efficiency assumption. Furthermore, significant quantitative differences between the efficiency predicted by the corrected correlations and the constant-efficiency assumption emerge, proving that this latter assumption is not suitable even when multi-stage arrangements are considered.

4.6 Computational methods for compressible non-ideal two-phase flows

The mean-line formulation neglects an important feature of sCO_2 compressors operating in near-critical conditions, namely the potential onset of a two-phase flow regime, which becomes increasingly more important at off-design conditions. As well known, within the turbocompressor the flow undergoes severe accelerations that generate sudden local expansions, and the local thermodynamic state may fall below the saturation curve. If such a condition persists for a sufficient amount of time, then the fluid can ultimately change phase, then setting the ground for two-phase flow operation within the compressor. Analogous flow features can also occur in other flow devices, which include (not exclusively) supersonic ejectors for refrigeration and valves. Interestingly, research activities in this field may also improve the economic feasibility of carbon capture and sequestration (CCS) technologies, e.g. by reducing the power consumption required by compressors or by increasing compressor operability (Lettieri *et al.*, 2014).

Depending on the entropy level of the intake supercritical condition, the phase transition might lead to the formation of either vapour (when $s < s_c$) or liquid (when $s > s_c$); in other words, expanding from a general supercritical state either cavitation (liquid $\mapsto$ vapour) or condensation (vapour $\mapsto$ liquid) can take place in compressors for closed power cycles, depending on the cycle configuration, the thermodynamic optimization, and the full-/part-load strategy of the plant. In all these flow devices the phase transition occurs within streams of high-speed fluid; the available experiments (see, for example, the visualization published in Lettieri *et al.* (2017)) indicate that the new phase (composed by either droplets or bubbles) appears dispersed into the main one, without evident interfaces between the phases. The onset of a dispersed phase is typically associated with a sudden drop of the speed of sound, which is comparably lower than that of the fluid in either of the saturated condition. As a result, the onset of two-phase flows is associated with a sudden increase of the Mach number of the stream, promoting the establishment of supersonic flows, shock waves, and choking with respect to single-phase flows of the same fluid (Bartosiewicz, 2013). In this context, a proper computational modeling of cavitation and condensation phenomena in sCO_2 compressible flows, and their subsequent implications on the flow morphology and on the thermodynamics of the process, is crucial for the design of sCO_2 devices and, ultimately, for the technical feasibility and market penetration of the entire sCO_2 energy technology.

Two-phase flows were the object of theoretical, computational, and experimental studies in the last decades; historically, the vast majority of these studies were focused on water for cavitation in pumps (Tan *et al.*, 2015) and valves (Diener & Schmidt, 2004, 2005), on cryogenic fluids for rocket turbopumps (Hosangadi & Ahuja, 2005; Zhu *et al.*, 2020) and on steam for condensation in turbines (Young, 1992; Grübel *et al.*, 2015; Schatz *et al.*, 2015). The outcome of these studies is best summarized in the excellent book of Brennen (2005), which provides a rigorous and comprehensive presentation of two-phase flows, with emphasis on both the physical and modelling perspectives. With reference to Brennen's classification, the so-called *two-fluid model* appears to be the most computational-effective formulation to model the dispersed phase transitions of interest in this work. In the so-called two-fluid model, the dispersed phase is considered mixed from an Eulerian perspective with the main phase in a unique continuous fluid, whose mean properties are defined on the basis of proper volume or mass averages of the corresponding single-phase properties. Even within this modeling framework, several alternative sub-models were proposed in the scientific literature to treat the generation of the dispersed phase and the interaction between the phases.

The typical short time-scale of the process might allow the supercritical fluid to expand below the saturation limit without incurring a phase change, reaching the so-called meta-stable state. Meta-stable states might exist within limited thermodynamic regions, comprised between the saturation curve (representative of the phase transition under thermodynamic equilibrium) and the spinodal curve (limit of the meta-stable equilibrium). Experiments for wet steam (Gyarmathy, 2005) and, recently, for sCO_2 (Lettieri *et al.*, 2017) indicate that in high-speed flows the transition occurs delayed with respect to the saturation line, thus proving the existence of meta-stable states, albeit in limited regions of the flow. When the two phases are established, velocity and temperature differences might arise between the phases, promoting mechanical and/or thermal non-equilibrium.

De Lorenzo *et al.* (2017*b*) reviewed the most relevant two-fluid models, classified them with respect to the character of non-equilibrium phenomena to be represented in the solution, and proposed a class of novel one-dimensional analytic solutions of two-phase flows in nozzles.

Such rich scientific background allows us to provide a classification of the most relevant models available for the prediction of cavitating/condensing high-speed flows, which could also be applied in presence of sCO_2 flows:

- the *homogeneous equilibrium model* (HEM), which excludes meta-stable states and assumes mechanical and thermal equilibrium between the phases;
- the *non-homogeneous equilibrium model* (NEM), which excludes meta-stable states and assumes thermal equilibrium between the phases, but allows for the existence of a relative velocity between the two phases;
- the *homogeneous frozen model* (HFM), which assumes mechanical equilibrium, but neglects the heat exchange between the phases;
- the *non-homogeneous frozen model* (NFM), which assumes neither mechanical nor thermal equilibrium;
- the *delayed equilibrium model* (DEM), which allows for the existence of meta-stable states (by considering a third phase, besides the saturated liquid and vapour, composed by the supersaturated supercritical fluid), and only considers mechanical equilibrium between the phases.

Brennen (2005) and De Lorenzo *et al.* (2017*b*) successfully applied these models in simple geometric configurations like ducts and nozzles, where quasi-one-dimensional analytical solutions provide a technically relevant representation of the flow. However, to pursue the thermofluid-dynamic design of the technical devices of interest for sCO_2 technology, the aforementioned models have to be reformulated in order to be implemented in a multi-dimensional computational fluid-dynamic (CFD) framework. Examples of two-phase models implemented in the frame of CFD tools are reported in Bartosiewicz *et al.* (2006) and Dang Le *et al.* (2018), mainly focusing on water cavitation. With respect to such studies, the supercritical condition of CO_2 complicates the thermodynamic modeling of the single phases, besides the inherent complication associated with the phase change. Recently, examples of CFD simulations of two-phase flows of sCO_2 were proposed (Palacz *et al.*, 2015; Giacomelli *et al.*, 2018; Hosangadi *et al.*, 2019; Bodys *et al.*, 2020), and compared with experiments performed on either cavitating or condensing flows of sCO_2 in converging-diverging nozzles. However, in none of the aforementioned publications the proposed CFD model is compared to both classes of phase transition.

Since sCO_2 compressors for closed power cycles can operate with both lower and higher entropy than the critical one, the computational model have to be assessed for both cavitating and condensing flows. Moreover, numerical models tailored for turbomachinery design have to be robust and computationally efficient for being used in the routine design and optimization tasks. To this end, two alternative CFD formulations are proposed for simulating compressible two-phase non-ideal flows of sCO_2, differing in terms of underlying physical assumptions and computational cost. To cope with the large departure from the ideal-gas model, state-of-the-art thermodynamic properties are incorporated into the CFD solver via LUT interpolations to speed up the calculations. LUT approaches represent the standard for simulating non-ideal flows in turbomachinery components, as widely documented in the literature, see, e.g., Pini *et al.* (2015*a*); Rinaldi *et al.* (2015); Ameli *et al.* (2018*b*). Therefore, the focus is herein on the multi-phase modeling; accordingly, the computational methodologies are tested on simplified converging-diverging ducts, which can effectively mimic the flow accelerations that may occur within compressor blade channels. Both cavitating and condensing flows are simulated and compared against experimental results of Nakagawa *et al.* (2009) and Lettieri *et al.* (2017), respectively.

As previously mentioned, both computational models stem from the two-fluid concept, but they differ in terms of the thermodynamic treatment and, ultimately, in the way in which the dispersed phase is generated and evolves within the main one. They are implemented in the Ansys-Fluent® framework making use of ad-hoc user-defined functions (UDFs).

The first model, named *mixture model* hereinafter, considers the mixture as a whole instead of being composed by two distinct phases. Such flow modeling allows for a drastic simplification in the mathematical description of the two-phase flow: the classical set of RANS equations is recovered and formulated in terms of mixture density and mixture center-of-mass velocity, eventually complemented with constitutive equations to model the relative motion between phases. Analogously, the energy equation is expressed in terms of the mixture enthalpy.

Defining the volumetric fraction of the main or principal phase as α_p and that of the dispersed phase as α_d, the mixture density ρ_{mix}, molecular viscosity μ_{mix} and thermal conductivity κ_{mix} result from the volume-weighted average as follows:

$$\rho_{mix} = \alpha_p \rho_p + \alpha_d \rho_d \tag{4.12}$$

$$\mu_{mix} = \alpha_p \mu_p + \alpha_d \mu_d \tag{4.13}$$

$$\kappa_{mix} = \alpha_p \kappa_p + \alpha_d \kappa_d \tag{4.14}$$

It is recalled that $\alpha_p = 1 - \alpha_d$ for single-component two-phase flows. Any specific thermodynamic quantity of the mixture ψ_{mix} (such as enthalpy, entropy, internal energy, etc...) is instead evaluated using mass averages, by resorting to the mass fractions of the phases. The mass fractions of the primary and dispersed phases, defined as w_p and w_d respectively, are evaluated as:

$$w_p = \frac{\rho_p}{\rho_{mix}} \alpha_p \tag{4.15}$$

$$w_d = \frac{\rho_d}{\rho_{mix}} \alpha_d \tag{4.16}$$

From mass conservation, the two mass fractions sum to unity, i.e. $w_p + w_d = 1$. They are used to determine the general specific mixture quantity ψ_{mix} as follows:

$$\psi_{mix} = w_p \psi_p + w_d \psi_d \tag{4.17}$$

An additional transport equation for the mass of the dispersed phase describes the generation and the evolution of the dispersed phase. The resulting set of governing equations can effectively track the evolution of averaged properties without resorting to sub-models that account for inner interactions between phases, whose modeling would require a deep knowledge of the interfacial properties (Ishii & Hibiki, 2011).

The second model, named *barotropic model* hereinafter, is still based on the two-fluid flow representation and strictly assumes that (i) the phases are in thermal and mechanical equilibrium, and (ii) any thermodynamic/transport property of the mixture ψ only depends on the pressure, e.g. $\Psi = \Psi(P)$. In general, the generic mixture property for a single-component fluid should depend on two independent thermodynamic quantities, for example $\psi = \psi(P, s)$. The barotropic assumption hence neglects any contribution besides the one of pressure on the quantity of interest; this means, in practice, to neglect the volumetric thermal expansion of the fluid. However, thanks to the barotropic assumption the equations of motion are decoupled from the energy equation, which does not need to be explicitly resolved. Such a model, albeit highly simplified, is deemed to be particularly relevant for turbocompressor application, since heat transfer is usually negligible in such components and the computational efficiency is crucial for their aerodynamic design and optimization.

4.6.1 Mixture model

The set of steady-state governing equations for the mixture model reads:

$$\begin{aligned}
\nabla \cdot (\rho_{mix}\boldsymbol{v}_{mix}) &= 0 \\
\nabla \cdot (\rho_{mix}\boldsymbol{v}_{mix} \otimes \boldsymbol{v}_{mix}) &= \nabla \cdot (\mathcal{T} + \mathcal{T}_{turb}) - \nabla P_{mix} \\
\nabla \cdot (\rho_{mix} h^t_{mix}\boldsymbol{v}_{mix}) &= -\nabla \cdot (\mathbf{q} + \mathbf{q}_{turb}) + \nabla \cdot [\boldsymbol{v}_{mix}(\mathcal{T} + \mathcal{T}_{turb})] \\
\nabla \cdot (\alpha_d \rho_d \boldsymbol{v}_{mix}) &= \mathcal{G} \qquad (4.18)
\end{aligned}$$

where no slip velocity is considered between phases, i.e. $\boldsymbol{v} = \boldsymbol{v}_{mix} = \boldsymbol{v}_p = \boldsymbol{v}_d$, and equal pressure and temperature is assumed between the phases, i.e. $P = P_{mix} = P_p = P_d$ and $T = T_{mix} = T_p = T_d$, thus imposing thermal and mechanical equilibrium. The shear-stress relationship for an isotropic Newtonian fluid is supplied $\mathcal{T} = \mu_{mix}(\nabla \otimes \boldsymbol{v}_{mix} + (\nabla \otimes \boldsymbol{v}_{mix})^T)$, where the contribution given by the volume viscosity coefficient is neglected in the mixture model implementation by Ansys-Fluent®. The influence of this latter contribution on compressible CO_2 flows in thermodynamic conditions of interest for this work was analyzed by Fang (2019), who concludes that the volume viscosity has only negligible effects on the main flow distributions in the present conditions. The Fourier's law $\mathbf{q} = -\kappa_{mix}\nabla T$ is used for the heat conduction. The gross effects of turbulence, expressed by the Reynolds stress $\mathcal{T}_{turb}$ and the turbulent heat transfer $\mathbf{q}_{turb}$, are introduced by means of the well-known two-equation $k - \omega$ SST model (Menter, 1994). Alternatively, the turbulence effects can also be included via the one-equation Spalart-Allmaras model (Spalart & Allmaras, 1992), which was proven to yield accurate predictions of the main near-wall distributions in presence of severe thermo-physical property variations (Otero *et al.*, 2018), such as the ones across the pseudo-critical line. Expansions passing through the pseudo-critical line are not considered in this work, hence the standard $k - \omega$ SST model is employed hereinafter for the turbulence modeling. It follows that a system consisting of seven partial differential equations has to be solved for a two-dimensional problem.

The last equation of system (4.18) is the specific feature of the proposed mixture model and its formulation is crucial to obtain smooth numerical convergence and accurate results. The role of this equation is actually to produce a certain amount of mass flow rate of the dispersed phase (left-hand side of the equation) when the local thermodynamic state resulting from the numerical calculation reaches the condition of phase transition by activating a mass-transfer source term $\mathcal{G}$ (right-hand side of the equation). Several formulations were proposed for this source term (see, for example, Dang Le *et al.* (2018); Giacomelli *et al.* (2018); Bodys *et al.* (2020)), typically referring to the Hertz-Knudsen physical model (Young, 1991). In the present work, a formulation similar to the one used in Hosangadi *et al.* (2019) is proposed, but with a different concept and implementation. $\mathcal{G}$ is defined as:

$$\mathcal{G} = \mathrm{sgn}(s_0 - s_c)\,\mathcal{K}\,[P - P_{sat}(T)], \qquad (4.19)$$

which is valid for both $P > P_{sat}(T)$, which implies condensing flows, and for $P < P_{sat}(T)$, which reproduces cavitating flows. Otherwise, $\mathcal{G} = 0$ because there is no phase change.

In our model, $P - P_{sat}(T)$ is the driving force of the phase change: when the local pressure exceeds (goes below) the saturation pressure at the local temperature, condensation (cavitation) locally occurs generating an increase in the mass of the dispersed phase. In this sense, this source term effectively mimics the Hertz-Knudsen model; however, the Hertz-Knudsen model was conceived to represent processes occurring at the microscale, which are not solved in the continuum macroscopic framework of the CFD. Hence, only the general intuition to construct the mathematical model is retained: from the mathematical perspective, this formulation is actually a *penalty* term introduced in the equation to numerically impose the satisfaction of a constraint, i.e. the onset of transition when $P = P_{sat}(T)$. As a matter of fact, under the assumption of a stable thermodynamic equilibrium, the last equation of the mixture model would be redundant if the CFD code uses either two specific or one specific and one intensive thermodynamic variable as primitive variables. Nonetheless, when using two intensive thermodynamic quantities, such as pressure and temperature as in the present work, there is the need to impose a constraint on those two variables to guide the solution towards thermodynamic equilibrium, i.e. $P = P_{sat}(T)$ Therefore, the numerical difference $P - P_{sat}(T)$ can be interpreted as a violation of the stable thermodynamic equilibrium and it becomes an artificial effect of the penalty formulation. To control $P - P_{sat}(T)$, and thus recovering an accurate numerical approximation of the two-phase solutions, i.e. $P \approx P_{sat}(T)$, the formulation of $\mathcal{G}$ features the penalty coefficient $\mathcal{K}$ [$\mathrm{s\,m^{-2}}$], which is dimensional and represents the weight of the penalty: the higher the $\mathcal{K}$, the lower $P - P_{sat}(T)$. In the result section, the influence of this parameter on the accuracy of the solutions is discussed. From the analytical perspective, the optimal choice of the penalty coefficient would be $\mathcal{K} \mapsto \infty$ to have infinitesimal constraint violations. However, in the numerical context such a choice would cause convergence issues because even a negligible violation of the constraint would dramatically affect the numerical value of the source term $\mathcal{G}$. Hence, the correct choice of $\mathcal{K}$ has to ensure a smooth convergence process alongside a negligible violation of the constraint, in the limit of the approximation of the numerical solution. It is only anticipated that $\mathcal{K} = \mathcal{O}(10^2 \div 10^3)\,\mathrm{s\,m^{-2}}$ is sufficient to impose that, in the two-phase region of the flow, the solution links the pressure field with the temperature field such that the actual P approximates $P_{sat}(T)$ with a small numerical error ($< 0.5\%$).

It is also worth mentioning that the present interpretation is fundamentally different from that of Dang Le *et al.* (2018), in which the pressure difference is assigned a priori, Hosangadi *et al.* (2019), in which the equilibrium condition $P = P_{sat}(T)$ is not recovered in the solution, and Bodys *et al.* (2020), in which a reference saturation pressure is defined and the source term monotonically increases along the expansion accordingly. In the present set-up, the source term is not representative of any physical considerations regarding thermal, mechanical or thermodynamic equilibrium, but only represents a mathematical expedient to enforce equilibrium conditions when using two intensive variables as primitive variables in the CFD solver.

As a final note on the source term formulation, in this work the phase transition was set at saturation, hence it was assumed that the fluid undergoes an instantaneous phase change. Under these circumstances, the mixture model (with negligible violation of the constraint) corresponds to a HEM formulated in a CFD framework, making use of pressure and temperature as primitive variables. However, depending on local thermodynamic conditions, a finite time is required to complete the phase-change process, exhibiting meta-stable states in the meantime. If a reliable expression of the Wilson line is available for the process of interest, the Wilson line might be specified to set the limit at which stable thermodynamic equilibrium is recovered, while separately modeling the meta-stable fluid, e.g. in a DEM fashion.

4.6.1.1 Thermodynamic modeling

A further issue of the mixture model, particularly relevant to sCO_2 application, is the thermodynamic modeling of the supercritical fluid in the single-phase region and of the individual phases in the two-phase region. Due to the near-critical conditions, a generalized thermodynamic description is required. In the present formulation, any generic property $\varPsi$ of the single-phase primary phase (when either $P > P_c, T > T_c$ or $P > P_{sat}(T)$ if the primary phase is liquid or $P < P_{sat}(T)$ if the primary phase is vapour) is expressed as a function of pressure and temperature, i.e. $\Psi_p = \Psi_p(P,T)$. A LUT approach was implemented in Ansys-Fluent® and supplied via a user-defined non-ideal model (UDRGM). Following this approach, discrete values of each thermodynamic property are stored in a tabular form assuming uniform steps in pressure and temperature, as sketched in figure 4.12(*a*). A uniform step allows for a faster search of the stored values at a generic location. As a drawback, the memory requirement is generally higher, because the inability to have localized refinements close to the critical point asks for larger tables, as the uniform step is dictated by the region in which the gradients in thermodynamic properties are larger. However, the cost reduction of the single CFD iteration is preferred over a reduced memory requirement. The value of Ψ_p at a generic pair (P, T) is then computed with a bilinear interpolation between the four closest thermodynamic nodes. Although meta-stable states are not simulated in the present work, the thermodynamic tables are built by extrapolating the single-phase properties until the corresponding spinodal limit to increase the margin from the discontinuous liquid-vapour change in thermodynamic properties, as exemplary reported in figure 4.12(*b*) for the density. Such expedient allows keeping the bilinear interpolation even in close proximity of the saturation curve, where one or more of the closest nodes may fall behind the saturation line but still within the meta-stable region. If an interpolating point falls behind the spinodal line (as it happens in the close proximity of the critical point, where the meta-stable region is narrowed), its value is set equal to the saturation one. A schematic representation of the bilinear interpolation is reported in figure 4.12(*c*).

When the primary phase is in equilibrium with the dispersed phase (when $P < P_{sat}(T)$ if the primary phase is liquid or $P > P_{sat}(T)$ if the primary phase is vapour), Ψ_p is only function of the saturation pressure at the local temperature, i.e. $\Psi_p = \Psi_p(P_{sat}(T))$. The local properties are thus computed with a linear interpolation as in figure 4.12(*d*) between the two closest saturation nodes (orange dots in figure 4.12(*a*)), which are determined by sampling the saturation line at the subcritical temperature locations. In practice, an if-statement discriminates between the two interpolation schemes in the developed UDRGM.

On the other hand, the dispersed phase can only exist in equilibrium with the primary one, hence the thermodynamic properties are always expressed as a function of the saturation pressure only, i.e. $\Psi_d = \Psi_d(P_{sat}(T))$. Therefore, the thermodynamic properties of the dispersed fluid are implemented with a standard UDF, which contains only the linear interpolation scheme discussed for the primary phase and reported in figure 4.12(*c*). It is worth mentioning that the dispersed-phase properties are functions of only one independent variable (temperature), which unequivocally determines the local saturation pressure on which the interpolation is performed.

For both phases, the thermodynamic tables are generated by making use of Refprop®, which implements a multi-parameter equation of state expressed in terms of the Helmholtz fundamental relation (Span & Wagner, 1996) for CO_2. Transport properties μ, κ are computed in analogy with the thermodynamic properties, employing the relationships made available by Refprop® in the construction of the tables. Overall, full *P–T* tables are generated for the primary phase, while saturation tables are generated for both phases. The resulting mixture properties follow the averaging procedures described in §4.6.

The accuracy of the LUT interpolation is verified by considering a quasi-one-dimensional isentropic flow with constant total enthalpy $h^t = h(P^t = 91\,\text{bar}, T^t = 310.45\,\text{K})$. The selected upstream total state is the closest to the critical point among all two-phase flows that will be investigated in this work, thus representing the most challenging case for the LUT testing. The associated entropy level is $s/s_c = 0.95$, hence the primary phase is liquid while the dispersed phase is vapour. The sampled thermodynamic region is $[230\,\text{K}, 320\,\text{K}] \times [10\,\text{bar}, 100\,\text{bar}]$ and three different grid refinements are considered, namely 601×601, 1201×1201 and 2401×2401. LUT predictions are compared against Refprop® estimates in figure 4.13 for density, enthalpy, and molecular viscosity. For all grid refinements, the largest discrepancy is found for the primary (*a*) Example of LUT discretization (7×7)

(*c*) Bilinear Interpolation
$P > P_{sat}(T)$ (cavitation) or $P > P_c$ or $T > T_c$

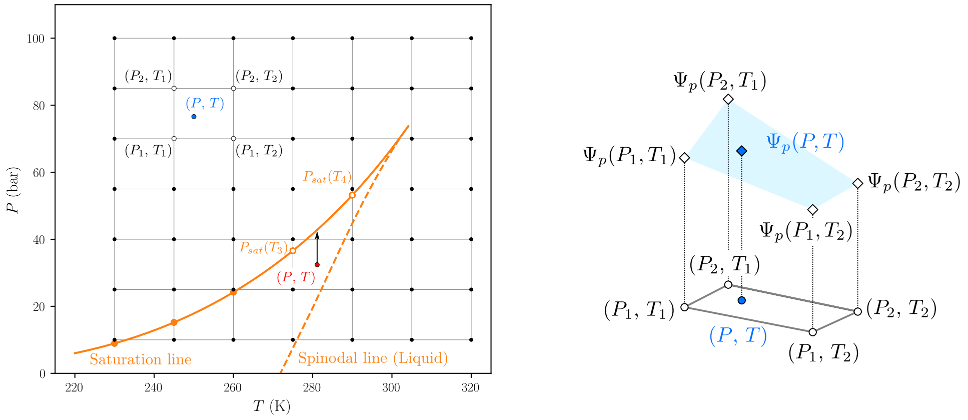

(*b*) Example of thermodynamic property, $\Psi = \rho$

(*d*) Linear Interpolation
$P \leq P_{sat}(T)$ (cavitation) and $P \leq P_c$ and $T \leq T_c$

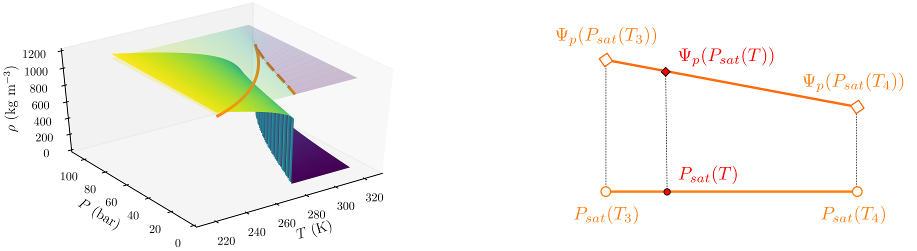

FIGURE 4.12. Schematic representation of the LUT approach implemented within the mixture model for the thermodynamic modeling of the primary phase. For illustrative purposes, the primary phase is considered as a liquid and the phase transition is cavitation (liquid-to-vapour), but the opposite scenario (vapour as primary phase and condensation as a phase-change phenomenon) follows the same conceptual steps. The LUT for the secondary phase only involves the linear interpolation.

phase in the proximity of the phase-change onset. The coarsest table returns an absolute error of 1.3%, which decreases to 0.2% for the most refined table. Within the two-phase region, where the properties are only functions of the saturation pressure, the maximum error is about 0.1% regardless of the LUT refinement. Therefore, thermodynamic tables 2401×2401 are selected for the following analyses.

4.6.2 Barotropic model

The set of steady-state governing equations for the barotropic model reads:

$$\begin{aligned} \nabla \cdot (\rho \boldsymbol{v}) &= 0 \\ \nabla \cdot (\rho \boldsymbol{v} \otimes \boldsymbol{v}) &= \nabla \cdot (\mathcal{T} + \mathcal{T}_{turb}) - \nabla P \end{aligned} \tag{4.20}$$

The two-equation $k-\omega$ SST model (Menter, 1994) completes the system of governing equations by taking into account turbulence effects.

The barotropic set of equations are simply the single-phase Reynold-Averaged Navier-Stokes equations, in which the fluid behaves like the mixture when the thermodynamic state falls below the

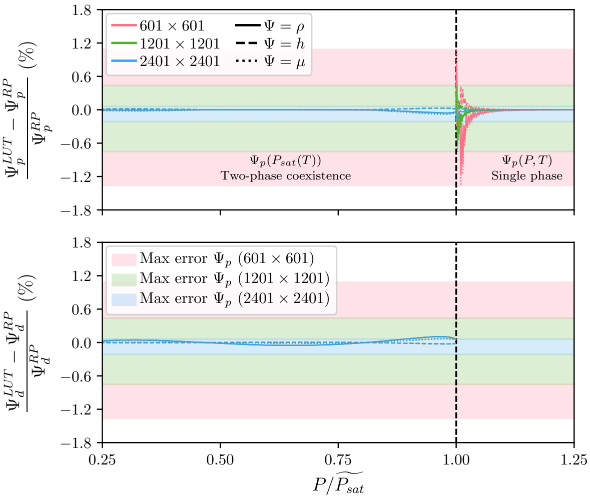

FIGURE 4.13. Errors of different LUT discretizations against Refprop® predictions in density, enthalpy and molecular viscosity estimates for an isentropic cavitating flows at constant total enthalpy $h^t = h(P^t = 91\,\text{bar}, T^t = 310.45\,\text{K})$ (labelled as case A later in the manuscript). The coloured bands show the maximum error found in the thermodynamic description of the primary phase for the given LUT discretization.

saturation curve. Compared to the mixture model, the barotropic formulation inherently excludes any mechanical or thermal disequilibrium between phases, and hence it strictly belongs to the HEM class. Furthermore, the barotropic assumption implies that the thermo-physical properties of the fluid, which should depend on two thermodynamic quantities, are only dependent on pressure, thus neglecting any thermal effect: the fluid is therefore considered compressible but not thermally expandable, i.e. $(\partial\rho/\partial P)_T \neq 0$ and $(\partial\rho/\partial T)_P = 0$ respectively. Such assumption simplifies the resulting flow representation with respect to the classical HEM (whose most general formulation is reported, for example, in Palacz *et al.* (2015)), but it provides crucial advantages from the computational perspective. The barotropic model decouples mechanical from thermal effects, removing the need of solving the energy equation to characterize the thermo-physical fluid properties. As a consequence, the mathematical problem is reduced to the resolution of five partial differential equations (for 2D systems), two less than the mixture model. Moreover, the solver becomes inherently more robust than the mixture model when dealing with supercritical fluids, because it does not handle the sharp gradients of c_P which arise close to the critical point (wherein c_P is singular). In a hierarchy of CFD models, the barotropic model is, therefore, the most robust and computationally efficient numerical formulation which can be conceived for tackling the numerical simulation of multi-dimensional two-phase flows of sCO_2.

The physical accuracy of the model strongly relies on the definition of the barotropic relationships for the three thermo-physical properties of interest for the solution, i.e. the density, the molecular viscosity, and the speed of sound c:

$$\begin{aligned} \rho &= \rho(P) \\ \mu &= \mu(P) \\ c &= c(P) \end{aligned} \tag{4.21}$$

Since these properties physically depend also on entropy, a choice on the entropy generation across the process has to be made to obtain the three relationships (4.21). An obvious possibility, considered in the simulations reported in this work, is to keep the entropy level constant at the upstream value $s = s_0$. This choice physically means that the thermal effects prompted by the entropy generation on the aforementioned properties are ignored. It is worth stressing that the choice of building barotropic relationships based on the upstream entropy does not mean to assume isentropic flows: the mechanical dissipation is indeed introduced via viscous and turbulent effects in the momentum equation; the model simply ignores the correction to the thermo-physical properties due to this dissipation, which would cause an increase of entropy. However, if a preliminary estimate on the entropy generation across the process is available, as often occurs for turbocompressor simulations (via the estimated aerodynamic efficiency, for example), the barotropic relations (4.21) could be in principle constructed considering the estimated entropy rise, thus refining the thermodynamic accuracy of the solution. In the validation section, the contribution given by the entropy generation is highlighted, by comparing the results of the mixture model with that of the barotropic models.

As barotropic relationships only depend on a single independent variable, a LUT approach based on the linear interpolation scheme described in §4.6.1.1 is encoded in a dedicated UDF. Tabular values for ρ, μ and single-phase c are computed via RefProp®, while different formulations for c in the two-phase region are tested and discussed later in §4.6.4. However, the choice of the two-phase speed of sound does not alter the obtained flow solutions, as the actual value only depends on the governing equations that are solved (De Lorenzo *et al.*, 2017*a*; Giacomelli *et al.*, 2018). Consistently with the mixture model, the tabular properties are generated in the pressure interval $[10\,\text{bar}, 100\,\text{bar}]$ with a step of 3.75×10^{-2} bar.

4.6.3 Validation

In this section, the reference cases for validation purposes are introduced. Since both the computational strategies focus on the mixture evolution, in principle there should be no differences among cavitating and condensing flows regardless of the phase change initialization. However, despite the generality of the mathematical formulation, the adequacy of the simulation tools in properly representing the macroscopic flow features of two-phase compressible flows has to be verified for both flow conditions. Specifically, experiments made by Nakagawa *et al.* (2009) are considered to validate the computational solver for CO_2 cavitating flows and the experimental data provided by Lettieri *et al.* (2017) for the validation of CO_2 condensing flows. For both experiments, the nozzle width is large enough compared to the nozzle height such that three-dimensional effects are expected to be negligible. Therefore, two-dimensional simulations are carried out for both cavitating and condensing flows.

Nakagawa *et al.* (2009) analyzed cavitating flows of CO_2 for several converging-diverging nozzle geometries, featuring different divergence angles, and for different stagnation conditions. They provided pressure and temperature measurements along the nozzle axis by means of pressure transducers and thermocouples. Specifically, four strain-gauge taps and nine thermocouple taps were distributed along the diverging section of the nozzle. Comparing pressure and temperature measurements in the two-phase region, Nakagawa *et al.* (2009) argued that stable thermodynamic equilibrium is established very soon in the diverging section. In the present work, the nozzle geometry with a divergence angle of 0.153° is selected for the two published upstream total conditions. Based on the isentropic homogeneous theory, the authors claimed that the flow regime is not supersonic for both expansion processes. This conjecture will be the object of specific analyses in §4.6.4. The authors also pointed out that a supersonic flow regime was established for nozzle geometries with a higher divergence angle, but the measured pressure falls below the triple point. To avoid dealing with three-phase flows, these latter cases are not considered in this work.

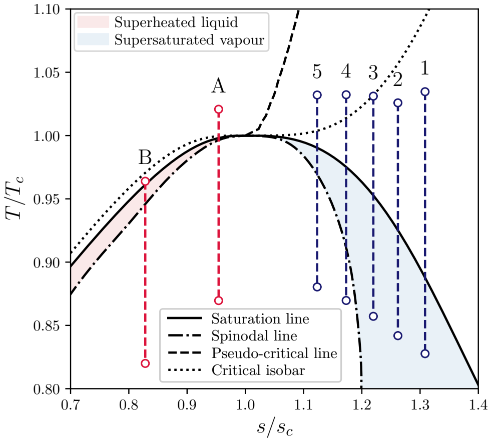

FIGURE 4.14. Reference isentropic expansions for the validation of the proposed computational methodologies.

Lettieri *et al.* (2017) performed five supersonic expansions at $s > s_c$, whose upstream total states progressively approach the thermodynamic critical point. They provided the pressure evolution along the nozzle, measured with pressure transducers at 13 axial locations; moreover, through an optical apparatus, they also obtained visualizations of the two-phase flows inside the converging-diverging nozzle as well as the experimental condensation onset for each condition. They showed that all expansion processes are characterized by a misty flow regime, where the two phases are practically indistinguishable (Lettieri *et al.*, 2017, Figure 9). By virtue of such experimental observations, a mixture description of the two-phase flow according to the two-fluid model appears an appropriate approximation.

Table 4.5 reports the boundary conditions for the cavitating and condensing flows that will be discussed in this work along with the upstream entropy level. Cavitating flows are denoted with a capital letter, while condensing flows are identified by a number. In figure 4.14 the corresponding isentropic processes in the T–s thermodynamic plane are reported. Out of the seven conditions available from experiments, case A, case 4 and case 5 are expansions evolving from a supercritical upstream state ($T > T_c$ and $P > P_c$). As a final note, the shaded areas in figure 4.14 represent the extent of the meta-stable region predicted by the multi-parameter equation of state included in the Refprop®. As already stated, in constructing the CFD models the onset of phase change was set at saturation, thus excluding any meta-stability effects. The plot shows that the extent of the meta-stable regions progressively reduces when approaching the critical point, suggesting a minor relevance of meta-stable effects for cases evolving in near-critical conditions, i.e. case A and case 5 and 4 for cavitating and condensing flows, respectively. These three cases are also the only ones, among the tested conditions, for that the expansion evolves from a supercritical state, thus being the most representative of the local expansions occurring in sCO_2 compressors.

4.6.3.1 Cavitating flows

Cavitating flows are first considered, occurring when the inlet entropy level is lower than the critical one. In this context, when the phase transition takes place the primary phase is liquid and the dispersed one is vapour, hence $\alpha_p = \alpha_L$ and $\alpha_d = \alpha_V$. The phase change occurs when $P < P_{sat}(T)$.

Total pressure and total temperature are prescribed at the inlet section as in table 4.5 for the two expansions considered, imposing $\alpha_V = 0$ therein (the flow enters only in liquid phase). For the

TABLE 4.5. Summary of boundary conditions for the cavitating (labelled with a capital letter) and condensing (labelled with a number) flows simulated in this work. For condensing flows, the outlet static pressure is not specified because its value is ignored as a consequence of the supersonic flow regime.

Case	P_0^t (bar)	T_0^t (K)	P_1 (bar)	s_0/s_c
A	91.00	310.45	27.5	0.95
B	61.00	293.15	17.5	0.83
1	58.96	314.67	-	1.31
2	65.35	311.99	-	1.26
3	73.53	313.60	-	1.22
4	79.99	313.94	-	1.17
5	84.74	313.88	-	1.12

barotropic model, only the total pressure is specified. As for the turbulent boundary conditions, a hydraulic diameter equal to 10.0 mm (i.e., twice the height of the inlet section) and an eddy viscosity ratio equal to 2.5 are assigned, representative of a low turbulence level as expected in a nozzle expanding flow from a reservoir; the algorithms implemented in Ansys-Fluent® obtain the corresponding values of k and ω assigned at the inlet. The static pressure is specified at the nozzle outlet as in table 4.5. However, it has to be noted that if a supersonic condition is reached at the nozzle outlet, the solver ignores the assigned pressure value and calculates the proper adapted pressure value.

No-slip and adiabatic boundary conditions are prescribed at the wall, which is not considered smooth. As reported in Banasiak & Hafner (2013), a mean roughness of 2 µm is considered on the nozzle wall; this value is converted into an equivalent sand-grain roughness using a conversion factor of 3.1 (Adams *et al.*, 2012), resulting in $k_s = 6.2\,\mu\text{m}$. Even though it might appear very small in absolute terms, the relevance of the wall roughness stems from the small scale of the experiment. A comparison with results obtained assuming smooth surfaces will be proposed later in this section when discussing the aerodynamics of the nozzle. Finally, a symmetry condition is imposed at the nozzle axis.

The system of equations for the mixture model is solved in the following order: the continuity and the momentum equations are solved together in a coupled fashion, then energy equation, vapour-mass equation and turbulence equations are solved separately in this order. The barotropic model makes use of the same resolution scheme, but energy and vapour-mass equations are not solved. All equations are discretized with a third-order QUICK scheme for both models. Furthermore, the PRESTO! scheme is used to interpolate the pressure at the cell face, while the gradient is reconstructed with a Green-Gauss node-based technique.

A grid convergence assessment is first carried out by generating three hexahedral grids with an increasing number of elements. Such grid assessment is undertaken by taking case A as a reference. The mixture model is considered for this mesh analysis but equivalent outcomes are found for the barotropic simulations as well. In increasing the mesh resolution, the number of elements is doubled each time in the x-direction while keeping the same wall resolution, i.e. 9 evenly spaced layers in the y-direction with a first-layer wall distance equal to 6.7×10^{-6} m at the throat. The number of elements along the y-direction is dictated by the selected surface roughness, i.e. the first center-cell distance has to be larger than the roughness value.

The results of this study in terms of main flow distributions are reported in figure 4.15, showing that only minor differences are found among three meshes with an increasing number of elements. The geometrical error is also quantified by computing the grid convergence index (GCI) at five axial locations along the diverging section of the nozzle for pressure, temperature and liquid mass

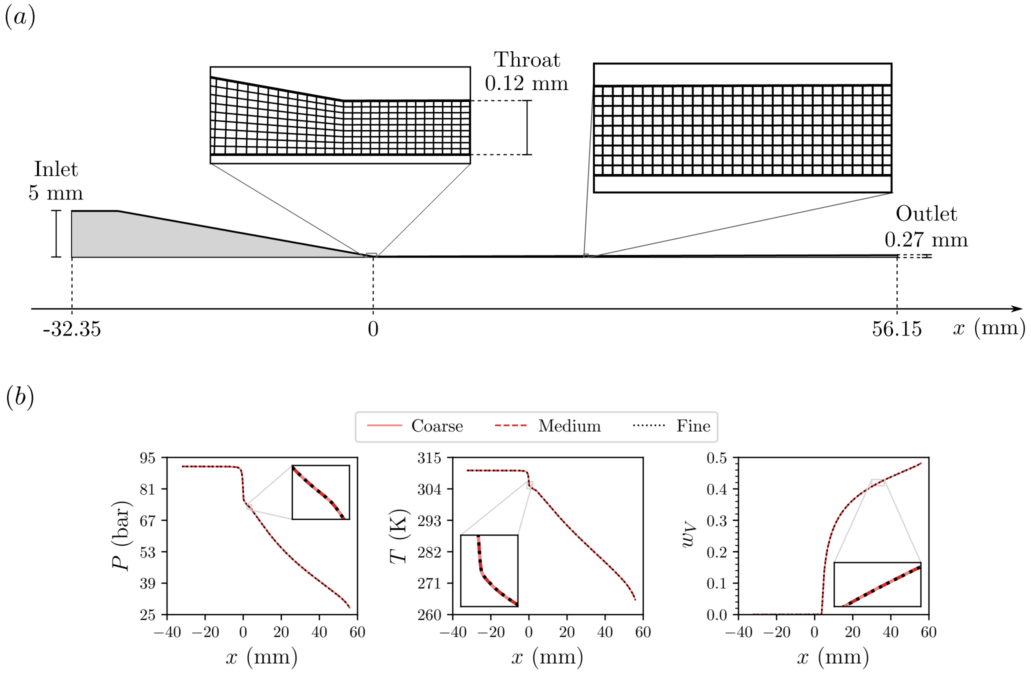

FIGURE 4.15. Grid-convergence assessment for cavitating-flow simulations: (*a*) the medium mesh selected as the grid-independent mesh (number of elements $\approx 3 \times 10^4$, grid resolution at the throat 2×10^{-5} m, 9 evenly spaced elements along the y-direction with a first-layer wall distance at the throat of 6.7×10^{-6} m) alongside the main nozzle dimensions, (*b*) pressure, temperature and vapour-mass fraction distributions for different grid refinements. The grid convergence study is performed on case A.

TABLE 4.6. Grid convergence indexes for pressure, temperature and vapour-mass fraction at selected axial locations along the diverging section. The grid-convergence study is performed on case A.

	GCI		
x (mm)	P (%)	T (%)	w_V (%)
0	0.01	0.00	0.00
15	0.00	0.00	0.00
30	0.00	0.00	0.00
45	−0.01	0.00	0.00
55	−0.01	0.00	0.00

fraction. The GCIs is evaluated by estimating the apparent order of convergence as outlined in Roache (1997). The GCIs between the medium and the fine mesh for the above quantities of interest are reported in table 4.6, showing that the maximum error is around 0.01%. The same error is also found when estimating the GCI for the mass-flow rate, demonstrating that a complete grid convergence is achieved for the medium mesh. Therefore, the medium mesh is selected for the following analyses, consisting in overall $\approx 3 \times 10^4$ elements, with a grid resolution at throat of 2×10^{-5} m. The aspect ratio is included between 1.4 and 2. The selected computational mesh is displayed in figure 4.15(*a*).

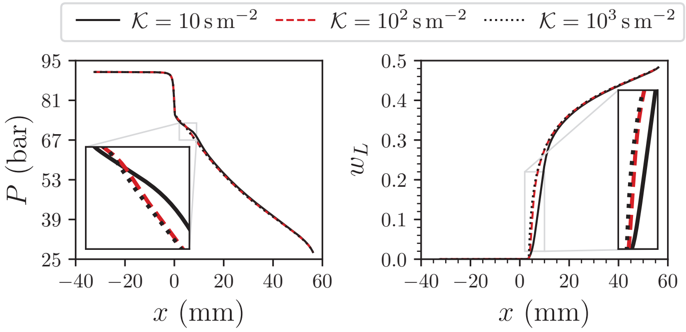

FIGURE 4.16. Influence of the penalty constant $\mathcal{K}$ on the solution of the case A.

As a final and most relevant modeling issue, the setting of the penalty term $\mathcal{G}$ in the mixture model is defined through a set of simulations featuring progressively higher values of the penalty constant $\mathcal{K}$, whose value is raised from $10\,\mathrm{sm^{-2}}$ to $10^3\,\mathrm{sm^{-2}}$. The results of the three calculations are reported in figure 4.16 in terms of pressure distributions (left) and vapour mass fraction (right). Simulation results denote an evident convergence process, showing significant differences when the penalty parameter is raised from $10\,\mathrm{sm^{-2}}$ to $10^2\,\mathrm{sm^{-2}}$, while nearly identical profiles are predicted when $\mathcal{K}$ is raised from $10^2\,\mathrm{sm^{-2}}$ to $10^3\,\mathrm{sm^{-2}}$. For these values of $\mathcal{K}$, the constraint $P - P_{sat}(T)$ is violated with a maximum error of 0.5% in the early stages of the phase transitions, which is also the region most affected by the penalty coefficient. The error is then reduced by one order of magnitude in the ongoing expansion. Higher values of $\mathcal{K}$ interfered with the convergence process, as small violations of the constraint provoked an extremely large source term, thus preventing from achieving a stable convergence. From the results of this analysis, $\mathcal{K} = 10^3\,\mathrm{s\,m^{-2}}$ is systematically set in all following simulations performed with the mixture model.

After the definition of the numerical set-up, the experimental assessment of the CFD models is discussed. Simulation results are compared against experimental data (Nakagawa *et al.*, 2009) for both cases A and case B in figure 4.17 in terms of pressure and temperature profiles along the nozzle axis. As in the experimental reference, temperature measurements are also converted in pressure values through RefProp® assuming stable thermodynamic conditions, i.e $T_{exp} \mapsto P_{exp} = P_{sat}(T_{exp})$.

First considering case A, the agreement between the predicted pressure trends and the experimental one is satisfactory with both the direct or indirect pressure measurements. The maximum relative deviation, defined as $\varepsilon = (P_{mix} - P_{exp})/P_{exp}$, is located at the last pressure tap and amounts to 8.5%. The temperature distribution predicted by the mixture model is also compared with the experimental temperature data, returning a maximum deviation of 1.3% found at the last thermocouple.

Apart from local deviations, the introduction of a single parameter that summarizes the deviation of numerical predictions with respect to experiments can be useful to evaluate the overall quality of the numerical model. In forecasting, the weighted mean absolute percentage error (WMAPE) is widely used to quantify the quality of a forecast. Whether X is pressure or temperature, this error can be formulated as:

$$\mathrm{WMAPE}(X) = \frac{\sum_i |X_{exp,i} - X_{mix,i}|}{\sum_i X_{exp,i}} \cdot 100 \quad [\%] \tag{4.22}$$

Applied to the case A, the error is 2.2% and 0.7% for pressure and temperature, respectively. The agreement with the experimental data drops when considering the non-supercritical case B,

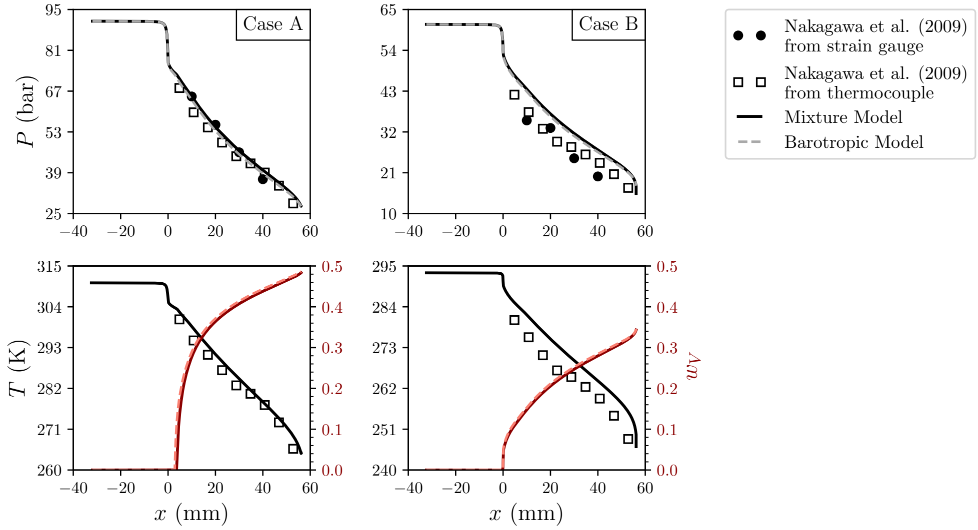

FIGURE 4.17. Comparison of the mixture (solid lines) and barotropic (dashed lines) model against experimental data (Nakagawa *et al.*, 2009) along the nozzle axis. The vapour-mass fraction predicted by the barotropic model is computed as post-processing.

whereby a systematic over-prediction affects the expansion, although the overall trend is properly reproduced. The overprediction of the experimental data by the mixture model is contained between 11.5% (second pressure tap) and 35.8% (last pressure tap) for the pressure measurements. One order of magnitude smaller deviations are, instead, found for temperature measurements, whose maximum discrepancy amounts to 3.0% in correspondence with the last thermocouple. The overall deviation from pressure and temperature trends, following the definition provided in equation 4.22, is 23.1% and 2.1%, respectively. One possible explanation for such large deviations is that meta-stable effects, negligible close to the critical point as in case A ($s/s_c = 0.95$), gain importance away from it as in case B ($s/s_c = 0.83$). Such differences are consistent with the results of Palacz *et al.* (2015), who also found a reduction in the HEM accuracy away from the critical point. However, a closer inspection of the experimental data for case B shows a certain scattering of the experimental pressure data, especially between direct and temperature-derived measurements. In particular, towards the end of the divergent the predicted pressure profile qualitatively follows the trend established by temperature and associated pressure data; in this region, relatively far from any potential delay introduced by meta-stable effects, conditions of stable thermodynamic equilibrium should have been recovered.

The above considerations apply identically for both the mixture and the barotropic models, which exhibit qualitatively equal predictions in terms of pressure profiles. Quantitatively, the maximum deviation between the mixture and barotropic estimates is 2.9% and 2.3% for case A and case B, respectively. However, the thermodynamic implications of the simplified barotropic assumption are interesting to investigate and, hence, a detailed post-processing was performed on the computed data to obtain estimates for:

- the enthalpy field, as $h_{baro} = h(P_0^t, T_0^t) - 0.5 \cdot v_{baro}^2$
- the entropy field, as $s_{baro} = s(P_{baro}, h_{baro})$
- the vapour mass-fraction, as $w_{V,baro} = w_V(P_{baro}, h_{baro})$

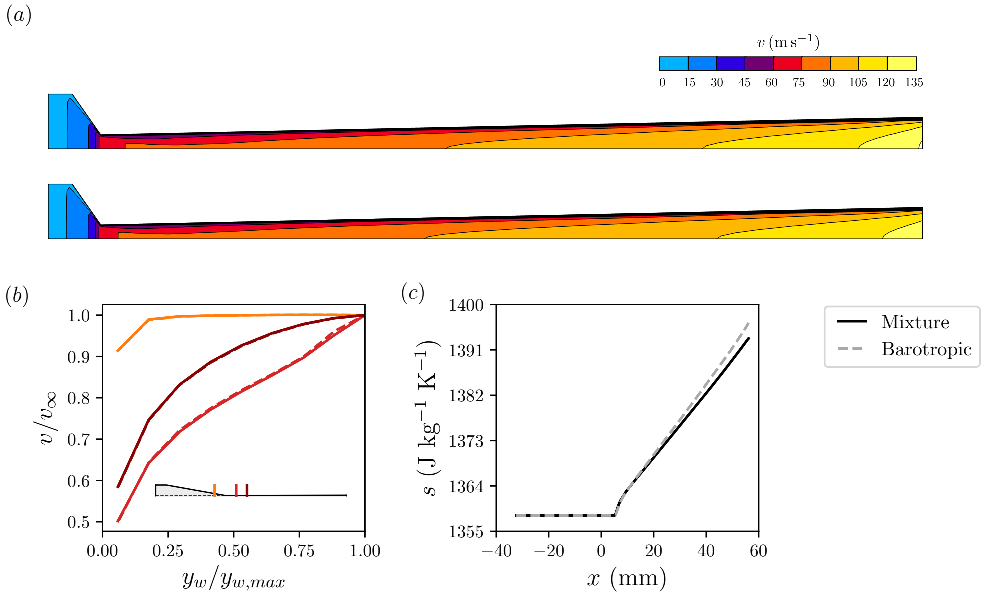

FIGURE 4.18. (*a*) Velocity fields predicted by the mixture model (top) and barotropic model (bottom) for the case A For visualization purposes, the x-direction is stretched such that $x/y = 0.125$ and the convergent section is not shown; (*b*) spanwise velocity profiles for three relevant sections, namely at $x = -5$ mm (orange lines), 5 mm (red lines) and 10 mm (dark-red lines); (*c*) entropy distributions along the nozzle axis for the mixture and the barotropic model.

These thermodynamic estimates can be performed straightforwardly if the total enthalpy is assumed uniform over the entire flow field. This assumption is actually a simplification of the actual flow configuration: even if the nozzle walls are adiabatic, implying that the flux of total enthalpy must be conserved, local gradients of the total enthalpy might arise as a consequence of internal heat-transfer processes between layers of fluid at different temperature. One classical example is the heat transfer between the boundary layer, heated by the viscous dissipation, and the adjacent free-stream region. The mixture model, by virtue of its complete thermodynamic formulation and its agreement with the experimental temperature profile, can be used as a benchmark for the aforementioned processing of barotropic-simulation data.

Figure 4.18 summarizes significant flow features predicted for the supercritical condition of case A. It reports the two-dimensional distributions of the velocity magnitude, as well as spanwise velocity profiles for three relevant sections across the throat, and the entropy distribution along the nozzle axis. For each of these plots, results obtained with the mixture model (solid lines) are compared with corresponding data extracted/processed from the barotropic flow field (dashed lines). First considering the velocity distributions, it is evident how the two simulation models predict very similar flow configurations in a relatively complex flow field. Indeed, while in the converging region of the nozzle a common configuration is recognized, with a wide isentropic free-stream contoured by a narrow boundary layer, in the diverging part the isentropic core rapidly vanishes and spanwise gradients affect the entire cross-section, leading to a fully-developed profile. By looking at the two-dimensional velocity contours in figure 4.18(*a*) sharp angle at the throat promotes the thickening of the boundary layer, whose dimension rapidly becomes comparable with the nozzle height in the diverging channel, as also confirmed by the spanwise velocity distributions before and after the throat in figure 4.18(*b*).

Such flow field in the diverging part of the nozzle is mostly due to the very low aspect ratio of

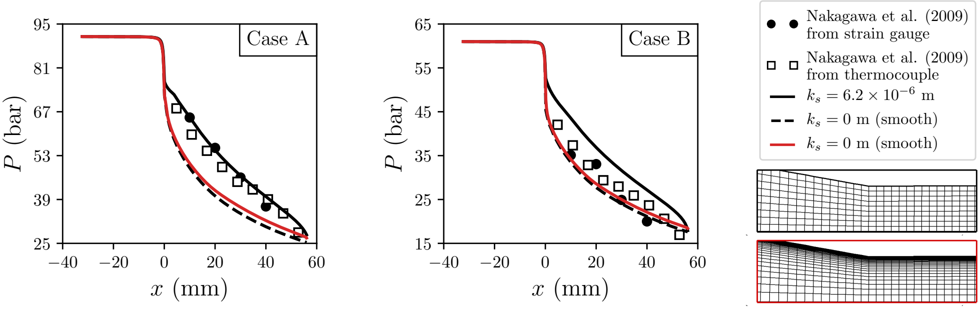

FIGURE 4.19. Influence of surface roughness on the flow solution for cavitating flows. Black lines correspond to results obtained with the rough-wall mesh (no wall resolution), while pressure distributions in red come from the mesh with a cell clustering at the wall ($y^+ < 1$). All these results are obtained with the mixture model.

the duct, but also the very small scale of the experiment plays a role. The diverging duct is indeed so narrow that the wall roughness also significantly contributes to determining the flow configuration. In this work, the surface roughness adopted in Banasiak & Hafner (2013) is considered, but two further comparative simulations for hydraulically smooth walls were performed. The first one employs the same wall resolution as the rough-wall simulations and hence resorts to wall functions for the near-wall treatment, while the second one features a refined mesh clustering at the wall so to achieve $y^+ < 1$ all over the wall boundaries. These two further simulations are compared to the one obtained with the rough wall in figure 4.19 for both cases A and case B. The two smooth-wall simulations show only marginal differences on the pressure profiles (with slight quantitative differences amplifying towards the nozzle outflow), but they exhibit a considerable difference with respect to the rough-wall simulation, highlighting the significance of the wall roughness in this experiment. Unfortunately, Nakagawa *et al.* (2009) did not provide any information about the actual roughness level; however, a level of roughness must be considered in the simulation as the wall cannot be considered hydraulically smooth given the small-scale nozzle. As a matter of fact, the roughness should be around two orders of magnitude lower than the one employed in this work to have hydraulically smooth surfaces, which is not compatible with up-to-date manufacturing processes. In this regard, a smooth-wall simulation is just intended to represent an idealized case for the quantification of the roughness effect and not an attempt to match experimental data. Indeed, the importance of roughness is not only quantitative but also qualitative. For smooth-wall simulations the flow regime is found to be supersonic in the diverging part, thus the expansion processes are driven by the converging-diverging shape of the nozzle. On the other hand, the rough-wall simulation does not predict a sonic Mach number at the throat, as it will be clearly shown in §4.6.4, in which several two-phase speed-of-sound formulations are discussed. The pressure drop in the diverging part of the nozzle is then prompted by frictional losses, as originally argued by Nakagawa and his co-authors when discussing the experimental trends. From this angle, the better quantitative adherence of case B with experimental data assuming a smooth wall is misleading. Furthermore, the rough-wall simulation better captures the overall pressure trend, albeit the systematic overprediction. The reason for such overprediction for case B can be twofold: uncertainty in the roughness level, although large deviations from the actual level are not expected in the light of present manufacturing processes, and meta-stable effects, which are more prominent far from the critical point.

The presence of the roughness also affects the mass-flow rate that passes through the nozzle, as reported in table 4.7, in which the error is defined as $\varepsilon_{mix-baro} = (\dot{m}_{baro} - \dot{m}_{mix})/\dot{m}_{mix}$. For both

Table 4.7. Comparison of the mass-flow rate predicted by the mixture and the barotropic model for all simulated cavitating flows.

	Wall functions	$\dot{m}_{mix}$ (kg/s)	$\dot{m}_{baro}$ (kg/s)	$\varepsilon_{mix-baro}$ (%)
			Case A	
Rough wall	✓	4.72	4.80	1.54
Smooth wall	✓	5.43	5.40	–0.59
Smooth wall		5.39	5.36	–0.45
			Case B	
Rough wall	✓	3.71	3.77	1.60
Smooth wall	✓	4.19	4.20	0.67
Smooth wall		4.16	4.17	0.33

upstream states, the mass flow rate increases by 10 – 15% from rough- to smooth-wall simulations owing to a decrease of frictional losses. All cases were also simulated with the barotropic model: the higher discrepancy in the elaborated mass-flow rate is found for rough-wall simulation and amounts to ∼ 1.5%. As rough-wall simulations do not predict a sonic throat, the mass-flow rate is determined by the flow conditions at the nozzle outlet, in which the neglected effect of entropy on the density value is maximum. For smooth-wall simulations, the flow conditions at the throat establish the mass-flow rate. Given that the core is isentropic at the throat, the only differences between the two models regard the spanwise density distribution and small discrepancies in the computed velocity field (∼ 0.5%).

Finally, in smooth-wall simulations the barotropic model overestimates both expansion processes compared to the mixture model, with an outlet pressure which is around 7% lower than the mixture-model counterpart. The larger discrepancy depends on the role of the density in determining the expansion process: in smooth-wall simulation, a supersonic expansion takes place in the diverging portion of the nozzle. The density predicted by the barotropic model does not consider the influence of the entropy that still raises along the axis, notwithstanding the smooth-wall assumption, hence the density is smaller than the one predicted by the thermodynamically complete mixture model. As a consequence, the flow expands more in the diverging duct, explaining the larger deviations. In rough-wall simulations, on the other hand, the expansion is dictated by frictional losses, therefore the volumetric evolution plays a minor role. It has to be noted that, for adiabatic flows, the barotropic model could be easily improved by resorting to non-isentropic laws for the variability of thermo-physical properties along the transformation. In practice, a preliminary barotropic simulation can be performed using isentropic laws, then the resulting entropy raise can be estimated with the procedure reported above and the barotropic relationships updated to incorporate the effect of the entropy rise (as done, for example, when computing the polytropic efficiency in turbomachinery analysis). Then, a new barotropic simulation, implementing the so-estimated non-isentropic relationships, can be performed to better approximate the actual density change. Figure 4.18(*b*) indicates that one iteration should be sufficient to estimate accurately the impact of entropy rise on the density.

For all cases the deviations between numerical models and the experimental data are quantified as $\varepsilon = (P_{exp} - P_{mix})/P_{exp}$ and reported in table 4.8.

The flow configuration is complex not only on the aerodynamic ground but also introduces thermodynamic challenges, resulting in a very critical benchmark for the present barotropic model, which was constructed by assuming an isentropic P–ρ relationship. However, the velocity field

TABLE 4.8. Comparison of numerical predictions against experiments (Nakagawa *et al.*, 2009) for cavitating expansions. Experimental results were only reported in a graphical form, hence the exact measurement locations as well as the associated values were graphically extrapolated. The smooth-wall results for cavitating flows refer to the ones obtained with the refined mesh at the wall ($y^+ < 1$).

	Case A						**Case B**					
	Rough			**Smooth**			**Rough**			**Smooth**		
x (mm)	P_{exp} (bar)	P_{mix} (bar)	ε (%)	P_{exp} (bar)	P_{mix} (bar)	ε (%)	P_{exp} (bar)	P_{mix} (bar)	ε (%)	P_{exp} (bar)	P_{mix} (bar)	ε (%)
10	65.17	65.18	0.0	65.17	50.51	−22.5	35.10	43.54	24.0	35.10	34.17	−2.6
20	55.47	54.70	−1.4	55.47	41.90	−24.5	33.06	36.87	11.5	33.06	28.58	−13.6
30	46.01	46.61	1.3	46.01	36.55	−20.6	24.90	31.60	26.9	24.90	24.99	0.4
40	36.78	39.90	8.5	36.78	32.27	−12.2	20.00	27.17	35.8	20.00	22.10	10.5
	T_{exp} (K)	T_{mix} (K)	ε (%)	T_{exp} (K)	T_{mix} (K)	ε (%)	T_{exp} (K)	T_{mix} (K)	ε (%)	T_{exp} (K)	T_{mix} (K)	ε (%)
4.8	300.61	302.57	0.7	300.61	293.32	−2.4	280.41	285.11	1.7	280.41	277.05	−1.2
10.8	294.93	298.07	1.1	294.93	287.16	−2.6	275.79	281.29	2.0	275.79	271.81	−1.4
16.8	291.06	293.49	0.8	291.06	282.38	−3.0	270.94	277.30	2.3	270.94	267.67	−1.2
22.8	286.90	289.27	0.8	286.90	278.70	−2.9	266.85	273.62	2.5	266.85	264.43	−0.9
28.8	282.81	285.33	0.9	282.81	275.57	−2.6	265.06	270.17	1.9	265.06	261.65	−1.3
34.8	280.55	281.57	0.4	280.55	272.65	−2.8	262.39	266.88	1.7	262.39	259.05	−1.3
40.8	277.52	277.86	0.1	277.52	269.93	−2.7	259.27	263.60	1.7	259.27	256.62	−1.0
46.8	272.84	273.96	0.4	272.84	267.40	−2.0	254.63	260.13	2.2	254.63	254.36	−0.1
52.8	265.72	269.20	1.3	265.72	265.05	−0.3	248.36	255.70	3.0	248.36	252.27	1.6

reproduced by the barotropic model is aligned with the mixture one (maximum deviations in the range of 0.5%), also in the region of developed profiles, where entropy is generated in the boundary layer. Moreover, by inspecting the entropy generation along the nozzle axis, it is evident that the barotropic flow solution, once properly post-processed, can be used to achieve realistic estimates of the mechanical dissipation processes, regardless of the isentropic pressure-density relationship adopted. As a result, when the estimated entropy and the computed pressure are combined to obtain the generation of vapour mass fraction along the nozzle, a remarkable agreement is found between the barotropic model and the complete mixture model, in terms of transition onset, overall trend, and quantitative levels, as visible in figure 4.17.

Due to the fully developed profiles observed in the diverging region of the nozzle, the distributions in cross-stream direction are expected to be highly non-uniform for all the quantities, including the vapour mass fraction. The spanwise distributions of w_V at three different axial locations are reported in figure 4.20 for case A, showing a consistent increase close to the wall. This can be explained by considering that a higher entropy level is found moving away from the nozzle axis, due to the dissipation in the boundary layer. The rise of entropy further increases the vapour quality with respect to that of the flow in the nozzle axis (which is, in turn, higher with respect to the ideal quality in presence of an isentropic expansion). As a result, the vapour-mass fraction at the wall is $3 - 5\%$ higher than the free-stream value. In these trends, slight but visible differences appear between the results obtained with the mixture model and with the barotropic one. This is a consequence of the uniform total enthalpy assumption in the post-processing of the barotropic solution: close to the wall, the fluid heated by dissipation exchanges heat with the fluid away from the wall, resulting in a slight reduction of the total enthalpy. This effect, as already noted, cannot be captured in the processing of the barotropic flow solution, which eventually results in a slight overestimate of the enthalpy close to the wall. Consequently, the mass fraction of vapour is slightly overestimated in barotropic estimation, although the discrepancy remains within 1% of the local nozzle-axis value.

The good accuracy of the barotropic flow solution is worth further physical investigations. As already remarked, the barotropic model implies to consider the fluid compressible but not thermally

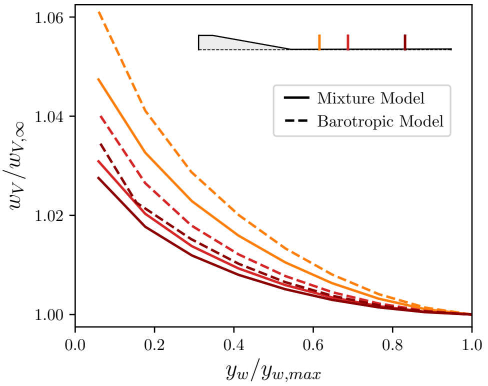

FIGURE 4.20. Vapour-mass fraction of case A normalised to the free-stream value at different axial locations, namely at $x = 10$ mm (orange lines), 20 mm (red lines) and 40 mm (dark-red lines).

expandable, i.e. to assume the thermal expansion coefficient $-\frac{1}{\rho}\left(\frac{\partial \rho}{\partial T}\right)_P$ equal to zero. Figure 4.21 reports the distribution of thermal expansion coefficient for the carbon dioxide in single-phase above saturation, including the liquid, the supercritical, and the superheated vapour region. To highlight the effects of thermal expansion, a logarithmic scale is used for the contours. The plot indicates that the carbon dioxide is prone to a thermal expansion only in a narrow region adjacent to the critical point, where the fluid exhibits severe gradients in all the thermo-physical properties. Among the thermo-physical properties of interest, in the critical region the isobaric heat capacity c_P grows significantly (becoming theoretically infinite at the critical point), as illustrated by the black dashed isolines superposed in the figure. The combination of high thermal expansion coefficient and high c_P in the critical region is a further indication of the technical relevance of the barotropic model: where thermal expansion is quantitatively significant, the amount of heat required to alter the fluid temperature is enormous and arguably not comparable with the heating due to viscous dissipation occurring in adiabatic flows.

The present theoretical interpretation indicates that the effects of the thermal expansion are limited for all cases investigated in this work, which are rather representative of technical applications such as compressors for sCO$_2$ power cycles. Therefore, if the above deviations between the simplified barotropic modeling and the thermodynamically complete mixture model are acceptable, the barotropic model would be recommended in the light of its computational robustness and efficiency.

4.6.3.2 Condensing flows

In condensing flows the primary phase is the vapour phase $\alpha_p = \alpha_V$, while the secondary phase is the liquid phase $\alpha_d = \alpha_L$. The phase change is activated when $P > P_{sat}(T)$.

The computational procedure resembles the one previously described for the cavitating case. Total pressure and total temperature are prescribed at the inlet section as in table 4.5 for the five flow configurations, imposing $\alpha_L = 0$ therein (the flow enters only in vapour phase). For the barotropic model, only the total pressure is specified. To impose the typical low turbulence level of a flow expanding from a reservoir, a hydraulic diameter equal to 12.6 mm, i.e. twice the height of the inlet section, and an eddy viscosity ratio equal to 2.5 are assigned as turbulent boundary conditions. As the flow regime is always supersonic, the solver ignores the static pressure value imposed at the

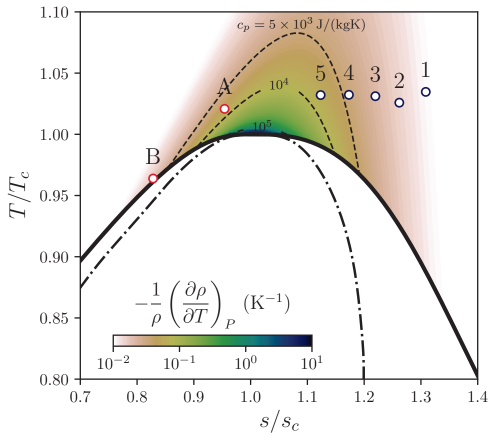

FIGURE 4.21. Volumetric coefficient of thermal expansion and isobaric specific heat (black dashed lines) for single-phase CO_2.

outlet. No-slip and adiabatic boundary conditions are prescribed at the wall, while a symmetry condition is imposed at the nozzle axis. Differently from the cavitation experiment, the nozzle used for the condensation study is of sufficiently large scale that the wall is modelled as smooth (the nozzle throat is one order of magnitude larger than that of the previous nozzle). Moreover, as a supersonic expansion always takes place in the diverging section, the effect of roughness is expected to be secondary in determining the flow evolution. The numerical schemes and the solver strategy are identical to the ones already introduced in §4.6.3.1. The penalty constant is set to $\mathcal{K} = 10^3$ as in the previous section. It is anticipated that the resulting constraint violation $P - P_{sat}(T)$ is limited to $\sim 1\%$ in the neighborhood of the phase-change onset, reducing of one order of magnitude in the ongoing expansion.

A grid convergence assessment was carried out by generating three structured meshes with an increasing number of elements. The number of elements was doubled each time in both x- and y-directions while keeping the same wall resolution. Coherently with the smooth-wall condition in combination to the $k - \omega$ SST turbulence model, the near-wall region of the mesh was constructed to avoid the use of wall functions and it is composed by 20 layers in the boundary layer, with a first-layer wall distance equal to 3×10^{-8} m. The maximum $y^+ = 1.2$ is found for case 5 with three cells within the viscous sub-layer ($y^+ < 10$). The flow model used in this grid study is the mixture model referring to the expansion closer to the thermodynamic critical point (case 5). Pressure, temperature, and liquid-mass fraction trends along the nozzle axis are reported in figure 4.22(*b*) alongside the turbulent kinetic energy distribution at a specified axial location ($x = 20$ mm). This latter quantity is reported in a logarithmic scale as a function of the dimensionless wall distance to better highlight the trend of the turbulent kinetic energy close to the wall. As in the previous section, the geometrical discretization error is quantified in table 4.9 by computing the GCI between the medium and the fine mesh of pressure, temperature and liquid mass fraction at the throat and at different axial locations along the diverging portion. The highest values are found at the throat location where the gradients are larger. In particular, the GCI for the liquid mass fraction is 2.53% as a consequence of the steep increase of the dispersed phase at the throat, see figure 4.22(*b*). Since the flow is supersonic, the mass-flow rate is determined by the flow conditions at the throat, and its estimate may be affected by the above gradients; however, the GCI for the mass flow rate is 0.02%. Such low value combined with GCIs smaller than 0.03% throughout the divergent

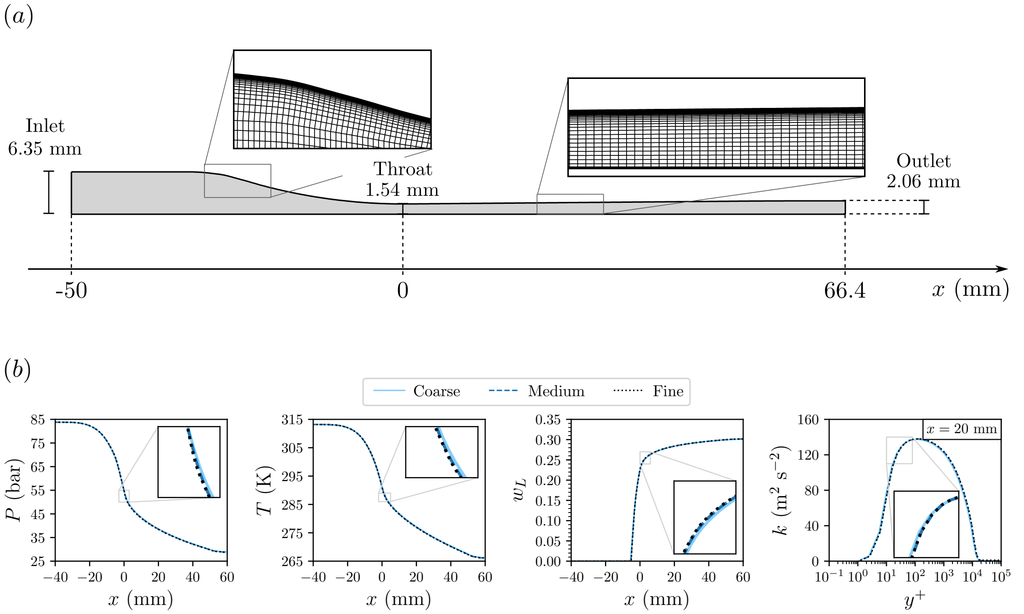

FIGURE 4.22. Grid-convergence assessment for condensing-flow simulations: (*a*) the medium mesh is selected as the grid-independent mesh (number of elements ≈ 5×10^4, grid resolution at the throat ≈ 2×10^{-4} m, 20 cells in the boundary layer with a first-layer wall distance of 3×10^{-8} m) alongside the main nozzle dimensions, (*b*) pressure, temperature, liquid-mass fraction and turbulent kinetic energy distributions for different grid refinements. The grid-convergence study is performed on case 5.

TABLE 4.9. Grid convergence indexes for pressure, temperature and liquid-mass fraction at selected axial locations along the diverging section. The grid-convergence study is performed on case 5.

	GCI		
x (mm)	P (%)	T (%)	w_L (%)
0	0.67	0.12	−2.53
15	0.03	0.00	−0.01
30	0.02	0.00	−0.01
45	0.01	0.00	0.00
60	0.00	0.00	0.00

testifies the adequacy of the medium mesh. Therefore, the medium mesh is selected for all the following analyses: it contains ≈ 5×10^4 hexahedral elements with a grid resolution at the throat of 2×10^{-4} m. Within the free-stream region, the aspect ratio is around 1.5 in the convergent, which raises up to 2.5 at the throat, then reducing to 2.0 in the divergent.

Figure 4.23 reports the comparison of pressure and the liquid-mass fraction distributions against experimental data for the five condensing flows. The differences in the distributions along the nozzle axis between the mixture and the barotropic do not exceed 1%. As the boundary layers remain confined in a narrow region close to the wall along the entire nozzle length, the barotropic model constructed using an isentropic P-ρ relationship provides an exact description of the thermodynamics of the fluid expansion in the core region of the nozzle, both in the single-phase

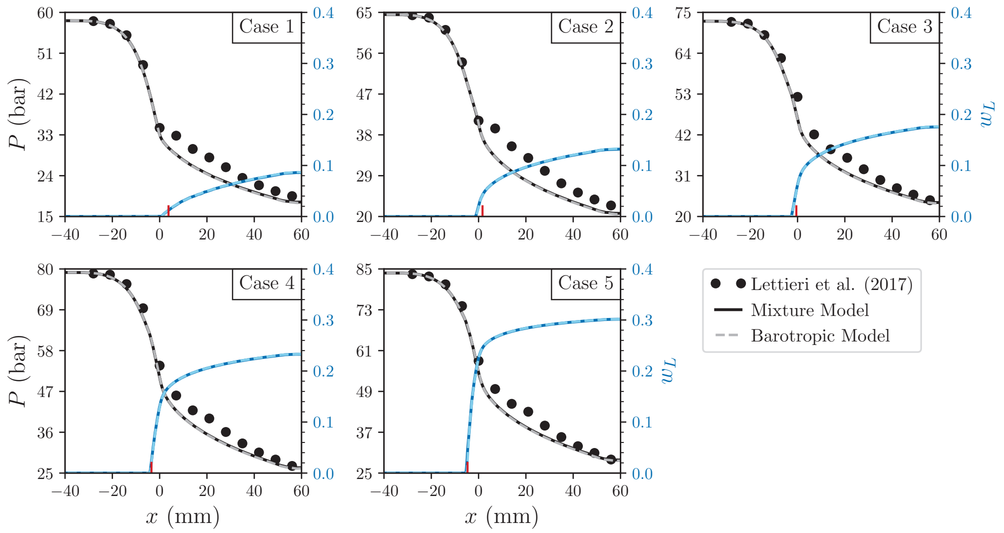

FIGURE 4.23. Comparison of the mixture (solid lines) and barotropic (dashed lines) model against experimental data along the nozzle axis. The red tick identifies the condensation onset observed experimentally by Lettieri *et al.* (Lettieri *et al.*, 2017, Tab. 3). The liquid-mass fraction predicted by the barotropic model is computed as post-processing.

TABLE 4.10. Comparison of the mass-flow rate predicted by the mixture and the barotropic model for all simulated condensing flows.

	$\dot{m}_{mix}$ (kg/s)	$\dot{m}_{baro}$ (kg/s)	$\varepsilon_{mix-baro}$ (%)
Case 1	29.43	29.46	0.08
Case 2	33.64	33.66	0.06
Case 3	38.97	38.99	0.04
Case 4	44.02	44.04	0.03
Case 5	48.94	48.95	0.02

and in the two-phase region - in the limit of a HEM two-phase flow representation. Further proof is provided by the excellent agreement (within 0.1%) of the mass-flow rate predicted by the two models, as reported in table 4.10. As the flow is supersonic, the mass-flow rate depends on the flow conditions at the throat. Depending on the specific case, the two-phase flow can already be established at the throat, confirming the quality of the barotropic modeling in also representing the two-phase flow.

When comparing the numerical results to the experiments in figure 4.23, the larger pressure discrepancy is found right after the onset of the phase change, where the experimental data exhibit a sudden change in the pressure trend. Furthermore, for the first two cases, an unconventional knee is noticed in the pressure trend close to the phase-transition onset, producing a concavity in the pressure trend which remains negative in the first part of the divergent. This feature is not captured by the models, which instead predict a more conventional pressure trend, which smoothly evolves from a negative concavity in the convergent to a positive concavity in the divergent. Such a peculiar trend in the experimental data probably originates from meta-stable equilibrium states, which

TABLE 4.11. Comparison of numerical predictions against experiments for condensing expansions.

	Case 1			Case 2			Case 3			Case 4			Case 5		
x (mm)	P_{exp} (bar)	P_{mix} (bar)	ε (%)	P_{exp} (bar)	P_{mix} (bar)	ε (%)	P_{exp} (bar)	P_{mix} (bar)	ε (%)	P_{exp} (bar)	P_{mix} (bar)	ε (%)	P_{exp} (bar)	P_{mix} (bar)	ε (%)
−28	58.08	58.02	0.1	64.38	64.36	0.0	72.44	72.46	0.0	78.77	78.88	0.1	83.47	83.63	0.2
−21	57.48	57.13	−0.6	63.85	63.41	−0.7	71.97	71.44	−0.7	78.46	77.84	−0.8	82.80	82.59	−0.3
−14	54.97	54.38	−1.1	61.14	60.53	−1.0	68.89	68.36	−0.8	75.94	74.70	−1.6	80.49	79.48	−1.3
−7	48.40	47.10	−2.7	54.01	53.08	−1.7	62.67	60.57	−3.3	69.42	66.98	−3.5	74.10	72.05	−2.8
0	34.54	33.08	−4.2	41.12	40.40	−1.8	52.24	46.04	−11.9	53.96	50.68	−6.1	57.99	54.54	−5.9
7	32.82	28.64	−12.7	39.41	33.14	−15.9	42.11	37.84	−10.1	45.90	41.83	−8.9	49.71	45.28	−8.9
14	29.89	26.14	−12.5	35.48	29.97	−15.5	38.11	34.28	−10.1	41.90	37.95	−9.4	45.35	41.17	−9.2
21	28.01	24.20	−13.6	32.91	27.65	−16.0	35.81	31.65	−11.6	39.71	35.09	−11.6	43.03	38.12	−11.4
28	25.87	22.57	−12.8	30.07	25.77	−14.3	32.74	29.53	−9.8	36.07	32.77	−9.1	38.95	35.64	−8.5
35	23.51	21.22	−9.7	27.31	24.20	−11.4	29.84	27.73	−7.1	32.99	30.81	−6.6	35.58	33.55	−5.7
42	21.89	20.03	−8.5	25.28	22.83	−9.7	27.63	26.18	−5.3	30.55	29.10	−4.7	32.90	31.72	−3.6
49	20.59	18.98	−7.8	23.75	21.63	−8.9	25.89	24.80	−4.2	28.63	27.59	−3.6	30.91	30.09	−2.6
56	19.50	18.24	−6.5	22.43	20.78	−7.3	24.39	23.84	−2.3	26.92	26.53	−1.5	28.98	28.94	−0.1

are expected to be prominent far from the critical point, delaying the phase transition. Lettieri *et al.* (2017) actually identified meta-stability effects in their results and even derived experimental samples of the Wilson line. They actually found that the largest departure from conventional saturation applies for cases 1 and 2, consistently with the largest discrepancy found in the present study, with a maximum of 16% for cases 2. Apart from the peculiar trend in correspondence of the phase transition onset, the overall pressure distribution is properly captured by the model. The global deviation in accordance with the error defined in equation 4.22 is quantified as 5.7% and 6.4% for cases 1 and 2, respectively.

The agreement between experiments and simulations improves as long as the upstream stagnation state gets closer to the thermodynamic critical point. For these cases, the meta-stability effects are reduced, although they are still present as reported in the experimental reference. An obvious development of this work would be to include meta-stable states in the mixture model formulation, e.g. in a DEM fashion, notwithstanding the cases of most interests for sCO$_2$ compressors are those in the proximity of the critical point (cases 4 and 5), for which deviations less than 10% are observed with respect to most of the experimental data. The overall trend is generally well captured, with a WMAPE of 4.5% and 4.1% for cases 4 and 5, respectively. All local deviations with respect to the available measurements are quantified in table 4.11.

Despite the meta-stability effects discussed above, it is worth highlighting that the present simulation model predicts the condensation onset in a very good approximation for all the cases. In the experiment, the position of transition onset was derived from optical measurement, and it is reported in the frames of figure 4.23 as a red tick. In fact, a slight discrepancy is found for the cases far from the critical point (Cases 1 and 2), while a perfect matching is achieved for the expansions evolving from a supercritical state (Cases 4 and 5). This is fully consistent with the above meta-stability effects, but it is also noted that the experimental identification of condensation point may be affected by a larger uncertainty for Cases 1, 2, and 3. In such cases, the transition is smoother and it is not straightforward to exactly identify the axial location at which the phase change starts, see (Lettieri *et al.*, 2017, Figure 9). The opposite occurs for the near-critical cases 4 and 5, for that the identification is made easier by the rapid growth of the condensed mass fraction, and the matching with the experiment becomes excellent.

The corresponding mass-fraction flow fields computed by the mixture models are reported in figure 4.24. The flow fields are qualitatively similar to the experimental visualization, in which the condensation location moves back in the nozzle while the upstream thermodynamic state gets closer to the critical point.

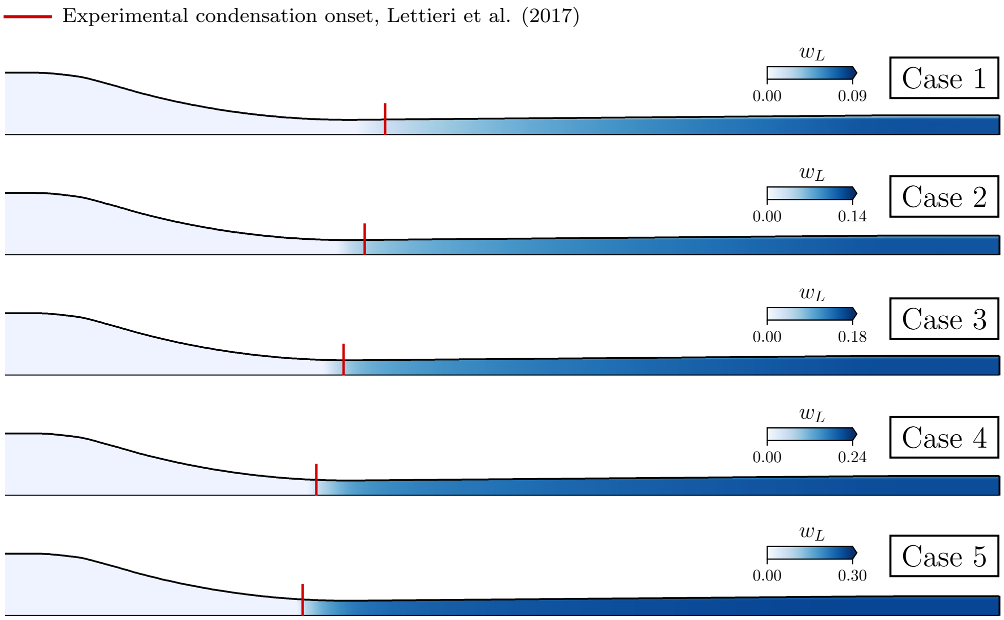

FIGURE 4.24. Liquid-mass fraction distributions for the five condensing flows as predicted by the mixture model. The red tick identifies the condensation onset observed experimentally by Lettieri *et al.* (2017, Tab. 3)

4.6.4 Mixture speed-of-sound formulation

The two computational models introduced in this work are shown to reproduce, with good or acceptable accuracy, the experimental results of compressible two-phase flows, both for cavitation and condensation. Since both models are built on the two-fluid concept, which describes the mixture evolution without detailing the local interfaces between phases, the concept of speed of sound can be extended to the mixture and a 'surrogate' expression for that can be defined.

The definition of the mixture speed of sound is closely linked to the employed two-phase model and its associated assumptions (De Lorenzo *et al.*, 2017*a*,*b*). Moreover, it was demonstrated that the more the system is constrained, the lower the corresponding speed of sound (Flatten & Lund, 2011; Pelanti & Shyue, 2019). It means that the HEM speed of sound will be lower than the speed of sound of an HFM, which relaxes the thermal equilibrium assumption. Specifically, the HEM speed of sound is expressed as:

$$c_{mix}^2 = \left(\frac{\partial P}{\partial \rho_{mix}}\right)_s \tag{4.23}$$

Given the assumptions of the mixture and barotropic model, this relationship is expected to be used in the determination of the speed of sound and to assess whether or not the flow regime is supersonic. By default, Ansys-Fluent® makes use of the speed-of-sound formulation originally conceived by Wood (1941):

$$\frac{1}{\rho_{mix} c_{mix}^2} = \frac{\alpha_L}{\rho_L c_L^2} + \frac{\alpha_V}{\rho_V c_V^2} \tag{4.24}$$

The expression says that the bulk modulus of the mixture $\rho_{mix} c_{mix}^2$ is the harmonic average of the bulk moduli of the components weighted on their volume fractions. Such definition is

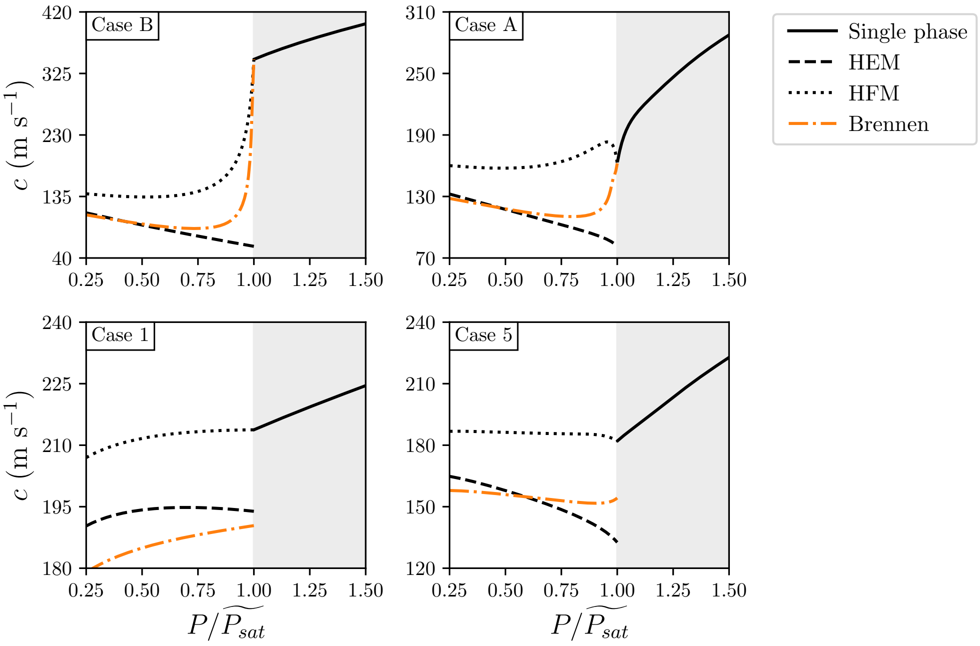

FIGURE 4.25. Comparison among different two-phase speed-of-sound formulations: homogeneous equilibrium model (Equation 4.23), homogeneous frozen model (Equation 4.24) and an hybrid formulation between the homogeneous equilibrium model and the homogeneous frozen model proposed by Brennen (2005) (Equation 4.26).

derived on the basis of the single-phase volumetric behaviours, hence it excludes any thermal effects between them. For this reason, it can be used under HFM assumptions and it is widely used in presence of multi-component flows which do not chemically react. In analogy with the analysis of Giacomelli *et al.* (2018), the definition of the mixture speed of sound provided by Brennen (2005) is also included.

$$\frac{1}{\rho_{mix}c_{mix}^2} = \frac{\alpha_V}{P}[(1-\epsilon_V)f_V + \epsilon_V g_V] + \frac{\alpha_L}{P}[(1-\epsilon_L)f_L + \epsilon_L g_L] \tag{4.25}$$

which considers that a portion of the phases can exchange heat and momentum instantaneously (ϵ_L, ϵ_V), promoting equilibrium, and the remaining portion ($1-\epsilon_L$, $1-\epsilon_V$) does not contribute to the exchange, promoting disequilibrium. In this way, depending on the portion of fluid involved in the phase change, either the HEM ($\epsilon_L = \epsilon_V = 1$) or the HFM ($\epsilon_L = \epsilon_V = 0$) can be recovered. On top of that, Brennen suggested the following approximations: $f_V = g_V \approx 1$, $f_L \approx 0$, $\epsilon_L \approx \alpha_V$, and $g_L \approx 2.1(P/P_c)^{-0.566}$ for carbon dioxide only. Plugging into equation (4.25) the above simplifications, the following expression for the mixture speed of sound is obtained:

$$\frac{1}{\rho_{mix}c_{mix}^2} = 2.1\frac{\alpha_L\alpha_V}{P^{1.566}}P_c^{0.566} + \frac{\alpha_V}{P} \tag{4.26}$$

Figure 4.25 reports the speeds of sound computed according to three expressions (4.23), (4.24) and (4.26) for isentropic expansions of cavitating (case A and B) and condensing (case 1 and 5) flows. The HEM speed of sound exhibits a discontinuity at saturation (Flatten & Lund, 2011), which is more pronounced for cavitating flows. Interestingly, the HEM speed of sound generally increases along isentropic expansion (unless case 1, which is far from the critical point and applications of interest) while the single-phase carbon-dioxide speed of sound always decreases along the isentropic expansion. Such evidence can be interpreted in terms of the fundamental derivative of the gas dynamics Γ, which is lower than the unity in the two-phase region of carbon dioxide. Moreover, under the HEM assumptions, $\Gamma < 0$ in the near-critical two-phase region (Nannan *et al.*, 2013), paving the way for the occurrence of non-classical effects (Thompson & Lambrakis, 1973). The HFM expression constantly overpredicts the speed of sound compared to the HEM predictions in accordance with the above explanation related to the equilibrium assumptions and associated speed-of-sound values. Regarding Brennen's expressions, as the simplified derivation was conceived between HEM and HFM, the speed of sound should be contained among the corresponding HEM and HFM values. When looking at cavitating cases, Brennen's formulation does exactly what it is meant to be. Right after the phase transition, the disequilibrium between phases is expected to be maximum and for this reason the speed-of-sound value is larger than the corresponding HEM value. However, as long as the expansion process proceeds, the two expressions collapse in a good approximation. It is worth specifying that the expression (4.26) shows a spike for cavitating flows at saturation, possibly due to the approximations that were introduced. To avoid this unphysical behaviour, the maximum speed of sound was limited at the single-phase speed of sound. On the other hand, when Brennen's formulation is applied to condensing flows, unphysical trends are obtained: in case 1, Brennen's speed of sound is lower than the corresponding HEM value, which is not admissible as the HEM should be the lowest among all speed-of-sound formulations. Approaching the critical point, as in case 5, it seems to recover the correct trend (similar to cavitating flows), but as long as the expansion proceeds, Brennen's expression tends to underestimate the HEM value with a non-negligible error. Finally, it is noted that the discontinuity in the speed of sound predicted by the HEM formulation is generally smaller in condensing flows than cavitating flows, as reported in figure 4.25 for exemplary upstream conditions. From this analysis, it is concluded that the expression provided by Brennen can be effectively used in modelling cavitating flows, while it is not adequate for condensing flows of carbon dioxide.

The three speed-of-sound formulations are then applied in the post-processing of case A (cavitation) and case 5 (condensation), which are the cases closest to the critical point among those presented in this work for the two categories of phase transition. Analogous studies involving the HFM and Brennen's formulation are reported in Yazdani *et al.* (2012); Giacomelli *et al.* (2018) for cavitating flows. To the authors' knowledge, similar studies for condensing flows are not available.

Figure 4.26 displays the Mach number fields for case A (cavitation). Specifically, figure 4.26(*a*) is the Mach number field as provided by Ansys-Fluent® for the mixture model, while figures 4.26(*b*–*d*) are obtained by setting the three different speed-of-sound formulations in the equation (4.21) of the barotropic model. First, the nearly identical distributions obtained in figure 4.26(*a*)–(*b*) confirms that the present version of Ansys-Fluent® makes uses of equation (4.24) as post-processing for the mixture speed of sound. As a consequence of the higher speed of sound under HFM assumptions, the Mach number is everywhere lower than unity, reaching the maximum value of $M = 0.82$ at the nozzle outlet. In accordance with figure 4.25, the main difference between figure 4.26(*c*)–(*d*) is located at the phase-transition onset, in which the HEM model predicts a sudden drop. Brennen's formulation instead smears the discontinuity, then recovering approximately the same Mach number evolution predicted by the HEM formulation towards the nozzle outlet, in which a slightly supersonic Mach number ($M = 1.06$) is predicted.

As a final comment, the Mach number field obtained with Brennen's model, which accepts a degree of disequilibrium, does not diverge significantly from solutions obtained with HEM simulation tools. This finding provides a crucial indication of the technical relevance of CFD

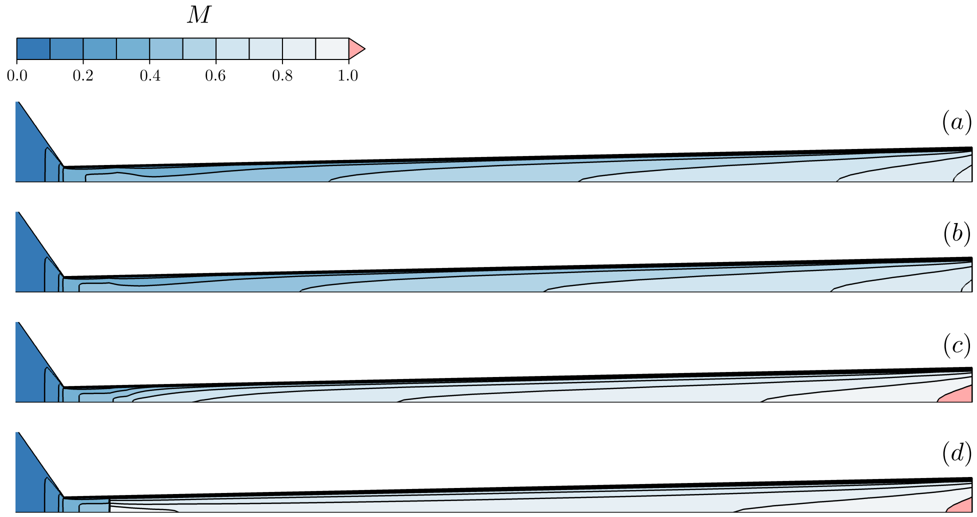

FIGURE 4.26. Mach number distributions for the case A (cavitating flow) using different two-phase speed-of-sound formulation: (a) Ansys-Fluent® mixture-model built-in formulation, (b) HFM, (c) Brennen, (d) HEM. For visualization purposes, the x-direction is stretched such that $x/y = 0.125$ and the convergent section is not shown.

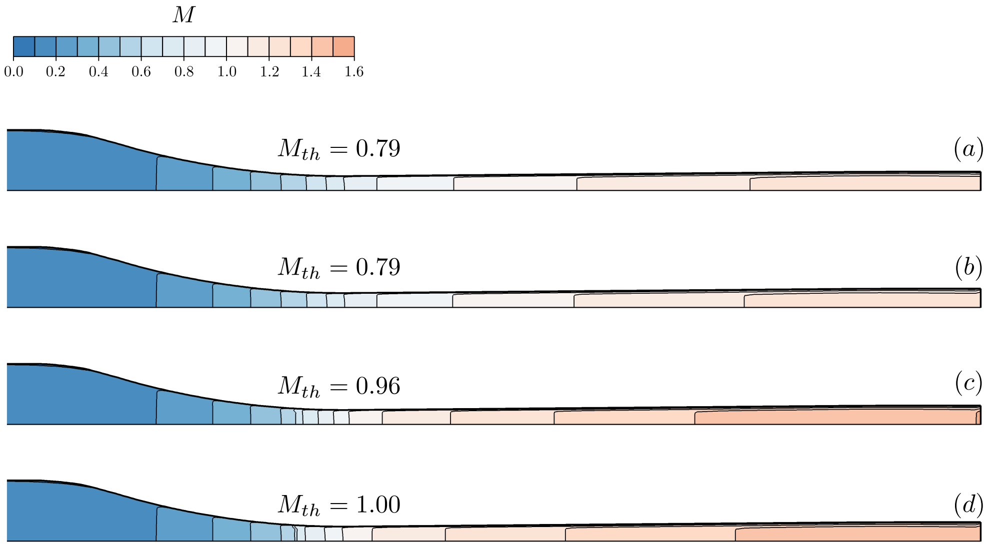

FIGURE 4.27. Mach number distributions for the case 5 (condensing flow) using different two-phase speed-of-sound formulation: (a) Ansys-Fluent® mixture-model built-in formulation, (b) HFM, (c) Brennen, (d) HEM. The Mach number at the geometrical throat M_{th} is also reported.

simulation tools based on the assumption of homogeneous equilibrium for sCO_2 compressor design and analysis, especially when it comes to the identification of the choking limit.

A similar analysis is illustrated in figure 4.27 for case 5 (condensation). Again, the default choice of Ansys-Fluent® , which corresponds to the HFM formulation, provides the lowest Mach

Table 4.12. Compressor requirements and overall boundary conditions.

Design conditions				
P_1^t	T_1^t	s/s_c	β	$\dot{m}$
78.7 bar	32 °C	0.93	3.25	413.4 kg/s

number, with the onset of the sonic Mach number after the geometrical throat. Although the sonic throat may be different from the geometrical one when the boundary layer is considered, the streamwise location where the sonic Mach number onsets seems not consistent with the boundary-layer displacement thickness. This observation corroborates the idea that the expression for the speed of sound in (4.24) is not consistent with the HEM governing equations. On the other hand, the HEM expression (4.23) predicts a sonic Mach number in the geometrical throat, consistently with the assumptions of the model. As a matter of fact, in presence of mechanical and thermal equilibrium among phases, the single-phase gas dynamics should be theoretically recovered for the mixture. Finally, although the supersonic expansion in the divergent, with an outlet Mach number larger than the HEM counterpart, Brennen's model does not predict a sonic Mach number at the throat; as already mentioned, the corresponding speed of sound exhibits an unphysical trend when applied to condensing flows.

4.7 Compressor design and off-design analysis in near-critical conditions

Once computational methods have been developed and validated for sCO_2 flows in near-critical conditions, the natural continuation is to apply them for the simulation of a realistic centrifugal compressor to understand how the compressor aerodynamics is affected by both non-ideal and two-phase effects.

To produce a meaningful compressor design for sCO_2 applications, preliminary cycle considerations are needed to set compressor boundary conditions and targets. The cycle layout and assumptions are reported in §4.5, making use of correlations developed for the turbomachinery efficiency. For this specific task, the hot-source temperature is fixed at $T_{max} = 550\,°C$, while the minimum cycle temperature is $T_{min} = 32\,°C$. The target electrical power is $\dot{W}_{el} = 50\,\mathrm{MW_{el}}$. According to Crespi *et al.* (2017*b*), this temperature range and power can fit both nuclear (Moisseytsev & Sienicki, 2009) and concentrating solar power applications (Padilla *et al.*, 2016). To derive the remaining conditions, the power cycle is optimized following the procedure outlined in §4.5. The optimal cycle obtained in this way sets the boundary conditions of the main compressor, which are best summarized in table 4.12.

A single-stage compressor is considered to have reduced costs and footprint. The saturation pressure along an isentropic expansion from the upstream thermodynamic state is $P_{sat} = 71.0\,\mathrm{bar}$, leading to a safety margin between the intake state and saturation condition lower than ten bars. All these aspects, i.e. non-ideal effect, occurrence of two-phase flows, high blade loading, potential transonic/supersonic flow regimes, lead to an extremely complex aerodynamic design, which will be the core of the following discussions.

4.7.1 Impeller design

The preliminary design aiming at establishing the main geometrical dimension is carried out with the aforementioned mean-line model. The mean-line code was run parametrically for several design variables to seek the highest compressor efficiency while complying with the requirements

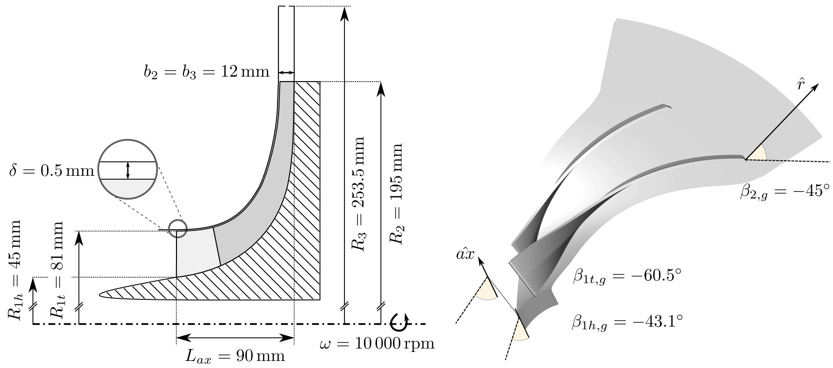

FIGURE 4.28. Meridional channel of the reference impeller geometry along with the main geometrical dimensions. The impeller has 8 main blades plus 8 splitter blades. The main and splitter blade are reported on the right along with the geometrical angles.

described in the previous section. A parametric study was preferred over a blind optimization technique to have a track of different compressor designs with comparable performance, then making a final decision based on the minimization of phase-change triggers (e.g., blade blockage and inlet velocities). Although the mean-line model includes all compressor components, only the impeller is considered for the detailed design hereinafter, as two-phase and non-ideal effects become marginal as long as the compression takes place.

As for the inlet section, the shaft diameter was determined by means of simplified mechanical calculations accounting for the transmitted power. Then, the hub diameter D_{1h} is selected assuming a safety factor of 1.08 on the shaft diameter, thus ensuring a torque transmission without mechanical issues. Given the hub diameter, the blade height b_1 was chosen to minimize the tip Mach number in the rotating frame of reference $M_{w,1t}$. During this phase, the inlet blade angle $\beta_{1,g}$ was constrained in the range $-80° \div -10°$ to prevent an excessive flow distortion. The number of blades is varied as well, also considering splitter blades. Notwithstanding comparable performance, the splitter configuration is ultimately selected, with splitters starting at the normalized full-blade streamwise location $s_{norm} = 0.175$. This choice represents a convenient trade-off between a reduction in the blade blockage at the inlet and a reduction of the blade loading due to the increased blade solidity at the splitter location. The rotational speed was also part of the parametric investigation, and it was varied in the range $8\,000 \div 13\,000$rpm. As for the outlet section, the absolute flow angle was constrained in the range $60° \div 75°$; the upper limit was imposed to prevent an excessive tangential flow direction in off-design conditions, which may be responsible for earlier instabilities in the diffuser component. To this end, backward blades ($\beta_{2,g} < 0°$) are chosen and varied in the range $-55° \div -35°$. Finally, an open impeller design is considered with a tip clearance of 0.5 mm.

From this analysis, a candidate compressor was selected and depicted in the left frame of figure 4.28 alongside the main geometrical dimensions. The design flow coefficient is $\phi = 0.021$, and the design peripheral Mach number is $M_{u_2} = 0.86$. Thanks to the combination of a liquid-like density and a gas-like viscosity, the peripheral Reynolds number $Re_{u_2} = 10^9$ is significantly higher than conventional air-breathing compressors, hence fully turbulent flows are expected.

The step from a mean-line design in terms of main geometrical quantities to a complete compressor prototype requires the definition of the blade profiles and the three-dimensional stacking. As for the blade profiles, the mean-line code provides information about the geometrical angles at the inlet and outlet sections. In particular, the inlet section is split into three relevant sections, namely the hub (0% span), midspan (50% span), and tip (100% span) section. As a result of the

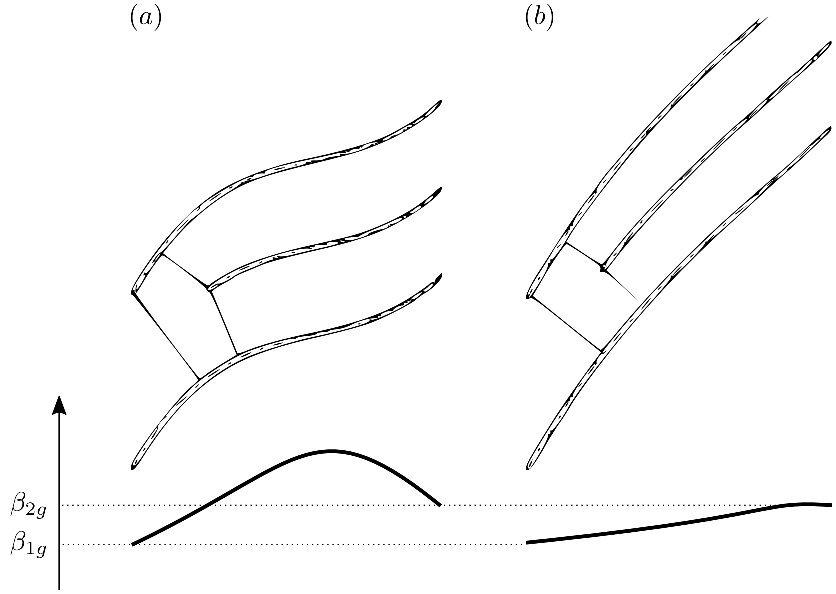

FIGURE 4.29. Influence of the wrap angle on the blade angle distribution: (*a*) low wrap-angle profile, and (*b*) high wrap-angle profile.

mean-line analysis, the geometric angles at these three sections are $\beta_{1,g} = -43.1°, -53.7°, -60.5°$, respectively, assuming optimal incidence (Whitfield & Baines, 1990). The outlet geometrical angle results $\beta_{2,g} = -45°$. Given these boundaries, several blade angle distributions are available to pass from inlet to outlet blade angle. In the context of sCO_2 centrifugal compressor, the choice of the blade angle distribution is particularly crucial, because it directly sets the aerodynamic loading in the front part of the blade. The more the front blade is loaded, the more the flow locally accelerates on the suction side, the more the local thermodynamic state penetrates inside the saturation dome. One key parameter that controls the blade loading is the wrap angle φ, i.e. the angle between the meridional plane passing through the leading edge and the one passing through the trailing edge.

A low wrap-angle profile, sketched in figure 4.29(*a*), is characterized by a limited wetted surface, thus limiting the skin-friction loss. For the same reason, the aerodynamic loading is generally high because it is concentrated on a smaller blade length. As a consequence, the fluid accelerating on the front part of the blade is more prone to phase transition. By increasing the wrap angle, the blade extends for a larger part of the circumference, hence the loading is distributed on a larger blade surface. The loading rise is generally smoother, as evidenced in figure 4.29(*b*) for an exemplary high wrap-angle profile. Although local accelerations prompted by the aerodynamic loading are reduced in this latter configuration, the available area for the flow passage is reduced as well, see the clear reduction in the impeller throat between the two examples in figure 4.29. A smaller impeller throat also promotes phase-change phenomena because the flow has to accelerate to compensate for the reduction in the flow passage. At the same time, a high wrap angle contributes to a long and narrow (i.e. of small hydraulic diameter) blade channel. From this analysis, it is clear that a trade-off in the wrap angle has to be found to reduce the skin friction and diffusion losses and, at the same time, the occurrence and the extension of phase transition in sCO_2 centrifugal compressor operating in near-critical conditions. For the present design, after preliminary CFD runs, a relatively high-wrap angle is selected, i.e. $\varphi = 85°$.

To ease the blade manufacturability, the three-dimensional profile stacking is performed with the Flank-Milling technique. The blade thickness distribution varies linearly from 2 mm at the leading edge to 3mm at the trailing edge regardless of the radial coordinate. The leading edge is generated with an ellipse arc with a ratio among semi-axis of 2.5. The trailing edge is cut-off at R_2. The final three-dimensional impeller shape is displayed in the right frame of figure 4.28.

4.7.2 Impeller performance maps at variable intake conditions

The barotropic model is exploited to simulate the above impeller geometry. It is worth recalling that the advantages of the barotropic model over a complete HEM are (i) a reduced computational cost, capitalizing the lower number of partial differential equations to be solved as well as a reduced cost for the computation of non-ideal thermodynamic properties, and (ii) enhanced numerical stability, as the large gradients with respect to temperature in thermo-physical properties are avoided. The improved solver robustness is particularly attractive in the context of compressor simulations due to the highly non-uniform flow subject to the adverse pressure gradient. Moreover, the adequacy of barotropic modeling for simulating compressible two-phase non-ideal flows in turbomachinery applications (with negligible heat transfer) was also demonstrated by Persico *et al.* (2021), who showed that local flow differences between barotropic and real-gas simulations were limited to 0.1% in the free-stream region and 0.5% in the boundary layers. The overall pressure ratio and isentropic efficiency were estimated with an error of 0.05% by the barotropic model. Preliminary calculations for entropy levels below the critical one have seemingly confirmed the suitability of the barotropic modelling for centrifugal compressor simulations also in presence of two-phase flows.

The barotropic model is implemented in ANSYS-CFX®, using a logistic function to interpolate separately the two branches (single- and two-phase) of the barotropic function with fifth-order polynomials. Simulations are performed assigning at the inlet total pressure and axial flow. The gross turbulence effect is introduced with the $k - \omega$ SST (Menter, 1994) model, providing as boundary conditions at the inlet a turbulence intensity equal to 5% and eddy viscosity ratio equal to 1. At the outlet, the mass flow rate was assigned at the design flow coefficient, while an average static pressure, accepting 5% of variability across the outlet domain, is assigned and varied each time to generate the off-design performance maps. No-slip boundary conditions are imposed to the solid walls, also assuming a sand-grain roughness of 6.2 μm (converted from an average roughness of $\sim$ 2 μm as representative of standard technological processes). Due to the large Reynolds number, the viscous sub-layer is expected to be smaller by around two orders of magnitudes than the expected roughness level, pointing to the significance of roughness effects on the boundary layer development. Counter-rotating boundary conditions are assigned both at the shroud (to simulate an open impeller with a tip clearance of 0.5 mm) and at the impeller outlet domain (to simulate a stationary vaneless gap). Finally, periodic boundary conditions are exploited to simulate a single flow passage containing both the main and the splitter blade as in figure 4.28 (right frame), placing the inlet and outlet interface sufficiently far from the impeller to avoid spurious pressure reflections in all design and off-design conditions. A TVD numerical scheme available in the commercial software is used in the discretization of the flow advection term, while the diffusion term is discretized with a second-order central difference scheme. The advection term in turbulence equations is discretized with a first-order upwind scheme.

Meshes are generated with ANSYS-Turbogrid®. A cell clustering is imposed close to the walls, with a center-cell distance of the first layer from the wall approximately equal to the sand-grain roughness, thus resorting to modified wall function to properly account for the roughness effects. Three hexahedral meshes are considered with an increasing number of elements, allocated as in the table 4.13. In terms of integral quantities, only small differences are found among the three meshes, with a maximum discrepancy in terms of isentropic efficiency of 0.15 percentage points between the coarse and the fine mesh. Some visible differences are found in the resolution of the flow field, especially in the front part of the blade where two-phase supersonic flows are established with consequent compression waves. The results are summarized in figure 4.30, where the blade loading

TABLE 4.13. Cell distributions across different grid refinements for the impeller.

	Coarse	Medium	Fine
Blade span	31	52	72
Tip clearance	9	18	28
Impeller blade-to-blade	2.5×10^4	7.5×10^4	1.5×10^5
Overall cells	1.0×10^6	8.8×10^6	2.4×10^7

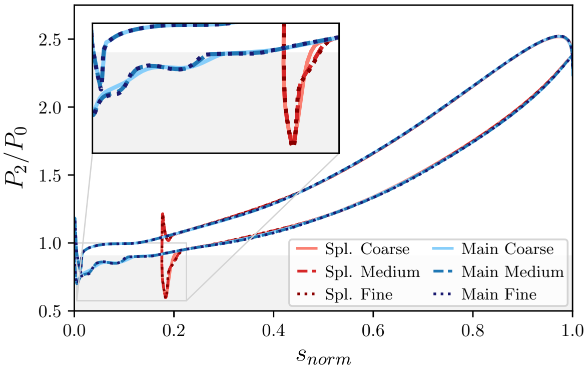

FIGURE 4.30. Blade loading distributions of the main and splitter blade at midspan for different grid refinements. The grid convergence is undertaken considering the intake thermodynamic state of case 1. The grey area identifies the region $P < \widetilde{P_{sat}}$, for which two-phase flows are established.

of the main and splitter blade is reported for the three meshes. The medium mesh closely follows the trends of the finer mesh, while the coarse mesh considerably smooths the loading distribution in the front part of the blades, albeit recovering a good agreement afterward. The medium mesh is ultimately selected for the following analyses as it provides a complete flow description at the minimum computational cost.

Besides the thermodynamic efficiency, the success of the sCO_2 closed cycle also lies in the superior flexibility at off-design conditions compared to conventional systems. However, such flexibility is based on the ability of the centrifugal compressor to provide the required head over an adequate range (Alfani *et al.*, 2020). Whenever the working fluid does not change and can be approximated as a perfect gas, the performance maps of a compressor can be generally expressed in terms of the following dimensionless parameters (Casey & Robinson, 2012):

$$\Psi, \eta = f(\phi, M_{u_2}, Re_{u_2}) \tag{4.27}$$

The functional dependency in equation (4.27) is referred to as *ideal similarity* hereinafter. If Re_{u_2} is large enough, the flow within the compressor is expected to be fully turbulent, and the performance will only depend on the flow coefficient ϕ and peripheral Mach number M_{u_2}. The above expression ensures that if two compressors are geometrically similar and share the same dimensionless parameters, then their performance and flow range will be equal. The problem can be also generalized if the working fluid changes. Sometimes, it is required to replace the working fluid during experimental tests for safety and cost reasons (especially in the field of sCO_2, which has to be operated at high pressure (Allison *et al.*, 2019)), with the goal of drawing general considerations on the expected in-field performance. In such cases, if the two working fluids can be approximated as perfect gases and the geometries are homotetically scaled, then the ideal similarity

TABLE 4.14. Different upstream thermodynamic conditions investigated in this study.

Case	P_1^t (bar)	T_1^t (K)	s/s_c	State
1	78.7	305.15	0.93	Supercritical Liquid
2	72.7	302.15	0.91	Subcritical Liquid
3	75.7	306.15	1.10	Supercritical Vapour
4	69.7	303.15	1.15	Subcritical Vapour

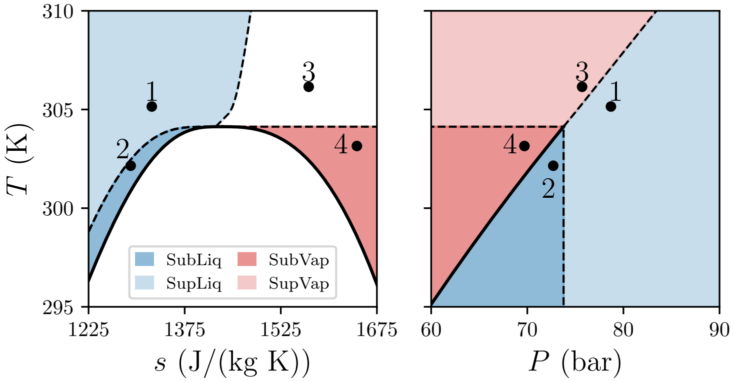

FIGURE 4.31. Intake thermodynamic states selected for the off-design conditions. The choice encompasses subcritical ($T < T_c$ and $P < P_c$) and supercritical (otherwise) states in both liquid-like and gas-like region.

can be complemented with γ, i.e. the ratio between specific heats, which conveniently summarizes any change in the gas dynamics prompted by the different fluid nature.

When it comes to compressors operating in near-critical conditions, two concerns arise about the generality of equation (4.27): non-ideal effects affect the compressor aerodynamics (Baltadjiev *et al.*, 2015; Ameli *et al.*, 2018*b*) and two-phase flows can originate from local accelerations (Pecnik *et al.*, 2012; Hosangadi *et al.*, 2019).

To test the similitude theory for centrifugal compressors that operate close to the thermodynamic critical point, four compressor-intake thermodynamic states are further considered in this study, as reported in table 4.14. 4.31. Any difference between a liquid and vapour phase vanishes close to the critical point, and in this region the supercritical fluid is neither a liquid nor a vapour but something in between. Some authors refer to the pseudo-critical line (Sengupta *et al.*, 2017), i.e. the locus of the maximum isobaric heat capacity at a given temperature, to set a boundary between the liquid and vapour phase in supercritical conditions. Across this line, all thermodynamic and transport properties exhibit sharp gradients against small variations in temperature. Based on this boundary, two states, one subcritical ($T < T_c$ and $P < P_c$) and one supercritical (otherwise) are selected in both the liquid and the vapour domain, see figure 4.31. It is worth stressing that the selected states feature variations in pressure and temperature that are consistent with those expected during start-ups, plant regulations and seasonal changes.

The barotropic equations of state for the four intake conditions are reported in figure 4.32. As previously mentioned, the approach is based on the use of the logistic function to merge the two polynomial interpolations for the single- and two-phase branch into a single analytical expression (as deemed by the commercial solver), returning a maximum discrepancy of 0.3% around the saturation pressure.

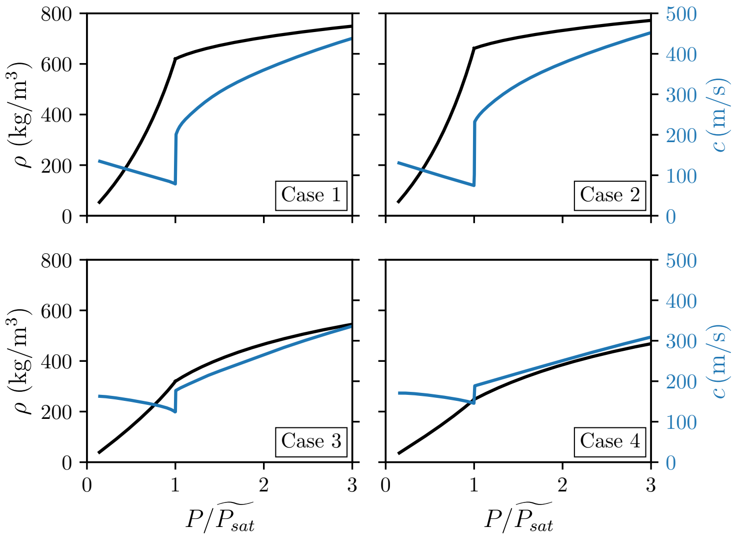

FIGURE 4.32. Barotropic equation of state $\rho = \rho(P)$ for the selected four intake thermodynamic states, alongside the speed of sound predictions under homogeneous equilibrium assumption.

As the scope of the present investigation is to assess how compressor performance changes in presence of non-ideal and multi-phase effects, the simulation of the sole impeller is further justified because it represents the region most affected by these phenomena. As long as the fluid is compressed, the thermodynamic state moves away from the critical point, in which non-ideal effects are predominant. Likewise, the phase transition is expected to occur at the blade intake region (Pecnik *et al.*, 2012; Hosangadi *et al.*, 2019), due to the vicinity of the local thermodynamic state to the saturation curve, which combines with local accelerations prompted by the blade blockage, front-loading, and incidence.

The impeller performance maps at different upstream total states are generated over the whole flow range by fixing the design peripheral Mach number $M_{u_2} = 0.86$ for all intake thermodynamic conditions reported in figure 4.31. In these conditions, the peripheral Reynolds number Re_{u_2} always exceeds 10^8, hence the flow can be safely assumed as fully turbulent in all conditions (Reynolds self-similarity).

All quantities are computed as mass averaged at the impeller trailing edge, with the only exception of the static pressure, which is area-averaged. The resulting performance maps in terms of isentropic head coefficient and pressure ratio are reported in figure 4.33 for the four conditions. The isentropic work coefficient Ψ is preferred over the real work input coefficient λ because it isolates the amount of work required for the actual pressure rise (useful effect). It is immediately evident that the four curves do not collapse in a single curve expressed in dimensionless form, as instead predicted by the ideal similarity in equation (4.27). The four curves differ both in terms of performance, with minor variations in the isentropic head curve but larger discrepancies in the delivered pressure ratio, and range, in which the right flow limit (choking) passes from 94% of case 2 to 166% of case 4 (the percentage is computed with respect to the design flow coefficient). As widely discussed, two effects that are not observed in conventional gas compressors are instead prominent when operating in near-critical conditions: non-ideal effects owing to complex thermodynamics for the single-phase flow and the occurrence of two-phase compressible flows at the impeller-intake region. It is shown in the following sections how these two effects combine in determining the observed deviations of dimensionless performance from the well-known ideal similarity.

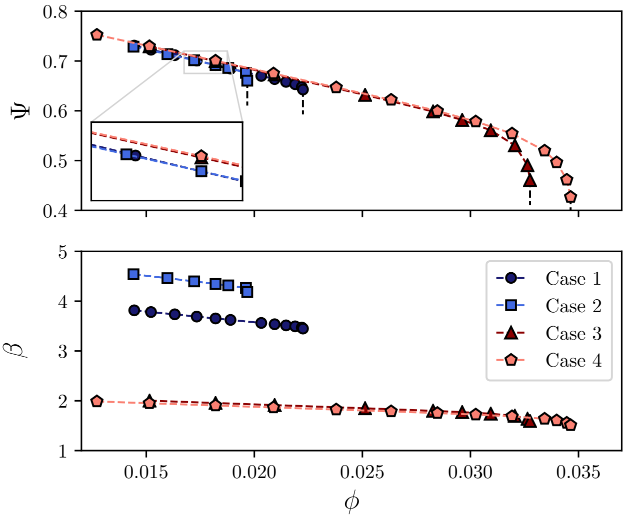

FIGURE 4.33. Performance maps for the selected intake thermodynamic states in terms of isentropic head coefficient and impeller pressure ratio at fixed peripheral Mach number $M_{u_2} = 0.86$ and Reynolds effects $Re_{u_2} > 10^8$ (ideal similarity).

4.7.2.1 Non-ideal effects - influence of k on performance maps

As already mentioned in the introductory section, the well-known ratio of specific heats γ is meaningless in presence of non-ideal fluids, i.e. not obeying the ideal-gas thermodynamics. Instead of γ, alternative coefficients can be defined for non-ideal flows depending on which isentropic relationship is considered (Kouremenos & Antonopoulos, 1987). For turbomachinery flows, the pressure-volume relationship is strictly connected with the work exchanged, hence a thermodynamic coefficient that links the pressure with the volume (or, equivalently, density) variation along an isentropic process is expected to affect the compressor aerodynamics. Such coefficient can be conveniently defined as:

$$k \overset{\text{def}}{=} -\frac{v}{P}\left(\frac{\partial P}{\partial v}\right)_s = -\frac{v}{P}\frac{c_p}{c_v}\left(\frac{\partial P}{\partial v}\right)_T \tag{4.28}$$

k is referred to as generalized isentropic coefficient in this work. By integrating its definition under the assumption that k is constant, the well-known isentropic relationship Pv^k = const can be recovered. Actually, k is not constant along the thermodynamic process, hence an average value $\bar{k}$ depending on the process is introduced to obtain the same isentropic relationship in an approximated manner, i.e. $Pv^{\bar{k}} \approx$ const. It can be easily proved by the second identity in equation (4.28) that k reduces to γ when the ideal-gas model is considered. Nonetheless, the strength of k lies in its general definition, which does not depend on the specific equation of state while preserving its physical meaning.

The introduction of k permits derive a general dimensionless formulation of the performance parameters Ψ and β, such that the effect of the local fluid nature on the compressor performance can be inferred without loss of generality. The derivation starts from making non-dimensional the Euler equation for the work exchanged under the assumption of meridional flow at the impeller intake:

$$\lambda = \mu_{slip} - \frac{v_{2m}}{u_2} \tan\beta_{2,g} \tag{4.29}$$

Through mass conservation, the ratio between velocities can be linked to the density evolution within the impeller:

$$\frac{v_{2m}}{u_2} = \frac{\phi D_2}{\pi b_2} \frac{\rho_0}{\rho_2} \tag{4.30}$$

After basic manipulations and assuming an isentropic thermodynamic transformation, the density ratio can be approximated as a function of the isentropic work, impeller reaction degree and peripheral Mach number, yielding:

$$\frac{\rho_2}{\rho_0} \approx \left[1 + (\bar{k} - 1) r \Psi M_{u_2}^2\right]^{\frac{1}{\bar{k}-1}} \tag{4.31}$$

By plugging equation (4.31) into (4.30), and then the resulting expression into equation (4.29), an implicit formulation for the isentropic head coefficient as a function of the generalized isentropic coefficient is obtained:

$$\lambda = \Psi/\eta \approx \mu_{slip} - \frac{\phi D_2}{\pi b_2} \frac{\tan\beta_{2,g}}{\left[1 + (\bar{k} - 1) r \Psi M_{u_2}^2\right]^{\frac{1}{\bar{k}-1}}} \tag{4.32}$$

After computing the isentropic head coefficient iteratively from equation (4.32), Ψ can be used to estimate the corresponding pressure ratio provided by the compressor with the following equation, which is just a generalization for non-ideal flows of the thermodynamic relationship between the isentropic enthalpy rise and the pressure ratio expressed in a dimensionless form:

$$\Psi \approx \frac{1}{M_{u_2}^2} \frac{1}{\bar{k} - 1} \left(\beta^{\frac{\bar{k}-1}{\bar{k}}} - 1\right) \tag{4.33}$$

The expressions in equations (4.32) and (4.33) can be used to show the dependency of Ψ and of β on k, after some additional assumptions: (i) the impeller reaction degree and the slip factor are independent of the fluid nature (approximately equal to 0.65 and 0.9, respectively, extracted from CFD results), (ii) ideal similarity, i.e. same ϕ and M_{u_2}, and (iii) the efficiency does not depend on the fluid nature. This last point is not properly true as better highlighted later in this section; however, the variation in efficiency is relatively limited and can be neglected in a first approximation. Therefore, for illustrative purposes, an intermediate value among the four cases is taken from CFD results and kept constant in the present analysis ($\eta = 0.92$). Under these hypotheses, figure 4.34 elucidates the relationship between Ψ and β on k for a fixed flow coefficient and for a number of speedlines. In the same figure the CFD results for the four intake conditions are also reported. Such a comparison is intended to illustrate the effect of the local fluid compressibility on the compressor performance, rather than finding a quantitative agreement between analytical expressions and CFD simulations. Albeit highly simplified, the derived relationships show a trend consistent with CFD results, thus highlighting the significant role on compressor operation of the flow non-ideality, which can be effectively summarized by the coefficient $\bar{k}$.

By first inspecting the trend of the isentropic work coefficient, a lower $\bar{k}$ yields a higher duty on the compressor, which decreases as long as $\bar{k}$ increases. By recalling the definition of $\bar{k}$ in equation (4.28), a small value of k means that the density changes more at a given pressure variation. On the contrary, the less the density varies at a given pressure variation, the higher $\bar{k}$ is. In the limit of an incompressible fluid, $\bar{k}$ grows to infinity and this clearly explains why all curves $\Psi(M_{u_2})$ tends to an asymptotic value as long as $\bar{k}$ increases, i.e. compressible effects represented by M_{u_2} play a

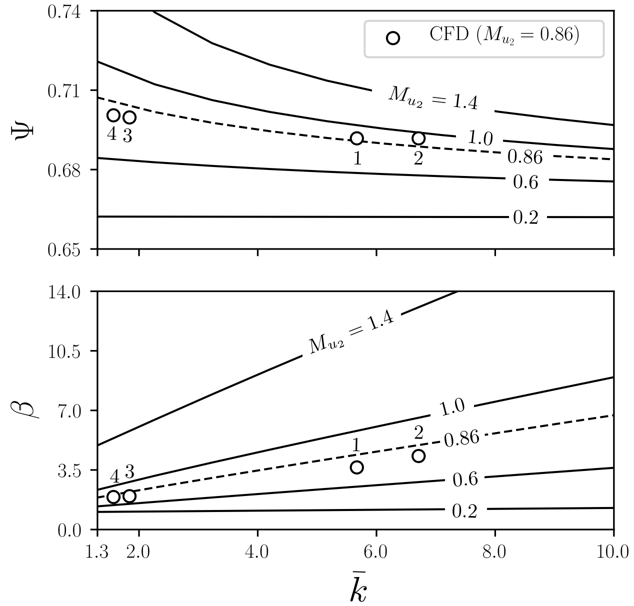

FIGURE 4.34. Effects of the generalized isentropic coefficient k on the performance of centrifugal compressors in conditions of ideal similarity: $\phi = 0.018$, $M_{u_2} = 0.86$ and $Re_{u_2} > 10^8$.

minor role on the fluid evolution and, in turn, on the compressor loading. Another perspective to support this interpretation can be gained by observing the density variation in eq (4.31). The lower $\bar{k}$ (gas-like behaviour), the more the density will increase across the compression process, the more the flow at the impeller outlet will be tangential, thus involving a larger eulerian work for the flow deflection. As long as $\bar{k}$ increases, the relative variation in density will be smaller, then obtaining approximately the same absolute flow deflection across the impeller. Although not treated in the present work, the variation in the absolute flow angle at the impeller outlet as a consequence of the local fluid compressibility may also have a detrimental effect on the matching between the impeller and the vaned diffuser. Finally, the variation in Ψ is generally limited for conventional values of M_{u_2}. It follows that the dependency of Ψ on $\bar{k}$ can be neglected in a first approximation, allowing for a straight generalization of the head compressor curve expressed in Ψ with respect to intake thermodynamic conditions.

The effect of $\bar{k}$ is more significant by observing the pressure ratio delivered by the compressor. Notwithstanding imparting approximately the same work on the fluid, this latter is compressed more when it features high $\bar{k}$. Based on previous explanations, this last result should not surprise: the fluid behaves more like a liquid for high $\bar{k}$, while it possesses gas-like features when $\bar{k}$ is low. Therefore, as a result of a decrease in $\bar{k}$ in conditions of ideal similarity, the compressor is generally more loaded whilst providing a significantly smaller pressure rise. For fluids compressed away from the critical point, $\bar{k}$ is approximately constant regardless of the stagnation state, and a change in the pressure rise is directly connected with the work provided by the compressor. This is what usually occurs in air-breathing compressors, in which $k \mapsto \gamma$ (ideal-gas limit) and the pressure ratio is directly linked with the work coefficient along a speedline, see equation (4.33).

Finally, $\bar{k}$ has also an effect on the compressor efficiency, as shown in figure 4.35. First, it is worth stressing that the quantitative efficiency values are comparably larger than those reported in §4.3, as only the impeller is simulated in the present analysis. Even the impeller efficiency is arguably overestimated, as the mixing process due to separation is not entirely concluded at the

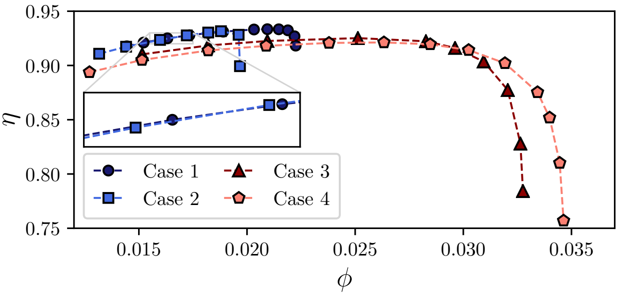

FIGURE 4.35. Efficiency maps for the selected intake thermodynamic states at fixed peripheral Mach number $M_{u_2} = 0.86$ and Reynolds effects $Re_{u_2} > 10^8$ (ideal similarity).

impeller trailing edge, but it proceeds downstream of that. In ideal conditions, all efficiency curves across a fixed speedline should collapse in a single dimensionless curve. As for the compressor loading, the additional complexities introduced by non-ideal effects require more conditions to be satisfied for a full compressor similarity. It is found that the compressor is more efficient when it deals with liquid-like CO_2 (high $\bar{k}$), whereby the compressor loading is also reduced. Therefore, the higher efficiency can be presumably attributed to a lower extent of loading-induced losses (e.g., separation, diffusion, tip clearance). These losses are particularly important at low flow rates, while skin-friction and choking-related losses usually predominate at high flow rates. About this last point, the four curves show significantly different choking limits (varying from 94% to 166% with respect to design conditions), which has not yet been explained. The next section, focusing on the effects of two-phase flows on compressor performance, will contribute to filling this knowledge gap.

4.7.2.2 Two-phase effects - influence of $\mathcal{C}$ on performance maps

Depending on the intake thermodynamic conditions, the flow may undergo a phase transition in the intake region of the impeller as a consequence of local flow accelerations. Certainly, the closer the compressor operates to the saturation curve, the smaller the acceleration that is required to prompt the phase change. Therefore, a similarity parameter that weights the minimum kinetic head to reach saturation with the kinetics expected at the impeller intake can be conveniently introduced to account for the extent of the two-phase region:

$$\mathcal{C} \overset{\text{def}}{=} \frac{2(h_1^t - h_{sat})}{u_{1m}^2} = \frac{2(h_1^t - h_{sat})}{f^2\, u_2^2} \tag{4.34}$$

where $f = D_{1m}/D_2$ is a normalization factor to pass from the impeller velocity at the inlet, where phase-change phenomena are expected to take place, to the impeller velocity at the outlet, which is known since the preliminary design phase. If the design of the inducer is not known, f can be taken in the range of $0.2 - 0.6$ (range re-elaborated from Ludtke (2004)) to have a first glimpse on the phase change that can potentially arise. The following estimates are performed with $f = 0.35 \approx D_{1m}/D_2$.

As an additional note, the limit for phase change in equation (4.34) is set to saturation in accordance with the homogeneous theory here employed. Nonetheless, $\mathcal{C}$ can be straightforwardly reformulated if an alternative limit is used to set the phase transition, e.g. spinodal or Wilson line. In general, the numerator is thought to represent the minimum kinetic head required to trigger the phase change regardless of where it occurs. Therefore, $\mathcal{C}$ can be interpreted as a generalization of

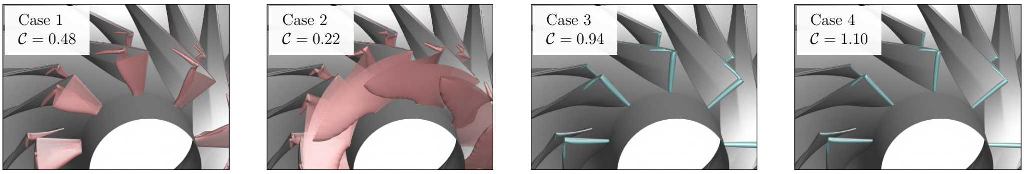

FIGURE 4.36. Extent of the two-phase region for the four selected intake thermodynamic states at $\phi = 0.018$. The two-phase region is colored in red when the phase change is liquid-to-vapour (cavitation) or in blue when the phase change is vapour-to-liquid (condensation).

the cavitation parameter, originally introduced for incompressible fluids in the pump field (Brennen, 2011).

Following the definition provided in equation (4.34), $\mathcal{C} \ll 1$ implies that velocities at the impeller intake ($\propto u_1$) are expected to be much larger than the one required by the flow to reach saturation conditions; hence, the phase transition is expected to be prominent. On the contrary, when $\mathcal{C} \gg 1$, the intake thermodynamic state is far enough from saturation that the velocities involved are not expected to be sufficiently high to trigger a phase change. Finally, $\mathcal{C} \approx 1$ means that the two kinetics are of the same order, hence local excursions can happen due to sudden flow acceleration (e.g., leading-edge curvature, incidence angle). It is worth specifying that, in the same spirit of M_{u_2}, $\mathcal{C}$ is intended only to provide an idea of the two-phase effects by dimensional similarity. The actual extent of the two-phase region will always depend on the local flow state and the detailed impeller shape. It follows that the confrontation of two impellers on the basis of $\mathcal{C}$ is meaningful only if the two geometries share similar geometries and loading, hence the blade angle distribution, leading-edge curvature, and all geometrical aspects concurring to the phase change have to be geometrically similar.

The relationship between $\mathcal{C}$ and the extent of the phase change is clarified by figure 4.36. The two-phase region, in which $P < \widetilde{P_{sat}}$, is highlighted by the colored surface (red for cavitation, blue for condensation) for the four cases at a given peripheral Mach number and flow coefficient. As predicted in the formulation of $\mathcal{C}$, the smaller $\mathcal{C}$, the larger the two-phase region extent. It is also clear that the flow coefficient and peripheral Mach number alone are not sufficient to state a similarity between compressor operations, given the different impact that the phase transition may have. By comparing the hierarchy established by the two-phase region extent with the choking limit in performance maps, see figure 4.33, it is found that the smaller $\mathcal{C}$, the more the choking limit is shifted to low flow rates, i.e. choking occurs earlier. Such evidence is not a fortuitous event, but it has a clear physical explanation. As long as the flow rate increases, the velocities at the impeller intake increase as well to elaborate the larger mass flow. When $\mathcal{C} \ll 1$, such as in case 2, then only a slight increase of the flow rate is required to have the whole blade channel filled by two-phase flows. This condition sets the ground for the choking condition, as the speed of sound in the two-phase flow regime is significantly lower than the one in the single-phase region, see, e.g., figure 4.32 for direct visualization. Although the present simulations are performed with a HEM for the speed of sound, a decrease, though smoother, in its value is also found when relaxing some of the equilibrium hypotheses, as demonstrated for cavitating flows by using Brennen's formulation, see §4.6.4. Hence, although the quantitative impact may be different in presence of strong non-equilibrium effects, which have yet to be verified for sCO_2 applications, a shift of the choking limit towards lower flow rates in presence of two-phase flows is eventually expected.

Finally, it is worth highlighting that $\mathcal{C}$ is arguably of general validity and not limited to the compressor investigated in this work. In support of this general claim, the value of $\mathcal{C}$ is estimated for the Sandia compressor at $\omega = 50\,000\,\text{rpm}$ (Wright *et al.*, 2010), for which the extent of the two-phase region was simulated by different authors (Ameli *et al.*, 2018*b*; Pecnik *et al.*, 2012).

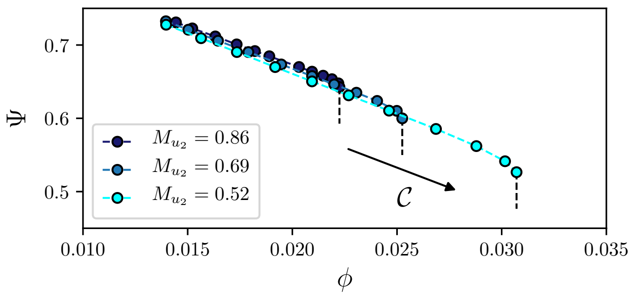

FIGURE 4.37. Influence of the phase-change coefficient on performance maps at a variable peripheral Mach number and fixed intake thermodynamic conditions (case 1).

It is found that $\mathcal{C} \approx 1.4$, indicating the minor relevance of two-phase effects on the compressor performance in these operating conditions. Such a result is consistent with the limited two-phase region found by Ameli *et al.* (2018*b*); Pecnik *et al.* (2012), in which the onset of transition in the front part of the blade is only induced by the flow curvature around the leading edge. The choking limit, experimentally observed at relatively large flow rates, is an additional confirmation of the suitability of the present parameter in properly establishing a direct link between the extent of the two-phase region and choking operation.

The larger extent of the two-phase region is also expected to influence the compressor efficiency. This latter aspect is only theorized in this context, as CFD simulations under HEM assumptions only consider the mixture as a whole instead of modeling the two phases separately. Therefore, all effects related to local interactions and exchanges of mass and heat are hence not explicitly accounted for.

The formulation of $\mathcal{C}$ in equation (4.34) can also be reworked to make appear explicitly the peripheral Mach number:

$$\mathcal{C} = \frac{2(h_1^t - h_{sat})}{f^2\, c_0^2\, M_{u_2}^2} \tag{4.35}$$

The two parameters $\mathcal{C}$ and M_{u_2} are inversely proportional; coherently with their physical meanings, as long as the peripheral Mach number increases, the velocities within the impeller increase as well, thus promoting the onset of phase change, as represented by a lower value of $\mathcal{C}$. This aspect is quantitatively assessed in figure 4.37 for the present compressor, in which different speedlines are considered while freezing the intake thermodynamic state to case 1. Under these circumstances, the distance from the saturation curve is fixed and the only parameter that varies in equation (4.35) is M_{u_2}. As a result, the same trend previously assessed when comparing the choking limit based on $\mathcal{C}$ is also observed in this additional comparison. The choking limit is shifted towards high flow rates as long as $\mathcal{C}$ increases, i.e. when M_{u_2} is reduced. By inspecting the extent of the two-phase region in figure 4.38, obtained for case 1 at different M_{u_2}, the same trend of figure 4.36 is qualitatively observed, with a larger two-phase region found at the highest speedline, which progressively decreases as long as the peripheral speed is reduced. The reduction in the peripheral speed has a twofold role in the increase of the choking limit: both the flow velocity and the two-phase region, characterized by lower values of the speed of sound, are reduced. The effects associated with the reduction in the speed of sound are thoroughly discussed in the next and last subsection.

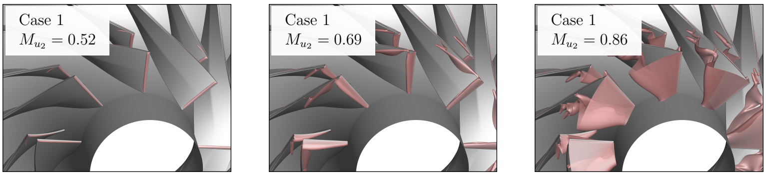

FIGURE 4.38. Extent of the two-phase region at a variable peripheral Mach number and for fixed $\phi = 0.021$ and upstream total state (case 1).

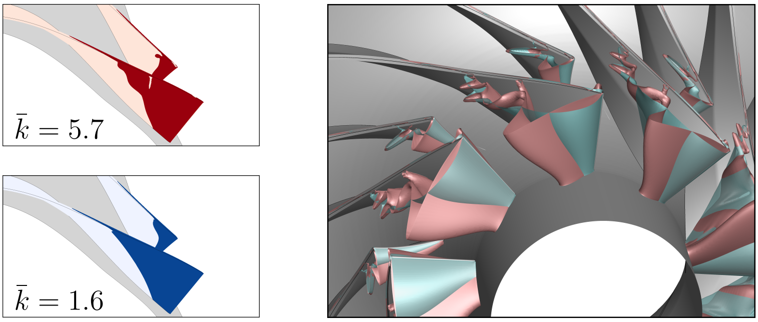

FIGURE 4.39. Influence of $\bar{k}$ on the phase change at constant $\phi = 0.021$, $M_{u_2} = 0.86$ and $\mathcal{C} = 0.48$ with $Re_{u_2} > 10^8$. The two-phase region is coloured in red when the phase change is liquid-to-vapour (cavitation) and in blue when the phase change is vapour-to-liquid (condensation).

4.7.2.3 Relationship between non-ideal effects and phase change

Although $\mathcal{C}$ arguably complements the effect of k in the determination of the compressor map, its definition only accounts for the quantitative excursion within the saturation dome. Therefore, there is still a question that needs a proper answer: assuming that approximately the same amount of flow undergoes a phase transition, does it have the same impact on compressor aerodynamics regardless of the specific phase change involved (whether cavitation or condensation)? To answer this question, a fifth case is selected such that the resulting operating conditions share the same $\mathcal{C}$ with case 1 and the same averaged isentropic exponent $\bar{k}$ with case 4. As evident by the value of $\bar{k}$, the intake thermodynamic conditions of this new case ($P_0 = 69.1$ bar, $T_0 = 302.04$ K) lie in the vapour domain. The analysis is undertaken by considering the same peripheral Mach number, while the peripheral Reynolds number is high enough to safely assume self-similarity in the Reynolds effects.

First, the effect of intake thermodynamic conditions on the phase change is analyzed by comparing the extent of the two-phase region at fixed $\mathcal{C}$ in figure 4.39. The detail of the suction sides on the left figures confirms that the two-phase region has approximately the same extent both streamwise and spanwise, notwithstanding the slightly higher aerodynamic loading that characterizes the compressor when dealing with CO_2 at low k. Nonetheless, the small variation in the overall blade loading is not consistent with the large pitchwise variation across the channel (right frame). To have a better insight, the mass-fraction distributions of the secondary phase are plotted on the midspan blade-to-blade plane in figure 4.40. The estimates of mass fractions using the barotropic model recall the procedure outlined in §4.6.3.1, but the rothalpy is used instead of the total enthalpy. The relative Mach number distributions, also reported in the same figure, help to understand the underlying physical motivation for these pitchwise variations. The mixture resulting from the phase transition of case 1 (cavitation) has larger compressibility than the mixture in case

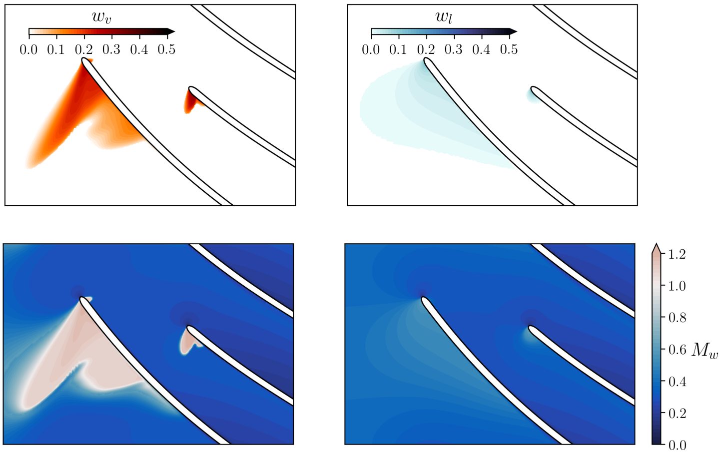

FIGURE 4.40. Mass fractions of the dispersed phases (top) and relative Mach number (bottom) at the midspan intake region with constant $\phi = 0.021$, $M_{u_2} = 0.86$, $\mathcal{C} = 0.48$ and with $Re_{u_2} > 10^8$ for a cavitating ($s/s_c < 1$, left frames) and condensing ($s/s_c > 1$, right frames) flow.

4 (condensation). The larger compressibility for the cavitating flow, whereby the secondary phase is lighter than the primary one, results in the onset of a transonic flow regime on the front suction side of the main blade, with consequent compression shock waves (see also the blade loading distribution in figure 4.30 for case 1), which severely alter the flow field. On the other hand, the mixture resulting from the condensation process, whereby the secondary phase is denser than the primary one, exhibits compressibility much similar to the single-phase, hence the flow evolves smoothly on the blade surface. A quantitative estimate of the change in compressibility can be appreciated by looking at the speed of sound evolution along the upstream isentropes in figure 4.32 for the different cases. In cavitating flows (cases 1 and 2), under the HEM assumption, the speed of sound is more than halved when the phase change occurs. On the contrary, the speed of sound still diminishes for condensing flows (cases 3 and 4), albeit to a significantly lower extent.

Actually, it is not surprising that $\mathcal{C}$ by itself is not able to discern any difference in the phase change. From its definition, $\mathcal{C}$ only expresses the distance from the saturation curve regardless of the specific upstream thermodynamic state. Hence, $\mathcal{C}$ is a quantitative index, which accounts for the extent of the phase transition based on similarity criteria. However, as $\bar{k}$ was introduced to account for the variable properties of the single-phase flow, likewise, it is reasonable to define a similar parameter that includes the variable compressibility of the mixture. As the main focus of the present discussion is on the reduced range brought by two-phase effects, a surrogate Mach number that characterizes the compressibility of the mixture can be conveniently defined:

$$M_{sat} \overset{\text{def}}{=} \frac{u_{1m}}{c_{sat}} = f\frac{u_2}{c_{sat}} \tag{4.36}$$

where c_{sat} is the speed of sound of the mixture in the condition of incipient transition. In the present work, this value is computed in accordance with the homogeneous equilibrium theory, but its formulation can be readily modified for different speed of sound formulations depending on the model assumption. When M_{sat} is in the order of unity, then the onset of a two-phase transition is expected to promote supersonic flow regimes. It follows that the phase transition becomes predominant in the establishment of choking operation. Whenever it is sufficient that the flow undergoes a phase change to meet sonic conditions, then the compressor will choke as soon as the two-phase region will extend over the whole blade channel. This is precisely what

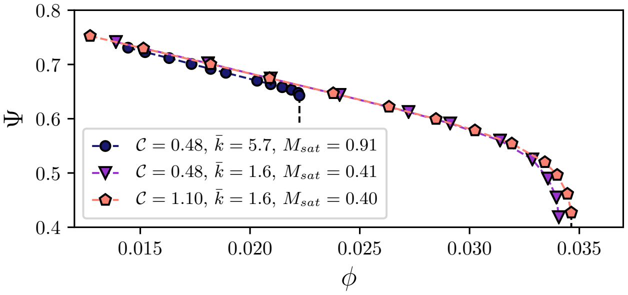

FIGURE 4.41. Combined effects of the phase-change coefficient and the generalized isentropic coefficient on the compressor range at fixed peripheral Mach number $M_{u_2} = 0.86$ and Reynolds effects $Re_{u_2} > 10^8$ (ideal similarity).

happens for case 1 and case 2, with M_{sat} equal to 0.91 and 1.02, respectively. For these two cases, the choking occurs at comparatively low flow rates, i.e. 106% and 94%, respectively, with respect to the nominal flow coefficient. Although similar M_{sat}, the choking onsets earlier in case 2 (surprisingly, for a flow coefficient below than the design one) because of the larger extent of the two-phase region (higher $\mathcal{C}$), as commented in figure 4.36.

When $M_{sat} \ll 1$, as in case 3 and 4 with a M_{sat} equal to 0.45 and 0.40, respectively, the choking does not occur necessarily when the two-phase region occupies the whole blade channel. In these conditions, a conventional choking process takes place, with the flow rate increasing until the corresponding flow velocity meets the sonic limit, which, in turn, does not dramatically change across the operational curve. As a consequence, the compressor right limit is increased to 156% and 164% for cases 3 and 4, respectively. A further peculiar feature of the cavitation-driven choking, observed for cases 1 and 2, is the sudden drop in the characteristic curve at high flow rates, opposed to the regular asymptotic trends observed for cases 3 and 4. Based on this explanation, i.e. the main driver for choking conditions is an increase in the flow velocity when $M_{sat} \ll 1$, $\mathcal{C}$ is expected to play a minor role in the determination of the choking limit. The contribution of M_{sat} and $\mathcal{C}$ on the choking limit becomes clearer by referring to the complete speedlines in figure 4.41. Although the extent of the two-phase region can be approximately the same at equal $\mathcal{C}$, the compressibility of the two-phase mixture plays a key role in the determination of the choking limit. If M_{sat} is low, then the flow velocity must be high enough to reach sonic conditions, hence the choking limit is shifted towards high flow rates and the two-phase extent slightly affects the process. If $M_{sat} \geqslant 1$, the choking will occur once the two-phase flow occupies the whole blade channel, then $\mathcal{C}$ has a fundamental role in the determination of the machine choking.

Although the early choking prompted by two-phase effects can be inferred in a more straightforward way by looking at M_{sat}, this latter coefficient is expected to be dependent on k, $\mathcal{C}$ and M_{u_2} in the following way. Apart from the magnitude of local flow accelerations, which is included in M_{u_2}, M_{sat} is mainly characterized by the mixture compressibility as a result of the specific phase change, i.e. whether the secondary phase is lighter (cavitation) or denser (condensation) than the primary one. Therefore, the resulting two-phase properties are largely dependent on the corresponding upstream total state, which can be determined by combining the information of k and $\mathcal{C}$ once M_{u_2} is fixed. The replacement of k with the averaged value $\bar{k}$ arguably does not alter the conceptual framework. Regardless of the effect of $\mathcal{C}$ in the determination of choking, $\mathcal{C}$ is still expected to affect the compressor performance by increasing the aerodynamic losses, even though they are not explicitly quantified in this work.

As a final comment, figure 4.41 also provides additional proof for the influence of non-ideal effects. In particular, CFD results show that, when $\bar{k}$ is the same, the performance maps overlap in terms of compressor loading, pressure ratio and efficiency (these two latter trends not reported here for the sake of brevity, but undistinguishable between the two cases up to the choking).

4.8 Concluding remarks and key findings

This chapter provides a broad overview of turbomachinery for sCO_2 closed power cycles.

The first part was devoted to the improvement of system analysis by including a tailored model for the turbomachinery by means of mean-line performance estimates. The compressor mean-line tool is validated against experimental data, including a dedicated uncertainty-quantification analysis to account for missing input information. The validation shows that nearly all data fall within the extended confidence intervals (±1.5 pp for peak efficiencies at three different rotational speeds). The turbine mean-line code was validated in the past (±2.0 pp against experiments) and used for several documented design tasks featuring non-ideal effects. Turbomachinery designs are obtained by combining the mean-line codes with an external optimization routine implementing an evolutionary-based algorithm. A comprehensive investigation about compressor maximum efficiency is performed by varying the intake-fluid thermodynamic conditions, the compressor pressure ratios, and mass-flow rates. Three main conclusions are drawn from this analysis:

- Compressors optimized for conditions representative of full-scale plants exhibit competitive efficiencies ($82 \div 85\%$ for pressure ratio $\beta \leqslant 3.5$).
- The intake-fluid thermodynamic conditions seem not to affect the design efficiency if dedicated optimizations are run ($\Delta\eta \leqslant 1$ pp, within the uncertainty of the mean-line code).
- Appreciable differences in compressor efficiencies are found by changing the compressor size and loading. Compressor efficiencies reduces of ≈ 2 pp both by increasing the pressure ratio ($\Delta\beta = 1.5$) and by moving to lower mass-flow rates (e.g. from 250 kg/s to 50 kg/s).

Efficiency correlations accounting for size and aerodynamic loading effects are then formulated for single-stage compressors and turbines by fitting the optimized designs. These correlations are used to infer optimal cycle parameters in a parametric way, changing the hot-source temperature, the minimum cycle temperature, and the power capacity of the plant. The results are compared with those obtained by employing constant turbomachinery efficiencies. Qualitative (different trends of cycle electrical efficiency with respect to overall pressure ratio) and quantitative (cycle-efficiency differences up to ≈ 4 pp in the worst-case scenario) discrepancies suggest that proper modelling of turbomachinery component is crucial to get reliable sCO_2 power-system optimizations.

To produce a complete three-dimensional design of the compressor, however, the mean-line model is not sufficiently reliable, as it neglects important local features that characterize the compressor aerodynamics. To gain a realistic picture of the flow fields within centrifugal compressors that operate near the critical point, the idea was to rely on CFD simulations. Nonetheless, the simulation of compressible non-ideal two-phase flows is not a straightforward task, as it needs to incorporate an accurate thermodynamic description of both phases alongside the mixture evolution. To this end, two CFD models are developed. Both models rely on the description of the mixture properties by resorting to the so-called two-fluid concept, thus eliminating the need of detailing the local interactions between phases. This enables to achieve a considerable simplification in the mathematical modeling, in view of their application to the design and analysis of sCO_2 compressors. The first formulation, named *mixture model*, consists of the full set of governing equations for the mixture plus an additional transport equation that governs the phase transitions; the onset of phase change is driven by the difference between the local pressure and the saturation pressure at the local temperature, by resorting to a penalty formulation. The second formulation, named *barotropic model*, strictly assumes mechanical and thermal equilibrium, and the mixture thermo-physical properties are expressed as functions of the pressure only. These simplifications lead to a reduction of the overall computational cost alongside increased solver robustness, by virtue of the simplified thermodynamic treatment.

The two models have been compared against experiments in converging-diverging nozzle published in the literature for cavitating (liquid ↦ vapour) and condensing (vapour ↦ liquid) flows. Both the comparisons involve expansions that progressively approach the critical point, where large discrepancies from the ideal-gas thermodynamics are observed. The two models exhibit a remarkable agreement with each other and are able to reproduce the trends set by the experimental data, also showing an overall good quantitative agreement with measured data. For the expansions evolving from supercritical states, the weighted mean absolute percentage error of pressure evaluated along the whole expansions resulted of about 2% and 4% for cavitating and condensing flow respectively; in the case of supercritical cavitating flows, for that also temperature measurements are available, the same global error in terms of temperature resulted below 1%.

More significant quantitative differences emerge when considering expansions evolving from subcritical states. It is conjectured that most of the deviations can be attributed to meta-stable effects, which might delay the phase-change onset in the conditions far from the critical point, or to the presence of a relative motion between phases. The mixture model, even though expressed under mechanical and thermal equilibrium in this work, is enough flexible to eventually relax these assumptions via constitutive equations, when detailed experimental data will enable their formulations for compressible flows of carbon dioxide. In the limit of the homogeneous equilibrium approximation, the barotropic model is shown to provide comparable predictions of the expansion processes at a lower computational cost and with improved solver robustness.

Therefore, the barotropic model is used to carry out three-dimensional viscous simulations of a centrifugal compressor for sCO$_2$ applications. Starting from the optimization of the thermodynamic cycle to derive realistic boundary conditions and requirements, a single-stage highly loaded compressor is considered, discussing the peculiar design of sCO$_2$ compressors operating in the near-critical region. In particular, the design focused on the blade-design strategies to minimize the front loading, with the aim of minimizing the onset of phase change at the compressor intake.

As one of the main requirements of the compressor is to provide the required head over the range, the analysis is performed on off-design conditions at both variable rotational speed and intake thermodynamic conditions. This latter point is particularly relevant for sCO$_2$ compressors as both non-ideal effects and two-phase flows are considerably dependent on that. It is found that the ideal similarity, i.e. keeping the same flow coefficient and peripheral Mach number with negligible Reynolds effects, is not sufficient to ensure full similar performances when the compressor operates at variable thermodynamic conditions in the near-critical region. Thanks to the flow insight enabled by CFD simulations, complemented by analytical and physical considerations, the identification of three main effects are found to be responsible for the performance deviations from the ideal similarity: (i) severe non-ideal effects affecting single-phase thermodynamic properties, (ii) a different extent of the two-phase region, and (iii) fundamental differences in the resulting mixture compressibility. Since the focus is on compressors operating with a single fluid, two independent parameters are sufficient to scale non-ideal and two-phase effects, leading to a generalized form of the similitude theory, which can be re-casted as:

$$\Psi, \eta = f(\underbrace{\phi, M_{u_2}, Re_{u_2},}_{ideal} \quad \underbrace{k, \mathcal{C}}_{non-ideal} \quad)$$

where k is the generalized isentropic coefficient to account for non-ideal effects in the single-phase flow and $\mathcal{C}$ accounts for the amount of flow that undergoes a phase change.

With reference to the ideal characteristic curves, the following modifications are recognized:

- the compressor loading increases when k reduces (i.e., when CO_2 features gas-like properties);
- the efficiency is reduced in these conditions due to a larger share of loading-induced losses (e.g., separation, diffusion, tip clearance);
- the choking limit is generally reduced by the onset of two-phase flows owing to a drop in the associated speed of sound;
- focusing on a single kind of phase change (whether cavitation or condensation), the choking limit reduces as $\mathcal{C}$ reduces;
- depending on the specific phase change, choking conditions are driven either by the drop in speed of sound (cavitation) or by the increase in flow velocity (condensation);
- the kind of choking can be straightforwardly inferred by a purposely defined dimensionless parameter M_{sat}, which directly establishes the weight of compressible effects on the mixture.

CHAPTER 5

CONCLUSION AND OUTLOOK

5.1 Conclusions

The study documented in this thesis offers a comprehensive overview of non-ideal effects arising in turbomachinery components for novel power systems. These energy-conversion systems are based on working fluids that are different from steam and are operated in thermodynamic regions characterized by significant departure from the ideal-gas thermodynamics. In this context, two power systems and corresponding turbomachinery are considered: organic Rankine cycles (ORCs) and supercritical carbon dioxide (sCO_2) closed power cycle. Despite their advantageous characteristics in terms of efficiency and flexibility compared to conventional Rankine cycles, their penetration in the market is dampened by sub-optimal turbomachinery designs, among other things. To promote the development of the entire technology, design criteria have to directly tackle the non-ideal behaviour of the fluid and the associated effects on the machine performance have to be understood.

The first result of this thesis is the development of an automated procedure for the shape optimization of turbomachinery profile. The turbomachinery performance throughout the optimization is obtained by resorting to computational fluid dynamic (CFD) simulations complemented by a generalized thermodynamic treatment for the equation of state. In this way, the non-ideal character of the fluid is inherently considered by resolving the set of governing equations. Likewise to any optimization routine, a large number of function evaluations are required and the procedure can become rapidly not feasible owing to the relatively high computational cost for the single CFD simulation. To circumvent this problem, a surrogate strategy is formulated, in such a way that only a limited number of CFD are run and used to build a response surface for the target quantity of interest. Then, the optimization is run on the surrogate of the flow solver, which can be interrogated many times at a negligible computational cost. The surrogate accuracy is then improved in the optimal region with additional CFD runs, to be sure that the surrogate is capable of finding the correct optimum. The optimization strategy is tested against exemplary design tasks representative of ORC turbines, encompassing different flow regimes, non-ideal effects, and cascade layout. A brief description of the test cases is reported as follows:

Converging-diverging cascade of an axial turbine

The baseline cascade faces a supersonic flow regime ($M > 2.0$) and ideal-like conditions ($Z \sim 1.0$, $\Gamma \sim 1.0$). The goal is the maximization of the performance at design conditions while accepting a deviation of ±1% in the datum mass-flow rate. The optimal blade exhibits a total-pressure loss coefficient halved with respect to the baseline value while coping with the mass-flow rate constraint. An additional optimization including multiple operating conditions in the definition of the objective function is carried out, yielding performance comparable to the single-point optimization. The single- and multi-point optimization are also undertaken by optimizing the profile when it operates in severe non-ideal conditions ($Z \sim 0.3$, $\Gamma \sim 0.3$), shedding light on the capability of the surrogate strategy to produce optimal profiles also in presence of considerable departures from the ideal-gas thermodynamics.

Full stage (stator and rotor) of a centrifugal turbine

Both turbine blades are characterized by a transonic flow regime (M up to 1.4) and significant non-ideal conditions ($Z \sim 0.6 - 0.8$). Both stator and rotor profiles are optimized with the aim of reducing the overall entropy generation while preserving the outflow angle and satisfying a minimum rotor area required for mechanical reasons. The optimal cascades produce an increase of 2.5 percentage points in the stage efficiency while complying with all prescribed constraints.

Moreover, the physical rationale behind the optimal profiles indicates that the shape optimization not only produces a better turbomachinery profile from the aerodynamic standpoint, but it can also suggest design avenues for those turbomachines for which well-established design practices are still not available.

Although shape optimization can effectively deal with complex non-ideal flows, there are still significant gaps in the current understanding of non-ideal flows on turbomachinery aerodynamics, both at design and off-design conditions. The character of non-ideal flows changes depending on whether ORC or sCO_2 applications are considered.

At first, non-ideal flows occurring in molecularly complex fluids, currently employed as working fluids in ORC plants, are addressed. The analysis is undertaken by considering the siloxane MM as a reference fluid, but most flow features are proved to be of general validity by analogy with the steady quasi-one-dimensional flow theory and with the two-dimensional wave theory. Three operating conditions are considered for the comparison, one as a representative of conventional subcritical ORC cycles (low-pressure case), while the other two expansions evolve from a supercritical state (high-pressure cases) and are representatives of future high-temperature transcritical ORC systems. These two latter cases are devised such that they involve stationary points of the Mach number in the proximity of the trailing edge. The outcomes of this study elucidate the significant role of non-ideal effects in determining the cascade aerodynamics; specifically, the following original findings are derived:

- remarkable qualitative differences are found between the conventional case and the two high-pressure cases at design conditions. The former recovers a flow field similar to the one expected in ideal-gas conditions, while unconventional flow features affect the high-pressure cases, such as the non-monotonic behaviour of the Mach number, non-ideal oblique shocks with an increase of the Mach number across the shock interface, and non-ideal Prandtl-Meyer fans with the Mach number decreasing across the expansion;

- the design of a cascade with a stationary point of the Mach number located at the blade trailing edge produces a uniform Mach number field downstream of the cascade, with beneficial implications for the subsequent rotating vanes;

- the flow modification to variations in the outlet pressure, at fixed upstream total state, is found to largely depend on the specific operating condition. Apart from the low-pressure cascade, in which ideal-gas responses are recognized, the high-pressure cases differ from which stationary point of the Mach number occurs at the trailing edge. If the stationary point is the local minimum of the Mach number, then the Mach number increases whether the outlet pressure increases or decreases. As a consequence, the departure from the unique incidence conditions at the rotor inlet is reduced. The opposite situation occurs when the stationary point is the local maximum, yielding a decrease of the Mach number regardless of the specific outlet pressure variation;

- the cascade losses are found to be largely sensitive to the value of the upstream total temperature. An increase of 20 °C in this value, at a fixed pressure ratio, amplifies the cascade losses of more than two times. Such observation is in contrast with the ideal-gas theory, in which the cascade losses are independent of the specific stagnation temperature when the pressure ratio is not changed.

This last point paves the way for a dedicated uncertainty-quantification study, which is aimed at quantifying the performance deviation in presence of uncertainty in the usual operation of the power cycle. As for the optimization, the quantification of uncertainty requires a large number of simulations to derive statistically meaningful indicators. To this end, a surrogate strategy is implemented by resorting to a polynomial chaos representation of the target quantities of interest with respect to operational uncertainty. Then, statistical indicators of the cascade performance are obtained by sampling the surrogate. The uncertainty quantification is performed for both ideal-like and non-ideal conditions, this latter featuring the local minimum of the Mach number at the blade trailing edge. The response to operational uncertainty is considerably different between the two cases, both at a quantitative and qualitative level. The main conclusions of the study are:

- operational uncertainty barely affects the aerodynamics when the cascade operates in ideal-like conditions. Otherwise, the flow field evolution under uncertainty is largely sensitive to small perturbation of the stagnation state, inducing variations in cascade performance ten times larger than the ideal-like counterpart;

- the critical mass-flow rate, which in turns establishes the mass-flow rate in the power cycles due to choked operations from the supersonic cascade, changes four times more than in the ideal-like case given the same relative operational uncertainty;

- the upstream total temperature is the main responsible for these variations, having a large influence on the determination of the area ratio corresponding to an adapted supersonic expansion;

- the flow field is entirely affected by operational uncertainty in non-ideal conditions; as a result, the flow delivered to the subsequent rotating vanes is severely altered as well, with local variations in the incidence angle up to 10°, opposed to almost null variations in ideal-like conditions.

All these non-ideal features are mainly associated with a value of the fundamental derivative of gas dynamics Γ lower than unity. For simple fluids, such as carbon dioxide, $\Gamma > 1$ in the single-phase region, although it becomes $\Gamma < 1$ in the two-phase region.

Therefore, other non-ideal effects are expected to be predominant in turbomachinery for sCO_2 applications. For example, as a consequence of a small change in the upstream total state in the proximity of the critical point, which usually identifies the intake region of the main compressor, carbon dioxide can exhibit either liquid-like or gas-like behaviour. The large volumetric variation of carbon dioxide in the region of interest for centrifugal compressors poses unprecedented challenges to the correct design of the machine. Therefore, the first contribution of the thesis to this field is the assessment of the maximum efficiency achievable by the compressor based on where the compression occurs in the thermodynamic plane. The analysis is carried out with a purposely developed mean-line code, which incorporates the cross-section-averaged flow features at each relevant interface among compressor components. The main outcome from this analysis is that competitive efficiency can be achieved ($82 - 86\%$) at design conditions after a dedicated optimization, and the most influential factors are the aerodynamic loading and the size rather than the upstream total state. Alongside the compressor mean-line optimizations, dedicated optimizations are also performed for the preliminary design of the axial turbine. All optimal designs are collected to generate polynomial correlations for both turbomachinery efficiency as a function of some key parameters, which can be readily computed by the cycle analyst. It is shown that proper modelling of turbomachinery components is crucial to get reliable sCO_2 cycle estimates from both a qualitative (different optimal pressure ratio that maximizes the cycle efficiency) and quantitative (differences in cycle efficiency up to ≈ 4 percentage points) standpoint.

After the mean-line analysis, the aim was to investigate in more detail the local flow physics occurring within centrifugal compressors that operate close to the critical point. Nonetheless, simulating compressible non-ideal two-phase flows is not an easy task. To this end, two CFD strategies are developed, both based on the tracking of mixture properties without detailing the local interactions between the two phases:

Mixture model

Besides the set of classical Reynolds-averaged Navier-Stokes equations declined in terms of mixture properties, an additional partial differential equation is resolved for the evolution of the secondary-phase mass. The thermodynamic properties are computed from pressure and temperature as primitive variables; whenever both phases are present, the fluid properties are only functions of the saturation pressure at the local temperature. As fluid properties are expressed at the thermodynamic equilibrium, the additional equation is interpreted as a constraint to link pressure and temperature as $P = P_{sat}(T)$ rather than introducing a relaxation in one of the equilibrium hypotheses. As a consequence, the equilibrium homogeneous model is recovered in the solution.

Barotropic model

Under the assumptions of homogeneous equilibrium, the model introduces an additional simplification in the thermodynamic description of the mixture: the thermo-physical properties are computed as a function of the local pressure and the stagnation entropy. As a consequence, any effect related to a temperature change is neglected in the estimation of fluid properties, thus decoupling the thermal from the mechanical side. In presence of adiabatic flows in the close proximity of the critical point, whereby the isobaric specific heat is large, such approximation can provide a fair compromise between computational cost and model accuracy in the field of homogeneous equilibrium models.

Capitalizing the lower computational cost and the increased solver stability, the barotropic model is used to simulate a realistic centrifugal compressor for sCO_2 applications. This latter is designed with the aim of minimizing the front aerodynamic loading, which is expected to promote phase transition in the intake region of the impeller. As the compressor is responsible for the proper regulation of the power cycle at off-design conditions, the analysis is extended to understand how a change in the upstream total state may affect the compressor aerodynamics. With reference to the conventional similitude theory, in which dimensionless performance maps are functions of the flow coefficient and peripheral Mach number (for a sufficiently high Reynolds number), the change in the upstream conditions alters the character of the non-ideal flow, the extent of phase change and how these two latter effects combine each other. The following findings are drawn from this analysis:

- given a small change in the upstream total state in the neighborhood of the critical point, CO_2 can exhibit either gas-like or liquid-like compressibility. When CO_2 is operated in its gas-like form, the compressor loading increases, with a consequent reduction in the efficiency;
- the main consequence associated with the onset of a phase change is a sudden drop in speed of sound. Such reduction can implicate an early choking of the machine;
- the increase in rotational speed promotes a two-phase flow regime with a consequent detrimental impact on the compressor rangeability;
- depending on the specific phase change (whether cavitation or condensation), choking conditions are driven either by the drop in speed of sound (cavitation) or by the increase in flow velocity (condensation).

Proper dimensionless parameters are proposed to evaluate the magnitude of all these phenomena and to anticipate shortcomings in the compressor operation.

5.2 Take-home messages

The topics covered by this research are several, and the practical implications are diverse.

About the shape optimization, this study has reported a significant improvement in blade performance for most of the case studies. It is worth noting, however, that the shape optimization is undertaken on blade profiles that operate in transonic/supersonic flow regimes. For such cases, the onset of shocks and the subsequent losses are largely connected with the local blade shape, thus a shape optimization can substantially improve performance. This is particularly relevant in the context of ORC turbines, whereby the utilization of organic fluids usually dictates transonic/supersonic flow regimes. Therefore, once a baseline blade is generated (e.g. adapted from conventional applications or based on semi-analytical methods), a shape optimization is strongly advised in these cases. On the contrary, for low Mach number applications ($M < 0.7$), the blade performance is mainly affected by viscous and secondary losses, for which the local blade shape is of second-order importance. Therefore, the computational cost for the shape optimization is eventually not justified in this situation, and classical design methods based on the blade-loading distribution are expected to be sufficient.

The usefulness of incorporating multiple operating conditions in the optimization should be carefully evaluated on the basis of the underlying physics and the extra computational cost. The multi-point optimizations carried out in this study have yielded poor improvements compared to their single-point counterparts. However, there was an important physical reason for that: due to the supersonic character of the flow, a unique equivalent-nozzle area ratio exists for any of the operating conditions, yielding optimized performance for the specific operating condition and poor performance away from that. In more general terms, there might be cases in which a multi-point strategy is worth the extra computational cost. Before formulating the multi-point problem, a cautious strategy may involve preliminary CFD simulations across the operating range to understand the physical relationship between the operating conditions and the cascade performance, and in which way the blade geometry is supposed to alter this relationship.

The analysis of non-ideal effects in supersonic turbine cascades has shown that peculiar gas-dynamic phenomena can occur when the blade cascade operates with molecularly complex fluids in a specific thermodynamic region close to the critical point. The main implication is that the sharp gradients in this region differently affect the flow evolution, hence the turbine performance becomes oversensitive to the specific operating point. To mitigate this risk, turbine expansions in thermodynamic regions where non-ideal effects are marginal ($\Gamma > 0.7$) are recommended, especially in the context of flexible power generation and/or variable heat load that often causes a departure from the nominal conditions.

Finally, the study regarding sCO_2 turbomachinery has introduced a number of novelties in the modelling approach and physical understanding. At first, the importance of integrating turbomachinery models in cycle analyses has been demonstrated. Bearing in mind the underlying assumptions of the study, most notably each turbomachinery rotates at its optimal speeds, any additional constraint (e.g., single shaft, adequate compressor range, . . .) arguably reduces turbomachinery efficiencies. Therefore, the derived efficiency correlations have to be seen as optimistic, and they can represent a good starting point for the thermodynamic analysis of the cycle.

Regarding the flow modelling, the barotropic model can effectively be used as a homogeneous equilibrium model to describe the volumetric evolution of the carbon dioxide in both single- and two-phase flow conditions. In presence of dissipation within the compressor flow path, the lack of a caloric correction is expected to be of second-order importance on the left-hand branch of the saturation curve in a T-s plane, whereby the compressibility of the fluid is limited (as usually done for hydraulic machines). Although the general trend should be recovered also on the right-hand branch, the larger fluid compressibility raises more prudence as the re-heat effect can be more important. Overall, however, the numerical tests presented in this thesis suggest that the barotropic model for sCO_2 flows provides satisfactory results in light of its simplicity from the implementation side and cheapness from the computational perspective.

Finally, as a result of the study on compressor performance map at variable intake conditions, it is shown that the isentropic head coefficient is rather insensitive to non-ideal effects, and, then, it can be effectively used regardless of the upstream thermodynamic condition. On the other hand, expressing the performance maps in terms of pressure should be avoided, as the pressure rise eventually depends on the specific upstream condition. Moreover, if the upstream point always lies in the vapor region, then the dependency between the choking limit and the ambient conditions can be neglected in a first approximation. The situation becomes more critical if the upstream point falls in the liquid region close to the saturation curve ($\mathcal{C} \ll 1$). For these cases, under the hypothesis of thermodynamic equilibrium, the speed of sound may dramatically change, and the associated effects on the choking are no longer negligible, although non-equilibrium effects may mitigate this issue. Overall, a larger uncertainty in the choking margin has to be considered when scaling the performance maps at variable intake thermodynamic conditions. Therefore, a compressor design that guarantees an extra margin from choking can be a prudent choice to avoid premature choking that eventually compromises the entire flexibility of the power cycle.

5.3 Outlooks

Notwithstanding the advancements in the flow-physic understanding illustrated in this work, there are still a lot of open questions that must be addressed in the future. Moreover, the continuous development of suitable computational methods and algorithms capable of handling such a complex fluid-dynamic framework has to be pursued to enable their usage in an industrial context.

As for the shape-optimization routine, although the surrogate strategy allows for a considerable reduction in the computational cost, this latter dramatically grows when increasing the number of design variables (curse of dimensionality). An important improvement is the integration of multi-fidelity approaches, which combine the information of many low-fidelity simulations with a limited number of expensive high-fidelity results when building the surrogate response. In this context, a larger number of design variables can be eventually included in the optimization, paving the way for three-dimensional and/or multi-stage optimizations. Analogous considerations hold in the context of robust optimizations when more uncertainties are included. The number of CFD simulations required for the multi-point strategy detailed in this work grows exponentially with the number of uncertainty, becoming quickly not feasible when more than two uncertainties are considered. Therefore, an additional surrogate for the stochastic response can be introduced in the optimization besides the one that accounts for the design variables.

Apart from non-ideal effects that arise when $0 < \Gamma < 1$, fluids composed of sufficiently complex molecule can also exhibit $\Gamma < 0$. In this thermodynamic region, non-classical gas-dynamic effects can take place, such as rarefaction shock waves. Although fluids exhibiting non-classical behaviours are presently not commonly employed in ORC power systems, the introduction of mixtures of organic compounds as a working fluid or the possibility to have a two-phase expansion as a means of further efficiency improvement might raise the interest in non-classical effects. Therefore, fundamental studies aiming at determining the impact of non-classical effects on cascade aerodynamics are deemed to be valuable for the scientific community.

Finally, many questions related to the effect of phase change in sCO_2 compressors are still awaiting answers. As mentioned earlier, the effect of phase change on the compressor efficiency was not analyzed in this thesis and there are presently no studies in the literature that address the problem. With this aim in mind, computational methods that consider the two-phase as a mixture are not appropriate because they inherently neglect any local interactions between phases, which are eventually responsible for the efficiency deterioration. In this framework, constitutive relationships that establish such local interactions must be supplied. However, the lack of detailed experimental shreds of evidence for CO_2 evolving close to the critical point complicates the formulation of reliable constitutive laws. Moreover, the assumptions of thermodynamic equilibrium and homogeneous flows, albeit reasonable, need experimental verification as well. Besides phase transition, many other fundamental problems have to be addressed in the context of sCO_2 flows, such as turbulence modelling in presence of large thermo-physical gradients and the deviation of bulk viscosity from the Stokes' hypothesis to name a couple.

Another important point involves the compressor regulation, which can be in principle accomplished via inlet guide vanes. However, this component precedes the impeller and, then, it is most exposed to phase-change phenomena and non-ideal effects. Understanding eventual shortcomings in this connection can help the selection of a safe regulation strategy, which can be ultimately beneficial for the correct operation of the power cycle at part-load conditions.

REFERENCES

Adams, B. M., Ebeida, M. S., Eldred, M. S., Jakeman, J. D., Swiler, L. P., Stephens, J. A., Vigil, D. M., Wildey, T. M., Bohnhoff, W. J., Eddy, J. P., Hu, K. T., Dalbey, K. R., Bauman, L. E. & Hough, P. D. 2017 Dakota, a multilevel parallel object-oriented framework for design optimization, parameter estimation, uncertainty quantification, and sensitivity analysis (version 6.7) .

Adams, T., Grant, C. & Watson, H. 2012 A simple algorithm to relate measured surface roughness to equivalent sand-grain roughness. *International Journal of Mechanical Engineering and Mechatronics* **1**, 66–71.

Ahn, Y., Bae, S. J., Kim, M., Cho, S. K., Baik, S., Lee, J. I. & Cha, J. E. 2015 Review of supercritical CO_2 power cycle technology and current status of research and development. *Nuclear Engineering and Technology* **47** (6), 647 – 661.

Alfani, D., Astolfi, M., Binotti, M. & Silva, P. 2020 Part load strategy definition and annual simulation for small size sCO_2 based pulverized coal power plant. In *Proceedings of the ASME Turbo Expo 2020*, pp. 1–11.

Allison, T. C., Moore, J., Pelton, R., Wilkes, J. & Ertas, B. 2017 7 - Turbomachinery. In *Fundamentals and Applications of Supercritical Carbon Dioxide (sCO_2) Based Power Cycles* (ed. Klaus Brun, Peter Friedman & Richard Dennis), pp. 147 – 215. Woodhead Publishing.

Allison, T. C., Smith, N. R., Pelton, R., Wilkes, J. C. & Jung, S. 2019 Experimental Validation of a Wide-Range Centrifugal Compressor Stage for Supercritical CO_2 Power Cycles. *Journal of Engineering for Gas Turbines and Power* **141** (6), 061011.

Ameli, A., Afzalifar, A., Turunen-Saaresti, T. & Backman, J. 2018*a* Centrifugal compressor design for near-critical point applications. *Journal of Engineering for Gas Turbines and Power* **141** (3), 031016.

Ameli, A., Afzalifar, A., Turunen-Saaresti, T. & Backman, J. 2018*b* Effects of Real Gas Model Accuracy and Operating Conditions on Supercritical CO2 Compressor Performance and Flow Field. *Journal of Engineering for Gas Turbines and Power* **140** (6), 062603.

Angelino, G. 1968 Carbon Dioxide Condensation Cycles For Power Production. *Journal of Engineering for Power* **90** (3), 287–295.

Askey, B. K. & Wilson, J. 1985 *Some Basic Hypergeometric Orthogonal Polynomials that Generalize Jacobi Polynomials*. American Mathematical Society.

Astolfi, M. 2017 3 - Technical options for Organic Rankine Cycle systems. In *Organic Rankine Cycle (ORC) Power Systems* (ed. Ennio Macchi & Marco Astolfi), pp. 67 – 89. Woodhead Publishing.

Astolfi, M., Alfani, D., Lasala, S. & Macchi, E. 2018 Comparison between ORC and CO_2 Power Systems for the exploitation of Low-Medium Temperature Heat Sources. *Energy* **161**, 1250–1261.

Astolfi, M., Romano, M. C., Bombarda, P. & Macchi, E. 2014 Binary ORC (Organic Rankine Cycles) power plants for the exploitation of medium-low temperature geothermal sources – Part B: Techno-economic optimization. *Energy* **66**, 435 – 446.

Aungier, R. H. 2000 *Centrifugal Compressors: A strategy for Aerodynamic Design and Analysis*. ASME Press.

Bahamonde, S., Pini, M., De Servi, C., Rubino, A. & Colonna, P. 2017 Method for the Preliminary Fluid Dynamic Design of High-Temperature Mini-Organic Rankine Cycle Turbines. *Journal of Engineering for Gas Turbines and Power* **139** (8), 082606.

Baltadjiev, N. D., Lettieri, C. & Spakovszky, Z. S. 2015 An Investigation of Real Gas Effects in Supercritical CO_2 Centrifugal Compressors. *Journal of Turbomachinery* **137** (9), 091003.

Banasiak, K. & Hafner, A. 2013 Mathematical modelling of supersonic two-phase R744 flows through converging-diverging nozzles: The effects of phase transition models. *Applied Thermal Engineering* **51** (1), 635 – 643.

Barth, T. J. & Jespersen, D. C. 1989 The design and application of upwind schemes on unstructured meshes. In *American Institute of Aeronautics and Astronautics*.

Bartosiewicz, Y. 2013 Modeling of two-phase choked flows. In *Flow Characteristics and performance of safety valves. Lecture Series 2013-08* (ed. S. Chabane & J.-M. Buchlin). Von Karman Institute for Fluid Dynamics.

Bartosiewicz, Y., Aidoun, Z. & Mercadier, Y. 2006 Numerical assessment of ejector operation for refrigeration applications based on cfd. *Applied Thermal Engeering* **26** (5-6), 604–612.

Bodys, J., Smolka, J., Palacz, M., Haida, M. & Banasiak, K. 2020 Non-equilibrium approach for the simulation of CO2 expansion in two-phase ejector driven by subcritical motive pressure. *International Journal of Refrigeration* **114**, 32 – 46.

Brennen, C. E. 2005 Homogeneous flows. In *Fundamentals of Multiphase Flow*, pp. 176–198. Cambridge University Press.

Brennen, C. E. 2011 Cavitation parameters and inception. In *Hydrodynamics of Pumps*, pp. 77–99. Cambridge University Press.

Bufi, E. A. & Cinnella, P. 2018 Preliminary design method for dense-gas supersonic axial turbine stages. *Journal of Engineering for Gas Turbines and Power* **140**, 112605–1–11.

Bufi, E. A., Cinnella, P. & Merle, X. 2015 Sensitivity of Supersonic ORC Turbine Injector Designs to Fluctuating Operating Conditions. In *Proceedings of the ASME Turbo Expo 2015*.

Callen, H. B. 1985 *Thermodynamics and an introduction to thermostatistics*, 2nd edn. Wiley.

Casati, E., Vitale, S., Pini, M., Persico, G. & Colonna, P. 2014 Preliminary design method for small scale centrifugal ORC turbines. In *Proceedings of the 2nd International Seminar on ORC Power Systems*.

Casey, M. & Robinson, C. 2012 A Method to Estimate the Performance Map of a Centrifugal Compressor Stage. *Journal of Turbomachinery* **135** (2), 021034.

Chernukhin, O. & Zingg, D. W. 2013 Multimodality and global optimization in aerodynamic design. *AIAA Journal* **51** (6), 1342–1354.

Cinnella, P. & Congedo, P. M. 2007 Inviscid and viscous aerodynamics of dense gases. *Journal of Fluid Mechanics* **580**, 179–217.

Coello, C. A. 2000 An updated survey of ga-based multiobjective optimization techniques. *ACM Computing Surveys* **32** (2), 109–143.

Colonna, P., Casati, E., Trapp, C., Mathijssen, T., Larjola, J., Turunen-Saaresti, T. & Uusitalo, A. 2015 Organic Rankine Cycle power systems: From the concept to current technology, applications, and an outlook to the future. *Journal of Engineering for Gas Turbines and Power* **137** (10), 100801.

Colonna, P. & Guardone, A. 2006 Molecular interpretation of nonclassical gasdynamics of dense vapors under the van der Waals model. *Physics of Fluids* **18** (5), 056101–1–14.

Colonna, P., Harinck, J., Rebay, S. & Guardone, A. 2008 Real-gas effects in organic Rankine cycle turbine nozzles. *Journal of Propulsion and Power* **24** (2), 282–294.

Craig, H. R. M. & Cox, H. J. A. 1970 Performance estimation of axial flow turbines. *Proceedings of the Institution of Mechanical Engineers* **185** (1), 407–424.

Cramer, M. S. 1989 Negative nonlinearity in selected fluorocarbons. *Physics of Fluids* **1** (11), 1894–1897.

Cramer, M. S. & Best, L. M. 1991 Steady, isentropic flows of dense gases. *Physics of Fluids* **3** (4), 219–226.

Cramer, M. S. & Crickenberger, A. B. 1992 Prandtl-Meyer function for dense gases. *AIAA Journal* **30** (2), 561–564.

Cramer, M. S. & Kluwick, A. 1984 On the propagation of waves exhibiting both positive and negative nonlinearity. *Journal of Fluid Mechanics* **142**, 9–37.

Crespi, F., Gavagnin, G., Sanchez, D. & Martinez, G. S. 2017*a* Analysis of the Thermodynamic Potential of Supercritical Carbon Dioxide Cycles: A Systematic Approach. *Journal of Engineering for Gas Turbines and Power* **140** (5), 051701.

Crespi, F., Gavagnin, G., Sanchez, D. & Martinez, G. S. 2017*b* Supercritical carbon dioxide cycles for power generation: A review. *Applied Energy* **195**, 152–183.

Crestaux, T., Le Maître, O. & Martinez, J. M. 2009 Polynomial chaos expansion for sensitivity analysis. *Reliability Engineering and System Safety* **94** (7), 1161 – 1172.

Dang Le, Q., Mereu, R., Besagni, G., Dossena, V. & Inzoli, F. 2018 Computational Fluid Dynamics Modeling of Flashing Flow in Convergent-Divergent Nozzle. *Journal of Fluids Engineering* **140** (10), 101102.

De Lorenzo, M., Lafon, Ph., Di Matteo, M., Pelanti, M., Seynhaeve, J.-M. & Bartosiewicz, Y. 2017*a* Homogeneous two-phase flow models and accurate steam-water table look-up method for fast transient simulations. *International Journal of Multiphase Flow* **95**, 199 – 219.

De Lorenzo, M., Lafon, Ph., Seynhaeve, J.-M. & Bartosiewicz, Y. 2017*b* Benchmark of delayed equilibrium model (dem) and classic two-phase critical flow models against experimental data. *International Journal of Multiphase Flow* **92**, 112 – 130.

Denton, J. D. & Xu, L. 1990 The trailing edge loss of transonic turbine blades. *Journal of Turbomachinery* **112** (2), 277–285.

Diener, R. & Schmidt, J. 2004 Sizing of throttling device for gas/liquid two-phase flow Part 1: Safety valves. *Process Safety Progress* **23**, 335–344.

Diener, R. & Schmidt, J. 2005 Sizing of throttling device for gas/liquid two-phase flow Part 2: Control valves, orifices, and nozzles. *Process Safety Progress* **24**, 29–37.

Dostal, V. 2004 A supercritical carbon dioxide cycle for next generation nuclear reactors. PhD thesis, Massachusetts Institute of Technology.

Eckert, B. & Schnell, E. 1961 *Axial-und Radial- Kompressoren*. Springer Verlag.

Eddy, J. 2009 JEGA (version 2.3).

Fang, Yu 2019 Advanced numerical simulations of two-phase CO_2 ejectors. PhD thesis, Universite catholique de Louvain.

Farin, G. 2006 *Curves and Surfaces for Computer-Aided Geometric Design: a practical guide*. Elsevier Inc.

Flatten, T. & Lund, H. 2011 Relaxation two-phase flow models and the subcharacteristic condition. *Mathematical Models and Methods in Applied Sciences* **21** (12), 2379–2407.

Freeman, J., Hellgardt, K. & Markides, C. N. 2015 An assessment of solar-powered organic rankine cycle systems for combined heating and power in uk domestic applications. *Applied Energy* **138**, 605 – 620.

Gaetani, P., Persico, G. & Osnaghi, C. 2010 Effects of axial gap on the vane-rotor interaction in a low aspect ratio turbine stage. *Journal of Propulsion and Power* **26** (2), 325–334.

Galiana, F. J. D., Wheeler, A. P. S. & Ong, J. 2016 A study of trailing-edge losses in Organic Rankine Cycle turbines. *Journal of Turbomachinery* **138** (12), 121003.

Galiana, F. J. D., Wheeler, A. P. S., Ong, J. & de M Ventura, C. A. 2017 The effect of dense gas dynamics on loss in ORC transonic turbines. *Journal of Physics: Conference Series* **821** (1), 012021.

Giacomelli, F., Mazzelli, F. & Milazzo, A. 2018 A novel cfd approach for the computation of R744 flashing nozzles in compressible and metastable conditions. *Energy* **162**, 1092 – 1105.

Giles, M. B. & Pierce, N. A. 2000 An introduction to the adjoint approach to design. *Flow, Turbulence and Combustion* **65**, 393–415.

Goldman, L. J. 1972 Supersonic Turbine Design and Performance. In *Proceedings of ASME Turbo Expo 1972*.

Gori, G., Vimercati, D. & Guardone, A. 2017 Non-ideal compressible-fluid effects in oblique shock waves. *Journal of Physics: Conference Series* **821**, 012003.

Grübel, M., Starzmann, J., Schatz, M., Eberle, T., Vogt, D.M & Sieverding, F. 2015 Two-Phase Flow Modeling and Measurements in Low-Pressure Turbines - Part I: Numerical Validation of Wet Steam Models and Turbine Modeling. *Journal of Engineering for Gas Turbines and Power* **137** (4), 042602.

Guardone, A. & Vimercati, D. 2016 Exact solutions to non-classical steady nozzle flows of Bethe-Zel'dovich-Thompson fluids. *Journal of Fluid Mechanics* **800**, 278–306.

Guardone, A., Zamfirescu, C. & Colonna, P. 2010 Maximum intensity of rarefaction shock waves for dense gases. *Journal of Fluid Mechanics* **642**, 127–146.

Gyarmathy, G. 2005 Nucleation of steam in high-pressure nozzle experiments. *Proceedings of the Institution of Mechanical Engineers, Part A: Journal of Power and Energy* **219** (6), 511–521.

Hacks, A.J., Schuster, S. & Brillert, D. 2019 Stabilizing effects of supercritical CO_2 fluid properties on compressor operationy. *International Journal of Turbomachinery, Propulsion and Power* **4** (3).

Han, Z., Gortz, S. & Zimmermann, R. 2013 Improving variable-fidelity surrogate modeling via gradient-enhanced kriging and a generalized hybrid bridge function. *Aerospace Science and Technology* **25** (1), 177 – 189.

Han, Z., Zhang, Y., Song, C. & Zhang, K. 2017 Weighted gradient-enhanced kriging for high-dimensional surrogate modeling and design optimization. *AIAA Journal* **55** (12), 4330–4346.

Harinck, J., Guardone, A. & Colonna, P. 2009 The influence of molecular complexity on expanding flows of ideal and dense gases. *Physics of Fluids* **21** (8), 086101.

Head, A. J., De Servi, C., Casati, E., Pini, M. & Colonna, P. 2016 Preliminary design of the ORCHID: A facility for studying non-ideal compressible fluid dynamics and testing ORC expanders. In *Proceedings of ASME Turbo Expo 2016*.

Hoffren, J., Talonpoika, T., Larjola, J. & Siikonen, T. 2002 Numerical simulation of real-gas flow in a supersonic turbine nozzle ring. *Journal of Engineering for Gas Turbines and Power* **124**, 395–403.

Hosangadi, A. & Ahuja, V. 2005 Numerical Study of Cavitation in Cryogenic Fluids . *Journal of Fluids Engineering* **127** (2), 267–281.

Hosangadi, A., Liu, Z., Weathers, T., Ahuja, V. & Busby, J. 2019 Modeling Multiphase Effects in CO_2 Compressors at Subcritical Inlet Conditions. *Journal of Engineering for Gas Turbines and Power* **141** (8), 081005.

International Energy Agency 2019 *World Energy Outlook 2019*.

Ishii, M. & Hibiki, T. 2011 *Thermo-Fluid Dynamics of Two-Phase Flow*. Springer-Verlag New York.

Jansen, W. 1967 A method for calculating the flow in a centrifugal impeller when entropy gradients are present. In *Royal Society Conference on Internal Aerodynamics (Turbomachinery)*, pp. 133–146.

Jones, D.R., Perttunen, C.D. & Stuckman, B.E. 1993 Lipschitzian optimization without the lipschitz constant. *Journal of Optimization Theory and Applications* **79** (1), 157–181.

Jones, D. R., Schonlau, M. & Welch, W. J. 1998 Efficient Global Optimization of Expensive Black-Box Functions. *Journal of Global Optimization* **13**, 455–492.

Keulen, L., Gallarini, S., Landolina, C., Spinelli, A., Iora, P., Invernizzi, C., Lietti, L. & Guardone, A. 2018 Thermal stability of hexamethyldisiloxane and octamethyltrisiloxane. *Energy* **165**, 868 – 876.

Kluwick, A. 2001 Rarefaction shocks. In *Handbook of Shock Waves* (ed. G. Ben-Dor, O. Igra & T. Elperin), pp. 339–411. Academic Press.

Kluwick, A. 2004 Internal flows of dense gases. *Acta Mechanica* **169**, 123–143.

Kouremenos, D.A. & Antonopoulos, K.A. 1987 Isentropic exponents of real gases and application for the air at temperatures from 150 k to 450 k. *Acta Mechanica* **65**, 81–99.

Lai, N. A., Wendland, M. & Fischer, M 2011 Working fluids for high-temperature organic Rankine cycles. *Energy* **36** (1), 199 – 211.

Laurenceau, J. & Sagaut, P. 2008 Building efficient response surfaces of aerodynamic functions with kriging and cokriging. *AIAA Journal* **46** (2), 498–507.

Le Maître, O. & Knio, O. M. 2012 *Spectral Methods for Uncertainty Quantification: With Applications to Computational Fluid Dynamics*. Springer Netherlands.

Lee, E.T.Y. 1989 Choosing nodes in parametric curve interpolation. *Computer-Aided Design* **21** (6), 363 – 370.

Lee, J., Lee, J. I., Yoon, H. J. & Cha, J. E. 2014 Supercritical Carbon Dioxide turbomachinery design for water-cooled Small Modular Reactor application. *Nuclear Engineering and Design* **270**, 76–89.

Lemmon, E. W., Huber, M. L. & McLinden, M. O. 2013 NIST reference database 23: reference fluid thermodynamic and transport properties–REFPROP, version 9.1. *Standard Reference Data Program* .

Lettieri, C., Baltadjiev, N. D., Casey, M. & Spakovszky, Z. S. 2014 Low-Flow-Coefficient Centrifugal Compressor Design for Supercritical CO_2. *Journal of Turbomachinery* **136** (8), 081008.

Lettieri, C., Paxson, D., Spakovszky, Z. & Bryanston-Cross, P. 2017 Characterization of Nonequilibrium Condensation of Supercritical Carbon Dioxide in a de Laval Nozzle. *Journal of Engineering for Gas Turbines and Power* **140** (4), 041701.

Ludtke, K. H. 2004 *Process Centrifugal Compressors: Basics, Function, Operation, Design, Application*. Springer.

Macchi, E. 2017 1 - Theoretical basis of the Organic Rankine Cycle. In *Organic Rankine Cycle (ORC) Power Systems* (ed. Ennio Macchi & Marco Astolfi), pp. 3 – 24. Woodhead Publishing.

Macchi, E. & Astolfi, M. 2017 9 - Axial flow turbines for Organic Rankine Cycle applications. In *Organic Rankine Cycle (ORC) Power Systems* (ed. Ennio Macchi & Marco Astolfi), pp. 299 – 319. Woodhead Publishing.

Macchi, E. & Perdichizzi, A. 1981 Efficiency Prediction for Axial-Flow Turbines Operating with Nonconventional Fluids. *Journal of Engineering for Power* **103** (4), 718.

Marchionni, M., Bianchi, G. & Tassou, S. A. 2020 Review of supercritical carbon dioxide (sCO_2) technologies for high-grade waste heat to power conversion. *SN Applied Sciences* **2** (4), 1–13.

Martin, J. D. & Simpson, T. W. 2005 Use of Kriging Models to Approximate Deterministic Computer Models. *AIAA Journal* **43** (4), 853–863.

Martin, J. J. & Hou, Y. C. 1955 Development of an equation of state for gases. *AIChE Journal* **1** (2), 142–151.

Mee, D. J., Baines, N. C., Oldfield, M. L. G. & Dickens, T. E. 1992 An Examination of the Contributions to Loss on a Transonic Turbine Blade in Cascade. *Journal of Turbomachinery* **114** (1), 155–162.

Meier, K., Laesecke, A. & Kabelac, S S. 2004 Transport coefficients of the Lennard-Jones model fluid - I. Viscosity. *The Journal of Chemical Physics* **121** (8), 3671–3687.

Menikoff, R. & Plohr, B. J. 1989 The Riemann problem for fluid flow of real materials. *Reviews of Modern Physics* **61(1)**, 75–130.

Menter, F. R. 1994 Two-equation eddy-viscosity turbulence models for engineering applications. *AIAA Journal* **32** (8), 1598–1605.

Meroni, A., Andreasen, J. G., Persico, G. & Haglind, F. 2018*a* Optimization of organic Rankine cycle power systems considering multistage axial turbine design. *Applied Energy* **209**, 339 – 354.

Meroni, A., Zuhlsdorf, B., Elmegaard, B. & Haglind, F. 2018*b* Design of centrifugal compressors for heat pump systems. *Applied Energy* **232**, 139–156.

Mitchell, M. 1996 *An Introduction to Genetic Algorithms*. MIT Press.

Moisseytsev, A. & Sienicki, J. J. 2009 Investigation of alternative layouts for the supercritical carbon dioxide brayton cycle for a sodium-cooled fast reactor. *Nuclear Engineering and Design* **239** (7), 1362–1371.

Mueller, L. & Verstraete, T. 2017 Cad integrated multipoint adjoint-based optimization of a turbocharger radial turbine. *International Journal of Turbomachiner Propulsion and Power* **2**, 1–14.

Musgrove, G. & Wright, S. 2017 1 - Introduction and background. In *Fundamentals and Applications of Supercritical Carbon Dioxide (sCO$_2$) Based Power Cycles* (ed. Klaus Brun, Peter Friedman & Richard Dennis), pp. 1 – 22. Woodhead Publishing.

Nakagawa, M., Berana, M. S. & Kishine, A. 2009 Supersonic two-phase flow of CO$_2$ through converging–diverging nozzles for the ejector refrigeration cycle. *International Journal of Refrigeration* **32** (6), 1195–1202.

Nannan, N. R., Guardone, A. & Colonna, P. 2013 On the fundamental derivative of gas dynamics in the vapor–liquid critical region of single-component typical fluids. *Fluid Phase Equilibria* **337**, 259–273.

Neises, T. & Turchi, C. 2014 A Comparison of Supercritical Carbon Dioxide Power Cycle Configurations with an Emphasis on CSP Applications. *Energy Procedia* **49**, 1187 – 1196.

Noall, J. S. & Pasch, J. J. 2014 Achievable Efficiency and Stability of Supercritical CO$_2$ Compression Systems Main Compressor Design Discussion. *The 4th International Symposium - Supercritical CO$_2$ Power Cycles September 2014* pp. 1–10.

Ntanakas, G., Meyer, M. & Giannakoglou, K. C. 2018 Employing the Time-Domain Unsteady Discrete Adjoint Method for Shape Optimization of Three-Dimensional Multirow Turbomachinery Configurations. *Journal of Turbomachinery* **140** (8), 081006.

Oh, H. W., Yoon, E. S. & Chung, M. K. 1997 An optimum set of loss models for performance prediction of centrifugal compressors. *Proceedings of the Institution of Mechanical Engineers, Part A: Journal of Power and Energy* **211** (4), 331–338.

Otero, R. G. J., Patel, A., Diez, S. R. & Pecnik, R. 2018 Turbulence modelling for flows with strong variations in thermo-physical properties. *International Journal of Heat and Fluid Flow* **73**, 114 – 123.

Padilla, R. V., Soo Too, Y. C., Benito, R., McNaughton, R. & Stein, W. 2016 Thermodynamic feasibility of alternative supercritical co2 brayton cycles integrated with an ejector. *Applied Energy* **169**, 49–62.

Palacz, M., Smolka, J., Fic, A., Bulinski, Z., Nowak, A. J., Banasiak, K. & Hafner, A. 2015 Application range of the HEM approach for CO2 expansion inside two-phase ejectors for supermarket refrigeration systems. *International Journal of Refrigeration* **59**, 251 – 258.

Pantaleo, A. M., Camporeale, S. M., Miliozzi, A., Russo, V., Shah, N. & Markides, C. N. 2017 Novel hybrid csp-biomass chp for flexible generation: Thermo-economic analysis and profitability assessment. *Applied Energy* **204**, 994 – 1006.

Pasquale, D., Ghidoni, A. & Rebay, S. 2013 Shape Optimization of an Organic Rankine Cycle Radial Turbine Nozzle. *Journal of Engineering for Gas Turbines and Power* **135** (4), 042308.

Pecnik, R., Rinaldi, E. & Colonna, P. 2012 Computational fluid dynamics of a radial compressor operating with supercritical CO_2. *Journal of Engineering for Gas Turbines and Power* **134** (12), 122301.

Pelanti, M. & Shyue, K.M. 2019 A numerical model for multiphase liquid–vapor–gas flows with interfaces and cavitation. *International Journal of Multiphase Flow* **113**, 208 – 230.

Peng, D. Y. & Robinson, D. B. 1976 A new two-constant equation of state. *Industrial & Engineering Chemistry Fundamentals* **15**, 59–64.

Perkins, R. A., Sengers, J. V., Abdulagatov, I. M. & Huber, M. L. 2013 Simplified model for the critical thermal-conductivity enhancement in molecular fluids. *International Journal of Thermophysics* **34** (2), 191–212.

Persico, G. 2017 Evolutionary optimization of centrifugal nozzles for organic vapours. *Journal of Physics: Conference Series* **821** (1), 012015.

Persico, G., Gaetani, P., Romei, A., Toni, L., Bellobuono, E.F. & Valente, R. 2021 Implications of phase change on the aerodynamics of centrifucal compressors for supercritical carbon dioxide applications. *Journal of Engineering Gas Turbines and Power* **143** (4), 041007.

Persico, G., Mora, A., Gaetani, P. & Savini, M. 2012 Unsteady aerodynamics of a low aspect ratio turbine stage: Modeling issues and flow physics. *Journal of Turbomachinery* **134** (6), 061030.

Persico, G. & Pini, M. 2017 8 - Fluid dynamic design of Organic Rankine Cycle turbines. In *Organic Rankine Cycle (ORC) Power Systems* (ed. Ennio Macchi & Marco Astolfi), pp. 253 – 297. Woodhead Publishing.

Persico, G., Pini, M., Dossena, V. & Gaetani, P. 2013 Aerodynamic design and analysis of centrifugal turbine cascades. *Journal of Engineering for Gas Turbines and Power* **137** (11), 112602.

PIERRET, S. & VAN DEN BRAEMBUSSCHE, R. A. 1999 Turbomachinery Blade Design Using a Navier-Stokes Solver and Artificial Neural Network. *Journal of Turbomachinery* **121** (2), 326–332.

PINI, M., PERSICO, G., CASATI, E. & DOSSENA, V. 2013 Preliminary Design of a Centrifugal Turbine for Organic Rankine Cycle Applications. *Journal of Engineering for Gas Turbines and Power* **135** (4), 042312.

PINI, M., PERSICO, G. & DOSSENA, V. 2014 Robust adjoint-based shape optimization of supersonic turbomachinery cascades. In *Proceedings of ASME Turbo Expo 2014*, pp. 1–13.

PINI, M, PERSICO, G., PASQUALE, D. & REBAY, S. 2015*a* Adjoint method for shape optimization in real-gas flow applications. *Journal of Engineering for Gas Turbines and Power* **137**, 1–13.

PINI, M., SPINELLI, A., PERSICO, G. & REBAY, S. 2015*b* Consistent look-up table interpolation method for real-gas flow simulations. *Computers & Fluids* **107**, 178 – 188.

PINI, M., VITALE, S., COLONNA, P., GORI, G., GUARDONE, A., ECONOMON, T., ALONSO, J. J. & PALACIOS, F. 2017 SU2: the open-source software for non-ideal compressible flows. *Journal of Physics: Conference Series* **821** (1), 012013.

POERNER, M. & RIMPEL, A. 2017 10 - Waste heat recovery. In *Fundamentals and Applications of Supercritical Carbon Dioxide (sCO$_2$) Based Power Cycles* (ed. Klaus Brun, Peter Friedman & Richard Dennis), pp. 255 – 267. Woodhead Publishing.

PREISSINGER, M. & BRUGGEMANN, D. 2016 Thermal Stability of Hexamethyldisiloxane (MM) for High-Temperature Organic Rankine Cycle (ORC). *Energies* **9** (3).

RAZAALY, N., PERSICO, G. & CONGEDO, P. M. 2019 Impact of geometric, operational, and model uncertainties on the non-ideal flow through a supersonic ORC turbine cascade. *Energy* **169**, 213 – 227.

RAZAALY, N., PERSICO, G., GORI, G. & CONGEDO, P. M. 2020 Quantile-based robust optimization of a supersonic nozzle for organic rankine cycle turbines. *Applied Mathematical Modelling* **82**, 802 – 824.

REISENTHEL, P. H., & ALLEN, T. T. 2010 Application of multifidelity expected improvement algorithms to aeroelastic design optimization. *10th AIAA Multidisciplinary Design Optimization Conference* .

RINALDI, E., PECNIK, R. & COLONNA, P. 2015 Computational fluid dynamic simulation of a supercritical CO$_2$ compressor performance map. *Journal of Engineering for Gas Turbines and Power* **137** (7), 072602.

RINALDI, E., PECNIK, R. & COLONNA, P. 2016 Unsteady operation of a highly supersonic orc turbine. *Journal of Turbomachinery* **128** (12), 121010.

ROACHE, P. J. 1997 Quantification of uncertainty in computational fluid dynamics. *Annual Review of Fluid Mechanics* **29** (1), 123–160.

ROMEI, A., CONGEDO, P. M. & PERSICO, G. 2019 Assessment of deterministic shape optimizations within a stochastic framework for supersonic organic rankine cycle nozzle cascades. *Journal of Engineering for Gas Turbine and Power* **141(7)**, 1–11.

Romei, A. & Persico, G. 2018 Novel shape parametrization technique applied to the optimization of a supersonic orc turbine cascade. In *Proceedings of ASME Turbo Expo 2018*.

Sabater, C. & Goertz, S. 2019 An efficient bi-level surrogate approach for optimizing shock control bumps under uncertainty. *AIAA Scitech 2019 Forum* pp. 1–20.

Sawyer, J. 1972 *Gas Turbine Engineering Handbook*. Gas Turbine Publications, Stamford (CT).

Schatz, M., Eberle, T., Grübel, M., Starzmann, J., Vogt, D.M. & Suerken, N. 2015 Two-Phase Flow Modeling and Measurements in Low-Pressure Turbines - Part II: Turbine Wetness Measurement and Comparison to Computational Fluid Dynamics-Predictions. *Journal of Engineering for Gas Turbines and Power* **137** (4), 042603.

Schiffmann, J. & Favrat, D. 2010 Design, experimental investigation and multi-objective optimization of a small-scale radial compressor for heat pump applications. *Energy* **35** (1), 436–450.

Schuster, A., Karellas, S. & Aumann, R. 2010 Efficiency optimization potential in supercritical organic rankine cycles. *Energy* **35** (2), 1033 – 1039.

Sciacovelli, L., Cinnella, P. & Gloerfelt, X. 2017 Direct numerical simulations of supersonic turbulent channel flows of dense gases. *Journal of Fluid Mechanics* **821**, 153–199.

Sengupta, U., Nemati, H., Boersma, B.J. & Pecnik, R. 2017 Fully compressible low-mach number simulations of carbon-dioxide at supercritical pressures and trans-critical temperatures. *Flow, Turbulence and Combustion* **99** (3-4), 909–931.

Simpson, T., Poplinski, J., Koch, P. & Allen, J.K. 2001 Metamodels for computer-based engineering design: Survey and recommendations. *Engineering with Computers* **17**, 129–150.

Sinha, K., Mahesh, K. & Candler, G. V. 2003 Modeling shock unsteadiness in shock/turbulence interaction. *Physics of Fluids* **15** (8), 2290–2297.

Spadacini, C., Centemeri, L., Xodo, L. G., Astolfi, M., Romano, M. C. & Macchi, E. 2011 A new configuration for organic rankine cycle power systems. In *First International Seminar on ORC Power Systems, Delft, The Netherlands, Sept*, pp. 11–23.

Spalart, P. R. & Allmaras, S. R. 1992 A one-equation turbulence model for aerodynamic flows. *AIAA Paper 92-0439* .

Span, R. & Wagner, W. 1996 A New Equation of State for Carbon Dioxide Covering the Fluid Region from the Triple–Point Temperature to 1100 K at Pressures up to 800 MPa. *Journal of Physical and Chemical Reference Data* **25** (6), 1509–1596.

Span, R. & Wagner, W. 2003*a* Equations of state for technical applications. I. Simultaneously optimized functional forms for nonpolar and polar fluids. *International Journal of Thermophysics* **24** (1), 1–39.

Span, R. & Wagner, W. 2003*b* Equations of state for technical applications. II. Results for nonpolar fluids. *International Journal of Thermophysics* **24** (1), 41–109.

Spinelli, A., Cammi, G., Gallarini, S., Zocca, M., Cozzi, F., Gaetani, P., Dossena, V. & Guardone, A. 2019 Experimental evidence of non-ideal compressible effects in expanding flow of a high molecular complexity vapor. *Experiments in Fluids* **59**, 1–16.

STARKEN, H 1993 *Basic fluid dynamic boundary conditions of cascade wind tunnels*. in Advanced Methods of Cascade Testing.

STARKEN, H, YONGXING, Z. & SCHREIBER, H.-A. 1984 Mass flow limitation of supersonic blade rows due to leading edge blockage.

STEIN, M. L. 1999 *Interpolation of Spatial Data: Some Theory for Kriging*. New York: Springer.

TAN, D., LI, Y., WILKES, I., VAGNONI, E., MIORINI, R. L. & KATZ, J. 2015 Experimental investigation of the role of large scale cavitating vortical structures in performance breakdown of an axial waterjet pump. *Journal of Fluids Engineering* **137** (11), 111301.

THOL, M., DUBBERKE, F. H., BAUMHÖGGER, E., VRABEC, J. & SPAN, R. 2017 Speed of Sound Measurements and Fundamental Equations of State for Octamethyltrisiloxane and Decamethyltetrasiloxane. *Journal of Chemical & Engineering Data* **62** (9), 2633–2648.

THOL, M., DUBBERKE, F. H., RUTKAI, G., WINDMANN, T., KÖSTER, A., SPAN, R. & VRABEC, J. 2016 Fundamental equation of state correlation for hexamethyldisiloxane based on experimental and molecular simulation data. *Fluid Phase Equilibria* **418**, 133 – 151.

THOMPSON, P. A. 1971 A fundamental derivative in gasdynamics. *Physics of Fluids* **14** (9), 1843–1849.

THOMPSON, P. A. 1988 *Compressilbe Fluid Dynamics*. McGraw-Hill.

THOMPSON, P. A. & LAMBRAKIS, K. C. 1973 Negative shock waves. *Journal of Fluid Mechanics* **60**, 187–208.

VERSTRAETE, T., ALSALIHI, Z. & VAN DEN BRAEMBUSSCHE, R. A. 2010 Multidisciplinary Optimization of a Radial Compressor for Microgas Turbine Applications. *Journal of Turbomachinery* **132** (3), 031004.

VIMERCATI, D., GORI, G. & GUARDONE, A. 2018 Non-ideal oblique shock waves. *Journal of Fluid Mechanics* **847**, 266–285.

VITALE, S., ALBRING, T. A., PINI, M., GAUGER, N. R. & COLONNA, P. 2017 Fully turbulent discrete adjoint solver for non-ideal compressible flow applications. *Journal of the Global Power and Propulsion Society* **1**, 252–270.

VITALE, S., PINI, M. & COLONNA, P. 2020 Multistage Turbomachinery Design Using the Discrete Adjoint Method Within the Open-Source Software SU2. *Journal of Propulsion and Power* **36** (3), 465–478.

WALTHER, B.AND NADARAJAH, S. 2012 Constrained Adjoint-Based Aerodynamic Shape Optimization of a Single-Stage Transonic Compressor. *Journal of Turbomachinery* **135** (2), 021017.

WHEELER, A. P. S. & ONG, J. 2013 The role of dense gas dynamics on organic rankine cycle turbine performance. *Journal of Engineering for Gas Turbines and Power* **135** (10), 102603.

WHITFIELD, A. & BAINES, N. C. 1990 *Design of radial turbomachines*. Longman Singapore Publishers (Pte) Ltd.

WIESNER, F. J. 1967 A Review of Slip Factors for Centrifugal Impellers. *Journal of Engineering for Gas Turbines and Power* **89** (4), 558–566.

WILSON, D. 1984 *The Design of High–Efficiency Turbomachinery and Gas Turbines*. MIT Press.

Wood, A. B. 1941 *A textbook of sound: being an account of the physics of vibrations with special reference to recent theoretical and technical developments*. New York: The Macmillan company.

Wright, S. A., Pickard, P. S., Vernon, M. E., Radel, R. F. & Fuller, R. 2009 Description and test results from a supercritical CO_2 Brayton cycle development program. *7th International Energy Conversion Engineering Conference* .

Wright, S. A., Radel, R. F., Vernon, M. E., Rochau, G. E. & Pickard, P. S. 2010 Operation and analysis of a supercritical CO_2 Brayton cycle. *Sandia Report SAND2010-0171* .

Yazdani, M., Alahyari, A. A. & Radcliff, T. D. 2012 Numerical modeling of two-phase supersonic ejectors for work-recovery applications. *International Journal of Heat and Mass Transfer* **55** (21), 5744 – 5753.

Ye, K. Q. 1998 Orthogonal column latin hypercubes and their application in computer experiments. *Journal of the American Statistical Association* **93** (444), 1430–1439.

Young, J.B. 1991 The condensation and evaporation of liquid droplets in a pure vapour at arbitrary knudsen number. *International Journal of Heat and Mass Transfer* **34** (7), 1649 – 1661.

Young, J. B. 1992 Two-dimensional, nonequilibrium, wet-steam calculations for nozzles and turbine cascades. *Journal of Turbomachinery* **114**, 569–579.

Yu, H., Feng, X., Wang, Y., Biegler, L. T. & Eason, J. 2016 A systematic method to customize an efficient organic Rankine cycle (ORC) to recover waste heat in refineries. *Applied Energy* **179**, 302 – 315.

Zamfirescu, C., Guardone, A. & Colonna, P. 2008 Admissibility region for rarefaction shock waves in dense gases. *Journal of Fluid Mechanics* **599**, 363–381.

Zanellato, L., Astolfi, M., Serafino, A., Rizzi, D. & Macchi, E. 2018 Field performance evaluation of geothermal ORC power plants with a focus on radial outflow turbines. *Renewable Energy* pp. 2896–2904.

Zhu, J., Wang, S. & Zhang, X. 2020 Influences of thermal effects on cavitation dynamics in liquid nitrogen through venturi tube. *Physics of Fluids* **32** (1), 012105.

Zweifel, O. 1945 The spacing of turbo-machine blading especially with large angular deflection. *Brown Boveri Rev.* **32**, 436–444.

NOMENCLATURE

Acronyms/Abbreviations

CCS	Carbon-capture sequestration
CP	Control points
CFD	Computational fluid dynamics
CoV	Coefficient of variation
DEM	Delayed equilibrium model
DoE	Design of experiments
GA	Genetic algorithm
GCI	Grid Convergence Index
HEM	Homogeneous equilibrium model
HFM	Homogeneous frozen model
JEGA	Java engine for genetic algorithms
LE	Leading edge
LHS	Latin hypercube sampling
LTR	Low-temperature regenerator
LUT	Look up table
MDM	Octamethyltrisiloxane
MM	Hexamethyldisiloxane
NEM	Non-homogeneous equilibrium model
NICFD	Non-ideal compressible-fluid dynamics
OP	Operating point
ORC	Organic Rankine cycle
PC	Polynomial chaos
pp	percentage points
PSS	Pressure side shock
PSW	Pressure side wake
RANS	Reynolds-averaged Navier-Stokes
RS	Reflected shock
sCO_2	Supercritical carbon dioxide
SSW	Suction side wake
TE	Trailing edge
TVD	Total variation diminishing
UDF	User-defined function
UDRGM	User-defined real-gas model
UQ	Uncertainty quantification
WMAPE	Weighted mean absolute percentage error

Latin alphabet

A	Area
b	Blade height
$\mathcal{B}$	Beta distribution
c	Speed of sound / chord
c_f	friction coefficient
c_p	Isobaric specific heat capacity
$c_{p,\infty}$	Isobaric specific heat capacity in the ideal-gas limit
c_v	Isocoric specific heat capacity
$c_{v,\infty}$	Isocoric specific heat capacity in the ideal-gas limit
C_P	Pressure recovery coefficient
$\mathcal{C}$	Phase-change coefficient
$\mathbf{d}$	Design variables
$\tilde{\mathbf{d}}$	Assigned design variables
D	Diameter
f	Brennen's constant / Normalization constant for $\mathcal{C}$
$\mathbf{f}$	Kriging functional bases
$\mathbf{F}$	Matrix containing functional bases evaluated at $\tilde{\mathbf{d}}$
g	Brennen's constant
$\mathcal{G}$	Phase-change source term
h	Specific enthalpy
$\mathcal{H}$	Hermite polynomials
i	incidence
$\overline{i_{rot}}$	pitchwise rotor incidence
J	Dimensionless derivative of Mach number with density
k	Turbulent kinetic energy / generalized isentropic coefficient
$\bar{k}$	Average generalized isentropic coefficient
$\mathcal{K}$	Penalty constant
k_μ	multiplicative constant for slip factor
$\dot{m}$	Mass-flow rate
M	Mach number
M_{sat}	Mixture Mach number
M_{u_2}	Peripheral Mach number
M_w	Relative Mach number
N	Molecular complexity
N_{bl}	Number of blades
N_{eff}	Effective number of blades
N_{vn}	Number of vanes
N^n	n-degree B-spline
$\mathcal{N}$	Normal distribution
P	Pressure
$\widetilde{P_{sat}}$	saturation pressure at the upstream entropy
P_{sat}	saturation pressure at the local temperature
Pr_t	Turbulent Prandtl number
q	Heat flux
r	Reaction degree
$\mathbf{r}$	Vector of spatial correlations between $\mathbf{d}$ and $\tilde{\mathbf{d}}$
$\mathbf{R}$	Correlation matrix
$\mathcal{R}$	Specific gas constant

R	Radius
R^2	Coefficient of determination
Re	Reynolds number
Re_{u_2}	Peripheral Reynolds number
s	Specific entropy
s^2	Kriging mean-square error
S^T	Total Sobol index
SF	Split factor
SP	Size parameter
t	thickness
T	Temperature / turbulence intensity
$\hat{T}$	Total temperature for multi-point optimization
$\mathcal{T}$	Stress tensor
$\mathcal{T}_{turb}$	Reynolds stress tensor
u	Peripheral velocity
u^+	Dimensionless velocity
$\mathcal{U}$	Uniform distribution
v	Specific volume / absolute velocity
$\dot{V}$	Volumetric flow rate
w	Data parameter for B-spline / relative velocity / weight / mass fraction
$\dot{W}$	Power
$\tilde{y}$	Blade response at $\tilde{\mathbf{d}}$
y^+	Dimensionless wall distance
Y	Generic Kriging process / Total-pressure loss coefficient
Z	Compressibility factor

Greek alphabet

α	Volumetric fraction / absolute angle
β	Pressure ratio / Relative angle
$\boldsymbol{\beta}$	Kriging regression coefficient
$\hat{\boldsymbol{\beta}}$	Least squares Kriging regression coefficient
γ	Ratio of specific heats
$\varGamma$	Fundamental derivative of gas dynamic
δ	Clearance
ϵ	Interacting fluid portion
ε	Error
η	Efficiency
ϑ	Flow deflection angle / Azimuthal coordinate
$\boldsymbol{\vartheta}$	Spatial-correlation hyperparameters
$\hat{\boldsymbol{\vartheta}}$	Least squares estimate of spatial-correlation hyperparameters
κ	Thermal conductivity
λ	Work coefficient
μ	Molecular viscosity / mean value
μ_{slip}	Slip coefficient
μ_t	Turbulent viscosity
ρ	Density
σ	Standard deviation
σ^2	Variance
$\hat{\sigma}^2$	Least squares estimate of Kriging variance

Σ	Covariance
ϕ	Flow coefficient
φ	Wrap Angle
ξ	Polynomial chaos coefficients
ψ	Orthogonal polynomials / generic thermo-physical variable
Ψ	Isentropic head
ω	Rotational speed

Superscripts

c	compressor
t	Total or stagnation thermodynamic state / turbine
T	Transpose
$*$	critical

Subscripts

A	Pre-shock state
ax	Axial
aux	Auxiliary
bl	Blade
$baro$	Barotropic
c	Critical / Compressor
$cond$	Condenser
cns	Constraint
d	Dispersed/secondary phase
des	Design
$diff$	Diffuser
el	Electrical
eul	Eulerian
exp	Experimental
ext	External
eva	Evaporator
$fine$	Computed with the finest grid
g	Geometric
h	Hub
id	Ideal
imp	Impeller
in	Inlet
is	Isentropic
L	Liquid phase
m	Midspan
max	Maximum
min	Minimum
mix	Mixture
nom	Nominal
$norm$	Normalized to unity
of	Objective function
out	Outlet
p	Primary phase

r	Reduced / radial / rotor
s	Stator
sat	Saturation
t	Turbine / Tip
tg	Tangential
th	Thermal / Throat
$turb$	Turbulent
TT	Total-to-total
TS	Total-to-static
V	Vapour phase
vn	Vaned
vol	Volute
w	wall
0	Stagnation / stator inlet
1	Stator outlet / impeller inlet
2	Rotor/impeller outlet
3	Vaned diffusur inlet
4	Vaned diffuser outlet
5	Volute outlet

Mathematical symbols

$\mathbb{E}$	Expected value
$\mathit{\Delta}$	Difference (out - in)
∇	Gradient
$\times$	Vector product
$\cdot$	Scalar product
$\mathcal{O}$	Big O

LIST OF FIGURES

LIST OF TABLES